CENPA

Center for Experimental Nuclear Physics and Astrophysics

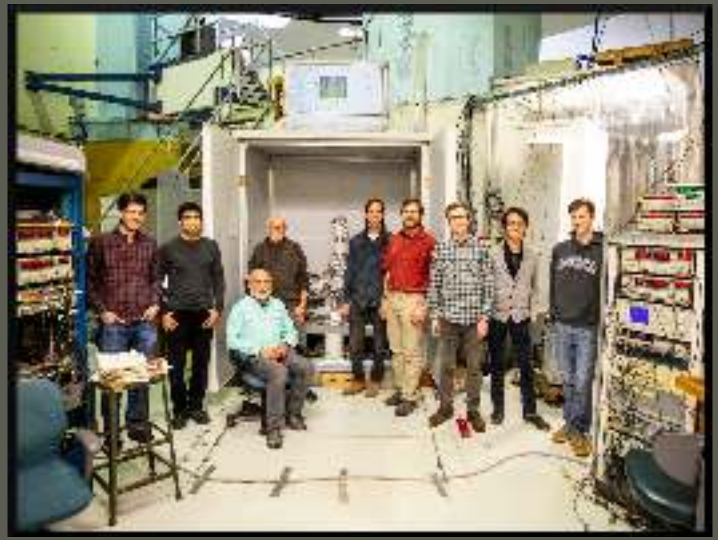

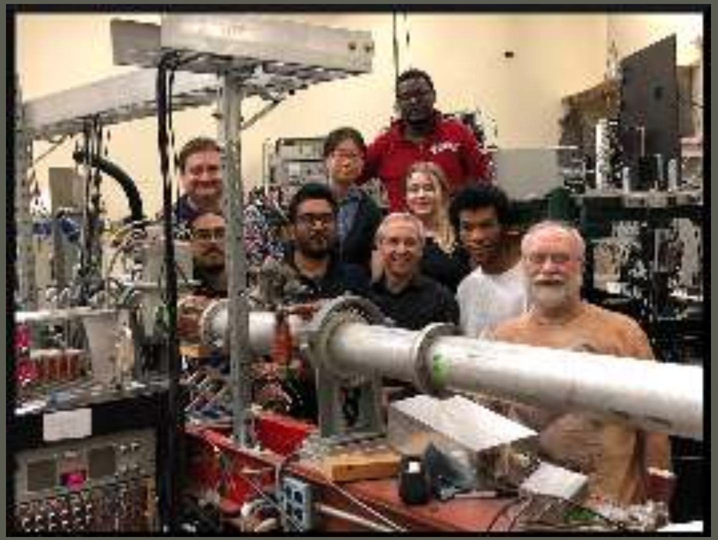

Annual Report 2019

University of Washington

Annual Report 2019 CENTER FOR EXPERIMENTAL NUCLEAR PHYSICS AND ASTROPHYSICS University of Washington

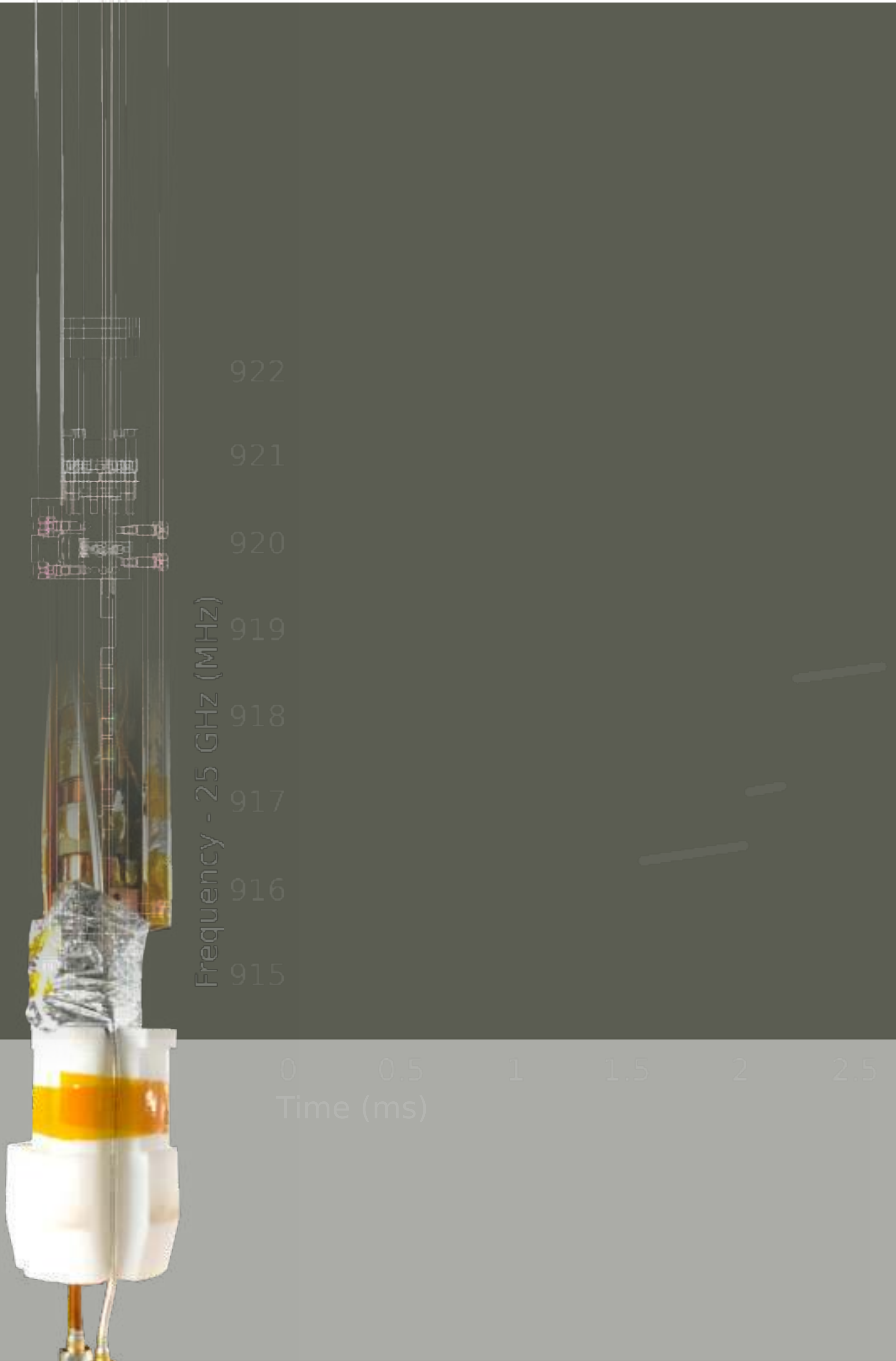

ANNUAL REPORT

Center for Experimental Nuclear Physics and Astrophysics
University of Washington
June 1, 2019

Sponsored in part by the United States Department of Energy
under Grant #DE-FG02-97ER41020.

Cover design by Gary Holman.
Photo credits: Dennis Wise for Gravity photo, ADMX collaboration for ADMX photo, Ida Boeckstiegel for all others.
Cover front: Research group photos - *Top left:* Gravity (Sec. 2.1), *Top right:* $^{21}\mathrm{Ne}^{+}$ (Sec. 7.3), *Bottom left:* Muon $g-2$ (Sec. 4.6), *Bottom right:* ADMX (Sec. 5.1).
Cover back: Project 8 circular wave guide assembly. Concept from idea, design, fabrication to results (Sec. 1.18).

INTRODUCTION

The Center for Experimental Nuclear Physics and Astrophysics, CENPA, was established in 1998 at the University of Washington as the institutional home for a broad program of research in nuclear physics and related fields. Research activities — with an emphasis on fundamental symmetries and neutrinos — are conducted locally and at remote sites. In neutrino physics, CENPA is the lead US institution in the KATRIN tritium beta decay experiment, the site for experimental work on Project 8, a collaborating institution in the Majorana ^{76}Ge and LEGEND-200 double beta decay experiments and in the COHERENT neutrino-nucleus scattering experiment. The Muon Physics group developed and completed the MuSun experiment to measure muon capture in deuterium at the Paul Scherrer Institute in Switzerland. The muon group has a major leadership role in the measurement of the muon's anomalous magnetic moment at Fermilab, which aims to even higher precision than it is presently known from the our previous work at Brookhaven. The fundamental symmetries program also includes "in-house" research on the search for a static electric dipole moment in ^{199}Hg, and an experiment using the local tandem Van de Graaff accelerator to measure the electron-neutrino correlation and Fierz interference in ^{6}He decay.

In addition to the research directly supported by DOE's Office of Nuclear Physics through the CENPA core grant, other important programs are located at CENPA, forming a broader intellectual center with valuable synergies. The "Gravity" group carries out, with both DOE and NSF support, studies of the weak and strong Equivalence Principles, fundamental precepts of General Relativity, as well as searches for non-Newtonian forces such as those predicted by theories with extra dimensions. In addition, they participate in LIGO. The DOE Office of High Energy Physics supports the unique ADMX axion search experiment.

CENPA is home to a large number of faculty, research faculty, postdoctoral researchers, graduate, and undergraduate students. The core professional engineering and technical staff provide diverse capabilities and skills such as state-of-the-art detector development, fabrication of custom electronics, large-scale computing, and design engineering. New advancements, capabilities, and ideas are regularly shared at seminars by CENPA members and visitors alike.

Transitions

We congratulate Jason Detwiler on his promotion to Associate Professor of Physics, with tenure.

Research Assistant Professor Martin Fertl (Project 8 / Muon g-2) will begin a position as an associate university professor with tenure at the Johannes Gutenberg University Mainz, Germany. Postdoc Kim Siang Khaw (Muon g-2) will begin a position as a T. D. Lee Fellow at TDLI, and a joint appointment of a Tenure-track Associate Professor at the School of Physics and Astronomy (SPA), Shanghai Jiao Tong University (SJTU). Postdoc Dan Salvat (MuSun) left CENPA in fall 2018 for a research scientist position at Indiana University. ADMX postdoc Rakshya Khatiwada departed for a senior postdoc appointment at Fermilab. Hg-199 Postdoc Megan Ivory accepted a staff position at Sandia National Lab. Postdoc Menglei Sun joined us in December 2018 to work on the KATRIN experiment. ADMX has added two new postdocs: Nicole Crisosto from the University of Florida, and Chelsea Bartram, from the University of North Carolina. We note that, at one point in Spring 2019, CENPA had five women postdocs on staff: Menglei Sun (KATRIN), Rachel Ryan (MuSun), Elise Novitski (Project 8), Megan Ivory (Hg-199), and Nicole Crisosto (ADMX).

We continue to train a large number of graduate students at CENPA. This past year, we graduated four, and several others are scheduling their defenses for summer quarter. Nathan Froemming (Muon g-2 Beam Dynamics) began a postdoc in accelerator physics at NIU. Aaron Fienberg (Muon g-2 Precession Analysis) is continuing with our group he starts a postdoc at Penn State in August, working on the IceCube experiment. Luke Kippenbrock (KATRIN spectrometer backgrounds) completed his thesis and is taking a short time off before starting work in industry. Rachel Ryan (MuSun Analysis) completed her defense in March, and will stay on through most of 2019 to help realize the first publications. Jennie Chen (NSF-supported,Hg-199) is now a postdoc at Indiana University working on the Los Alamos neutron EDM experiment. Former UW Ph.D. student Eric Martin has taken a postdoc at the University of North Carolina, working on KATRIN and LEGEND. Sebastian Alvis left the program in Summer 2019 with a Master's degree to train for a career in data science.

Notable

We are in the second year of our three-year DOE Office of Nuclear Physics award to CENPA, which is supporting the bulk of the efforts described in this Annual Report.

Alvaro Chavarria became spokesperson of DAMIC at SNOLAB experiment. Aaron Feinberg's outstanding muon g-2 thesis was recognized with the Henderson Prize by the Department of Physics. Selena graduate student Alex Piers won an NSF Graduate Research Fellowship.

The CENPA Seminar Series, initiated and run by Martin Fertl, has been extremely successful. Over the past 12 months, we have hosted 22 speakers, covering a wide range of topics of interest to the Center. These talks are very popular and very well attended. Kim Siang Khaw took over the leadership in 2019.

Research Highlights

- The TRIMS experiment has acquired a year's high-quality data on both HT and T_2 to measure the branching ratios to ionic final states in tritium decay. This is a test of the molecular theory that is used to interpret the KATRIN data. Our results support the theoretical expectations and disagree strongly with older experiments. The analysis continues and a publication is in preparation.

- KATRIN began its first operations with tritium. The spectral quality is outstanding, and the data match the expected spectrum beautifully. The initial run was with a concentration of 1% T_2 in D_2, at half the design column density. Following careful checks for possible transmission of tritium down the beam line, the intensity has been raised to 25% pure T_2 for the first physics run now in progress.

- Project 8 took its first tritium data in the fall of 2018, a week-long run with tritium in the small waveguide cell that is used in Phase II. A low-statistics spectrum showing the last 2 keV of the spectrum with no background events above the endpoint was clearly seen.

- The large magnet for Phase III of Project 8 was installed in the Physics-Astronomy building, commissioned, shimmed, and mapped. The magnet formerly served as a hospital MRI. In this phase of Project 8, the acquisition of cyclotron radiation emission signals from electrons not confined in a waveguide will be developed.

- The MAJORANA DEMONSTRATOR produced new limits on neutrinoless double-beta decay, published in Phys. Rev. C, showing world-leading energy resolution and new information on background processes. The experiment continues to take data while preparations are underway for a cabling upgrade in late 2019, followed by the eventual relocation of the HPGe detectors to LEGEND 200.

- The LEGEND Collaboration now has the resources in hand to mount the LEGEND-200 first phase, and preparations are underway for data taking to begin as early as 2021. R&D for the follow-on LEGEND-1000 phase is also being pursued vigorously.

- The accelerator was fixed to allow using the terminal-ion source to deliver high-current low-energy beams for a 21Ne(p,g) experiment. An angular correlation system and associated electronics for a total of 12 detectors was assembled with appropriate lead shielding. We expect to run the experiment through the summer of 2019.

- The data analysis on extraction of little-a from laser-trapped 6He has progressed. Additional detailed studies of the detection systems were carried out to address systematic uncertainties and these were cleared up. The analysis is now in its final stages.

- We are moving on with mounting the experiment to search for Tensor currents via little-b from 6He. The design for the cryo systems was finished and is now being built. The RF and daq are working. The superconducting solenoid was cooled down and biased successfully. We expect to get signals before the end of 2019.

- The first MuSun production run has been analyzed in a UW Ph.D. thesis (defense March 2019), and the analysis of the full data set is well advanced. A first physics result is expected in 2019.

- The Muon $g-2$ experiment completed its first data taking campaign and has been vigorously analyzing the data in anticipation of a physics release in early fall, 2019.

- The Muon $g-2$ experiment has upgraded key components of the Storage Ring and has begun Run-2 in its campaign toward a fourfold improvement in the precision of the measurement of the muon anomalous magnetic moment.

- The ADMX G2 experiment continued to operate searching for QCD Axion Dark Matter.

- The DAMIC experiment at SNOLAB completed taking data for its WIMP search. The final DAMIC Analysis Workshop was hosted at CENPA. Results are being prepared for publication.

- The first development skipper CCDs for the DAMIC-M experiment arrived at CENPA. These new devices are the first large-format CCDs with single-charge response.

- Dark matter may consist of"fuzzy" ultra-low-mass bosons whose quantum mechanical behavior can impact galactic structures. Experimentally, such dark matter behaves as a coherent waves rather than as a collection of particles. The Eot-Wash group has analysed a 6.7 year span of data taken with a quantum electron gyroscope containing no moving parts. They made the first direct search for the axion-like wind from this new form of dark matter for axionlike masses as low as 10^{-23} eV.

- The CENPA LIGO Group built four tiltmeters at LIGO Livingston Laboratory which has improved its seismic isolation and will likely increase duty-cycle for gravitational-wave observation. A new Observing run, O3, started in April 2019 with improved detection range which is expected to yield 3-4 times higher event rate than previous runs.

As always, we encourage outside applications for the use of our facilities. As a convenient reference for potential users, the table on the following page lists the capabilities of our accelerators. For further information, please contact Gary Holman, Associate Director (holman@uw.edu) or Eric Smith, Research Engineer (esmith66@u.washington.edu) CENPA, Box 354290, University of Washington, Seattle, WA 98195; (206) 543 4080. Further information is also available on our web page: `http://www.npl.washington.edu`.

We close this introduction with a reminder that the articles in this report describe work in progress and are not to be regarded as publications nor to be quoted without permission of the authors. In each article the names of the investigators are listed alphabetically, with the primary author underlined in the case of multiple authors, to whom inquiries should be addressed.

David Hertzog, Director

Gary Holman, Associate Director and Editor
Elise Novitski and Clint Wiseman, Technical Editors

TANDEM VAN DE GRAAFF ACCELERATOR

Our tandem accelerator facility is centered around a High Voltage Engineering Corporation Model FN purchased in 1966 with NSF funds, with operation funded primarily by the U.S. Department of Energy. See W. G. Weitkamp and F. H. Schmidt, "The University of Washington Three Stage Van de Graaff Accelerator," *Nucl. Instrum. Methods* **122**, 65 (1974). The tandem was adapted in 1996 to an (optional) terminal ion source and a non-inclined tube #3, which enables the accelerator to produce high intensity beams of hydrogen and helium isotopes at energies from 100 keV to 7.5 MeV.

Some Available Energy Analyzed Beams

Ion	Max. Current (particle μA)	Max. Energy (MeV)	Ion Source
^{1}H or ^{2}H	50	18	DEIS or 860
^{3}He or ^{4}He	2	27	Double Charge-Exchange Source
^{3}He or ^{4}He	30	7.5	Tandem Terminal Source
^{6}Li or ^{7}Li	1	36	860
^{11}B	5	54	860
^{12}C or ^{13}C	10	63	860
*^{14}N	1	63	DEIS or 860
^{16}O or ^{18}O	10	72	DEIS or 860
F	10	72	DEIS or 860
* Ca	0.5	99	860
Ni	0.2	99	860
I	0.001	108	860

*Negative ion is the hydride, dihydride, or trihydride.

Several additional ion species are available including the following: Mg, Al, Si, P, S, Cl, Fe, Cu, Ge, Se, Br and Ag. Less common isotopes are generated from enriched material. We recently have been producing the positive ion beams of the noble gases He, Ne, Ar, and Kr at ion source energies from 10 keV to 100 keV for implantation, in particular the rare isotopes ^{21}Ne and ^{36}Ar. We have also produced a separated beam of 15-MeV ^{8}B at 6 particles/second.

Contents

1 Neutrino Research

KATRIN

1.1 Status of the KATRIN neutrino mass experiment

J. F. Amsbaugh, A. Beglarian*, T. H. Burritt, P. J. Doe, S. Enomoto, J. A. Formaggio†, F. M. Fränkle*, M. Hanley, A. Vizcaya Hernandez‡, L. Kippenbrock, A. Kopmann*, E. L. Martin§, D. S. Parno‡, D. A. Peterson, A. W. P. Poon¶, R. G. H. Robertson, S. Schmid*, M. Sun, D. Tcherniakhovski*, L. A. Thorne‡, T. D. Van Wechel, J. F. Wilkerson§, and S. Wüstling*

This has been a momentous and exciting year for the KATRIN experiment. After 18 years of planning, designing, constructing and commissioning, data have been taken with the tritium source at the nominal intensity of 10^{11} Bq, confirming that the major components; the source, transport, spectrometers and detector function in concert, as designed. On 11th June, 2018 the KATRIN tritium inauguration took place with the simultaneous pressing of 15 buttons by a number of dignitaries, including two Nobel laureates and our very own Hamish Robertson representing the US institutes. The result of this team effort can be seen in Fig. 1.1-1

The goals of First Tritium were modest but important. The gaseous source contained only 0.5% tritium, with the balance made up of deuterium. Electrons from the source were successfully transported to the spectrometers and imaged by the detector, where they were counted. After 14 days of running it was shown that the overall stability of the apparatus met the design goal of 0.1%. At this reduced source strength the data could not establish a new limit on the neutrino mass but was sufficient to exercise and check the data analysis strategies. In addition, the low source intensity, and therefore low event rate deep into the spectrum, allowed a preliminary search for evidence of a sterile neutrino. The beta decay spectrum was probed to 1.6 keV below the 18.6 keV endpoint, entering a previously unexplored region of phase space and laying a foundation for further investigation. A paper summarizing this work will appear in the summer.

The next data-taking campaign involved the source and transport system (STS3a) running through September and October 2018. Three years in the planning, it consisted of 16 areas of investigation that would characterize the entire source and transport components of KATRIN to be conducted over a 13-week period. Scheduling pressures reduced this to 7 weeks and 8 areas of investigation. Nevertheless a rich harvest ensued requiring over 4 months of analysis.

Understanding the energy loss of electrons escaping the source is critical for KATRIN.

*Karlsruhe Institute of Technology, Karlsruhe, Germany.
†Massachusetts Institute of Technology, Cambridge, MA.
§University of North Carolina, Chapel Hill, NC.
‡Carnegie Mellon University, Pittsburgh, PA.
¶Lawrence Berkeley National Laboratory, Berkeley, CA.

Figure 1.1-1. Are they applauding or praying? The first electrons from tritium beta decay can be seen in the detector image, shown in the upper right of the screen. To the left is shown a tense KATRIN control room.

Energy loss measurements by time of flight showed excellent agreement with the conventional integral measurements, giving an additional handle on this important systematic. Also demonstrated was the ability to derive the source column density by measuring the survival probability of electrons traversing the source. Using the lines associated with the ^{83m}Kr spectrum enabled studies of the efficacy of biasing the rear wall to control the source plasma potential.

We have entered a new calendar, KNM1, KATRIN Neutrino Mass Cycle #1. KNM1 ran from March through April 2019, yielding 34 days of tritium spectral data taken at 25% column density. With this data it is expected to achieve a 1 eV result, or better, by years end. As KNM1 proceeded, the column density was steadily increased while the stability and performance of the entire apparatus was monitored. At column densities of 50%, and more so at 100%, it was found that returning the gas to the source was increasingly difficult, resulting in a reduction of the column density. Investigation revealed that the effect of the intense radiation on the stainless steels walls of the source was producing tritiated methane, CT_4, which freezes at the 30K temperature of the source, thereby constricting the capillary supply tube. The solution is to place a cold trap in-line, removing the CT_4 before it has a chance of freezing and constricting the narrow tube. This will be implemented during the summer maintenance period. The remainder of the tritium data taking took place at a column density of 25%, which provided sufficient stability.

KATRIN is a large and complex instrument, and commissioning has been an adventure of surprises and unexpected challenges as illustrated by the CT_4 experience. Elevated backgrounds in the main spectrometer, associated with the production of Rydberg atoms and the presence of radon from the NEG pumps remain a challenge, however innovative proposals such as moving the analysis plane in the main spectrometer and reducing the temperature of the baffles designed to trap radon are being studied.

With the completion of the summer maintenance period, KATRIN will embark on regular cycles of tritium data taking at 100% column density. Three, three-month periods of data taking will be interspersed with 1 month of maintenance. The MoU between the US institutes and KATRIN has been extended until 2025. KATRIN is expected to reach the design sensitivity of 0.2 eV by 2024.

1.2 KATRIN Data-taking

J. F. Amsbaugh, A. Beglarian*, T. H. Burritt, P. J. Doe, S. Enomoto, J. A. Formaggio†, F. M. Fränkle*, M. Hanley, A. Vizcaya Hernandez‡, L. Kippenbrock, A. Kopmann*, E. L. Martin§, D. S. Parno‡, D. A. Peterson, A. W. P. Poon¶, R. G. H. Robertson, S. Schmid*, M. Sun, D. Tcherniakhovski*, L. A. Thorne‡, T. D. Van Wechel, J. F. Wilkerson§, and S. Wüstling*

After many years of construction and commissioning runs, KATRIN started data acquisition in 2018. Tritium gas was injected into the Windowless Gaseous Tritium Source (WGTS) for the first time on May 18. Following the two-day Very First Tritium campaign on May 18 and 19, KATRIN performed two weeks of First Tritium measurements of the integral beta-decay spectrum starting from June 5. Then the system went through eight months of maintenance, upgrades, and electron gun measurements. Starting from March 2019, KATRIN entered a new measurement phase, the First Neutrino Mass campaign, with the goal of achieving a sensitivity of 1 eV.

The Very First Tritium Campaign

The main goals of the Very First Tritium campaign are to prove the blocking and removal of positive ions and to test the system configuration for tritium scans. A variety of positive ions can arise from beta decays of tritium molecules and ionization of the tritium gas. These ions can cause a tritium contamination in the spectrometer as well as create a large background for the beta electron measurements. To block

*Karlsruhe Institute of Technology, Karlsruhe, Germany.
†Massachusetts Institute of Technology, Cambridge, MA.
§University of North Carolina, Chapel Hill, NC.
‡Carnegie Mellon University, Chapel Pittsburgh, PA.
¶Lawrence Berkeley National Laboratory, Berkeley, CA.

the ions, two ring electrodes are installed in the transport section and biased at +200 V. The blocked ions will be removed by four dipole electrodes installed between the WGTS and ring electrodes. The positive ions can be detected by the Faraday cup on the Forward Beam Monitor (FBM) or as electrical current on the electrodes. During the Very First Tritium campaign, no ion flux was observed in the FBM, indicating that ions were successfully blocked. Furthermore, the pre-spectrometer was filled with argon gas to detect any residual ions. Positive ions, that could potentially overcome the blocking electrodes, would ionize the argon gas and produce secondary electrons. No electrons were observed in the FPD, verifying that ions are blocked.

After confirming the removal of positive ions, the first scans of the tritium beta-decay spectrum were performed on May 19. The average column density was approximately 4.62×10^{17} molecules/cm^2, corresponding to 90% of the nominal value. The gas used in this measurement phase contains about 1% DT and 99% D_2, for a tritium activity of 0.5% nominal value. Due to hardware limitations, the magnetic fields of the source and pinch magnet were set to 70% of the design values. A total of 8 scans of the beta spectrum were conducted during the Very First Tritium campaign, each covering the retarding potential from 16.676 kV to 18.605 kV.

The First Tritium Campaign

The continuous measurements of tritium beta decay started on June 5th and are referred to as the First Tritium campaign. The operational settings used in this measurement phase are the same with the Very First Tritium campaign. A total of 61 scans, equivalent to a cumulative measurement time of approximately 4.9 days, were recorded and deemed to be suitable for a neutrino mass study. To eliminate any drift in the retarding potential due to the change of voltage, the scans were performed in both ramping up and ramping down modes.

This data-taking phase has two main goals: firstly, to demonstrate a global system stability to the 0.1% level, and secondly, to investigate the impact of system effects on the beta spectrum and test analysis strategies. To evaluate the stability, multiple operational parameters were monitored during the data taking. For example, Fig. 1.2-1 shows the source temperature, buffer pressure, and DT concentration over 12 hours. It demonstrates that the source parameters are stable within their specifications. Analysis of the data is still ongoing, and the results are expected to be available in the summer of 2019.

The First Neutrino Mass (KNM1) Campaign

After the First Tritium measurement phase, KATRIN spent eight months in system maintenance and upgrades. In March 2019, the collection of beta-decay data was restarted with an increased tritium activity, aiming for a sensitivity of the neutrino mass of 1 eV. The column density is approximately 1.1×10^{17} molecules/cm^2, equivalent to 25% of the nominal value. Unlike the D_2 gas with 1% DT concentration used in First

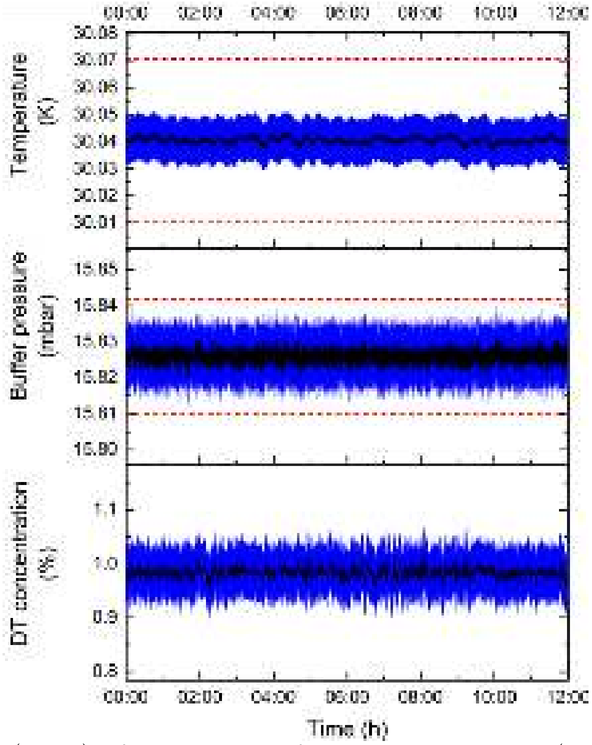

Figure 1.2-1. Values (black) of the sensors of source temperature (*top*), buffer pressure (*middle*), and DT concentration (*bottom*) over 12 hours. The blue area indicates the systematic uncertainties, and red dashed lines are the 0.1% stability required for a neutrino mass measurement.

Tritium measurement, T_2 gas with 95% purity is used for the KNM1 campaign. The beta-decay spectrum is scanned with the retarding potential ramping up or ramping down, covering the voltage from 18.373 kV to 18.623 kV.

In the beginning of the KNM1 data taking, effort was made to optimize the bias voltage setting for the rear wall, which is a gold plated disk located at the end of the experiment. The rear wall defines the potential of the gas in the source. An optimized rear wall voltage will improve the homogeneity of the potential in both the radial and longitudinal directions. A dedicated study of the rear wall potential shows that good performance can be achieved at -150 mV, and this value is now used as the default setting for the KNM1.

The system has been operating smoothly during this data taking phase, and more than 200 scans have been accumulated by the end of April 2019. Data taking for KNM1 is expected to continue until the second week of May.

1.3 KATRIN Data Quality

S. Enomoto, S. Hickford† D.S. Parno*, R.G.H. Robertson, and M. Sun

The UW KATRIN group has been deeply involved in the development of a system to ensure the quality of the data used for the neutrino mass analysis. Our strategy is to determine the quality of the data based on the operating status of the apparatus. Data will be excluded from the analysis if it is collected during times when the monitored values of the hardware are not in the specified range.

We have implemented a software toolkit to evaluate and record the quality of data. The status of the KATRIN hardware is monitored by multiple sets of sensors. The first step of the quality analysis workflow is to define the quality criteria of these sensors. We have been working with various subsystem task groups to determine these criteria and recorded them in user-friendly spreadsheets. Our toolkit can read the quality criteria from spreadsheets and convert them into software-readable format. The second step is to configure a chain of quality analysis modules using the criteria previously defined. The current software includes various quality control modules, including an alert on values beyond upper/lower thresholds, an alert on missing data points, etc. These analysis modules take the readout values of sensors as input, classify the data as "Good", "Bad" or "Use with caution", and then record the quality results in files for bookkeeping.

The data quality analysis toolkit has been integrated into KAFFEE, which is a software system that automatically applies analysis chains to process KATRIN data. This allows the quality results to be available shortly after data taking. We have been using this toolkit to monitor the data during the KNM1 measurement phase. The overall quality of the KNM1 data is good, except for a few short periods of missing sensor data due to network problems.

1.4 KATRIN spectrometer backgrounds

L. Kippenbrock and D.S. Parno*

We have recently completed an investigation into KATRIN backgrounds from three distinct sources: muon-induced secondary electrons, gamma-induced secondary electrons, and the Penning trap between the pre-spectrometer and the main spectrometer. Here, we summarize the results documented in the PhD thesis of Luke Kippenbrock (March 2019).

The first two types of background arise from the operating principles of the main-spectrometer MAC-E filter. A β that is transmitted through to the focal-plane detector

†Karlsruhe Institute of Technology, Karlsruhe, Germany.
*Carnegie Mellon University, Chapel Pittsburgh, PA.
*Carnegie Mellon University, Pittsburgh, PA.

is first decelerated to nearly zero kinetic energy by the longitudinal retarding potential, before being reaccelerated. Low-energy secondary electrons created in the central portion of the main spectrometer are therefore particularly pernicious backgrounds, because they arrive at the detector with essentially the same energy as signal βs. Many processes can produce such low-energy secondaries; this study focused on those induced by cosmic-ray muons and by gammas from environmental radioactivity. These analyses have been described in earlier reports[1], but were both finalized within the last year.

The background contribution originating from cosmic-ray muons was studied via background measurements taken December 2014 – January 2015. In those measurements, plastic-scintillator modules were mounted at the main spectrometer to provide muon timing information. Measurement runs alternated between three different electromagnetic configurations, including one configuration designed to directly image secondary electrons from the spectrometer walls. These data were used to validate our model of the background mechanism (Fig. 1.4-1, left panel), which is based on simulation in the Kassiopeia framework[2]. A correlation analysis, comparing measured muon rates with measured backgrounds, constrained this background contribution at less than 0.115 counts per second (90% confidence) in the nominal configuration[3].

Gammas in the KATRIN spectrometer hall were mitigated during construction via selection of low-background materials for the main-spectrometer hull and the concrete floor. Using the original radioassay data, we built a GEANT4 model of the environmental radioactivity in order to predict the gamma flux through the main spectrometer. Fig. 1.4-1, right panel, compares this simulated gamma energy spectrum with the energy spectrum measured using a portable germanium detector. Our model allowed us to predict the impact on the gamma flux of two special background-measurement configurations from the summer of 2015: the introduction of an intense ^{60}Co source just outside the main spectrometer (enhancing the gamma flux) and the addition of water shielding below the main spectrometer (suppressing the gamma flux). We inferred that, under nominal conditions, the contribution from this background is less than 0.006 counts per second (90% confidence)[4].

The final background type under investigation originates from the tandem operation of two MAC-E filters – the pre-spectrometer and the main spectrometer – in series. Both spectrometers are held at high negative potential, with the beam pipe between them at ground; in this central region the electrons also pass through a strong magnetic field within a superconducting solenoid. This field configuration inevitably traps electrons between the spectrometers. These trapped electrons have a long path length, and in scattering interactions with residual gas they create positive ions. These ions escape into the bulk of the main spectrometer and undergo ionization interactions in turn, producing low-energy ionization electrons that register as backgrounds in the

[1] CENPA Annual Report, University of Washington (2018) p. 8.
[2] D. Furse *et al.*, New J. Phys. **19** 053012 (2017).
[3] K. Altenmüller *et al.* (KATRIN collaboration), Astropart. Phys. **108** 40 (2019).
[4] K. Altenmüller *et al.* (KATRIN collaboration), arXiv:1903.06452 [physics.ins-det].

detector. We have previously reported on our finding that backgrounds due to the Penning trap are heavily dependent on the pressure in the spectrometers, and that these backgrounds make a negligible contribution to the overall background level measured before the introduction of tritium[1]. Since that time, we have completed a first Kassiopeia[2] simulation of the backgrounds resulting from this process, allowing us to study the detector acceptance of background electrons based on the initial properties of their progenitor ions. If the Penning-induced background becomes significant in tritium operations, this study will be extended.

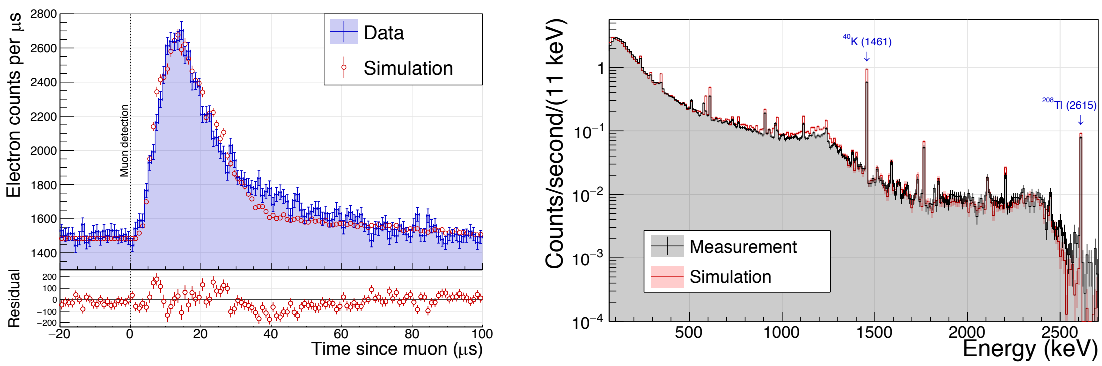

Figure 1.4-1. *Left:* Measured (blue) and simulated (red) distribution of timing differences between electron and muon events, collected with a magnetic field setting that mapped a portion of the main-spectrometer walls directly to the detector. $t = 0$ μs corresponds to the detection of a muon event. The simulated background ($t < 0$) and signal $t > 0$ are scaled separately to minimize the χ^2/ndf. Error bars are statistical. The residuals in the bottom panel give the simulated values minus the data[3]. *Right:* Measured (black) and simulated (red) energy spectrum of gammas from environmental radiation in the KATRIN spectrometer hall. The measurement was performed with a portable germanium detector. The simulation, which uses a simplified model for the detector, is scaled to the measurement with a single normalization factor[4].

TRIMS

1.5 TRIMS Analysis Update

M. Kallander, Y.-T. Lin, E. M. Machado, D. S. Parno*, R. G. H. Robertson, and A. P. Vizcaya Hernandez*

The Tritium Recoil-Ion Mass Spectrometer (TRIMS) experiment measures the branching ratio between bound (^{3}HeT+) and unbound (T+, ^{3}He+) ions that are produced by molecular-tritium (T_2) beta decay. The experiment sets up a uniform magnetic field of 0.237 Tesla and a uniform electric field of 60 kV/20 cm that run parallel to

*Carnegie Mellon University, Pittsburgh, PA.

[1] CENPA Annual Report, University of Washington (2018) p. 7.

each other coaxial with a cylindrical acceleration chamber. Inside the chamber, tritium decays and the product ions are accelerated toward a silicon ion detector at the cathode and the betas to a silicon beta detector at the anode. By performing energy and time-of-flight measurements of the coincident ions and betas, TRIMS can categorize these events and measure the branching ratio in question. The knowledge of this branching ratio will provide a verification of the theoretical framework that has been applied to describe the final state distribution of the beta decay spectrum measured by the KATRIN experiment[1].

Bound and unbound ions have different masses, and can be categorized by measuring their energy and time-of-flight. The TRIMS data taken since 2018 is shown as an ion energy versus ion mass 2D histogram in Fig. 1. The ion energy on the y-axis has been corrected based on a SRIM simulation[2]. After fitting the corrected ion energy as a quadratic polynomial function of the detected ion energy, we get the following conversion,

$$E_{\text{ion}} = 3.945 + 1.3529 E_{\text{ion,det}} - 0.0017346 E_{\text{ion,det}}^2. \tag{1}$$

The fit was specifically done for ^{3}He, but since we cannot distinguish the ion types a priori, the polynomial is applied as an effective energy correction to all ion types. We can see in Fig. 1 that the ^{3}He+ mass-3 band extends close to 60 keV at the high-energy end as expected. As for the ion mass on the x-axis, we derive the following formula based on non-relativistic kinematics,

$$m_{\text{ion}} = 2E_{\text{ion}} \left(\frac{T_{\text{ion}}}{\frac{2E_{\text{ion}}}{qV} L + L_{\text{ion}}} \right)^2, \tag{2}$$

where L is the chamber length and qV is the applied voltage in keV. The parameter L_{ion} is the extra distance between the mesh cathode and the ion detector, where there is no electric field. The parameter T_{ion} is the ion time-of-flight derived from the following formula,

$$T_{\text{ion}} = t_{\text{ion}} - (t_\beta - \overline{T}_\beta) - t_0, \tag{3}$$

where t_{ion} and t_β are the particle arrival times to the detectors, $\overline{T}_\beta$ is the mean beta time-of-flight obtained by a Geant4 simulation[3], and t_0 is the time-zero correction to our electronics setup. By substituting Eq. 1 and Eq. 3 into Eq 2, we can reconstructe the ion mass m_{ion} for each event. The mass axis in Fig. 1 uses a square-root scale to make sure the mass bands have similar width, exhibiting the separation power of TRIMS for ions that have different masses.

For a pure T_2 source, mass-3 (T+ and ^{3}He+) and mass-6 (^{3}HeT+) bands would be dominant. However, our source has a high percentage of HT as well, which produces mass-1 (H+), mass-3 (^{3}He+), and mass-4 (^{3}HeH+). Furthermore, we are able to

[1] L. I. Bodine, D. S. Parno and R. G. H. Robertson, Phys. Rev. C **91**, 035505 (2015).
[2] J. F. Ziegler, M. D. Ziegler, and J. P. Biersack, Nucl. Instr. Meth. B., **268**, 11-12 (2010).
[3] S. Agostinelli et al., Nucl. Instr. Meth. A., **506**, 3 (2003)

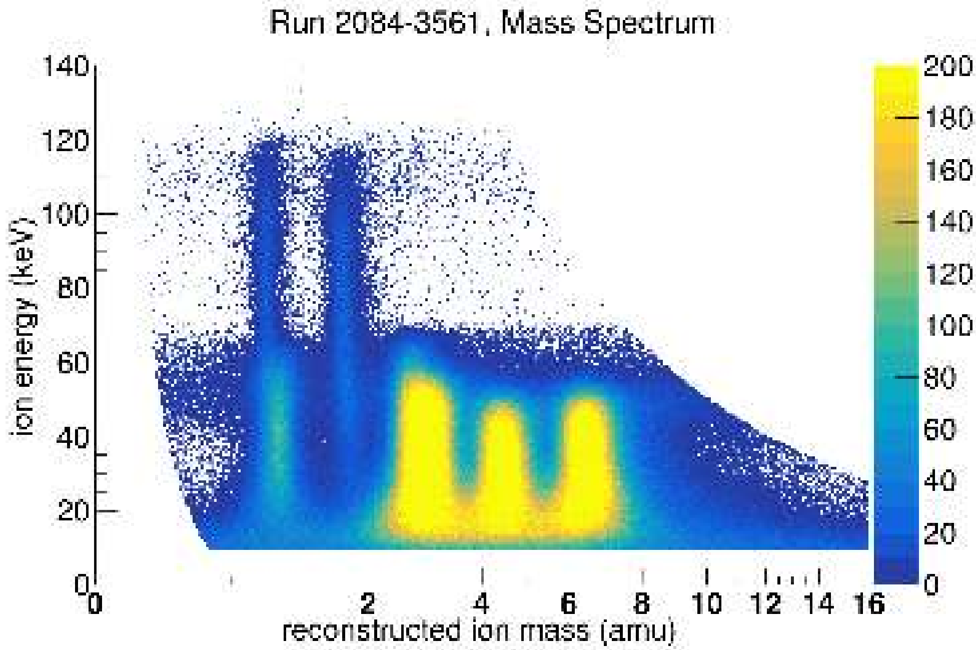

Figure 1.5-1. TRIMS T_2+HT data in incident ion energy versus reconstructed ion mass.

observe two-ion events and doubly charged events, both of which result in bands going up to 120 keV. The two-ion events come from either combinations of (He+, T+) or (He+, H+) and appear as a mass-$\frac{3}{2}$ band. The doubly charged events come from He++ that appears as a mass-$\frac{3}{4}$ band. Because of these detailed structures that we are able to observe, clean event-type separation has been one of the main goals of our ongoing analysis effort.

Majorana

1.6 Status of the Majorana Demonstrator neutrinoless double-beta decay search

M. Buuck, J. A. Detwiler, I. Guinn, A. Hostiuc, W. Pettus, N. W. Ruof, and C. Wiseman

The Majorana Demonstrator neutrinoless double-beta decay search continues to take data at the Sanford Underground Research Facility in Lead, SD. The Collaboration released their second result with a limit that contributes significantly to the global sensitivity in ^{76}Ge, but also observed a higher than expected background in the vicinity of the region of interest for the double-beta decay search. CENPA group members played a central role in the development and tuning of some of the key analysis parameters for that result, and are working on new analysis developments to enhance the sensitivity of the experiment's neutrinoless double-beta decay search. We are also helping to lead the investigation the source of the high background, while pursuing searches for other rare physics with the Demonstrator, such as ^{76}Ge double-beta decay to excited states of ^{76}Se, or scattering with Dark Matter or axion-like particles.

1.7 Multi-Site background rejection in the Majorana Demonstrator

S. I. Alvis, M. Buuck, C. Cuesta*, J. A. Detwiler, I. Guinn, A. Hostiuc, W. Pettus, N. W. Ruof, and C. Wiseman

Majorana's P-type point contact (PPC) detectors were selected for their excellent multi-site background rejection derived from waveform pulse shape analysis (PSA). The long drift times across the detector bulk ($> 10\,\mu$s) combined with the heavily localized weighting potential near the point contact yield waveforms with fast rising edges. The current waveform is calculated from the digitized charge waveforms, both shown in Fig. 1.7-1, and a discriminating variable is calculated from the maximum value of the current waveform[1], A. The cut parameters are tuned for each detector individually to optimize background rejection with minimal signal loss across a wide energy range.

*Presently at Centro de Investigatciones Energéticas, Medio Ambientales y Technológicas, Madrid, Spain.

[1]CENPA Annual Report, University of Washington (2018) p. 20.

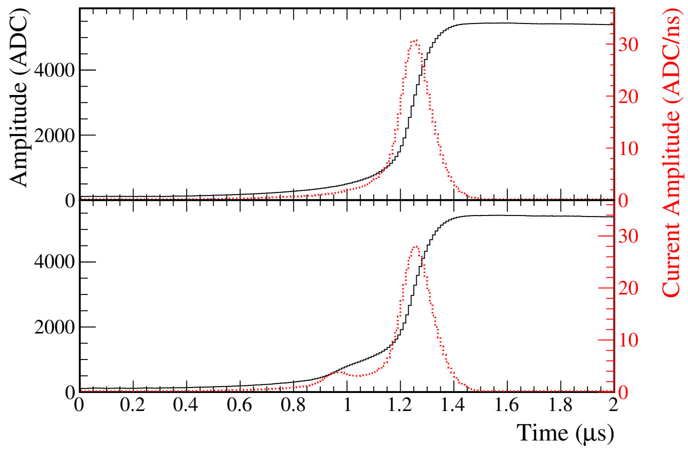

Figure 1.7-1. Example charge (solid black) and current (dashed red) single-site (*top*) and multi-site (*bottom*) waveforms from a single detector with energies near $Q_{\beta\beta}$ from calibration data. The MAJORANA detectors have excellent ability to identify and reject background events comprised of multiple energy depositions.

The MAJORANA DEMONSTRATOR has transitioned from commissioning data characterized by more rapid changes in the experimental configuration and detector settings to stable physics data-taking. This operational shift redirects the emphasis of new PSA work to understand stability over extended time periods. The newest data release from MAJORANA includes over one year of continuous data taken at consistent operating conditions with multiple interleaved extensive calibration datasets.

In assessing the PSA performance throughout this new data, the dominant behavior observed was stability throughout, as expected for stable operation. However, there were a set of discontinuities followed by relaxations to baseline performance. These instabilities were strongly correlated with known high voltage (HV) events: full-array or single-detector bias changes, and breakdowns. The response of individual detectors varied significantly; some detectors returned to baseline in less than a day following their own rebiasing, while others drifted over a month or more following an HV event in a different detector (see Fig. 1.7-2). These correlated changes in PSA performance could potentially be mitigated by a planned future upgrade to the cables and connectors used in the experiment. A Kolmogorov-Smirnov test has been implemented to characterize the stability of the PSA and inform data quality decisions.

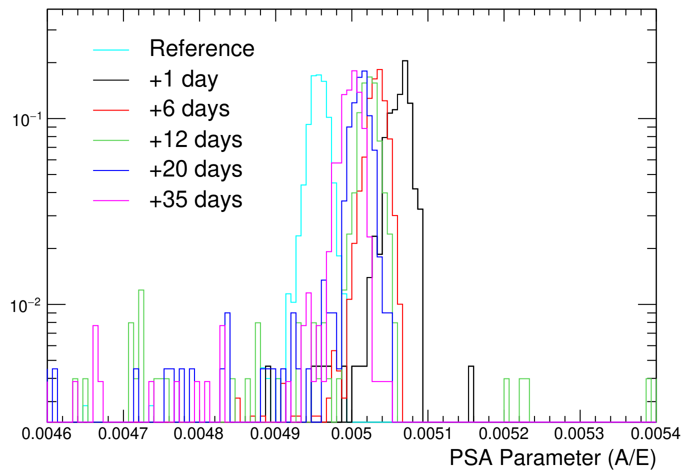

Figure 1.7-2. Evolution of PSA peak position over time following a full-array rebiasing. Detectors like this one exhibit slow drift of the pulse shape over a period of weeks to months following HV events, resulting in instability of the PSA performance.

The details of the MAJORANA PSA and its impact on the experiment's background rate has been submitted for publication[1]. This manuscript in press provides important supporting analysis to the physics releases, as well as documents the several-year UW effort in PSA improvements.

1.8 The search for $\beta\beta$-decay to excited states

S. I. Alvis, M. Buuck, J. A. Detwiler, I. Guinn, A. Hostiuc, W. Pettus, N. W. Ruof, and C. Wiseman

^{76}Ge can $\beta\beta$-decay into three different excited states of ^{76}Se. Each decay mode has a reduced Q-value compared to the ground state decay and promptly emits the remaining energy as one or more γ-rays. In addition, each decay mode will have a $2\nu\beta\beta$ mode with a broad energy spectrum below the Q-value, and, if neutrinos are Majorana fermions, a $0\nu\beta\beta$ mode with a peak at the Q-value. Fig. 1.8-1 contains a level diagram showing the Q-values and γ energies of each decay mode. Because each decay mode contains γs with known energy, a peak measurement can be performed to determine the rate of these decays. Because of the γs, $\beta\beta$-decays to excited states are inherently multi-site events (unlike the decay to the ground state, which is inherently single-site), and most events are detected between multiple detectors. For this reason, we can search for a peak in events with detector multiplicity of 2 or greater. The detectors in coincidence with events in the γ peak will provide many additional observables that can be used to refine this analysis, resulting in a nearly background-free peak search. GERDA

[1] S. I. Alvis *et al.*, arXiv:1901.05388, *accepted in Phys. Rev. C.*

Phase I has the best published half-life limits for each $2\nu\beta\beta$ excited state decay mode[1]. Fig. 1.8-2 shows an energy spectrum of all multiplicity 2 events from a simulation of the $2\nu\beta\beta$ decay to the 0^+_1 state of ^{76}Se and from Majorana Demonstrator data.

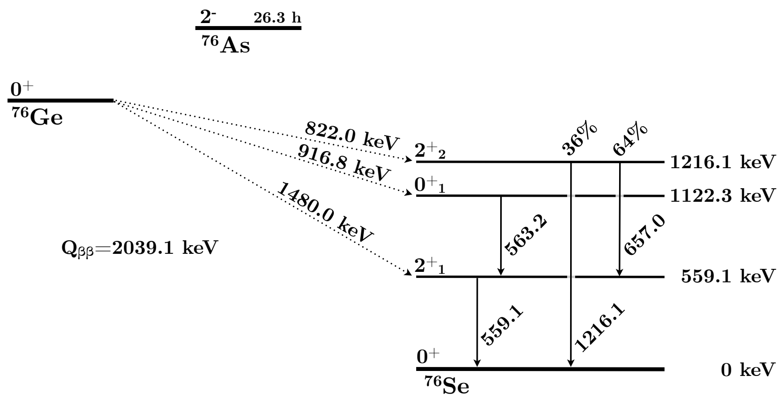

Figure 1.8-1. Level diagram showing the Q-value and emitted γ energies for $\beta\beta$ to each ^{76}Se excited state.

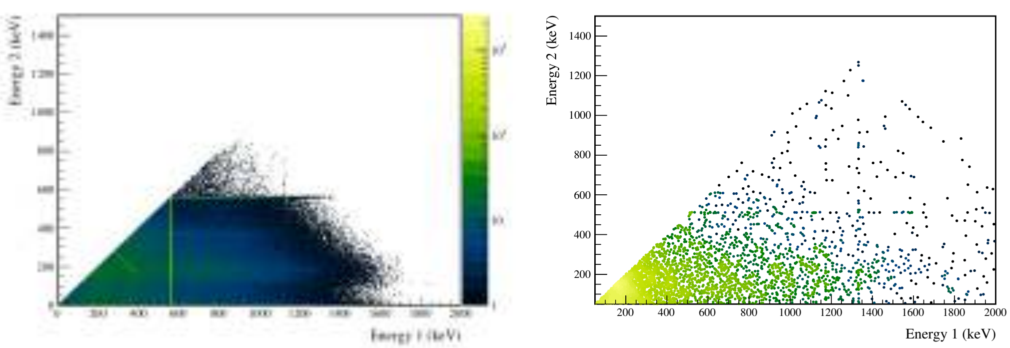

Figure 1.8-2. 2D energy spectrum of multiplicity 2 events from a simulation of the $2\nu\beta\beta$ to the 0^+_1 state (*left*). Scatter plot of all multiplicity 2 events from MAJORANA DEMONSTRATOR data, colored using a Gaussian kernel density estimator (*right*).

Each candidate $\beta\beta$ to excited state event can be divided into the "gamma" detector, which will fall into a region of interest around the γ energy, and the coincident detectors, which can be used to remove background events. For decay modes that involve just a single γ, only multiplicity 2 events will be used; otherwise, multiplicity 2 or greater events will be used. Since the $\beta\beta$-decay will originate with a ^{76}Ge nucleus, most of which are contained in enriched detectors, we will cut events in which none of the coincident detectors are enriched. Most backgrounds will originate from γ-rays that either Compton-scatter between multiple detectors or are emitted in γ-cascades. Compton-scattered γs that deposit all of their energy in active detectors will have a

[1] M. Agostini, *et al.*, Journal of Physics G **43**, 4 (2015).

measured sum energy equal that of the γ, and can be cut based on this signature. γ-cascades in which one of the γs is fully absorbed inside of a detector can be similarly cut if the energy in a coincident detector matches a known background γ. These cuts are designed algorithmically by choosing sum energy ranges and coincident energy ranges that maximize the sensitivity of this search. Fig. 1.8-3 shows the combined effect of these cuts for the $2\nu\beta\beta$ to the 0^+_1 state of ^{76}Se. The analysis is performed independently for each γ peak and for array of detectors, which are referred to as modules 1 and 2. These results are then combined to obtain a half-life limit on the decay mode. After applying these cuts, the detection efficiency for this decay mode (i.e. the fraction of all excited state decays, including in dead detectors, that are detected) is estimated using a simulation of the excited state decay mode in question. For the $2\nu\beta\beta$ to the 0^+_1 state, the detection efficiency is 2.3% in module 1 and 0.97% in module 2, with all effects shown in Table 1.8-1. While this detection efficiency is low, it represents an improvement over the GERDA phase I search, largely due to the fact that GERDA has immersed their detectors in a liquid Argon active shield, which shields γs as they travel between detectors[1]. This low detection efficiency is the result of carefully optimized trade-offs between cutting backgrounds and keeping signal events, and this optimization leaves significant room for improvement in future searches by using additional observables, such as the PSA techniques discussed in (Sec. 1.7).

Source	Module 1	Module 2
M. S. Event Signature	$5.2 \pm 0.2\%$	$2.8 \pm 0.5\%$
Region of Interest	$87.9 \pm 1.4\%$	$87.9 \pm 1.4\%$
Dead Layer	$74.5 \pm 4.3\%$	$65.7 \pm 6.0\%$
Detector Dead Times	$97.5 \pm 1.2\%$	$98.1 \pm 0.9\%$
Enriched Source Detector Cut	$98.7 \pm <0.1\%$	$95.7 \pm <0.1\%$
Coincident Energy Cut	$93.5 \pm <0.1\%$	$93.1 \pm <0.1\%$
Sum Energy Cut	$63.4 \pm <0.1\%$	$59.3 \pm <0.1\%$
Final Efficiency	$2.29 \pm 0.17\%$	$0.97 \pm 0.19\%$

Table 1.8-1. Table of efficiencies for $2\nu\beta\beta$ to the 0^+_1 excited state

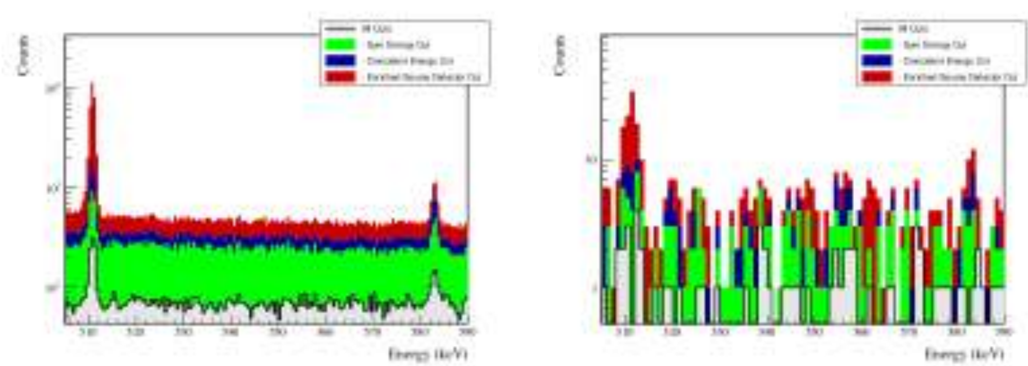

Figure 1.8-3. Events near the $2\nu\beta\beta$ to 0^+_1 region of interest before and after applying each data cut in a simulation of the MAJORANA DEMONSTRATOR background model (*left*) and in data (*right*).

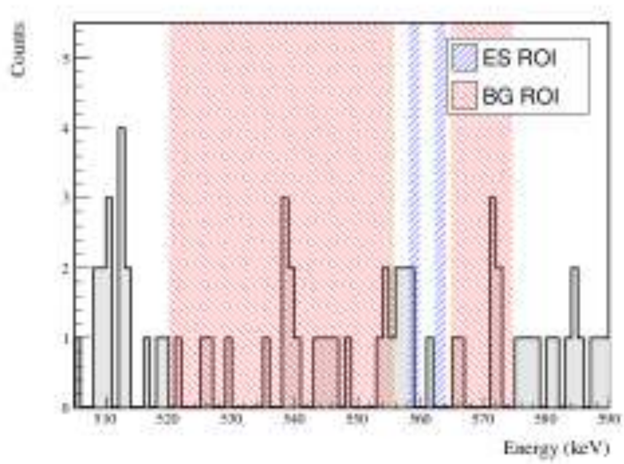

Figure 1.8-4. Events after applying all cuts, with the background (red) and excited state (blue) ROIs shown for the $2\nu\beta\beta$ to the 0_1^+ excited state decay.

After applying all cuts, the remaining events are shown in Fig. 1.8-4, with the ROIs for the $2\nu\beta\beta$ to the 0_1^+ excited state of ^{76}Se highlighted. The excited state ROIs are the energy ranges in which we expect to find a peak. They have widths of 1.6 keV each and detection efficiency given above. The background ROIs are the energy ranges used to estimate the background level in the excited state ROIs, with a measured background index of 2.02 events in the combined ROI for both peaks, in both modules. With a total isotopic exposure of 21.2 kg $\cdot$ y, this yields a half-life 90% confidence limit for the $2\nu\beta\beta$ to the 0_1^+ excited state of $T_{1/2} > 6.8 \cdot 10^{23}$ y. Limits have been found for all excited states for both $2\nu\beta\beta$ and $2\nu\beta\beta$, and are shown in Table 1.8-2. These are the best limits and sensitivities to date for all ^{76}Ge $\beta\beta$ to excited state decay modes, with the previous best set by GERDA Phase I[1].

Decay Mode	Peaks	90% Confidence Limit	90% Confidence Sensitivity
$0^+_{g.s.} \to 0^+_1(2\nu)$	559 & 563 keV	$> 6.8 \cdot 10^{23}$ y	$> 7.0 \cdot 10^{23}$ y
$0^+_{g.s.} \to 2^+_1(2\nu)$	559 keV	$> 9.6 \cdot 10^{23}$ y	$> 5.3 \cdot 10^{23}$ y
$0^+_{g.s.} \to 2^+_2(2\nu)$	559, 657 & 1216 keV	$> 5.6 \cdot 10^{23}$ y	$> 5.3 \cdot 10^{23}$ y
$0^+_{g.s.} \to 0^+_1(0\nu)$	559 & 563 keV	$> 2.1 \cdot 10^{24}$ y	$> 2.1 \cdot 10^{24}$ y
$0^+_{g.s.} \to 2^+_1(0\nu)$	559 keV	$> 1.1 \cdot 10^{24}$ y	$> 1.1 \cdot 10^{24}$ y
$0^+_{g.s.} \to 2^+_2(0\nu)$	559, 657 & 1216 keV	$> 1.6 \cdot 10^{24}$ y	$> 1.6 \cdot 10^{24}$ y

Table 1.8-2. 90% limits and sensitivities from the MAJORANA DEMONSTRATOR's search for each ^{76}Ge $2\nu\beta\beta$ and $0\nu\beta\beta$ excited state decay mode.

[1]M. Agostini, *et al.*, Journal of Physics G **43**, 4 (2015).

1.9 Radiogenic background model for the Majorana Demonstrator

S. I. Alvis, M. Buuck, J. A. Detwiler, I. Guinn, A. Hostiuc, W. Pettus,
N. W. Ruof, and C. Wiseman

Work this year has been ongoing in creating the background model for the Majorana Demonstrator. A full mock-up of the experiment has been built in the Geant4 simulation package[1], with the add-on MaGe[2], that specifies all of the experiment-specific geometry and particle tracking and generates ROOT[3] output files. Geant4 is able to simulate the full dynamics of particle interactions within the various components of the Demonstrator model, including the shield, vacuum system parts, and the HPGe detectors themselves. The simulation records energy depositions in the detectors and saves those interactions to disk, where they are then additionally processed by Majorana Collaboration's GAT analysis software to apply realistic temporal and spatial groupings, as well as the measured detector response function. See Fig. 1.9-1 for visualizations of the encoded geometry of the Demonstrator.

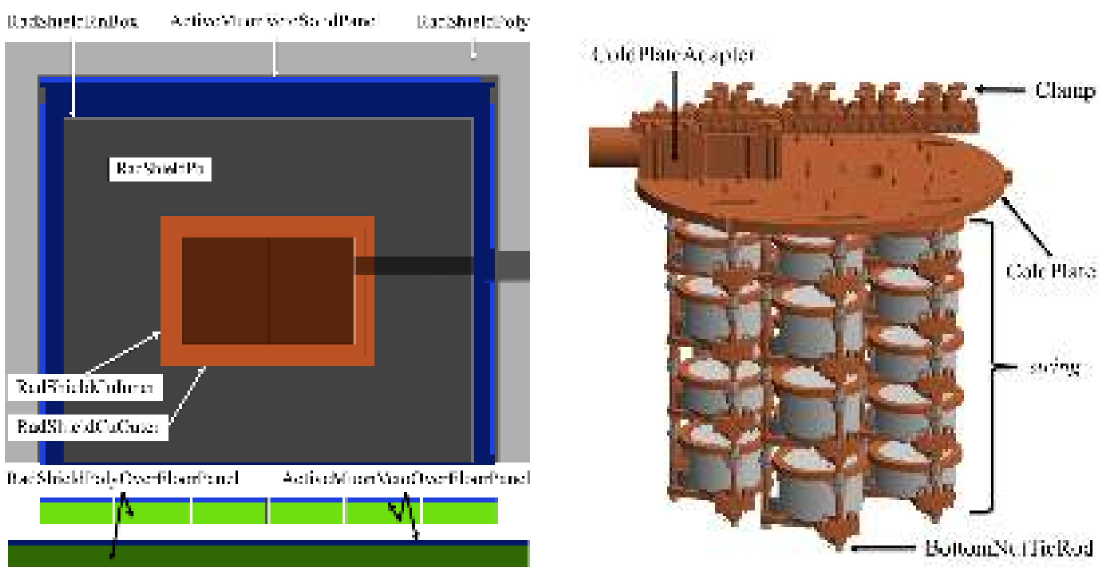

Figure 1.9-1. *Left:* Cross-section of the radiation shield for the MAJORANA DEMONSTRATOR as constructed in the Geant4 model. *Right:* Strings of germanium detectors as they are arranged in the MAJORANA DEMONSTRATOR Geant4 model.

The resulting simulated spectrum has been tested against the Majorana ^{228}Th calibration source, which produces gamma lines at 2614.511 keV and other energies with a detailed coincidence structure. The simulated spectrum matches the measured one with high fidelity, as shown in Fig. 1.9-2. The simulation is produced by simulating the

[1] S. Agostinelli *et al.*, Nucl. Instrum. Methods A **506**, 250 (2003).
[2] M. Boswell *et al.*, Nuclear Science, IEEE Transactions on **58**, 1212 (2011).
[3] I. Antcheva *et al.*, Computer Physics Communications **180**, 2499 (2009).

decay chain of ^{228}Th to ^{208}Pb in the calibration source, tracking the emitted particles until they have deposited all of their kinetic energy or left the simulation volume, and applying just the Gaussian and low-energy tail components of the detector peak-shape function.

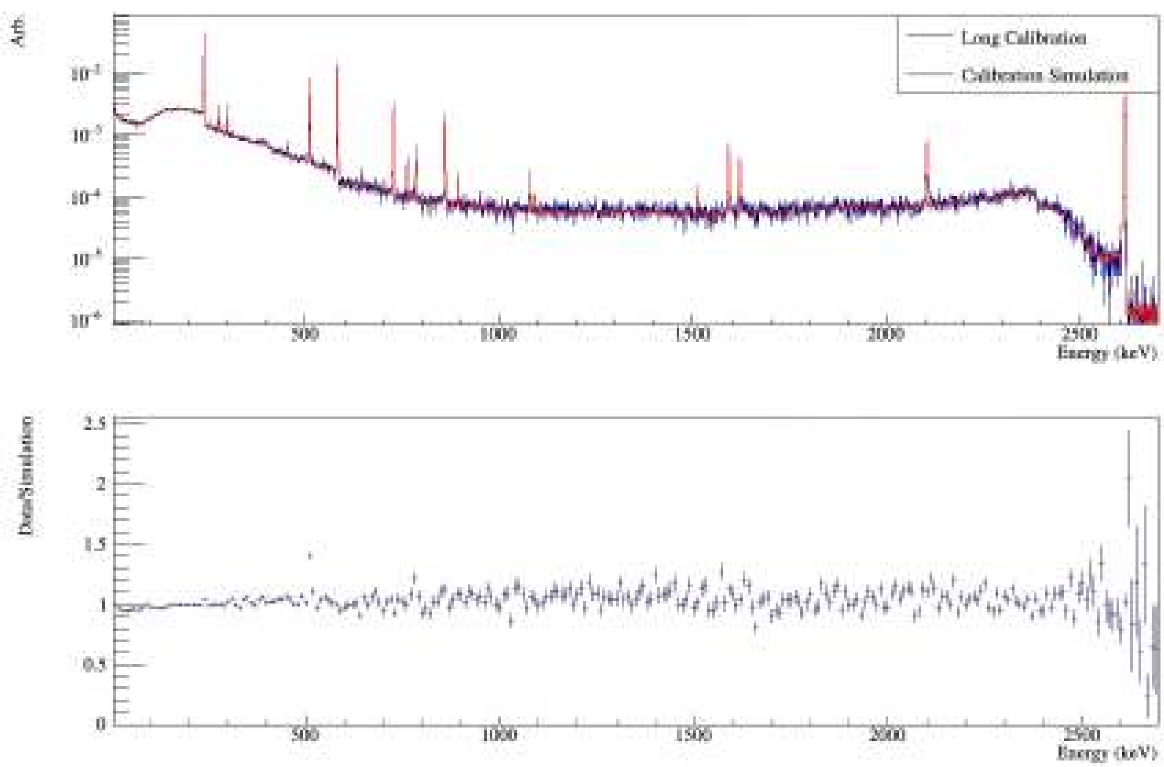

Figure 1.9-2. A comparison of the simulated calibration spectrum to the measured calibration spectrum.

The volume surrounding the cryostats is usually filled with ultrapure nitrogen gas, but at several instances the N2 purge has been disabled to allow for the acquisition of a radon spectrum. This spectrum also agrees very well with the simulated version, the results of which can be seen in Fig. 1.9-3.

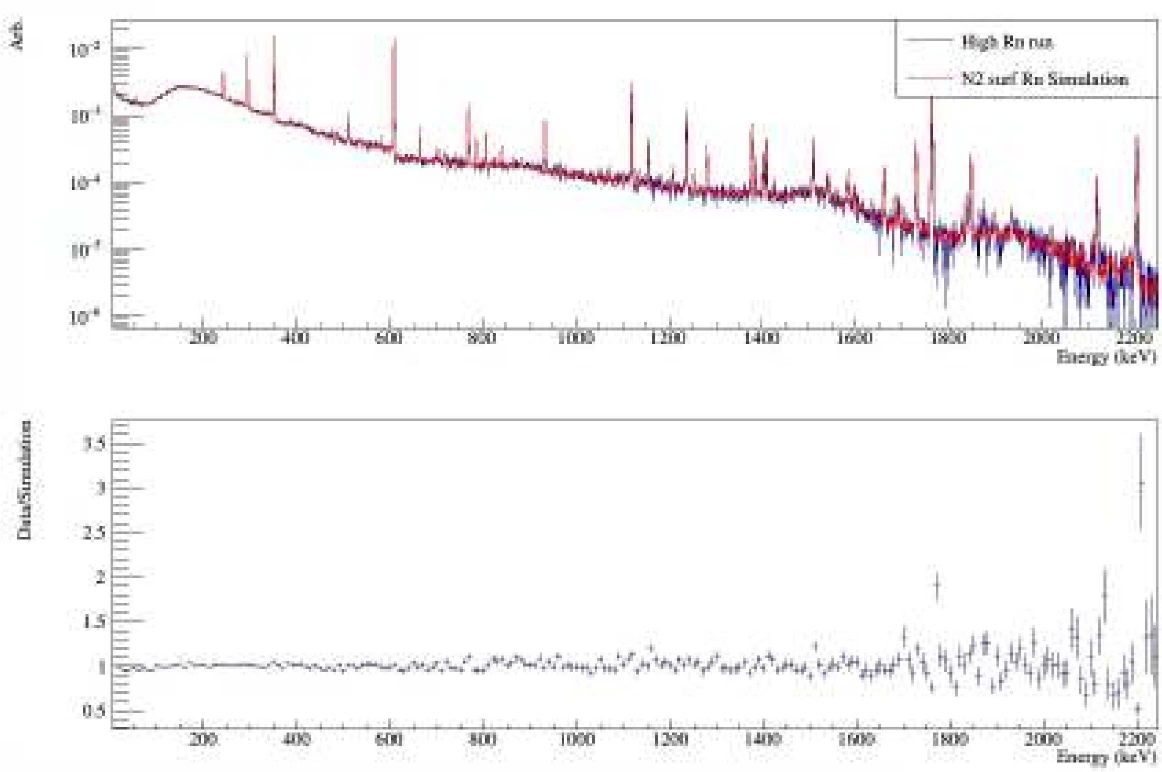

Figure 1.9-3. A comparison of the simulated N2 volume radon spectrum in DS0 to the measured spectrum.

A framework has been constructed for fitting simulated PDFs of various contaminants in various locations in the Demonstrator to data. Fig. 1.9-4 shows a fit of the simulated N2 volume radon and thorium calibration source to a synthetic cocktail of data drawn from thorium calibration runs and high-radon runs. The fit is done using the technique presented in Barlow and Beeston[1], with variable-width bins at the optimal locations to detect known gamma lines. The framework is able to extract the correct ratio of radon to thorium, and efforts to fit the Demonstrator background data are underway.

[1]R. Barlow and C. Beeston, Computer Physics Communications **77**, 219-228 (1993).

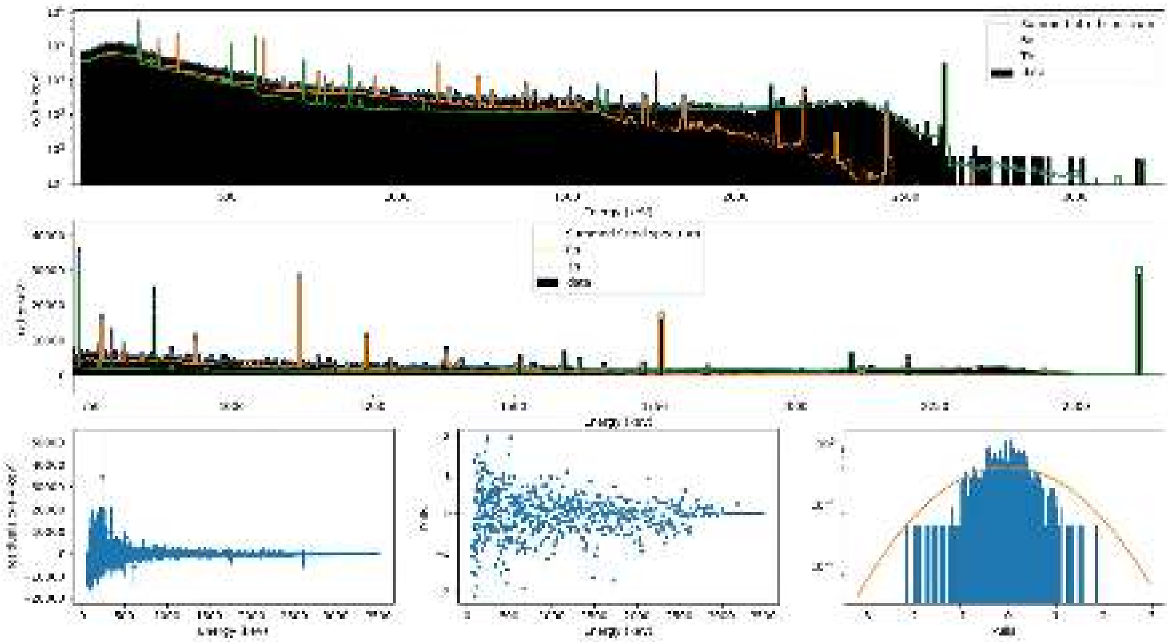

Figure 1.9-4. Simulated radon and thorium calibration spectra (colored lines) fit to a synthetic dataset created from separate calibration runs with a known ratio of radon to thorium.

1.10 Denoising Majorana waveforms with the wavelet transform

S. I. Alvis, M. Buuck, J. A. Detwiler, I. Guinn, A. Hostiuc, W. Pettus, N. W. Ruof, and C. Wiseman

The Majorana Demonstrator contains strings of high purity P-type point contact germanium detectors that are enriched to 88% in ^{76}Ge. Physics events that occur inside these detectors produce current pulses that can be read out as charge collected waveforms. All waveforms originating from the Majorana Demonstrator have intrinsic noise levels that vary waveform by waveform. These noise levels can potentially improve the precision of rejecting certain backgrounds, such as multi-site interactions and delayed charge recovery. It is therefore of interest to discover whether or not a waveform denoiser will improve the efficiency of a multi-site cut and a delayed charge recovery cut, without effecting the energy spectrum in any way. There are two classes of waveform noise that have been identified: baseline noise, the limited stability of the baseline that effects the entire waveform, and transient noise, pulses at about 30 MHz that can occur anywhere on the waveform. Wavelet denoising is an analysis technique that removes Gaussian noise by imposing a wavelet transform on a time series signal and thresholds a series of transform coefficients, which gives a smooth waveform after an inverse transform is performed. This analysis smoothes out the baseline noise, but does not completely eradicate the transient noise, which will be assessed in future research.

The simplest discrete wavelet transform is the Daubechies Wavelet Transform. The Daubechies Wavelet Transform decomposes a signal into a set of low-pass scale coefficients and high-pass detail coefficients in the Daubechies basis, where the number of transforms and number of coefficients in the basis are free parameters. The transform itself is linear and can be represented as matrix multiplication for each level of the specified number of transforms. To introduce this analysis scheme as part of the Majorana data processing, a wavelet denoiser software package was developed. The denoiser is a Daubechies Transform with two coefficients and 3 transform levels. A hard threshold is applied to the detail coefficients of the first three levels of the transform, where the baseline fluctuations reside. The thresholded Daubechies decomposition is then inverse-transformed to return a denoised waveform. Fig. 1.10-1 shows an example of what a typical waveform looks like before and after denoising. Thresholds are calibrated for each detector channel by taking the mean absolute deviation of the detail coefficients waveform by waveform and selecting the most common threshold given some range.

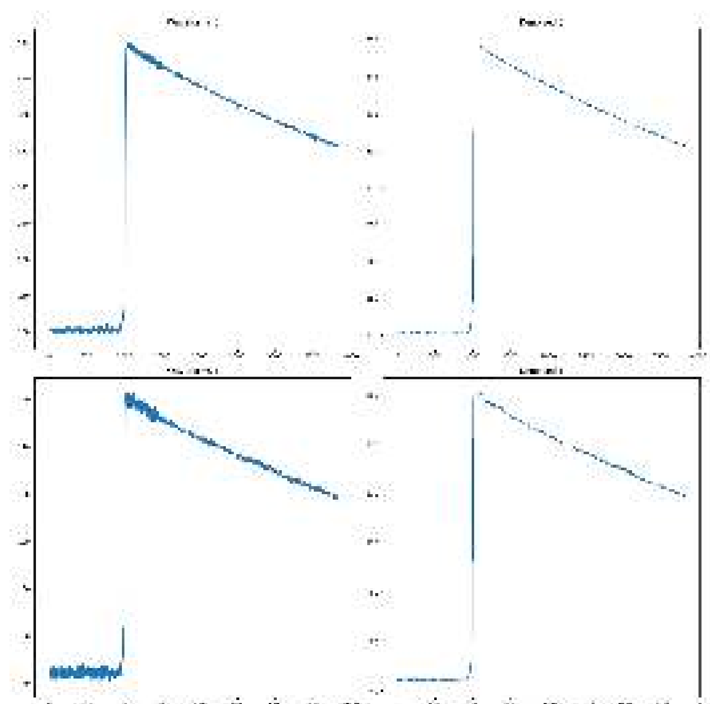

Figure 1.10-1. An example of what raw waveforms typically look like (*left*) and what waveforms may look like after denoising (*right*). A Daubechies level 3 transform with two coefficients was performed and all detail coefficients were set to zero before inverse-transforming to the denoised waveform.

When manipulating the shapes of the detector waveforms, it is important to understand any changes that occur to the energy spectrum, multi-site rejection, and delayed charge recovery. All tests done thus far show minimal effect on the large scale structure of all three of the mentioned spectrums channel by channel, including energy resolution. The multi-site rejection parameter show a reshuffling of outlier A/E values (amplitude over the energy), which either makes the main A/E distribution slightly narrower or induces no change at all, as shown in Fig. 1.10-2. This indicates an increase in efficiency for a multi-site rejection cut as some waveforms are being categorized incorrectly due to high noise waveforms. The delayed charge recovery parameter and energy spectrum remain virtually unchanged, but further analysis will be done to accurately estimate any differences.

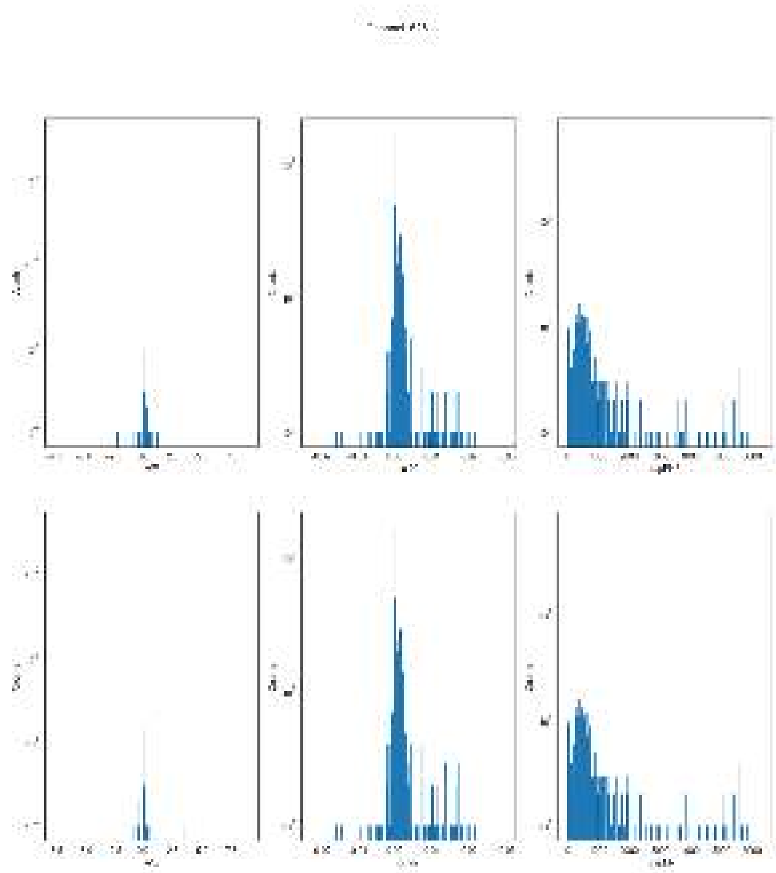

Figure 1.10-2. Default data processing (*top*) compared with data processing where wavelet denoising (*bottom*) is turned on for one channel in a calibration run exposed to Thorium-228. From left to right are the multi-site rejection spectrum, delayed charge recovery parameters, and energy spectrum.

1.11 Low-energy analysis for the MAJORANA DEMONSTRATOR

J. A. Detwiler, M. Stortini, and C. Wiseman

The MAJORANA Low Energy Working Group has been involved in an ongoing analysis of DEMONSTRATOR data over a 3+ year period of physics data taking, searching for physics beyond the Standard Model including bosonic scalar (axion-like) and vector dark matter, solar axions, and other rare events. A large dataset has been accumulated with varying noise conditions and detector operating parameters, and analysis is nearing completion. In parallel, efforts to understand the role of ^{210}Pb in the spectrum have led to a collaboration at CENPA between MAJORANA and Project 8, where two gaseous ^{83m}Kr sources have been examined with the "MJ60" germanium test stand. The group is also pursuing a database-driven effort to precisely quantify the amount of time during their fabrication that the MAJORANA $^{\mathrm{enr}}$Ge detectors spent above-ground. In this note we will briefly summarize several ongoing efforts for the Low Energy Working Group.

An extensive effort was made to identify robust noise rejection and pulse shape parameters suitable for the signal to noise ratio, and to identify methods for calculating the efficiencies of pulse shape analysis cuts. Validation of these techniques is nearing completion, and we are working with a MAJORANA Technical Review Committee to prepare these analyses for publication. The most recent energy spectrum from MAJORANA is shown in Fig. 1.11-1. Since March 2017, over two years of data has been processed and is currently being analyzed.

Fig. 1.11-1 highlights the effect of controlling the amount of surface exposure in the $^{\mathrm{enr}}$Ge detectors, obtaining a factor-4 reduction in the background above 20 keV (the endpoint of tritium β-decay). Since it is much less pronounced, the systematic error in the fitted tritium beta decay spectrum is an essential component of the low energy background model, and a precise estimate of the surface exposure time is needed to predict its allowed weight in the model. During detector fabrication at ORTEC, an enriched germanium materials tracking database was kept, following each batch of enriched material as it was transported between its underground storage location and the processing plant[1]. Each distinct "piece" of germanium material was tracked, connecting it with other pieces of material via processing, transportation, and transformation records. Work is underway to parse this database to examine the composition of each finished detector in time, and calculate the corresponding surface exposure of each piece. One example of this "history tree" is shown in Fig. 1.11-2. We are collaborating with undergraduate studnents at North Carolina State University, and MAJORANA collaborators at Oak Ridge National Laboratory to finish the surface activation calculations for the $^{\mathrm{enr}}$Ge material and apply them to our analysis of the low-energy spectra.

[1] F. T. Avignone III *et al.* (MAJORANA Collaboration) "The Processing of Enriched Germanium for the MAJORANA DEMONSTRATOR and R&D for a Next Generation Double-Beta Decay Experiment", NIM A **877**, 314-322 (2018).

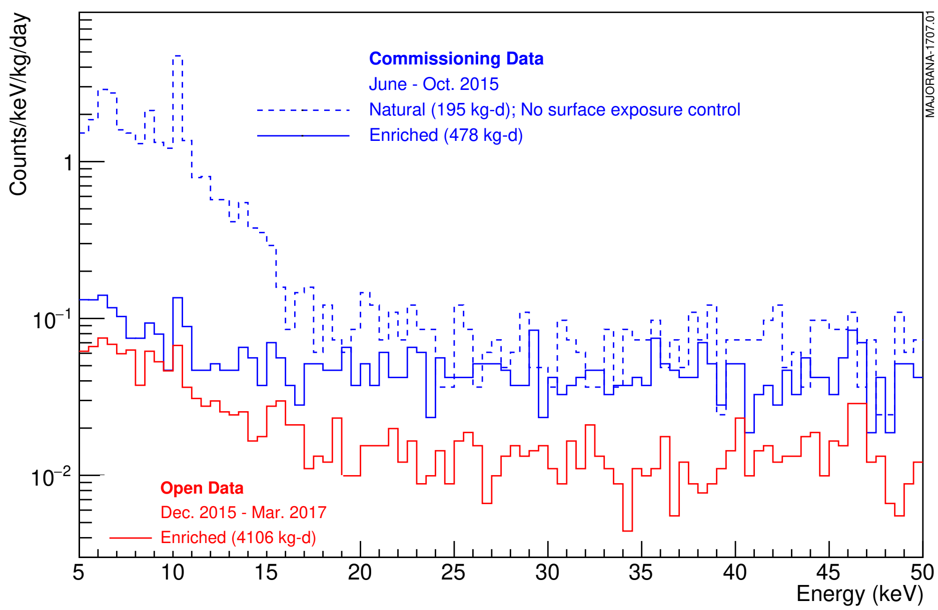

Figure 1.11-1. The most recent MAJORANA low energy spectrum. The effect of surface exposure is shown between the enriched and natural detectors, while the red spectrum shows the effect of increasing the shielding around the array during construction. The difference is attributable to surface exposure alone, since the isotopes of natural Ge (including ^{76}Ge) are all stable.

A complete understanding of the background model at low energies in the DEMONSTRATOR involves the measurement of cosmogenic peaks (with height proportional to the amount of surface exposure), the cosmogenic tritium β-decay continuum, Compton-scattering backgrounds, and other spectral shapes. Near the $0\nu\beta\beta$ region, the DEMONSTRATOR observes α events that can be rejected via pulse shape analysis. These events are known to originate from components near the passivated surface of the detector, and it is of interest to determine if there is also a low-energy component.

The Low Energy Working Group is pursuing studies of the ^{210}Pb decay system, which has observable gammas at 46 and 10.8 keV. Comparing the observed and expected heights of these peaks is a potential method to determine the location of hotspots in the array and to quantify the interaction of very low-energy gamma and x-rays with different detector surfaces.

The passivated surfaces of the detectors are fabricated differently than the n$^+$ contact (Sec. 1.16), and pulse shape simulation software has been used to calculate the paths of charge carriers at different crystal depths, applying different models of energy loss. An exaggerated example of an additional dead layer at the passivated surface is shown in Fig. 1.11-3.

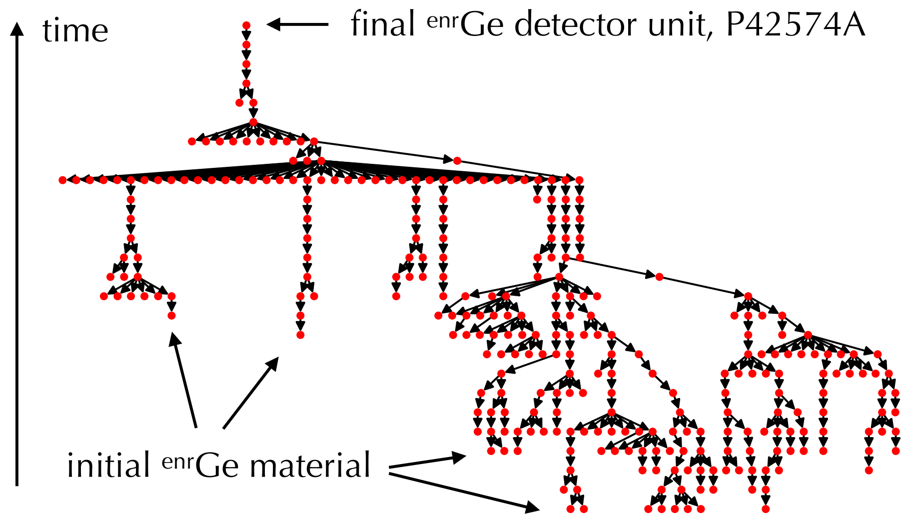

Figure 1.11-2. A “history tree” view of an example PPC detector. Red nodes represent pieces of germanium material, and links between nodes show processing, transportation, and transformation, where the surface exposure time during each link is recorded. The starting material received by ORTEC is on the bottom, and the final detector unit is on top.

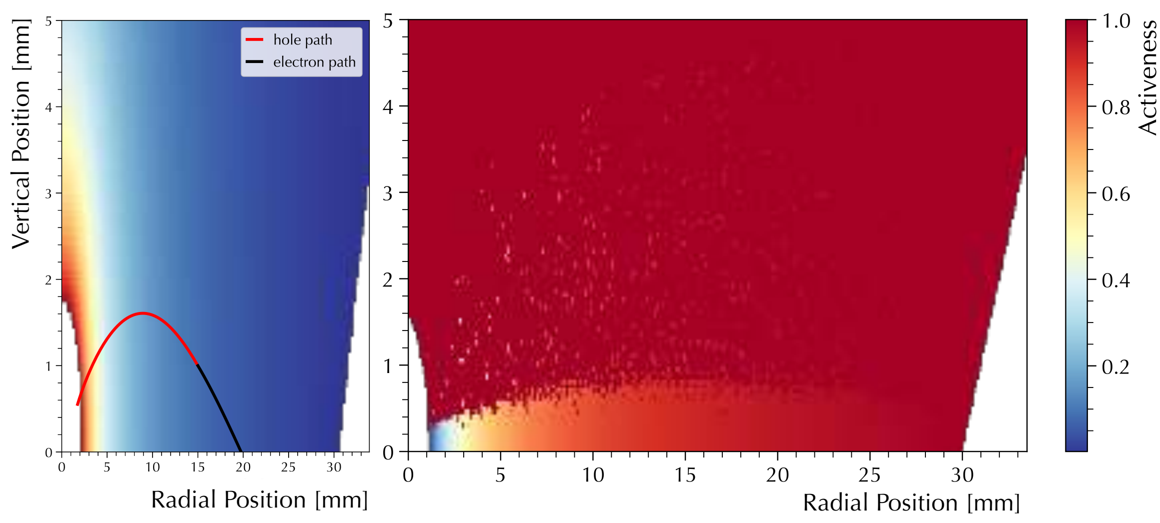

Figure 1.11-3. *Left*: The path of charge carriers through a PPC detector when a simulated surface charge is applied uniformly to the detector passivated surface. *Right*: The resulting “activeness” of an interaction at varying points in the crystal (exaggerated).

The MJ60 test stand at CENPA has also provided another means of investigating energy loss at the passivated surface. Two metastable ^{83}Kr sources have been lent to us by the Project 8 collaboration and attached to a repurposed MAJORANA String Test

Cryostat (STC) containing MJ60, an early PPC prototype detector from ORTEC. The cryostat and first Kr source are shown in Fig. 1.11-4.

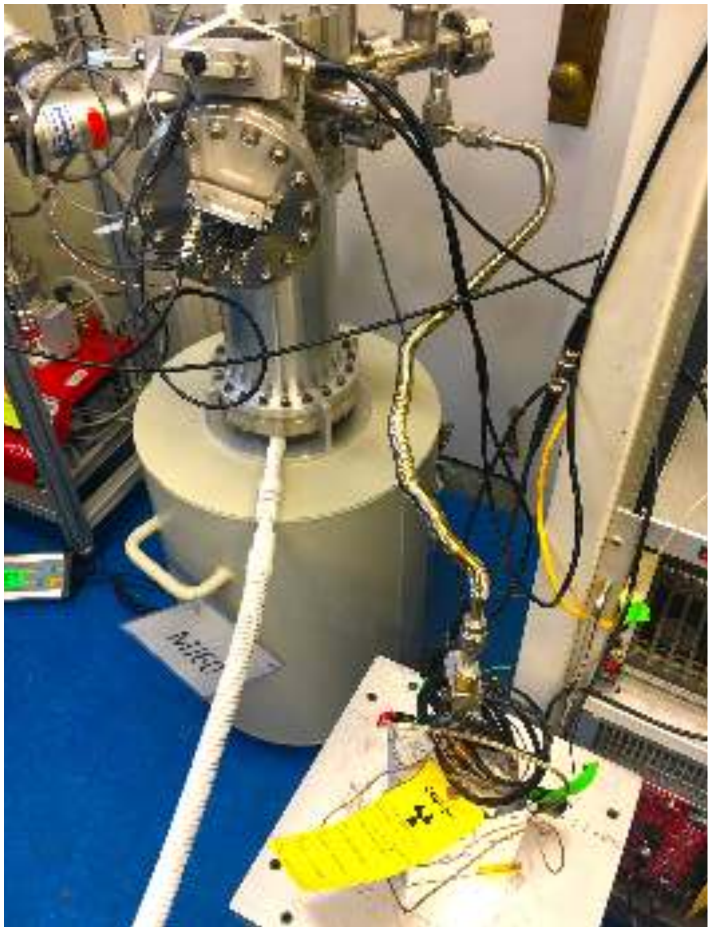

Figure 1.11-4. The MJ60 String Test Cryostat, with the first Kr source attached. The detector is mounted in the central volume, under the multi-port feedthrough flange. During Kr data taking, the turbopump (back) is valved off to allow cryopumping of the Kr onto the detector surfaces.

The STC cools the detector by submerging a copper rod in a liquid nitrogen dewar, which is thermally connected to a copper cold plate, IR shield, and HPGe detector. In typical operation, a vacuum turbopump is run on the cryostat for the best possible vacuum, but in order to accumulate sufficient amounts of Kr in the cryostat, the pump is valved off during operation. The freezing point of Kr is 115 K, while the STC is operated at ∼85 K. At this operating temperature, the gaseous Kr inside the volume is "cryo-pumped" onto the cold germanium surfaces, and the ^{83}Kr then decays. Its decay products are extremely low in energy, emitting several monoenergetic electrons, and notable gammas at 9 and 12 keV. In the first stage of data taking, dozens of hours of Kr data have been taken and processed with the `pygama` analysis software (Sec. 1.17). These results have been used to develop automatic energy calibration and pulse shape analysis parameters. In parallel, an as-built simulation using the `g4simple` software (Sec. 1.16) has been developed to simulate Kr decays on various detector surfaces, for comparison to data, shown in Fig. 1.11-5. This data will also be examined for any hints of new pulse shape discrimination parameters that could help distinguish between gamma and electron events on HPGe surfaces, with potential application to the ongoing MAJORANA and LEGEND analyses.

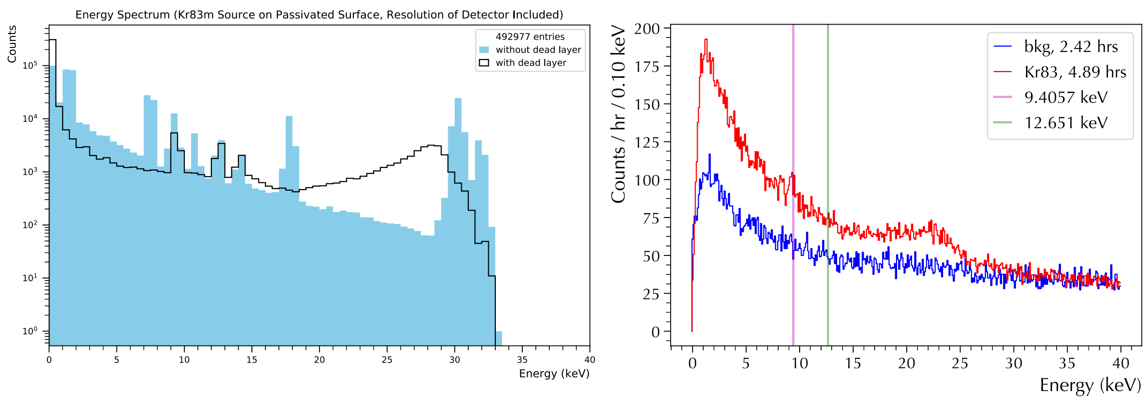

Figure 1.11-5. Comparison of a simulated Kr spectrum, incorporating an additional passivated surface dead layer, to the observed signal from MJ60. Further optimization of the energy resolution and other parameters is underway.

1.12 Alpha particle discrimination in the MAJORANA DEMONSTRATOR

M. Buuck, J. A. Detwiler, I. Guinn, A. Hostiuc, W. Pettus, N. W. Ruof, and C. Wiseman

Alpha background

The delayed-charge recovery (DCR) parameter is used in the MAJORANA DEMONSTRATOR to identify and reduce the alpha background. The physical effect that DCR characterizes is that the charge deposited by the alpha particle does not get collected all at once. Rather, some of the charge is trapped and then released slowly, on the timescale of the waveform digitization. This increases the slope of the waveform, appearing as extra charge. Charge trapping occurs on the passivated surface between the point contact and the dead layer of the MAJORANA DEMONSTRATOR and is therefore indicative of an external alpha particle. The DCR parameter in its current instantiation allows for an effective rejection of background alphas while maintaining ∼99% of the bulk-detector events, as measured during Thorium-228 calibrations.

DCR Stability

Currently, DCR is calculated using the slope of the event waveform tail. The slope is caused by electronics bleeding off charge; there is a consistent, known time constant.

Recently, work was undertaken to be able to use pulser events for DCR analyses, rather than just calibration data. Pulser signals are injected, non-physics, events. They need to be used as the regular background data is mostly blinded. Previous studies showed that detector-injected pulser events can show shifts in the waveform slope that match the shifts we see in calibration data. Generally, calibration runs happen roughly every week, whereas we have pulser events for every run, for most channels. This means that using pulser data should improve performance over simply using calibration data. For example, we could pinpoint the exact time when the DCR value significantly changed, improving the alpha background rejection. In summary, using pulser events also allows for an accurate shift in run coverage in background data without violating our blinding scheme.

In stable data-taking mode, the stability of the DCR parameter is an important benchmark. The existing DCR analysis aids data quality and channel selection by analyzing the stability in pulser events over time. Plotting the difference in DCR for any given run using pulser events vs. the previous (or initial) calibration run, as shown in Fig. 1.12-1, is one way to show the stability of a given channel over time.

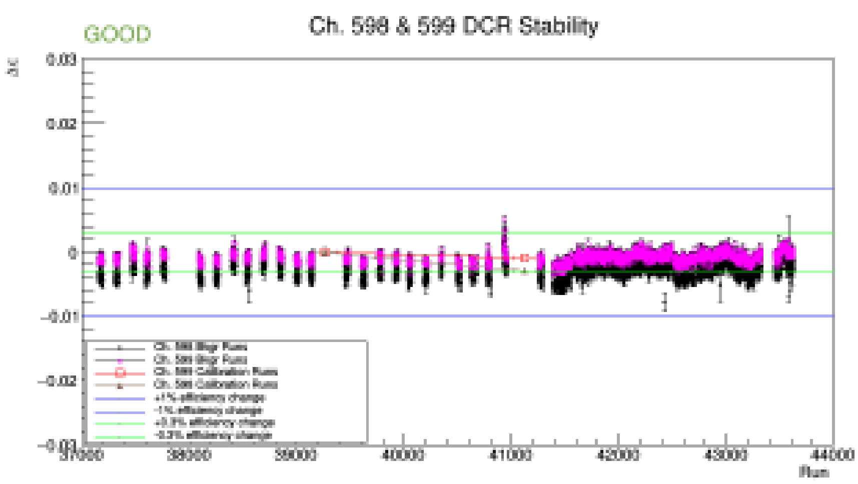

Figure 1.12-1. Example of DCR stability for one detector (high and low gain channels)

DCR Improvements

Improvements to the DCR calculation are being tested. Using pole-zero corrected, electronics-deconvolved waveforms ensures a flat top waveform, removing the electronics' charge release effect. Therefore, the distribution of raw DCR events in calibration will be centered around zero, with some small spread. We can use the mean and sigma of this distribution to create the new DCR parameter, centered at 0, with a standard deviation of 1. Then, to retain 99 of the bulk detector events, we can reject any events with a DCR value greater than roughly 2.6. Further work is ongoing to test and implement this different DCR and check that it achieves the necessary efficiency and improves alpha background rejection.

LEGEND

1.13 Status of the LEGEND neutrinoless double-beta decay search

T. Burritt M. Buuck, J. A. Detwiler, C. Farrell, I. Guinn, A. Hostiuc,
T. Mathew, D. A. Peterson, W. Pettus, N. W. Ruof, M. Stortini
T. D. Van Wechel, and C. Wiseman

The LEGEND experiment is a next-generation search for neutrinoless double-beta decay in ^{76}Ge that merges the techniques of the Majorana Demonstrator and GERDA experiments. Preparations are underway to mount the Majorana and GERDA HPGe detectors in the GERDA cryostat along with new detectors, for a total mass of 200 kg of enriched germanium. This LEGEND 200 phase will probe half lives an order of magnitude beyond current searches, and is key R&D for a subsequent LEGEND 1000 phase that will extend the sensitivity another order of magnitude further, essentially covering the phase space for the inverted neutrino mass ordering in the case of light neutrino exchange. The CENPA LEGEND group plays a leading role in the development of the analysis framework for the new experiment. We are also involved in R&D efforts to understand the interactions of alpha, beta, and low-energy gamma/x-ray interactions near HPGe detector surfaces that pose a background risk for the experiment. We are also investigating R&D aimed at improved LAr scintillation light collection and alternative HPGe detector electronic readout in LEGEND 1000.

1.14 Forward-biased preamplifiers for LEGEND

J. A. Detwiler, A. Hostiuc, D. A. Peterson, W. Pettus, N. W. Ruof,
T. D. Van Wechel, and C. Wiseman

A charge-sensitive preamplifier with forward-biased reset is currently under testing for the LEGEND project. This will be referred to as the Forward-biased JFET-based Option for Research and Development (FJORD). The classic charge-sensitive preamplifier circuit uses a feedback resistor for stabilizing the DC operating point and providing a DC path for the detector leakage current. The forward-biased reset preamplifier eliminates the feedback resistor that is a major source of noise when using a low-leakage detector. In LEGEND, this also eliminates the need to find a low-background resistor that can survive repeated liquid argon (LAr) immersion, and thus represents an attractive alternative to the baseline technology[1].

Currently, a small Hamamatsu S4204 dual-element Si PIN photodiode is attached to FJORD. ^{241}Am-241 and ^{133}Ba sources are being used to test the performance of the pre-amp. Gammas from the sources are seen using the Si detector and then amplified in FJORD. The output signal can then be analyzed and thoroughly tested.

The device was tested in liquid nitrogen: FJORD continues to work at Liquid Nitrogen (LN) temperature and after returning to room temperature. FJORD data has been taken using a ^{133}Ba source using the DT5725 digitizer from CAEN. Good discrimination between physics and noise events was observed. The rise-time for physics pulses is on the order of 100ns, similar to a germanium detector. Therefore, the silicon detector can be used as a proxy for germanium.

Work continues on understanding spectral features in order to understand the energy calibration needed. The first test using a ^{241}Am-241 source (59.5 keV line) is complete; these results will be used to calibrate the CAEN CoMPASS energy output. Changes to the test stand are ongoing, with the goals of reducing the effect of external noise sources (e.g., microphonics), optimizing the output (e.g., minimizing threshold and using the optimal energy estimator) from the CAEN CoMPASS software when using a radiation source, and characterizing the performance of both low-gain and high-gain output from the post-amp box (built by by CENPA engineers Tim van Wechel and David Peterson).

[1]CENPA Annual Report, University of Washington (2018) p. 27.

1.15 Characterization of silicon photomultipliers

J. A. Detwiler, A. Hostiuc, D. A. Peterson, W. Pettus, N. W. Ruof,
T. D. Van Wechel, and C. Wiseman

In LEGEND, strings of germanium detectors will be submerged in liquid argon, which simultaneously acts as a cryogen and an active veto. Energetic particles that originate from natural radioactivity and pass through the liquid argon are able to scintillate, producing photons of 128 nm wavelength. This scintillation is measured by shifting the wavelength to 420 nm and guiding it to a readout composed of silicon photomultipliers (SiPM) via a shroud of optical fibers.

For future phases of LEGEND, it is of interest to investigate the characteristics of SiPMs at liquid argon temperature to improve the light collection efficiency of the liquid argon active veto. Located in the MAJORANAlab is a SiPM teststand setup that has been running to characterize SiPMs at room temperature and liquid nitrogen temperature. The test stand is a steel vessel dark box with an open LN dewar inside. The open LN dewar allows for the SiPMs to be dipped in liquid nitrogen. To expose the SiPMs to low light and measure the photon detection an integration sphere, shown in Fig. 1.15-1, is placed at the bottom of the open dewar. The integration sphere is used to evenly disperse light coming from a LED to calibrate a reference photodiode, which is necessary to estimate the number of photons incident on the SiPMs.

The SiPMs being tested are 3x3 mm modules from Hamamatsu, KETEK, and sensL. Each module is attached one at a time to a custom pre-amplifier that is connected to a CAEN DT5730 digitizer for pulse and charge collection readout. Measurements from CAEN CoMPASS sent to a custom python analysis tool kit, SiPMStudio[1], which is still under development.

The current setup is capable of measuring the dark count rate, direct cross-talk, and the photon detection efficiency. The photon detection efficiency is measured by comparing the photocurrent of the SiPM to that of a reference photodiode under continuous illumination by an LED. Typical gain and cross-talk probability for a KETEK SiPM is shown in Fig. 1.15-2. Dark count rate populations are trivial to measure in liquid nitrogen; however, a photon detection efficiency measurement is not and requires that the reference photodiode be at room temperature, while the SiPM is at liquid nitrogen temperature. Preliminary measurements of dark count rates have been made for each of the SiPMs, but more reliable measurements will be attainable once the software is fully functional.

[1] `https://github.com/nickruof/SiPMStudio`

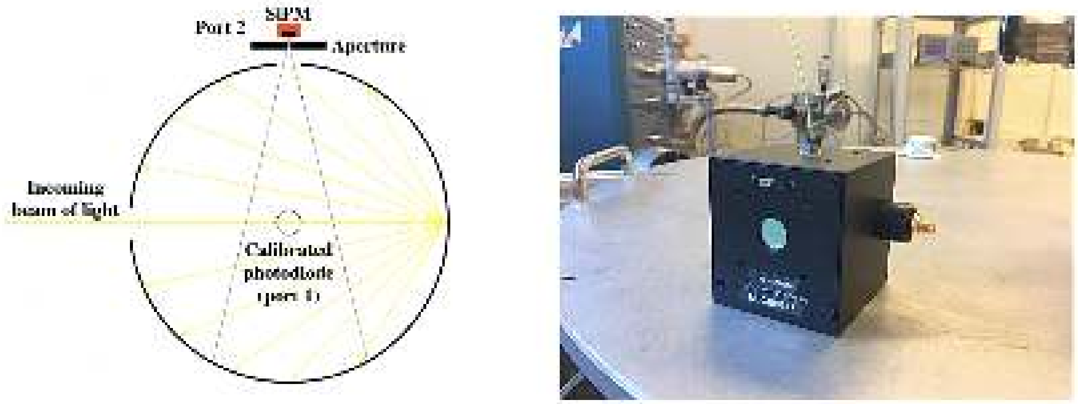

Figure 1.15-1. In order to make a photon detection efficiency measurement the photon rate incident on the SiPM must be known. This is achieved by using an integration sphere, which disperses light evenly to multiple devices connected to its various ports. Shown above are a schematic (*left*) and an actual model obtained from Thorlabs (*right*). The interior of the integration sphere is coated with a diffusive material that evenly disperses incoming light from one port to all other ports on the sphere. The responsivity of the photodiode is used to convert generated photocurrent to number of photons per second.

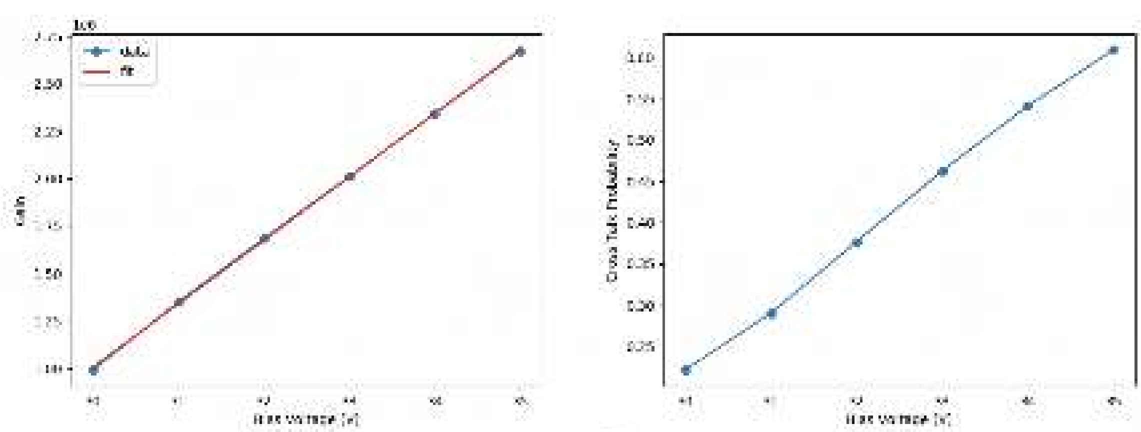

Figure 1.15-2. Shown above are gain (*left*) and cross-talk probability (*right*) vs. bias voltage for a KETEK SiPM at room temperature. The gain measures the number of photoelectrons created by one photon that triggers a pixel in the SiPM; the cross-talk probability measures the probability for photoelectrons in one pixel to trigger a neighboring pixel. These factors modify and are included in a photon detection efficiency calculation.

1.16 CAGE: An internal-source scanning cryostat for Collimated Alphas, Gammas, and Electrons on PPC HPGe detectors

T. Burritt, J. A. Detwiler, C. Farrell, T. Mathew, G. Othman, D. A. Peterson, W. Pettus, M. Stortini, T. D. Van Wechel, D. I. Will, and C. Wiseman

Current-generation neutrinoless double beta decay ($0\nu\beta\beta$) experiments in ^{76}Ge have shown that radioactivity near the surfaces of high-purity germanium (HPGe) detectors can constitute a significant source of unwanted background. In many cases, they can be overcome by finding improved detector designs and applying new pulse shape discrimination techniques. A test stand is being constructed at CENPA that will allow a variety of collimated radioactive sources to be placed very near the sensitive surfaces of a germanium detector, using vacuum-rated motors in a custom-built cryostat to conduct a variety of "internal source" scans. This project has been named CAGE (Collimated Alphas, Gammas, and Electrons) to highlight the versatility of the design in accomodating various collimated sources and HPGe detector geometries, and is shown in Fig. 1.16-1.

The P-type point contact (PPC) detectors used by Majorana, GERDA, and LEGEND are intrinsic "p-i-n" diodes, where the highly pure bulk material is surrounded by an outer wraparound n$^+$ contact created by lithium diffusion, a p$^+$ point contact from boron implantation, and an amorphous Ge passivated surface created by sputtering with a high resistance separating the contacts. It is a well-known problem in the $0\nu\beta\beta$ and dark matter communities that events in the n$^+$ dead layer can be energy-degraded, but the response of a PPC to signals interacting with the passivated surface is less well-studied. Surface events are expected to be one of the dominant background contributions in LEGEND, and since a wide variety of PPC geometries will be used (BEGes, Majorana-style PPCs, and inverted-coaxial PPCs), it is essential to develop a test stand capable of conducting dedicated scans of each detector's response to various surface signals.

The CAGE cryostat design is centered around the manipulation of a moveable copper IR shield surrounding the PPC to be scanned, both of which are in thermal contact with a wide copper "cold plate" connected to a liquid nitrogen dewar. A G-10 insulating material is used in several locations to keep the vacuum-side motors in their operating temperature ranges, while the detector, IR shield, and radioactive source are kept at cryogenic temperatures. The radioactive source is held by a combination aluminum/G-10 shaft that passes through the IR shield, allowing the source itself to be cooled to near-liquid-nitrogen temperatures. The shaft can be rotated by a stepper motor, changing the incident angle of the beam to the HPGe surface. To move the beam to different spots on the detector, the IR shield is raised from the cold plate a very short distance by a hand-operated rack and pinion mount, rotated and translated by the vacuum-side motors, and then lowered back onto the cold plate to re-establish a thermal connection. Depending on the radioactive source and scan of interest, data taking for a single collimator position may last for hours or days, ensuring that the

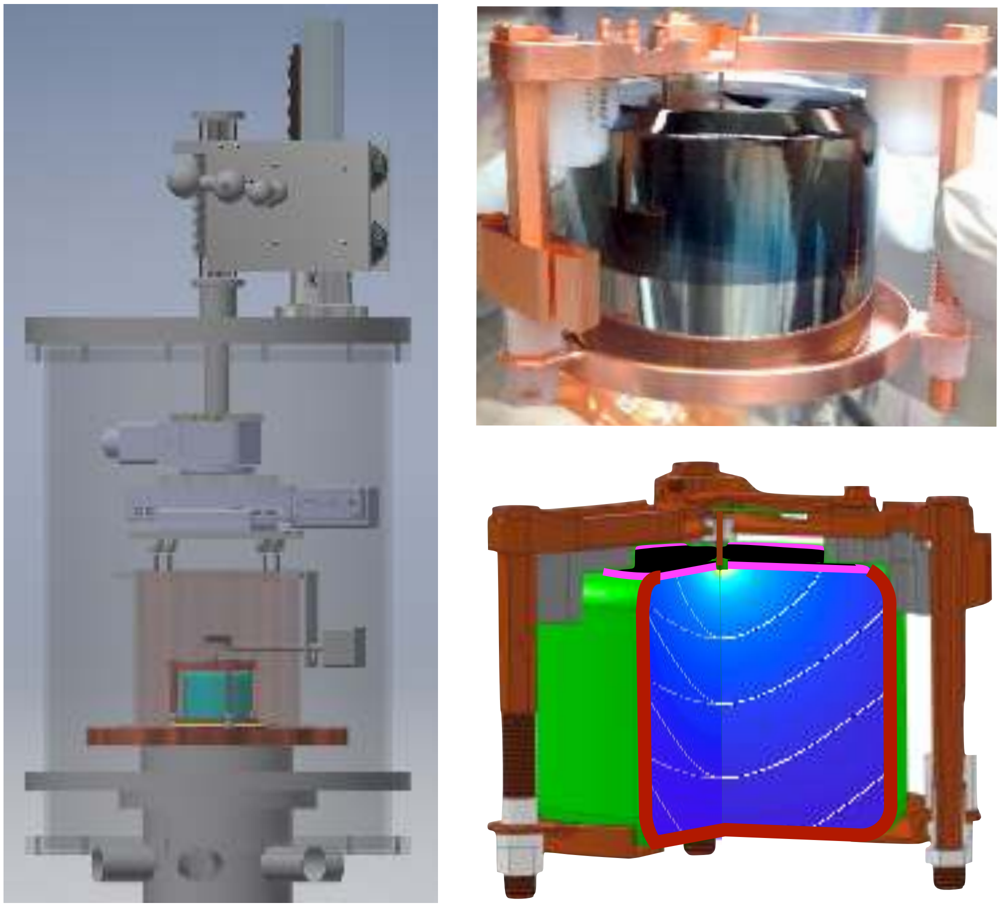

Figure 1.16-1. *Left*: CAGE cross section. *Upper right*: A Majorana ^{enr}Ge PPC detector. *Lower right*: cross section of a PPC, showing different detector surfaces and internal weighting potential.

system remains in thermal equilibrium after the initial IR shield movement.

Construction of the CAGE detector is ongoing on several fronts, with a goal of first data taking in mid-Summer 2019. A modified Majorana detector holder is being designed which will expose more of the passivated surface to the areas covered by the collimator beam. Custom electronics and software are being built at CENPA for the HPGe signal readout, as well as "slow controls" vacuum and high voltage safety interlocks for extended data taking, and accurate operation of the motor system. Currently, the outer vessel construction is complete, passing leak checks to $< 10^{-6}$ mbar. All major components are in-hand, including a Majorana-style PPC ("OPPI1") with a large passivated surface on loan from Los Alamos National Laboratory, an aluminum gantry and hoist to raise and lower components in and out of the cryostat on loan from ADMX, a vacuum turbopump station, motor controllers, and data acquisition software. The majority of custom hardware has been fabricated on-site at CENPA with extensive support from the engineering staff. Once the detector is commissioned and ready for data taking, several radioactive sources of interest and collimator designs will be installed. Planned sources include a ^{241}Am source housed inside a lead collimator (for α and γ events), a ^{90}Sr source housed in PTFE and tungsten (for β events), and a low-energy x-ray source currently under development by our collaborators at Los Alamos. There is also interest in using the tandem accelerator at CENPA to create ^{56}Co, ^{55}Fe, and other sources.

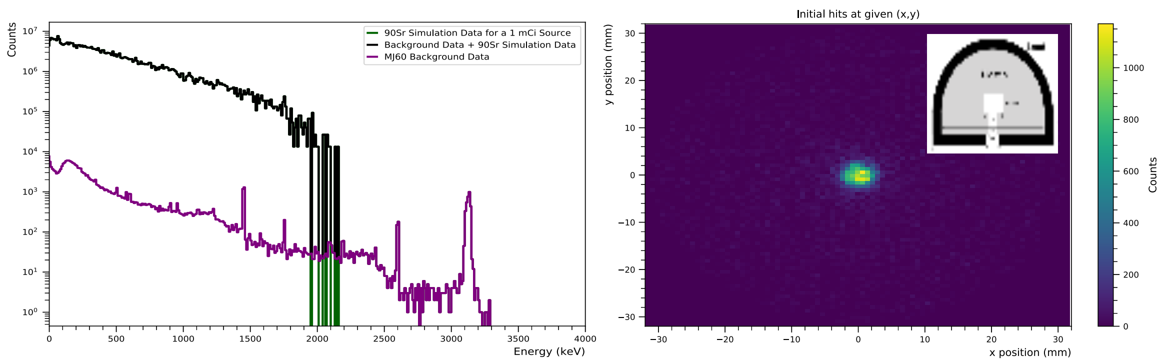

Figure 1.16-2. As-built `g4simple` simulation results. *Left*: ^{90}Sr spectrum from a 1 mCi source, orders of magnitude above measured room background rates. *Right*: The spatial extent of the collimated beam ("spot size") is restricted to ~3 mm for one collimator design.

An extensive simulations campaign using the `g4simple` Geant4 application by J. Detwiler is in progress, where an "as-built" simulation of CAGE is being used to tune collimator dimensions, muon veto and shielding configurations. As an example, Fig. 1.16-2 shows that the estimated "spot size" for one ^{90}Sr collimator geometry is ~3 mm, comparable to the size of the p$^+$ point contact, with an expected rate for a 1 mCi source far exceeding room backgrounds. Other sources (^{241}Am and the LANL x-ray device) are likely to have lower event rates, requiring the addition of extra lead shielding and a muon veto surrounding the cryostat. These upgrades are currently planned for Fall 2019 after initial commissioning runs are successful.

1.17 Digital signal processing for LEGEND

J. A. Detwiler, M. Stortini, B. Shanks*, S. Meijer†, and C. Wiseman

The LEGEND Collaboration is searching for neutrinoless double beta decay ($0\nu\beta\beta$) in ^{76}Ge, taking a staged approach to the deployment of a ton-scale array of high-purity germanium (HPGe) detectors. Planning for the first stage, LEGEND-200 (L200), is nearly complete, with commissioning runs expected to begin in 2021. L200 will be

*Formerly at Oak Ridge National Lab, TN.
†University of North Carolina at Chapel Hill, NC.

located at Gran Sasso, utilizing hardware from both the GERDA and MAJORANA experiments, including upgrades to the existing GERDA cryostat and liquid argon (LAr) veto, and underground-electroformed copper and ^{enr}Ge detectors from MAJORANA. In preparation for first data, the LEGEND Simulations and Analysis Working Group is pursuing a redesign of its data processing and analysis frameworks. During data taking, L200 will have 150+ individual ^{enr}Ge digitized data streams, dozens of silicon photomultiplier (SiPM) streams from the LAr, and PMT streams from the outer Cerenkov water veto.

After the data is acquired and saved to disk for offline processing, an analysis framework must parse each data stream, performing digital signal processing of waveforms, automatic energy calibration, pulse shape analysis, and veto system integration. The resulting data set must then be built into a coherent and accessible whole. This "tiered" data processing algorithm is depicted in Fig. 1.17-1.

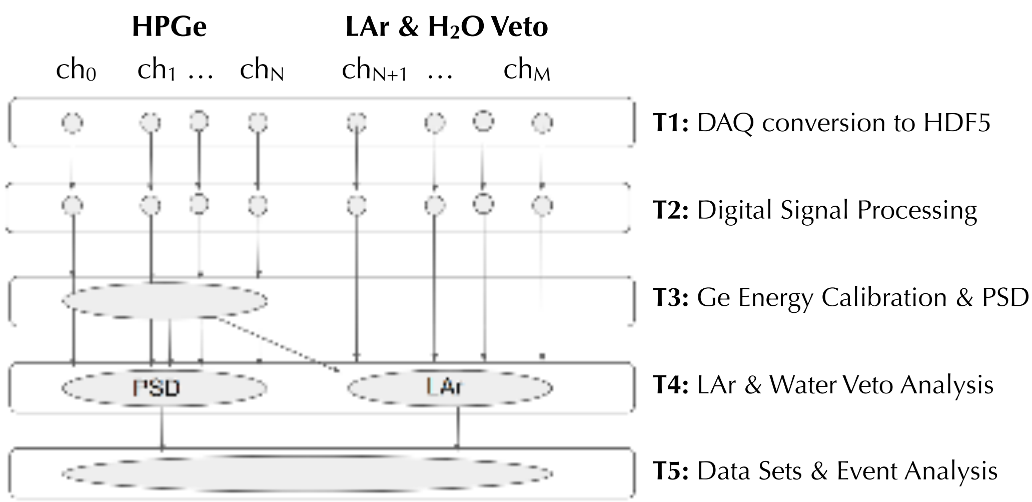

Figure 1.17-1. High-level depiction of the Tier data processing algorithm for LEGEND-200. Independent data streams are processed in parallel as much as possible to increase performance.

The choice of programming language for this task must be carefully considered. Much of the processing needed can be parallelized, and it should be scalable to a ton-scale experiment (LEGEND-1000) and run on large computing clusters such as Cori at NERSC. Advanced analysis techniques including machine learning, Bayesian statistics, and high-dimensional fitting algorithms often have very well-maintained and straightforward implementation in the Python ecosystem. Packages like NumPy, SciPy, Pandas, Cython, and Numba allow large-scale data analysis to be optimized for "near-C" speed. It is also very desirable for the analysis to be written with internals containing a minimum of boilerplate code, easily accessible to a large user base of analysts (typically students and postdocs) with varying skill levels.

A working prototype of this software has been developed at CENPA, making use of an in-house test stand containing an early MAJORANA-style PPC HPGe detector (MJ60), and a custom cryostat, described in more detail in (Sec. 1.11). `pygama` ("py-gamma") is an open-source Python 3 module providing a set of tools to decode digitizer data and run digital signal processing algorithms at near-C/C++ speed, utilizing as many CPU threads as are available on a given compute node. All data are saved in the HDF5 format, which allows fast access to "blocks" (typically 2-d arrays of ∼3000 waveforms), which can be processed in parallel. Currently the development of `pygama` has focused on 1) decoding raw data from various digitizers to HDF5, 2) using JSON-based metadata to combine runs into data sets with specific processing parameters, and 3) implementing HPGe-specific processing, including trapezoidal filters (using various kernel functions), and filters to identify and remove multi-site γ bulk events, events from surface α backgrounds, and more. Two examples are shown in Fig. 1.17-2. Immediate future areas of development include automatic (database-driven) energy calibration and pulse shape discrimination cuts.

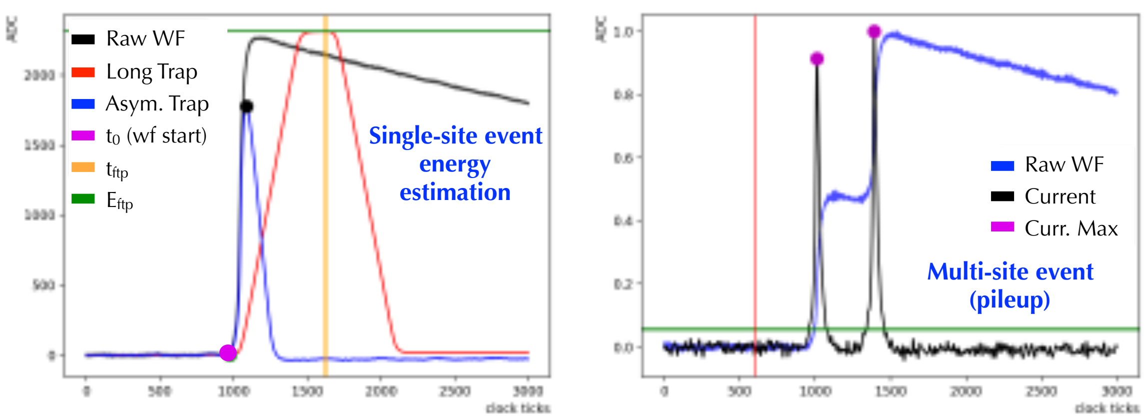

Figure 1.17-2. Two examples of HPGe waveform processing with `pygama`. *Left*: A "fixed-time-pickoff" event energy estimation using two trapezoidal filters. *Right*: A "pileup" calculator is used to find multiple maxima in the current signal.

Several HPGe and SiPM test stands are currently planning to implement the software for in-house data taking. Using the JSON metadata system, multi-detector test stands can set individual processing parameters, specify data sets, and apply detector-specific energy calibration and pulse-shape rejection. Notably, the software will be used for the upcoming characterization campaign of the new ^{enr}Ge detectors for L200 at the HADES underground laboratory in Belgium. Several LEGEND-affiliated institutions (including CENPA) plan to run the software in multi-detector test stands. These data taking campaigns will increase the user base and help create a robust processing framework for LEGEND-200.

Project 8

1.18 Project 8 - overview

A. Ashtari Esfahni, C. Claessens*, R. Cervantes, P. J. Doe, M. Fertl, M. Guigue†, B. H. LaRoque†, E. Machado, E. Novitski, W. Pettus, R. G. H. Robertson, and G. Rybka

Project 8 is a tritium endpoint experimental program targeting neutrino mass sensitivity ultimately covering the range allowed by the inverted hierarchy. The detector principle is the novel Cyclotron Radiation Emission Spectroscopy (CRES) technique, providing a differential energy spectrum measurement with high precision. The experiment has been conceived as a phased program spanning over a decade to achieve critical R&D milestones while also producing science results[1].

The collaboration is currently operating its "Phase II" apparatus. Following the first successful demonstration of the CRES technique[2], the apparatus was redesigned to increase the sensitive volume, optimize the signal-to-noise ratio, and allow use of tritium as the source gas. This year, we made the first measurement of a continuous spectrum using the CRES technique, advancing from our previous measurements of the monoenergetic conversion electrons from ^{83m}Kr. This preliminary measurement has allowed for enormous strides in understanding the hardware (described in Sec. 1.19) and analysis of tritium data (described in Sec. 1.20). A higher-statistics run utilizing these improvements is in preparation.

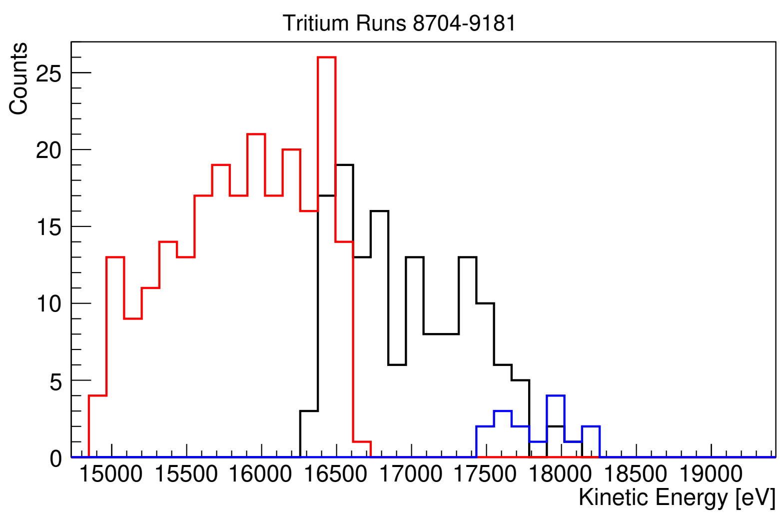

Figure 1.18-1. Preliminary measurement of tritium endpoint electrons with the Project 8 Phase II apparatus.

*Johannes Gutenberg-Universität Mainz, Germany.
†Pacific Northwest National Laboratory, Richland, WA.

[1] A. Ashtari Esfahani *et al.*, J. Phys. G **44** (2017) 054004.
[2] D. M. Asner *et al.*, Phys. Rev. Lett. **114**, 162501 (2015).

As the host institution for Project 8, CENPA is home to personnel that continue to lead the hardware design and implementation, experiment operations, as well as DAQ and slow control development. We have also published an analytical derivation of the CRES signal features expected in a waveguide, allowing for improved energy resolution[1]

The next demonstration necessary for Project 8 will be to scale up the volume, and thus tritium decay statistics, which will be the focus of Phase III. The waveguide implementations of earlier phases are cm^3-scale or smaller, and do not present a clear path forward for significant scaling. Phase III will instrument a $\sim$200 cm^3 volume. In preparation for this next phase of the experiment, an MRI magnet has been installed in the B037 laboratory space (Sec. 1.21).

Achieving the target neutrino mass sensitivity of 40 meV will require scaling Phase IV of the experiment to 10 m^3 of sensitive volume and switching to an atomic tritium source to avoid the final state broadening intrinsic to molecular tritium[2]. Overcoming the challenges inherent to production and trapping of atomic tritium is one more key focus area of the CENPA Project 8 group (Sec. 1.22).

1.19 Project 8 - Phase II - insert refurbishment

A. Ashtari Esfahni, C. Claessens*, R. Cervantes, P. J. Doe, M. Fertl, M. Guigue†, B. H. LaRoque†, E. Machado, E. Novitski, W. Pettus, R. G. H. Robertson, and G. Rybka

Several hardware upgrades have recently been made to the Project 8 Phase II apparatus that have improved data quality, enabled studies of frequency-dependent systematic effects, and made it possible to take CRES data with tritium in addition to ^{83m}Kr. The Phase II apparatus is shown in Fig. 1.19-1.

*Johannes Gutenberg-Universität Mainz, Germany.
†Pacific Northwest National Laboratory, Richland, WA.

[1] A. Ashtari Esfahani *et al.* (Project 8 Collaboration) "Electron Radiated Power in Cyclotron Radiation Emission Spectroscopy Experiments", Phys. Rev. C **99**, 055501 (2019).

[2] CENPA Annual Report, University of Washington (2017) p. 31.

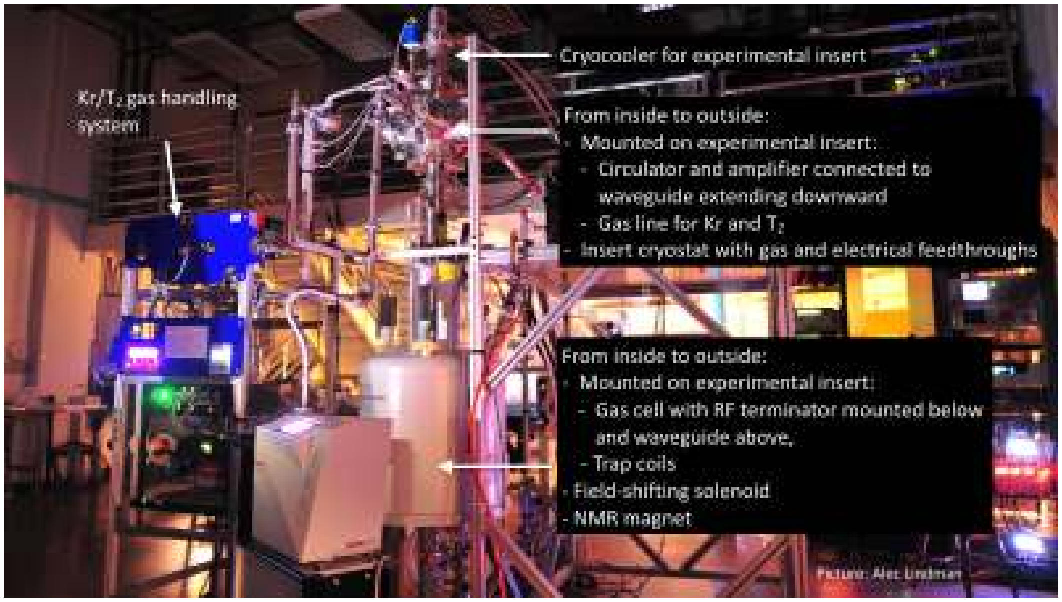

Figure 1.19-1. The Phase II apparatus with the combined ^{83m}Kr/tritium gas system installed.

Thermal break for lower noise temperature A vertical-bore NMR magnet, shown in Fig. 1.19-1, provides the ∼1-T background magnetic field needed for CRES. Several crucial elements of the phase II apparatus are mounted on a support structure ("the insert") that extends downward into the magnet bore: the gas cell containing ^{83m}Kr or tritium, the waveguide that carries electrons' cyclotron radiation (the CRES signal) toward the RF detection system, and the circulator and first amplifier of this detection system. Thermal noise is reduced and the signal-to-noise ratio of the CRES signal is improved by cooling the circulator and amplifier as much as possible, which is done by cooling the insert with a Gifford-McMahon cryocooler that can reach 22 K. However, in order to prevent ^{83m}Kr from freezing to the walls of the gas cell, this lowest part of the insert must be kept above about 80 K. A copper section of the waveguide between the gas cell and the amplifier was recently replaced by a gold-coated stainless steel section, creating a thermal break and allowing the two sections to be temperature-controlled more independently. These improvements, along with a rebuild of the GM cryrocooler led by J. Amsbaugh that enabled it to deliver more cooling power to the insert, resulted in a 40 K lower circulator temperature of 43 K and a 10 K lower amplifier temperature of 32 K, thereby improving the CRES signal-to-noise ratio.

Waveguide RF terminator for better-quality CRES signals In the Phase II apparatus, cyclotron radiation from electrons emitted in beta decay is conveyed to the RF detection system via the TE_{01} mode of a waveguide. Originally, an RF short was installed at the opposite end of the waveguide in order to maximize detection efficiency by reflecting back toward the detection system any radiation initially going in the "wrong" direction. However, this led to frequency-dependent destructive interference, in some cases eliminating the main carrier CRES signal[1]. To mitigate this problem, the RF short at the end of the waveguide was replaced by an RF terminator. No terminator with the correct geometry was available from commercial sources, so the terminator was made at CENPA by casting a 1.7"-long cone using 80% Stycast 1266 and 20% graphite powder, by weight. Fig. 1.19-2 shows the terminator. The terminator's reflection coefficient was measured in the testbed shown in Fig. 1.19-3. As shown in Fig. 1.19-4, the terminator was shown to attenuate reflections as well as or better than commercial solutions for other geometries like an SMA terminator or Eccosorb HR-25. After the terminator was installed, the destructive interference was eliminated and the interpretation of CRES signals was greatly simplified.

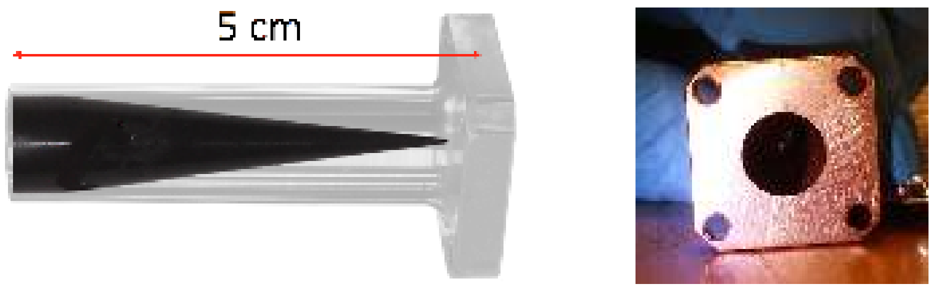

Figure 1.19-2. *Left*: the RF terminator, shown superimposed on a model of the waveguide section into which it was mounted. *Right*: end-on view of the terminator after installation in waveguide section.

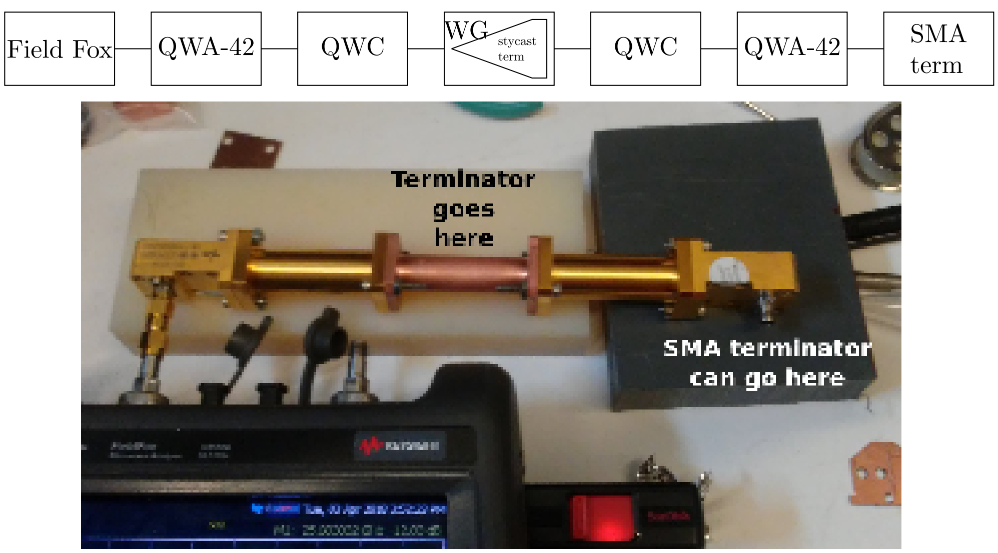

Figure 1.19-3. A testbed to measure the reflection coefficient S11 of the terminator inside of a waveguide. The Field Fox is a network analyzer, the QWAs are coaxial cable-to-waveguide adaptors, and the QWCs are rectangular-to-circular waveguide adaptors.

[1]A. Ashtari Esfahani *et al.* (Project 8 Collaboration) "Electron Radiated Power in Cyclotron Radiation Emission Spectroscopy Experiments", Phys. Rev. C **99**, 055501 (2019).

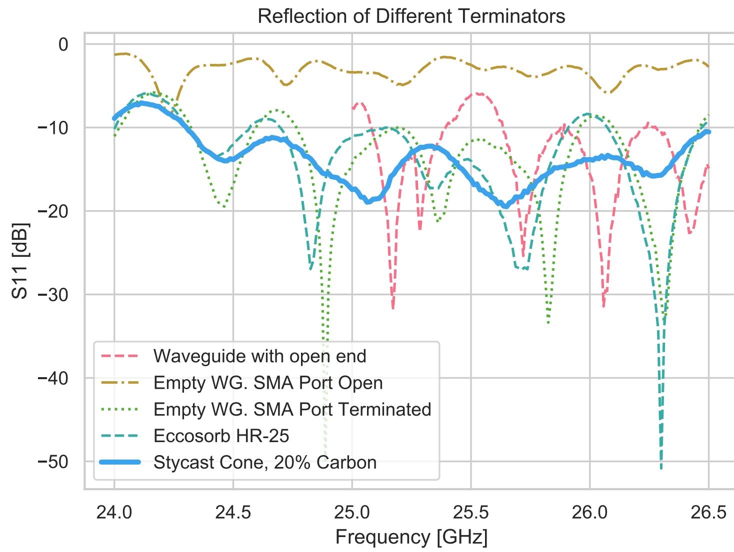

Figure 1.19-4. The reflection coefficient S11 of the terminator, compared to an open-ended waveguide, an SMA terminated waveguide, and a waveguide filled with Eccosorb HR-25.

Improved thermal mounting for trap coils After emission in beta decay, electrons are axially confined by a magnetic bottle trap created by up to currents up to 1 A through coils wound around the gas cell. After the first round of measurements with the Phase II apparatus, the insulation on these coils was found to have burned as a result of overheating due to insufficient thermal coupling to the cooling capacity of the insert. A new support structure for the coils was made from thermally-conductive Torlon and the coils re-wound onto it, shown in Fig. 1.19-5. GE 7031 varnish was used to thermally anchor the coils to the support structure and the support structure to the cooled gas cell. Additional leads were also added to the trap coils to enable a four-wire measurement of their resistance, making it possible to monitor their temperature in situ via the dependence of resistance on temperature. These improvements eliminated the coil-overheating problem.

Figure 1.19-5. New trap coils with improved thermal anchoring.

Field-shifting solenoid for systematics studies As demonstrated by the frequency-dependent destructive interference that was observed before the waveguide short was replaced by a terminator, it is crucial to be able to investigate frequency-dependent systematic effects. By changing the overall ∼1-T background magnetic field experienced by the monoenergetic 17.8-keV electrons emitted from ^{83m}Kr, the electrons' cyclotron frequency can be swept from through the frequency region of interest around the 18-keV tritium endpoint in the nominal background field. Unfortunately, the current in the NMR magnet used to create this background field cannot be ramped easily because of the cost in helium from connecting the charging cables and the need to re-map and re-shim the field after any current change. Therefore, the gas cell/waveguide assembly on the insert was modified to have less than a 1.800" outer diameter, and an additional solenoid, shown in Fig. 1.19-6, was constructed and installed in the limited space available between the insert and the 2.047"-inner-diameter NMR magnet bore. The coils were made 13.5" long to limit the shape uncertainty added the background magnetic field to 1 ppm. By ramping the current in this solenoid between ±1.06 A, electrons' cyclotron frequencies are shifted within a 180 MHz range, corresponding to an energy range of 2.1 keV below the tritium endpoint to 1.5 keV above it. Part of this range shown in Fig. 1.19-7. The field-shifting solenoid makes it possible to measure how CRES signal properties such as signal-to-noise ratio vary with frequency and makes it possible to correct the final tritium spectrum for any dependence of efficiency on frequency.

Figure 1.19-6. *Left*: The field-shifting solenoid. *Right*: Top view of the field-shifting solenoid with the experimental insert containing the gas cell and trap coils inserted.

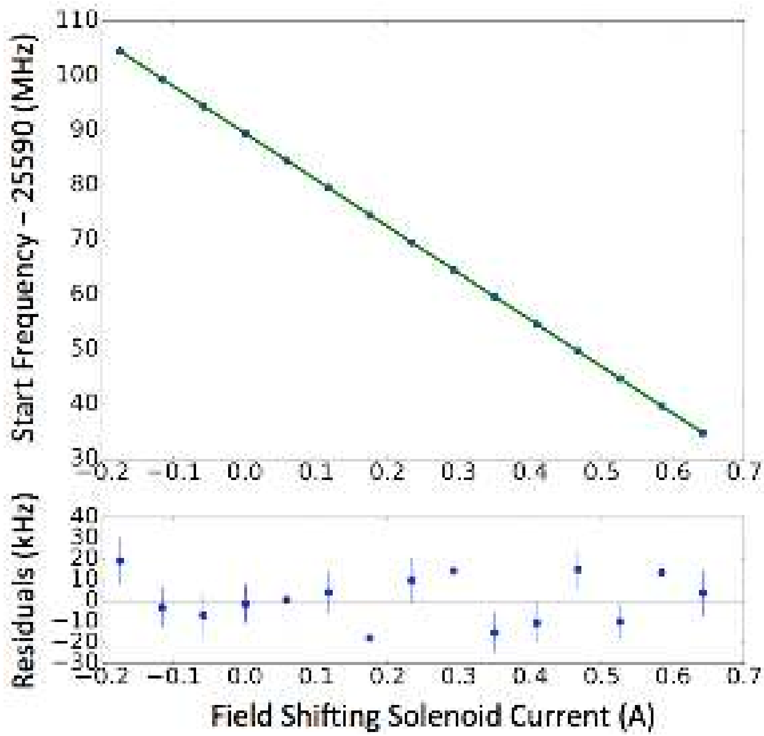

Figure 1.19-7. ^{83m}Kr 17.8-keV CRES signal frequency vs. field-shifting solenoid current, demonstrating linearity of frequency with current.

Combined gas system provides choice of pressure-regulated ^{83m}Kr or tritium Phase II of Project 8 uses both gaseous tritium for the beta decay measurement and ^{83m}Kr for calibration purposes. Therefore, a new gas system was designed to source the CRES cell with these radioactive gases. A 2 mCi reservoir of tritium was attached to the gas system. Tritium was then transferred from the reservoir to storage in a non-evaporable zirconium based getter. Tritium gas can be released into the CRES cell by increasing the getter temperature using the designated filament inside the getter. The getter also pumps on the background gas to maintain a high fraction of tritium among gas species in the cell. The getter succeeded in providing a stable pressure during tritium data taking, as shown in Fig. 1.19-8. Pressure control in higher-statistics ^{83m}Kr systematic studies also made it possible to find the pressure that maximizes the tritium count rate for the long tritium data taking campaign planned for the coming year.

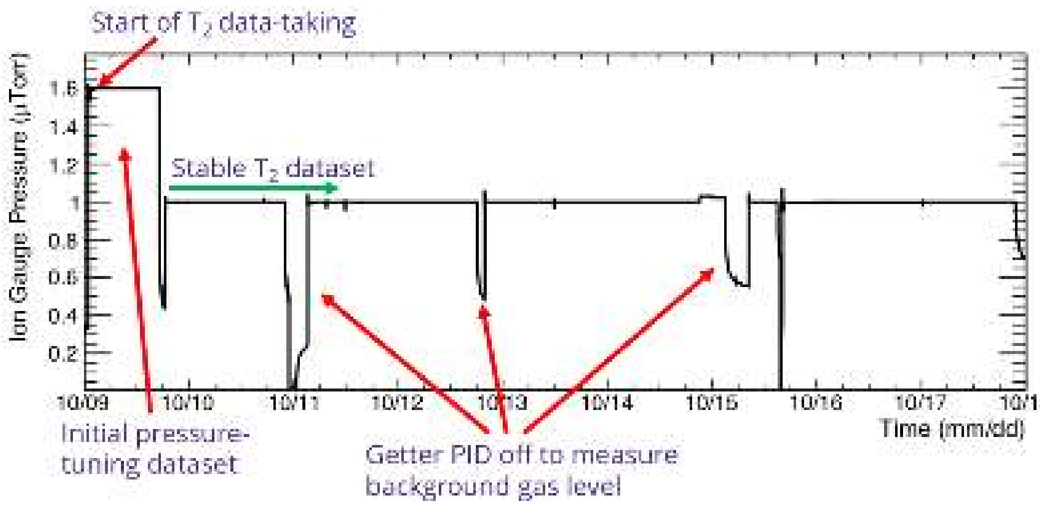

Figure 1.19-8. Pressure in the gas cell during the inaugural tritium data campaign.

1.20 Project 8 - Phase II - analysis tools and T_2 spectrum

A. Ashtari Esfahni, C. Claessens*, R. Cervantes, P. J. Doe, M. Fertl, M. Guigue†, B. H. LaRoque†, E. Machado, E. Novitski, W. Pettus, R. G. H. Robertson, and G. Rybka

In CRES, cyclotron radiation from an electron produces a signal that increases in frequency with time, producing characteristic "tracks" in a power spectrogram. Fig. 1.20-1 shows the first event in Project 8's tritium data. The analysis pipeline distinguishes signal from noise to identify each of these tracks in data, groups tracks belonging to a single electron together into an event, extracts each event's associated "start frequency" (the electron's cyclotron frequency at the time of its production in beta decay), takes into account any dependence of efficiency and start frequency precision on frequency to correct for systematic effects, and finally converts frequencies to energies to produce a spectrum.

*Johannes Gutenberg-Universität Mainz, Germany.
†Pacific Northwest National Laboratory, Richland, WA.

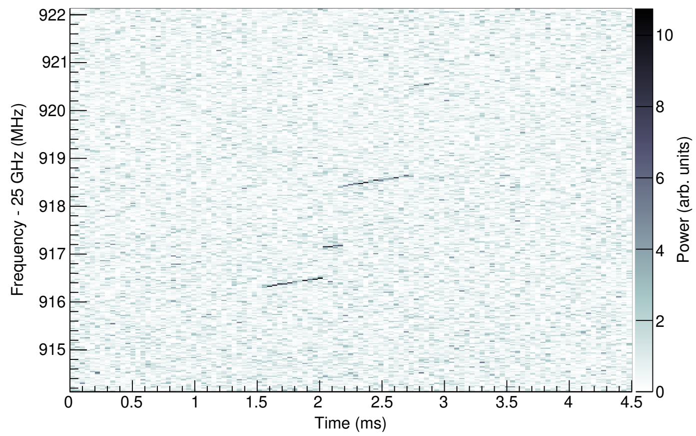

Figure 1.20-1. "Tritium Event 0" spectrogram, the first electron event identified from tritium in Project 8. The event begins at 1.5 ms. Frequency jumps between tracks are caused by inelastic collisions with gas molecules.

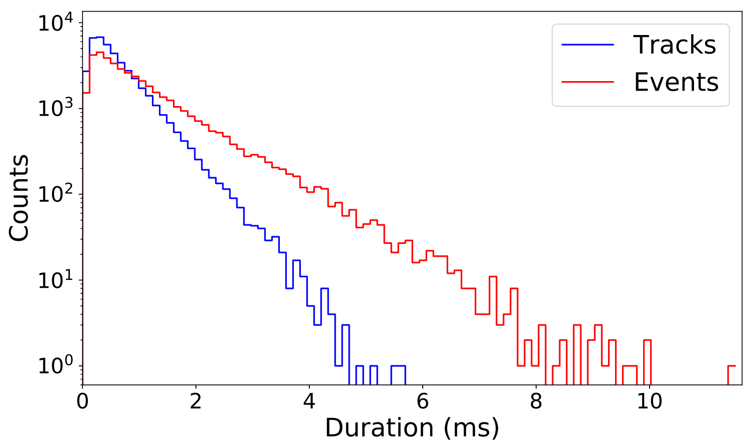

Figure 1.20-2. Distribution of track (blue) and event (red) durations. Improvements to the reconstruction have yielded high efficiency down to 250 μs tracks and distributions matching the expected exponential shape.

A UW-led effort this year targeted critical improvements in track and event reconstruction. Optimization of the reconstruction algorithms yielded improvements in identifying tracks, properly combining tracks into events, and rejecting noise false-track features. Tools are also under development to characterize the reconstruction associated systematics using analysis of simulated data. These improvements make the analysis more robust to changes in the RF system and experimental insert that impact the SNR, as occurred with the switch from the RF short to the RF terminator.

The distribution of electron track lengths in time is exponential, so many tracks that we hope to detect are short. However, the shortest electron tracks are the most difficult to distinguish from noise, and our goal of a low background rate requires stringent cuts to exclude all false events. We have recently optimized the parameters of track and event reconstruction to better distinguish tracks from noise. Fig. 1.20-2 shows high efficiency for tracks above 250 μs, improved from 3 ms as of a year ago. This improvement in short track reconstruction efficiency allows the experiment to operate at higher gas pressure and thus improve the active tritium event rate.

Fig. 1.20-3 shows start frequency spectra of the monoenergetic ^{83m}Kr 17.8 keV line in two traps. Scattering of electrons before detection creates a high-frequency (low-energy) tail. A fit model has been implemented which accounts for the natural linewidth of ^{83m}Kr and known energy loss due to scattering off residual hydrogen gas, and agrees well with the data. The extracted peak width in the shallow trap of 3.9 eV (FWHM) for the ^{83m}Kr 17.8 keV line is dominated by the natural Lorentzian linewidth of 2.83 eV and yields an instrumental resolution of 2 eV. To improve the endpoint sensitivity for the tritium run, a deep trap is used; this provides a significant increase in the tritium statistics of Phase II with acceptable loss in resolution.

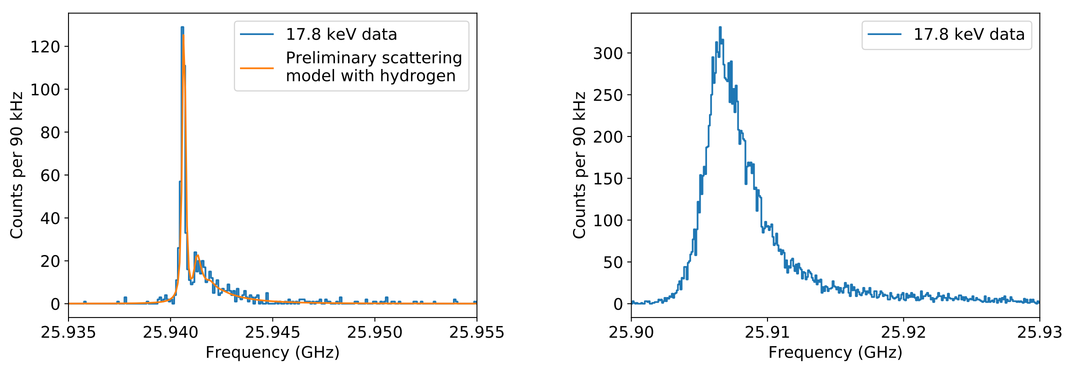

Figure 1.20-3. Spectrum of 17.8 keV ^{83m}Kr conversion electrons in shallow (*left*) and deep (*right*) trap configurations. The shallow trap yields excellent 2 eV FWHM instrumental resolution, whereas the deep trap is used to increase statistics. The high-frequency (low-energy) tail is from electrons which scatter on residual gas before being detected.

Following an extensive ^{83m}Kr systematics dataset campaign, we recorded a short nine-day tritium run in October 2018 and reported first results at the DNP conference later that month. Using three independent digitization windows the data covers the last several keV of the spectrum and extends an additional 0.5 keV beyond the 18.6-keV endpoint, as shown in Fig. 1.20-4. The limits of each DAQ channel have well-understood losses of efficiency do to digital filtering in the FPGA. The efficiency in the low-energy (high-frequency) channel rolls off due to decreased SNR from image noise approaching the Nyquist frequency of the digitizer.

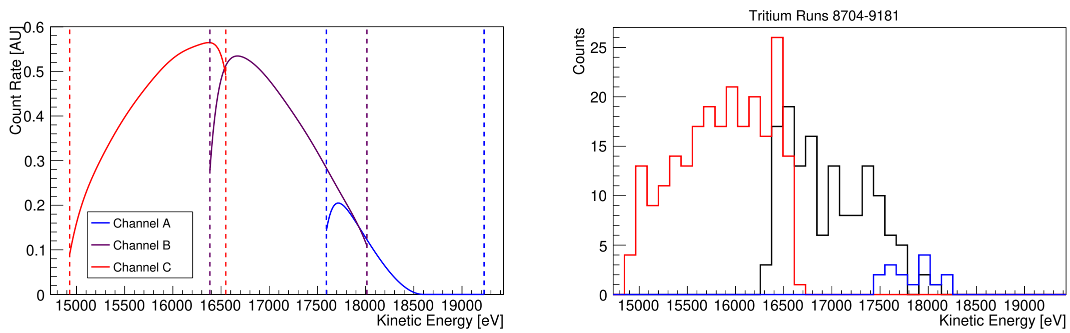

Figure 1.20-4. Predicted (*left*) and measured (*right*) tritium spectrum from nine-day run in October 2018. The measured spectrum matches the prediction well within statistics and no events are observed beyond the endpoint.

A 100-day tritium data campaign with a projected $\sim 10,000$ events and endpoint resolution of ~ 10 eV is planned for summer 2019. Systematics studies with ^{83m}Kr and with simulation tools are also ongoing to optimize the count rate and endpoint sensitivity and fully explore any frequency-dependent effects impacting the analysis.

1.21 Project 8 - Phase III - MRI magnet installation

A. Ashtari Esfahni, C. Claessens*, R. Cervantes, P. J. Doe, M. Fertl, M. Guigue†, B. H. LaRoque†, E. Machado, E. Novitski, W. Pettus, R. G. H. Robertson, and G. Rybka

To accurately reconstruct decay electron energies with cyclotron radiation emission spectroscopy (CRES), undisturbed microwave signals of (on average) 100 µs are required. Given a fixed scattering cross section for electrons of a certain energy this implies a maximum density for the electron source gas. Therefore, higher counting statistics can only be achieved by increasing (scaling up) the source gas volume, which directly implies the requirement for a large volume, high-precision magnetic field setup.

Superconducting magnets from clinical magnetic resonance imaging (MRI) units are particularly well suited for a Project 8 Phase III setup, as they provide magnetic field in the range of 1.0 T to 1.5 T with parts-per-million inhomogeneity over spherical volumes with 40 cm diameter and are easily available on the secondary market. We recently commissioned such a magnet as test bed in our laboratory in the physics and astronomy building.

*Johannes Gutenberg-Universität Mainz, Germany.
†Pacific Northwest National Laboratory, Richland, WA.

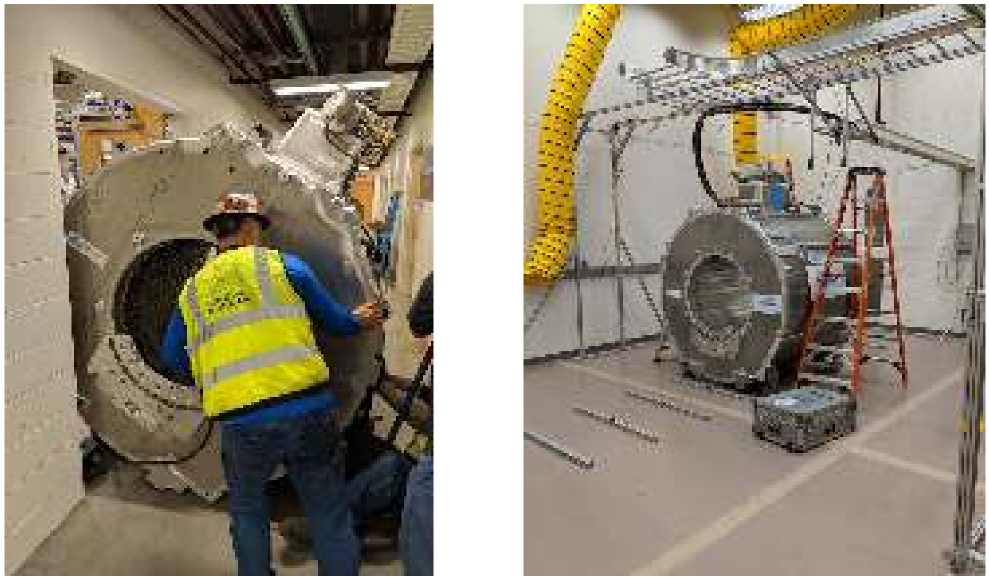

Figure 1.21-1. The liquid-helium-filled magnet had to be rotated to its side to clear the the door frame of the laboratory. The mechanical and electrical installation work had to be completed before the magnet was ramped to ≈0.96 T.

During summer and fall 2018 we prepared our laboratory for the installation of a Philips ICG F2000 magnet. Given the particular research setting compared to the normal hospital MRI unit environment we worked in close exchange with the UW EH&S (environmental, health and safety) department and campus facilities to provide for safe operations before our magnet started its 2000 mi journey from Bettendorf, Iowa, across the Rocky Mountains to Seattle, Washington. After an assessment of the oxygen deficiency hazard (ODH) related to the 1600 L of liquid helium in the magnet we installed additional air ducts and ODH monitors. On basis of a detailed review of the hazards related to the large-volume, strong magnetic field we developed the required site-specific safety training material. In December 2018, the magnet arrived at UW and was carefully rigged through tight aisles and low door frames into the laboratory, as shown in Fig. 1.21-1. Before ramping the magnet, the electrical and mechanical infrastructure around the magnet had to be completed. A non-magnetic safety barrier was installed around the magnet to prevent unauthorized access and non-magnetic cable trays were installed to support the signal cables in the future experiment.

To compensate for losses during the transport, 750 L of liquid helium where transferred into the cryostat, as shown in Fig. 1.21-2, just before ramping the magnet close to its nominal magnetic field of 0.96 T. To homogenize the magnetic field, small iron pieces are installed in so-called shim trays on the inner surface of the magnet bore. In four iterations of a cycle consisting of mapping the magnetic field with a nuclear magnetic resonance probe, calculating an optimized iron distribution and physically installing the iron pieces, we positioned ≈12 kg of iron (see Fig. 1.21-2) to achieve a magnetic field inhomogeneity of 1 ppm resp. 0.31 ppm (peak-to-peak resp. RMS) over a 30 cm diameter sphere. This is sufficient for Phase III of Project 8 and provides an ideal setup to develop and test the instrumentation required to track the magnetic field over the (longer) time scale of the experiment.

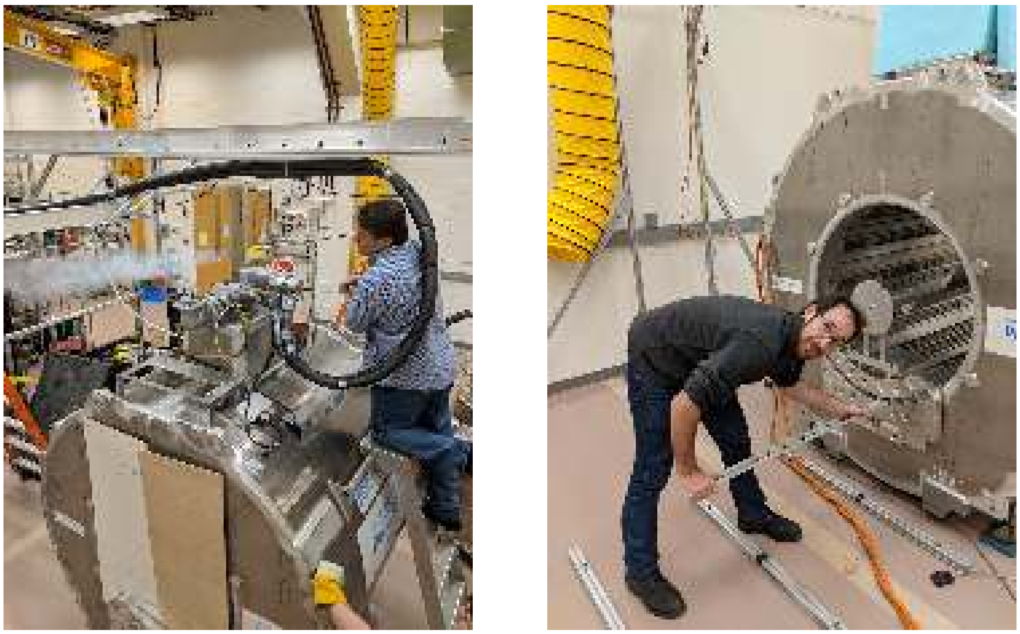

Figure 1.21-2. The magnet was refilled with liquid helium before ramping. The magnetic field was homogenized using an iterative cycle of of magnetic field measurement, iron distribution calculation and installation of the physical iron pieces in the so-called shim trays of the magnet.

1.22 Project 8 - Phase IV - atomic hydrogen testbed

A. Ashtari Esfahni, C. Claessens*, R. Cervantes, P. J. Doe, M. Fertl, M. Guigue†, B. H. LaRoque†, E. Machado, E. Novitski, W. Pettus, R. G. H. Robertson, and G. Rybka

In the beta decay of molecular tritium (T_2), the rotational and vibrational states of the bound HeT^+ molecular ion systematically modify the endpoint of the beta spectrum, as shown in Fig. 1.22-1. The exceptional energy resolution and scalablity of the CRES technique means that the Project 8 experiment will eventually be able to push limits on neutrino mass ($m_\beta = \sqrt{\sum_{i=1}^{3} |U_{ei}|^2 m_i}$) to the point where these states will impose a fundamental limit on sensitivity to m_β.

This limitation can be avoided by using atomic tritium, which is one of the major goals of the Project 8 experiment. This introduces many additional R&D challenges,

*Johannes Gutenberg-Universität Mainz, Germany.

†Pacific Northwest National Laboratory, Richland, WA.

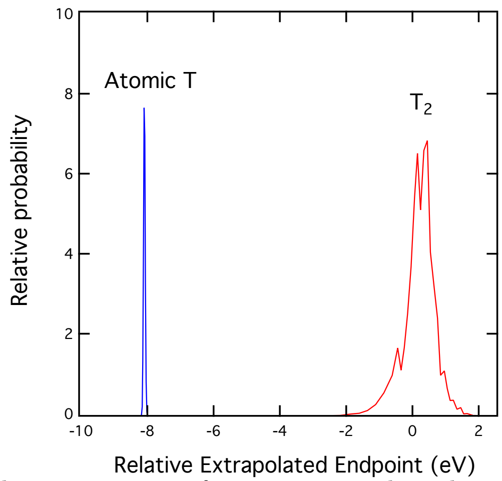

Figure 1.22-1. The final state smearing for T_2 compared to that of atomic tritium. Note that the resulting endpoint of the beta spectrum from atomic tritium is 8 eV lower than the endpoint from the decays of T_2.

owing to the the fact that the recombination of tritium atoms is dominated by interactions with physical surfaces. Fortunately, the nonzero magnetic moment of hydrogen isotope atoms means that they may be manipulated through their $-\vec{\mu} \cdot \vec{B}$ interaction with magnetic fields. It is possible to transport, cool, and trap these atoms using magnetic fields, but losses can result at each step of the chain from dissociator to trap. So far, using the best estimates of losses from the trap and transport chain, we expect to need to crack 10^{19} or more atoms/sec. To do this, we will pass tritium through a dissociator that features a $\sim$2500K tungsten capillary, which splits the molecules.

R&D efforts at CENPA are focused at first on producing atomic hydrogen rather than atomic tritium, since the processes are nearly identical, but hydrogen is much safer to work with. One goal of the testbed is to characterize the beam of hydrogen atoms from two atom sources: the commercially available Hydrogen Atom Beam Source (HABS) from United Mineral Corp., as well as a custom-designed source. The HABS source has been studied and characterized by the manufacturer and will give us some confidence in our ability to measure and characterize atomic hydrogen beams. However, the HABS source does not fully satisfy our needs, which motivates the design of the custom source. Table 1.22-1 shows useful metrics where the design of the custom source has been modified to better suit our needs. A larger diameter gives better atom fluence. Exclusively coaxial currents enable the source to function much better in the presence of external magnetic fields, which we know will be present. Finally, since the tungsten parts of the custom source are thicker than those of the commercial source, we believe that the evaporative losses of tungsten will be mitigated, leading to a longer lifetime of the source: an important consideration for operating with tritium.

For each of these sources, the goal is to perform mass spectroscopy on the beam, while satisfying certain conditions. Firstly, we want to set the ionization energy of

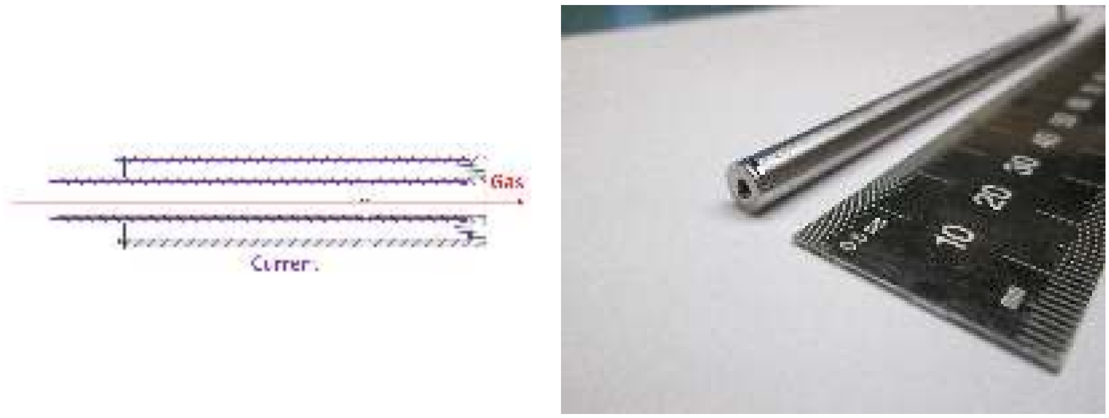

Figure 1.22-2. The tungsten part of the custom source is specially designed to have coaxial currents.

Characteristic	HABS	Custom source
Capillary diameter	1 mm	2 mm
Heating	Radiative	Direct current
External magnetic field compatible?	No, helical current-carrying filaments	Yes, axial currents only

Table 1.22-1. Comparison of atom sources to be tested

the electrons in our mass spectrometer between 13.6 eV and 15.4 eV. This way atomic hydrogen will be ionized, but molecular hydrogen will not be. For electron energies higher than 15.4 eV a systematic error is introduced, where an increase in H_2 necessarily results in an increase in the observed 1 amu mass peak, making it challenging to differentiate the effects of the dissociator. Secondly, we want to be able to cleanly resolve the mass-0, mass-1, and mass-2 peaks. Thirdly, we want to allow translation of the measurement device so that a portion of the angular dependence of the beam can be mapped. Finally, we want to introduce a beam chopper, so that time-of-flight measurements can be used to interpret the velocity distribution of the beam. We have identified a mass spectrometer that will be able to satisfy all four of these requirements in Hiden's 3F/PIC quadrupole mass spectrometer.

Fig. 1.22-3 shows the schematic layout of the experimental testbed, the structure of which allows the mass spectrometer to be translated to map the angular distribution of the beam. The addition of a rotating disk chopper allows a time-of-flight measurement of beam velocities, which will be valuable for studying methods for cooling the beam. This testbed is currently under construction in B037 and will be ready to be commissioned soon.

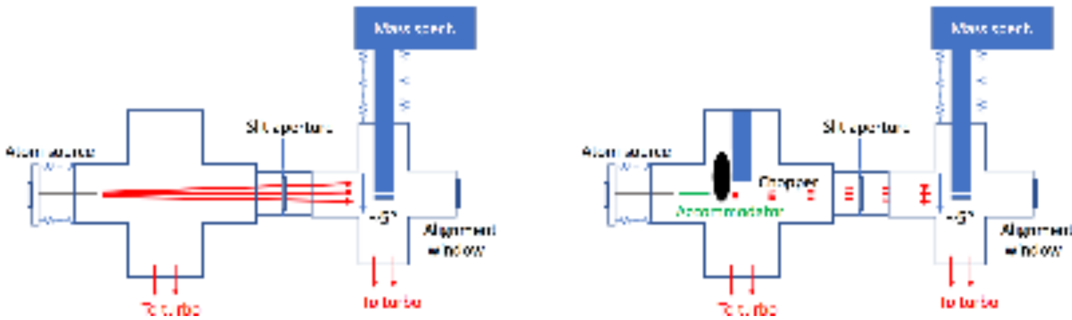

Figure 1.22-3. Two layouts of the atomic hydrogen testbed. The second layout shows the addition of a rotating-disk chopper, to be used for time-of-flight measurements of beam velocity.

Selena

1.23 Selena R&D

A. E. Chavarria, C. Galbiati*, X. Li*, A. Razeto†, and A. Piers

The Selena project is a proposed neutrinoless double beta decay ($0\nu\beta\beta$) experiment that leverages an advantageous isotope, ^{82}Se, and novel detector scheme to suppress background events. ^{82}Se is an isotope that undergoes regular double beta decay ($2\nu\beta\beta$) with a Q-value of $Q_{\beta\beta} = 2998$ keV and a half life of $\tau_{1/2} = 1 \times 10^{20}$ yrs; the Q-value lies outside of the energy range of γ-rays from the uranium and thorium decay chains and the half-life is long enough to reduce the number of $2\nu\beta\beta$ events that carry almost the entire decay energy. The proposed detector is a stack of layers of amorphous selenium (a-Se) evaporated onto a pixelated CMOS array that records the energy and spatial distribution of events, allowing us to distinguish the signature double beta decay tracks originating from a singe vertex from unwanted background, further reducing the

*Princeton University, Princeton, NJ.
†Laboratori Nazionali del Gran Sasso, L'Aquila, Abruzzo, Italy.

background rate[1].

One common use of a-Se is in medical x-ray devices, which means that the technology to build a-Se sensors is quite developed. However, medical x-rays operate at a much lower energy (~10s of keV) than the the $Q_{\beta\beta}$ for ^{82}Se, and some properties of a-Se are not well enough known for the necessary operating conditions of a $0\nu\beta\beta$ detector. Most significantly, the work-function—the number of charge carriers created per unit energy—and the energy resolution are not known at high energies and electric fields. This past year, we, along with our collaborators at Princeton University, designed, simulated, and constructed a calorimeter to measure these properties.

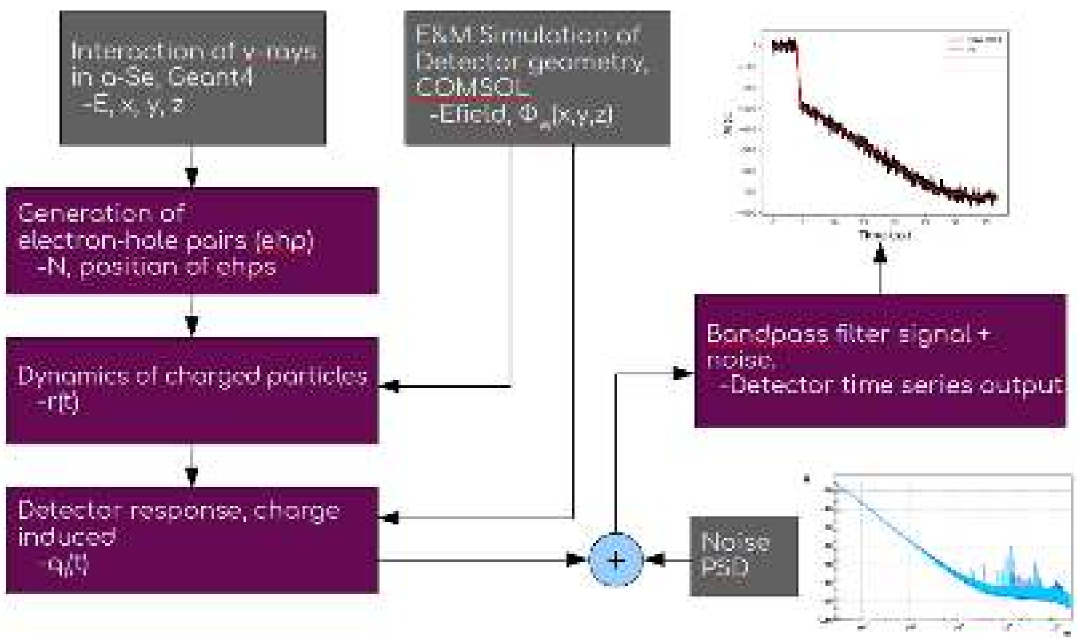

Figure 1.23-1. Flow chart of the simulation package developed to calculate a detector's response. We used this software to optimize the detector designs.

We developed a robust simulation tool to accurately recreate the detector response given some incident γ-ray. We simulated the location of energy deposition of incident γ radiation on our detector in Geant4, converted the energy to electron-hole pairs including statistical fluctuations in the charge generation, computed the dynamics of the charge given the electric field computed in COMSOL Multiphysics, and calculated the time-varying charge induced using the weighted potential of the detector. A summary of our simulation package is in Fig. 1.23-1. We used these simulations to optimize the detector geometry and operating conditions.

Based on our simulations, we constructed two detectors: a bipolar sensor consisting of a circular electrode surrounded by a grounding ring and a unipolar sensor of two

[1] A. E. Chavarria *et al* 2017 *JINST* **12** P03022.

interlaced electrodes. In a-Se, the hole mobility (μ_h) is ∼100 greater than the electron mobility (μ_e). The bipolar detector is sensitive to both charge carriers, which results in a "fast" hole and "slow" electron pulse, whereas the unipolar detector response is the differential signal between the two electrodes so that the slow-moving electron component gets subtracted out and only the hole component remains. Fig. 1.23-2 shows the detector geometries and pulse outputs. Additionally, because the detector size is approaching the mean free path of electrons, the electrons are susceptible to permanent trapping, reducing the amount of charge collected. Thus the bipolar detector, which is sensitive to these slow-electron effects, exhibits a lower signal-to-noise ratio and worse performance than the unipolar sensor (see Fig. 1.23-3) as a calorimeter.

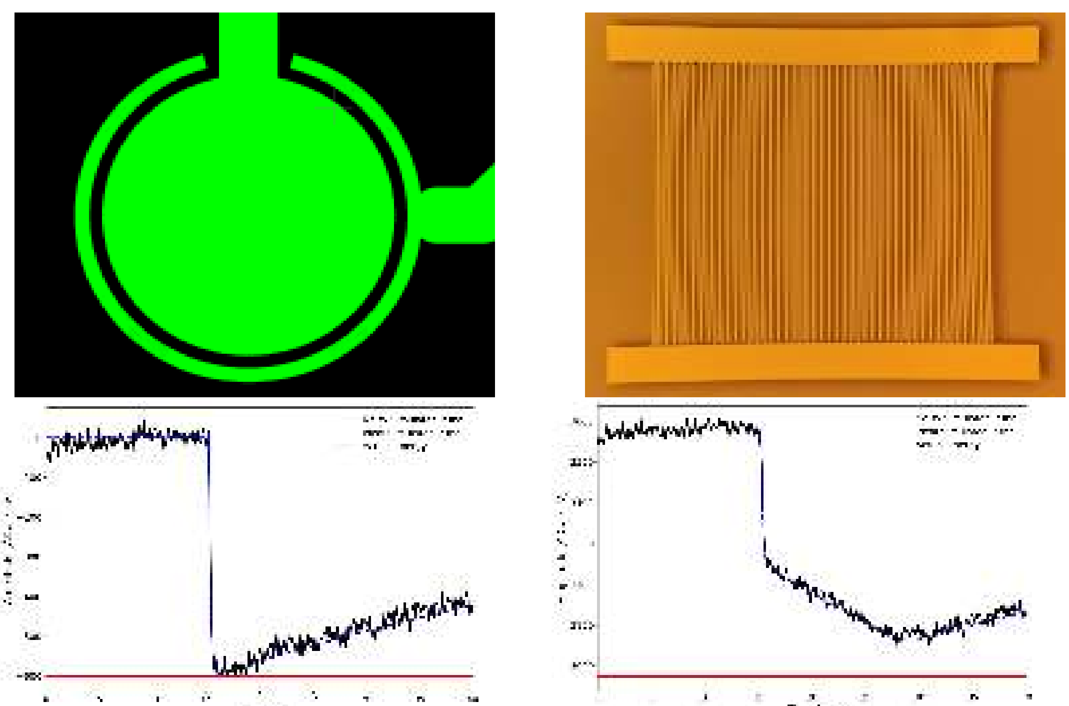

Figure 1.23-2. *Left:* Geometry and simulated pulse (raw and with instrumentation noise) of the bipolar sensor. *Right:* Unipolar sensor.

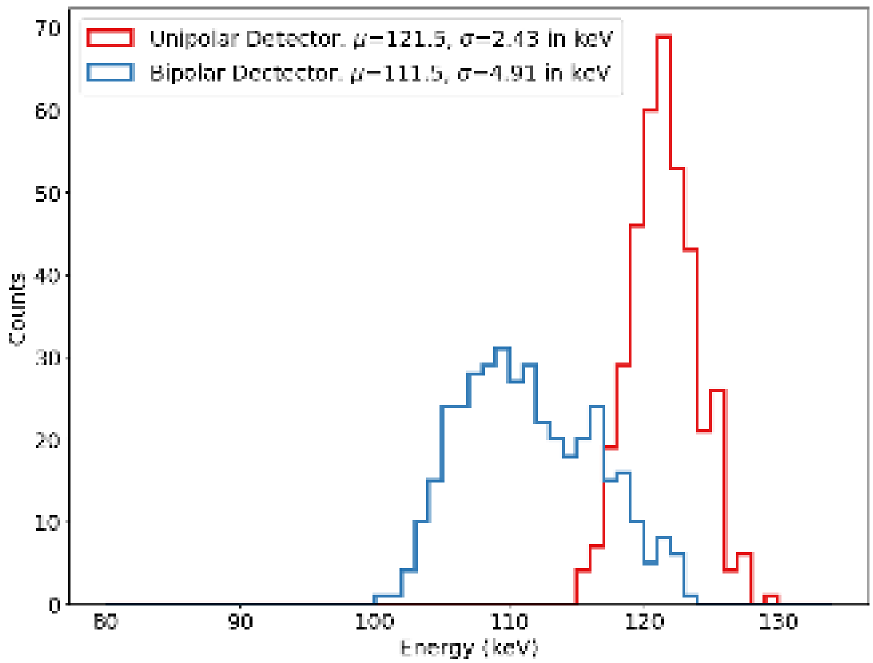

Figure 1.23-3. Simulated energy reconstruction of the ^{57}Co 122 keV line for a bipolar and unipolar detector. The geometry of the unipolar detector has a factor of ∼2 better energy resolution.

Despite the limitations of the bipolar sensor, we constructed one to test our electronic setup (consisting of a HV power supply, low noise XGLab CUBE amplifier, and bandpass filter) and compare our initial results to literature values. We obtained preliminary results on the work-function of selenium and energy resolution as a function of the bias electric field (10-30 V/μm). We are currently adapting the front-end amplifier to accommodate the two-channel unipolar sensor; we will begin the next round of testing soon, which should allow us to investigate the relevant parameter space of E-field and energy used in a $0\nu\beta\beta$ experiment.

2 Fundamental symmetries and non-accelerator-based weak interactions

Torsion-balance experiments

2.1 A gravitational calibrator for LIGO

J. H. Gundlach, K. R. Kumar, M. P. Ross, and K. Venkateswara

Precise and accurate calibration of the gravitational-wave (GW) strain measured by the current and future network of GW detectors will play an increasingly prominent role in the astrophysics enabled by such measurements. For example, resolving the tension in measurements of the Hubble constant with gravitational-wave observations will require calibration uncertainty below 1%. Currently, calibration is performed using radiation pressure exerted by an auxiliary laser and calibrated detector, known as the Photon Calibrator (PCal) system with calibration uncertainty of ∼5%. Performing a complementary calibration using a gravitational calibrator, which would have different systematics compared to the PCal system, would give further confidence in the calibration and lead to accurate calibration with uncertainty below 1%.

We have developed a gravitational calibrator consisting of a high-speed rotor with large and precise gravitational multipoles. It is made of an aluminum disk with an outer pattern of six holes and an inner pattern of four holes machined precisely with wire-Electrode Discharge Machining. They will be filled by matched tungsten alloy cylinders to form an outer mass-hexapole and inner mass-quadrupole. When located close to the LIGO test-mass optic just outside the vacuum chambers, and spun at a frequency $\underline{f}$, they will produce a gravitationally induced displacement of the test-mass at $3\underline{f}$ and $2\underline{f}$ respectively. The ratio of the two signals will allow us to measure the distance to the test-mass, thereby reducing this important source of systematic uncertainty and allowing a precise calibration of the test-mass displacement. The calibrator is intended to be deployed at the LIGO Hanford Observatory (LHO).

Over the course of the last year, we have developed a smooth and robust rotor design capable of being spun at speeds of ∼30 Hz while consuming a total power below ∼40 W. The tungsten cylinders weigh 1.056 kg each and the full rotor weighs about 12 kg. We have iterated and improved the mechanical aspects of the rotor deisgn to minimize vibrations and frictional losses. For easier integration with LIGO's DAQ, the angular position of the rotor is output as an analog voltage signal using an optical encoder mounted on the rotor shaft and a circuit being developed by the CENPA Electronics Shop. We are also developing a new rotor control system built on a TwinCat 3 network, which is used by LIGO for slow-controls.

In parallel, we are developing MATLAB code for numerical modeling of the gravitational displacement of the test mass based on an FEA technique. The model will be used to set the theoretical uncertainty on the expected signal given the uncertainties in test mass and rotor location, mass and geometries. We expect to test the gravitational calibrator at LHO in summer 2019.

This work was supported by National Science Foundation Grant PHY-1607385.

2.2 Development of precision rotation sensors for the LIGO seismic isolation systems

J. H. Gundlach, C. A. Hagedorn, A. S. Lockwood, M. P. Ross, and K. Venkateswara

To operate in the presence of the persistent seismic motion that is present on earth, the Laser Interferometer Gravitational-Wave Observatory (LIGO) employs a complex seismic isolation system that consists of multiple layers of passive and active isolation. As part of the active isolation, the signal from a seismometer placed on the floor of the observatory is fed forward to the first isolation stage to correct for the ground motion contribution of a relative position sensor. As seismometers sense motion relative to an inertial proof mass, they are susceptible to contamination by forces acting on the proof mass, for example the change of the gravitational force when the device is tilted. In the context of the LIGO seismic isolation, this limits our ability to use the ground seismometer when the observatory floor deforms. These deformations are primarily driven by wind pressure acting on the walls of the building.

To correct for this contamination, our group has developed and installed precision ground rotation sensors consisting of a 1 m long beam hung from 10-15 μm thick flexures. The angle of the beam relative to the vacuum chamber it is housed in is sensed by an autocollimator giving a sensitivity of 0.1 nrad/$\sqrt{Hz}$ above 10 mHz. During the upgrade period between the first and second LIGO observing runs (2016), two rotation sensors were installed at the LIGO Hanford Observatory, one at each end station, which allowed the observatory to operate at higher wind speeds in the second run when compared to the first. Following this success, our group installed four rotation sensors at the LIGO Livingston Observatory, one at each end station and two at the corner station, during a similar period between the second and third observing runs (2018). All six of these sensors are now regularly used in the seismic isolation systems and we expect similar improvements at the Livingston observatory as we saw after installing the sensors at Hanford.

Additionally, we are continuing the development of a compact version of these rotation sensors that have interferometric angular readouts with the aim of installing them on the LIGO seismic isolation platforms. In the same manner as the ground seismometers, the seismometers that are used to sense the motion of the platform suffer from tilt contamination, which we hope to bypass by installing these compact rotation sensors. This scheme has the further benefit that our sensors are projected to have significantly lower noise floors than the current on-platform rotation sensors, allowing increased performance of the rotational feedback systems. As the device will be installed on the isolation platform that is held within the primary LIGO vacuum chamber, it must be designed to meet the stringent LIGO vacuum requirements while also allowing for remote operation. To meet these requirements, we have developed a process for constructing vacuum-compatible beamsplitter-coated optical fibers (a primary component of the readout) and have removed all non-vacuum compatible materials from the design. In parallel, we are in the early stages of developing a system to remotely center the instrument, which in previous devices had to be done by hand. After these systems are perfected, we plan to install a prototype at the LIGO test interferometer located at MIT to develop a control system that includes these sensors and, subsequently, to show the improved isolation performance.

This work was supported by National Science Foundation Grant PHY-1607385.

2.3 Updates on Fourier-Bessel pendulum experiment for testing short-range gravity

E. G. Adelberger, B. R. Heckel, B. M. Iritani, J. R. Johnson, J. G. Lee, C. E. Matt, and H. E. Swanson

The Fourier-Bessel pendulum experiment tests the Inverse-Square Law (ISL) for gravity at tens of micrometers, currently placing the shortest distance limit on new forces coupling to matter at gravitational strength[1,2]. We began operating the Fourier-Bessel pendulum experiment again in June of 2018 after briefly opening up to attempt to decrease the separation between the attractor test-mass and electrostatic screen. We are happy to report that we succeded and have achieved the shortest face-to-face separations of the test-masses to date.

Data taking has progressed for approximately eight months, and we are currently performing checks of various systematic cross-couplings. The ISL test consists of measuring torques on the test-masses as a function of separation and comparing to the predicted Newtonian or Newtonian + Yukawa models. We have taken data at separations as far as 3.5mm and as close as 50 μm, as shown in Fig. 2.3-1.

The analysis of the final dataset is forthcoming, but we have identified a number of couplings that may lead to simple improvements in any future iteration of the experiment.

1. **Vertical sensitivity:** The pendulum vertical bounce mode due to stretching of the fiber and damper system can couple vertical ground-motion into twist. The

[1] CENPA Annual Report, University of Washington (2017) p. 39.

[2] D. J. Kapner, T. S. Cook, E. G. Adelberger, J. H. Gundlach, B. R. Heckel, C. D. Hoyle, and H. E. Swanson, Phys. Rev. Lett. **98**, 2 (2007).

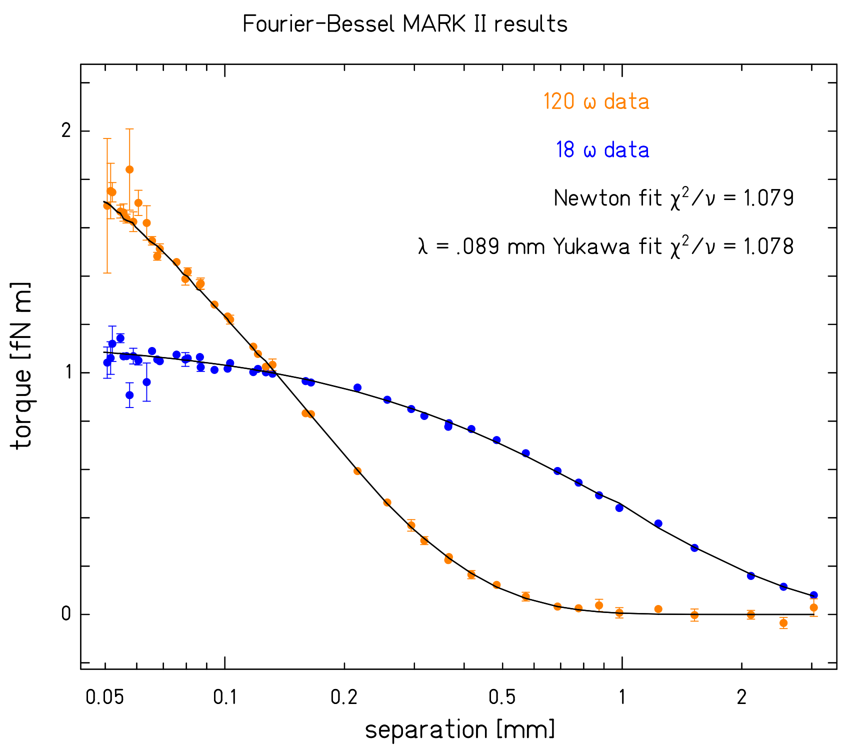

Figure 2.3-1. In-phase component of 120 ω and 18 ω torques as a function of total separation.

pendulum is especially sensitive to this at small separations, where we see excess torque noise due to this coupling. We have purchased a new Kinemetrics MBB-2 seismometer to build a seismic isolation platform that does not contribute to motion in twist.

2. **Tilt:** The 120 ω torque signal quickly dies away when the axis of the turntable and pendulum fiber axis are misaligned, such that at 30 μm of radial misalignment, the torque amplitude is decreased by about 1%. With a 1 m long fiber suspending the pendulum, 1μ rad of tilt leads to 1 μm of misalignment. It is reasonable to operate with a shorter fiber, sacrificing torque noise for lower tilt sensitivity, because the instrument is not currently limited by the fiber thermal noise.

3. **Swing:** In a similar manner to tilt, the random horizontal displacements due to the swinging of the pendulum average down the torque signal. It was noticed that the swing damper in the fiber suspension is fairly ineffective, with a large quality factor of $Q \approx 1000$. Again, the shorter length fiber coupled with a slightly larger damper might drastically improve this effect.

Over the course of the year, we have also attempted various other improvements, led by undergraduates:

1. **Temperature:** Temperature drifts can change separations and tilts of the apparatus. We revived the temperature feedback control in the lab[1] again and started writing the data to a PostGreSQL database.
2. **Off-center Calculations:** The program used to determine the effects of radial misalignment has been improved to handle new symmetry patterns for potential future test-mass designs. The program also runs nearly an order of magnitude faster for calculations of harmonics due to a small change in the algorithm.
3. **First Contact^{TM}:** We tested the potential use of First Contact^{TM} for surface cleaning of the test-masses on a set of mock test-masses. It appears to interact with the Stycast 1266 epoxy used for fixing the test-mass patterns to the substrate.

This work was supported by National Science Foundation Grants PHY-1305726 and PHY-1607391.

2.4 Limits on equivalence-principle violating ultralight dark matter

E. G. Adelberger, J. H. Gundlach, C. A. Hagedorn, J. G. Lee, E. A. Shaw, and K. Venkateswara

A recent paper[2] motivates torsion-balance experiments for setting limits on the mass and coupling constants of ultra-light vector dark matter. One example is vector dark matter coupled to baryon minus lepton number (B-L). B-L is a conserved quantity in all known interactions and remains so in grand-unified and supersymmetric theories beyond the Standard Model. This makes it a well-motivated conserved charge that may have a corresponding massive gauge boson coupled to it. Additionally, a baryon-number (B) coupled vector boson is of interest. We can search for a torque signal from these dark matter candidates using the composition dipole pendulum of our 8-test-body pendulum[3]. The torque on the composition dipole from this field-like dark matter would be equivalent to the torque induced by an oscillating electric field on an electric dipole. This dark matter field would oscillate at the Compton frequency of the particles with a coherent amplitude in an unknown direction in the frame of our solar system. As the Earth turns in this field the signal woiuld be modulated with the sidereal day.

We have ∼6 months of data that we began analyzing last year[4]. To set confidence limits we now analyze the data in a similar way to an experiment with our spin pendulum[5]. The main difference in the analysis is that the spin experiment was a rotating

[1] CENPA Annual Report, University of Washington (2017) p. 41.

[2] P. W. Graham, D. E. Kaplan, J. Mardon, S. Rajendran, and W. A. Terrano, Phys. Rev. D **93**, 075029 (2016).

[3] CENPA Annual Report, University of Washington (2018) p. 50.

[4] CENPA Annual Report, University of Washington (2018) p. 51.

[5] W. A. Terrano, E. G. Adelberger, C. A. Hagedorn, and B. R. Heckel, arXiv:1902.04246 [astro-ph.CO] (2019).

experiment in which the signal of interest was modulated at the turntable frequency. In contrast, in this experiment, we do linear fits for the dark matter signal in an unknown direction in geocentric equatorial coordinates on data chunks with duration of the sidereal day. The quadrature amplitudes for signals in the X, Y, and Z directions are related to the means of the fits for the 6 basis functions over the entire dataset. The uncertainties are computed using the standard deviations of the fit distributions. Limits set in this way (Fig. 2.4-1) do not show any statistically significant signal. This type of search complements equivalence principle tests like ours[1] and the MICROSCOPE mission[2]; it is more sensitive to the mass of these particles and would be able to determine whether a particle is the dark matter or a sub-component of the dark matter. This work was supported by National Science Foundation Grants PHY-1305726 and PHY-1607391.

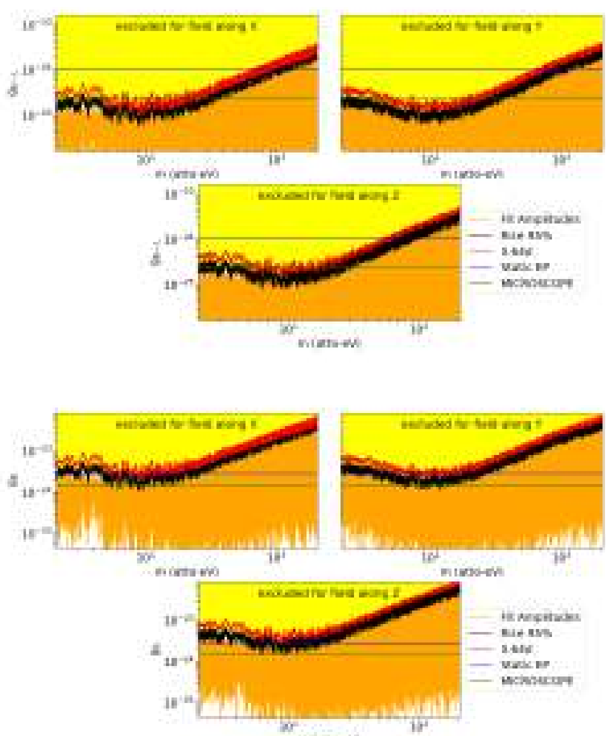

Figure 2.4-1. The top three plots are limits on the B-L coupling constant g_{B-L} and the lower three are limits on the B coupling constant. The yellow shaded regions above the black 95-percent confidence limits are excluded parameter space for the signal of interest computed from the Rice distribution. In orange are fit amplitudes for each direction of interest. If there is no signal in the data, the Rayleigh ditribution predicts there is only a 5 percent chance that a single amplitude at any mass in our search would lie above the red 5.64σ (none do). Static EP are the limits set by our equivalence principle test. The MICROSCOPE is a new equivalence principle limit set by the MICROSCOPE mission.

[1] T. A. Wagner, S. Schlamminger, J. H. Gundlach, and E. G. Adelberger, Class. Quantum Grav. **29**, 184002 (2012).

[2] P. Touboul *et al*, Phys. Rev. Letters **119**, 231101 (2017).

2.5 Probing fuzzy dark matter with a quantum gyroscope

E. G. Adelberger, C. A. Hagedorn, B. R. Heckel, and W. A. Terrano*

It has recently been recognized that dark matter may consist of ultra-low-mass particles whose quantum mechanical behavior can impact galactic structures. Experimentally, such dark matter acts like coherent waves rather than as particles.

We analyzed an 6.7-year span of data taken with a quantum gyroscope that contains no moving parts (formerly known as the Eöt-Wash spin pendulum) suspended in a rotating torsion-balance to search for the "wind" from ultralight, axionlike dark matter with masses between 10^{-23} and 10^{-18} eV/c^2. Over much of this mass range, this gyroscope, which contains $\sim 10^{23}$ polarized electrons but a negligible external magnetic, allowed us to set a 95% confidence limit $F_{\rm a}/C_{\rm e} > 2 \times 10^{15}$ eV where $F_{\rm a}$ is the symmetry-breaking scale of the axionlike particle and $C_{\rm e}$ is a dimensionless quantity that characterizes its coupling to electrons. A paper on this work has been acceepted Physical Review Letters[2]. This work was supported by National Science Foundation Grants PHY-1305726 and PHY-1607391.

This work was supported by National Science Foundation Grants PHY-1305726 and PHY-1607391.

Non-accelerator-based weak interactions

2.6 The mercury electric-dipole-moment experiment

Y. Chen*, B. Heckel, M. Ivory, and E. Lindahl†

The Hg edm experiment is an NSF project whose grant was renewed in 2017 for another 4 year cycle (NSF Grant 1707573, PI. Heckel). In 2018, Yi Chen (who was supported by the NSF) successfully defended her PhD dissertation. The dissertation topic was searching for a time-varying electric dipole moment signal as might be produced by a low mass axion-like particle background field. Yi Chen has since begun a postdoctoral research position at Indiana University working on the Los Alamos neutron electric dipole moment project. In 2018, Megan Ivory joined the edm project as a 50% FTE postdoc (supported by CENPA).

[2] W. A. Terrano, E. G. Adelberger, C. A. Hagedorn and B. R. Heckel, arXiv 1902.04246 (2019).

*Princeton University, Princeton, NJ.
*University of Washington graduate student supported by NSF.
†University of Washington glass blower.

A limiting factor in our recent edm measurement[1] was magnetic field gradients at the level of 0.2μG/cm. In 2018, we installed new correction coils that terminate the ends of our open-ended cosine theta coil that produces the static magnetic field for the Hg edm experiment. (An infinite cosine theta coil produces a uniform magnetic field while a finite one does not.) The new correction coils satisfy the boundary conditions for a uniform magnetic field within the high permeability magnetic shields. We also installed a second degauss coil that allows us to degauss the innermost magnetic shield alone, after the outer two shields are degaussed. An electronic circuit was built that provides feedback to the degauss current source to ensure that the degauss current is an exponentially decaying sine wave with vanishing dc offset.

We are currently making measurements of the magnetic field gradients and the reproducibility of our degauss protocol. Preliminary results look promising. Upon magnetic field reversal, the new degauss protocol produces a magnetic field amplitude that is the same for the two field directions to one part in 4000. This represents a roughly factor of 4 improvement over our previous degauss performance. The new correction coils reduce the dominant quadratic magnetic field gradient by a factor of 12, and deguass to degauss, the quadratic gradient is stable at the level of 20%, again an improvement of roughly 4 over past degauss performance. The quadratic field gradient changes sign upon magnetic field reversal, indicating that the gradient is produced by the cosine theta coil, rather than external leakage fields. (Gradients that change sign upon field reversal do not produce a false edm signal, while non-reversing gradients may give rise to a systematic error.) We are currently investigating the field gradients along the axes perpendicular to the main field axis.

We have also begun to design new high voltage feed-throughs into the vessel that hold the Hg vapor cells. We are investigating materials other than high density polyethylene (used previously) as it was found that charge accumulation in the polyethylene feed-throughs led to electric field forces on the stack of vapor cells that were linear in the applied electric field. Such linear forces can lead to systematic errors. We anticipate beginning a new round of edm measurements by the end of 2019.

[1]B. Graner, Y. Chen, E. G. Lindahl, and B. R. Heckel, Phys. Rev. Lett. **116**, 161601 (2016).

3 Accelerator-based physics

^{6}He-CRES

3.1 Overview of the ^{6}He experiments

Y. S. Bagdasarova, K. Bailey*, W. Byron, M. Fertl, X. Fléchard†, A. García, B. Graner, M. Guigue‡, R. Hong*, K. S. Khaw, A. Knecht¶, A. Leredde*, P. Müller*, O. Naviliat-Cuncic‖, T. P. O'Connor*, N. S. Oblath‡, J. Pedersen, R. G. H. Robertson, G. Rybka, G. Savard*, E. Smith, D. Stancil** D. W. Storm, H. E. Swanson, B. A. VanDevender‡, and A. R. Young‡‡

We are searching for tensor currents in two different experiments, both looking at the beta decay of ^{6}He. In one of the efforts laser traps are used to determine the $\beta - \nu$ angular correlation. A second effort is under construction using the cyclotron radiation emission spectroscopy (CRES) technique to determine the shape of the spectrum.

Chrality-flipping tensor currents are forbidden in the standard model, but could appear in precision beta-decay experiments as a consequence of new physics at energies beyond the TeV scale. Beta-decay measurements sensitive to tensor couplings in the $< 10^{-3}$ level would extend sensitivity to new physics into the 10-TeV scale, which would surpass the sensitivity of the LHC[1].

Fig. 3.1-1 shows a comparison of limits from several sources. The limits from the LHC obtained by Cirigliano et al.[2] are presently similar to those from beta decays[3], but will improve as the LHC gathers more data. The expected limits, assuming no events are observed after 300 $(\mathrm{fb})^{-1}$ at 14 TeV, are shown in dashed lines. Shown in red are limits that we could expect from our work, showing that new physics could be discovered in nuclear beta decays.

$\beta - \nu$ correlation from laser trapped ^{6}He

This experiment aims at determining the $\beta - \nu$ angular correlation from trapped ^{6}He in a magneto-optic trap. The electron is detected via a combination of a multi-wire proportional chamber and a scintillator. The recoiling Li ions are detected via a focusing

*Physics Division, Argonne National Laboratory, Argonne, IL.
†LPC-Caen, ENSICAEN, Université de Caen, Caen, France.
‡Pacific Northwest National Laboratory, Richland, WA.
¶Paul Scherrer Institute, Villigen, Switzerland.
‖Department of Physics and Astronomy and National Superconducting Cyclotron Laboratory, Michigan State University, East Lansing, MI.
**Electrical Engineering Department, North Carolina State University, Raleigh, NC.
‡‡Physics Department, North Carolina State University, Raleigh, NC.

[1] Cirigliano, Gardner, Holstein, Prog. Part. Nucl. Phys. **71**, 93 (2013).
[2] Gupta et al., Phys. Rev. D **98**, 034503 (2018).
[3] Gonzalez-Alonso, Naviliat-Cuncic, Severijns, Prog. Part. Nucl. Phys. **104**, 165 (2019).

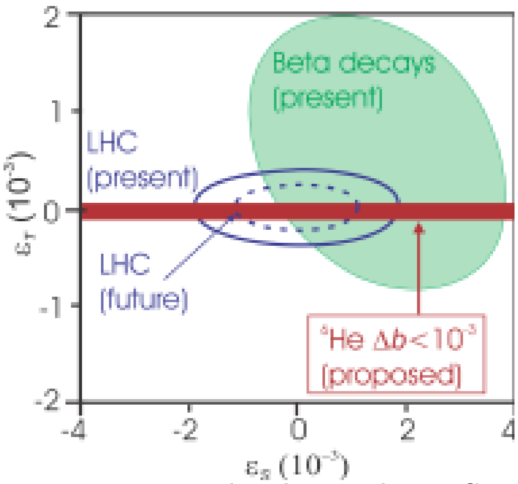

Figure 3.1-1. 95%-C.L. limits on tensor and scalar couplings. Green tilted ellipse: beta decay data[3], generated principally by the neutron-beta-decay data. Blue: upper limits extracted by Cirigliano et al.[2] from present LHC data, and from future LHC data assuming no events are detected by the time 300 fb^{-1}are collected at 14 TeV. The red-shaded area is what would be obtained from a spectrum-shape determination with uncertainty $\Delta b = 10^{-3}$, the expected sensitivity of the ^{6}HeCRES experiment.

electric field that guides them onto a position-sensitive micro channel plate detector. By measuring the time of flight and the landing position of the Li ion its momentum can be reconstructed. Together the electron and Li momentum can be used for reconstructing the anti-neutrino momentum.

This effort has been carried out since 2009. During the past year we have been working mainly on data analysis. In order to understand issues with the timing of our detectors, we took ancillary data with a ^{249}Cf source and with a laser UV source. We plan to finish the analysis soon.

Shape of the ^{6}He β spectrum using the CRES technique

On a different front, we have established a collaboration to extend the use of the CRES technique (developed by the Project 8 collaboration) to determine the shape of the ^{6}He beta spectrum and potentially apply the method to nuclear spectroscopy at FRIB[1].

The CRES technique is potentially the most accurate way of determining beta energies. The beta energies are determined by measuring their cyclotron frequency at birth in a B field via:

$$E = \frac{q\ B}{\omega_{cyc}\ c^2}$$

Fig. 3.1-2 shows a sketch of our experimental setup. ^{6}He is injected into a cylindrical 1.156-cm diameter RF wave guide which is read from both ends in the 18–24 GHz band with low-noise amplifiers (LNAs). Frequencies are extracted from wave packets ≈ 10–

[1]Facility for Rare Isotope Beams, Michigan State University.

100 μs long. A few percent of the betas are confined in a magnetic trap, produced using additional coils as shown in the figure. The trapped betas yield observable signals while the others are quickly absorbed in the walls.

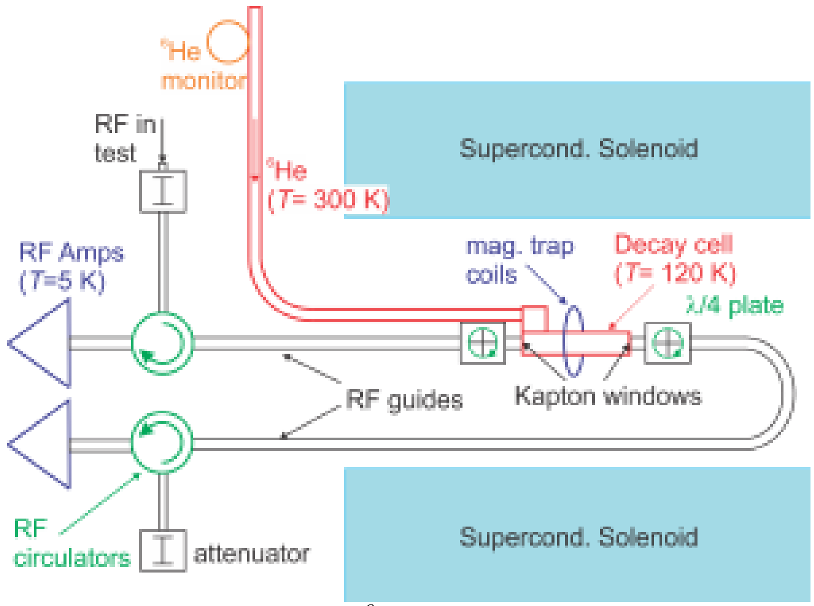

Figure 3.1-2. Sketch of He6-CRES setup. ^{6}He is injected into an RF wave guide. Betas undergo cyclotron motion in the B field and their energies are determined from the cyclotron radiation frequency, measured in the 18–24 GHz band.

Because the RF power expected from betas is $\approx$ 1 fW, a low signal-to-noise ratio may necessitate cuts which could bias the spectrum with respect to frequency. (Sec. 3.2) discusses signal-to-noise estimates propagated through the receiver system.

Another issue of concern is the Doppler shifts due to the axial motion of the trapped betas. In order to overcome this issue signals are read from both ends of the waveguide. Details on this as well as a description of the DAQ can be found in (Sec. 3.3).

To optimize the signal-to-noise ratio, the LNAs are cooled to $\approx$ 5 K with a Gifford-McMahon-type cryocooler. Through last year we worked on designing a system that would enable us to keep the LNAs at $\approx$ 5 K while injecting ^{6}He from a system at room temperature into the decay cell at $\approx$ 120 K. The decay cell must be relatively warm to prevent Kr and Xe calibration sources from freezing to the guide walls. Some of the other considerations and work done during last year are detailed in (Sec. 3.4).

In order to contain the ^{6}He in the decay volume we use polyimide windows. The ^{6}He can penetrate the windows and we had some concern that the solubility may be high enough to imply a significant reduction in expected rates. The issue is being addressed by comparing measurements of the ^{6}He half-life in a stainless steel cell with and without Kapton foil and is described in (Sec. 3.5).

The superconducting solenoid to be used was re-purposed from other experiments by Argonne National Laboratory. The first cool down at Seattle is scheduled for the end of May. Some of the work for the magnet setup and cooling, and the system for recirculating helium is described in (Sec. 3.6).

The 18–24 GHz band does not allow determination of the whole beta spectrum of ^{6}He at a given magnetic field. In order to cover the spectrum we plan to take data at fields from 1 to 5 Tesla. To "stitch together" the spectra we are developing a monitoring system. (Sec. 3.7) shows some of the work in this direction.

We have started an effort to simulate the experiment. This is described in (Sec. 3.8).

Finally, (Sec. 3.9) describes developments for a ^{19}Ne source. The distortion to the beta spectra implied by tensor currents has opposite signs in positron versus electron emission. Thus, we are aiming at using both (^{19}Ne and ^{6}He) measurements as a way to check for systematic uncertainties or confirm observation of a signal.

The shop is presently constructing parts that we plan to assemble during the summer.

3.2 ^{6}He-CRES receiver design and signal-to-noise ratio estimation

A. Allen[*], J. Amsbaugh, R. Buch, W. A. Byron, D. Combs[*], R. Farrell, M. Fertl, A. García, G. T. Garvey, B. Graner, M. Higgins, N. Hoppis, K. Knutsen, P. Mueller[†], N. S. Oblath[‡], J. Pedersen, G. Savard[†], E. Smith, D. Stancil[§], H. E. Swanson, J. Tedeschi[‡], B. A. VanDevender[‡], F. Wietfeldt[¶], A. Xiong, and A. R. Young[*]

Given a raw input signal generated from the acceleration of a single electronic charge, the amplification system of any CRES-based experiment is critical to achieving acceptable sensitivity. Fig. 3.2-1 shows a Monte Carlo simulated distribution of microwave power coupled to the TE_{11} mode of a circular waveguide for individual beta-decay electrons undergoing cyclotron motion in a 2.0 T magnetic field. Anticipated signals are on the order of femtowatts (10^{-15} W).

In the last year, our collaboration has designed and constructed a radio-frequency (RF) receiver system that is capable of amplifying these low-power signals to detectable levels without excessive noise power. The receiver is divided into two sections: the cascaded cryogenic amplifiers which sit in vacuum at or near 5.0 K and are directly coupled to the waveguides, and the ambient temperature receiver which sits outside the vacuum system and is responsible for mixing down the signal of interest from >

[*]Department of Physics, North Carolina State University, Raleigh, NC.
[†]Argonne National Laboratory, Lemont, IL.
[‡]Pacific Northwest National Laboratory, Richland, WA.
[§]Department of Electrical Engineering, North Carolina State University, Raleigh, NC.
[¶]Department of Physics, Tulane University, New Orleans, LA.

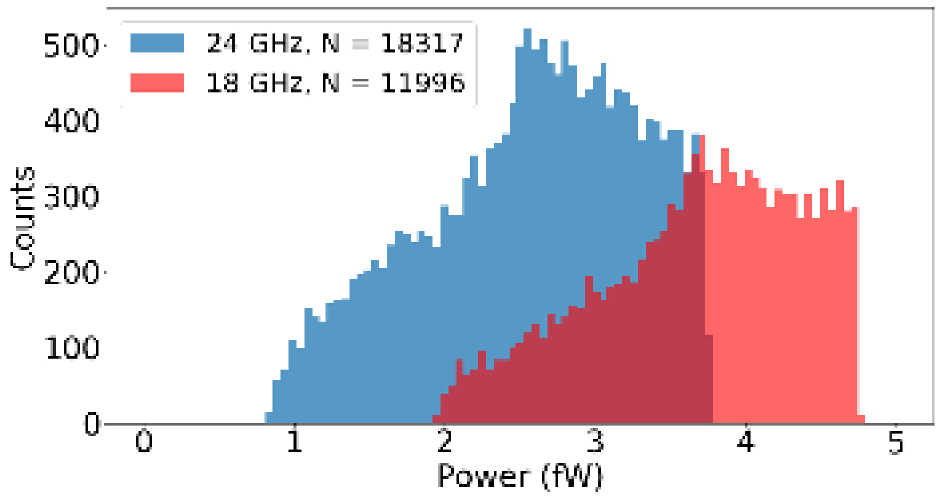

Figure 3.2-1. Monte Carlo calculation of power received at a single amplifier from individual electrons uniformly-distributed within the cylindrical decay volume making circular orbits not hitting the guide walls. The two distributions correspond to the bounds of the 18-24 GHz frequency band at $B = 2$ T. The cyclotron frequency goes as $1/\gamma$, so the 18 GHz electrons have more energy than those at 24 GHz. Coupling to the TE_{11} mode is enhanced near the guide center, producing a sharp cutoff for orbits centered at the origin.

18GHz to near 1 GHz so that it can be digitized with the DAQ described in the previous section. The cryogenic amplifiers have a characteristic noise temperature of only 7.0 K, which is vital to achieving the input noise power density objective of -182 dBm/Hz. This correpsonds to an input noise temperature of $10^{-182.6/10}/k_B = 39.7$ K.

The system noise temperature is obtained by treating the terminator, waveguides, and cryogenic amplifiers as a cascaded system using the Friis noise formula:

$$T_{cascade} = T_1 + \frac{T_2}{G_1} + \frac{T_3}{G_1 \times G_2} + ... \tag{1}$$

where $T_1 \approx 5$ K is the source (terminator) physical temperature, T_2 is the waveguide noise temperature, G_1 is the signal attenuation of the waveguides, T_3 the initial amplifier noise temperature, G_2 the initial amplifier gain, and so on. The form of the Friis equation makes it clear that the first stages in the cascade are typically the dominant contributions to the overall noise temperature. We treat the waveguides as an attenuator; at a physical temperature T_{phys} and input/output ratio L, the noise temperature T_{noise} is given by $T_{noise} = T_{phys}(L-1)$. Assuming a guide temperature of 100 K and no more than 1 dB of attenuation, the noise temperature will be no higher than $100(10^{\frac{1}{10}} - 1) = 25.89$ K. At this attenuation, the passive waveguides will be the dominant contribution to the cascaded noise temperature. Limiting the losses in the waveguide will therefore be of primary importance in achieving the expected noise level.

If the waveguides can be prepared and the initial amplifiers cooled to design temperature, we expect to achieve a signal to noise ratio (SNR) of 6 dB or better for even

Table 3.2-1. Summary of relevant RF receiver parameters and noise figures. All values are based on the assumption of a -120 dBm (=1.0 fW) source, 1 dB or less of RF losses in the waveguide, and terminators sourcing thermal noise at 5.0 K.

Parameter	18 GHz	19 GHz	20 Ghz
Cryogenic Stage Gain (dB)	63.5	63.5	63.0
Ambient Stage Gain (dB)	18.0	20.9	20.1
Thermal Noise Density (dBm/Hz)	-182.6	-182.7	-182.8
Total DAQ bandwidth (GHz)	1.8	1.8	1.8
FFT Bins	4096	4096	4096
FFT Bin Width (kHz)	439	439	439
Input Noise Power Per Bin (dBm)	-44.63	-41.89	-43.21
Input Signal Power(dBm)	-38.45	-35.64	-36.89
SNR for RMS Thermal Noise (dB)	6.18	6.25	6.32
ADC Peak Input (mVpp)	500	500	500
ADC Resolution (bits)	8	8	8
ADC Bit Noise Floor (dBm)	-50.2	-50.2	-50.2
SNR for ADC Bit Noise (dB)	11.75	14.56	13.31

the weakest ^{6}He beta-decay signals with a single FFT. Because the signals from CRES electrons persist and do not change frequency very rapidly, we can also average many sucessive FFT spectra to improve the SNR. Table Table 3.2-1 gives a summary of the relevant parameters that go into calculation of the SNR for thermal noise and bit noise on the DAQ system.

In the coming year, we expect to assemble and test our experimental apparatus. Direct thermal control over the terminators atached to the waveguide will enable us to validate the noise termperature of the system using the y-factor method. Following assembly and RF testing, we can begin to calibrate the system with keV-scale conversion electrons from the decay of metastable Krypton gas atoms.

3.3 Data acquisition for Doppler-free cyclotron radiation signals

A. Allen*, J. Amsbaugh, R. Buch, W. A. Byron, D. Combs*, R. Farrell, M. Fertl, A. García, G. T. Garvey, B. Graner, M. Higgins, N. Hoppis, K. Knutsen, P. Mueller†, N. S. Oblath‡, J. Pedersen, G. Savard†, E. Smith, D. Stancil§, H. E. Swanson, J. Tedeschi‡, B. A. VanDevender‡, F. Wietfeldt¶, A. Xiong, and A. R. Young*

The axial motion of a radiating electron in a CRES experiment will cause the signal

*Department of Physics, North Carolina State University, Raleigh, NC.
†Argonne National Laboratory, Lemont, IL.
‡Pacific Northwest National Laboratory, Richland, WA.
§Department of Electrical Engineering, North Carolina State University, Raleigh, NC.
¶Department of Physics, Tulane University, New Orleans, LA.

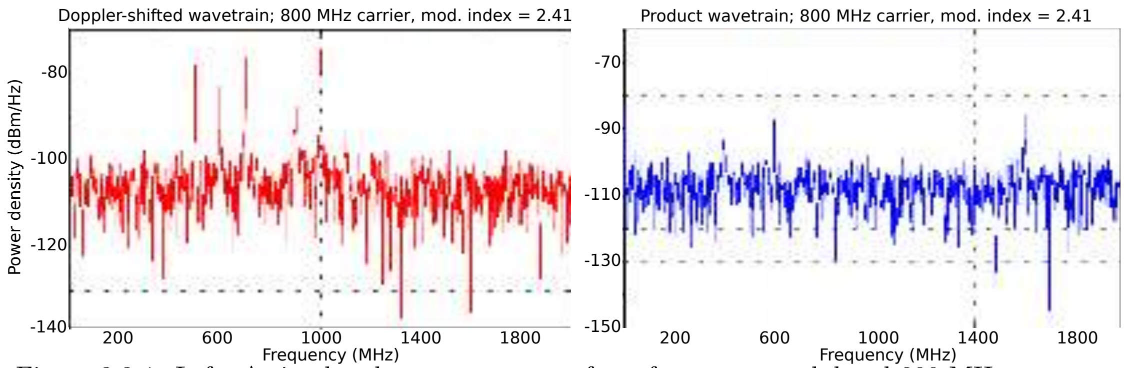

Figure 3.3-1. Left: A simulated power spectrum for a frequency-modulated 800 MHz wave with a modulation index of 2.41 and a modulation frequency of 100 MHz. The power in the 800 MHz carrier goes to zero, while the signal is fanned out into multiple pairs of sidebands. Right: The result of multiplying the Doppler-shifted signals as they appear at either end of the waveguide. The product signal contains a component at twice the carrier frequency, plus a component with sidebands at twice the modulation fequency.

received by an on-axis observer to have a time-dependent Doppler-shift. The magnitude of the Doppler shift (proportional to the electron's maximum axial velocity) and the frequency of axial oscillation together define the *modulation index*, denoted here as h:

$$h = \frac{\omega z_{max}}{v_p} \tag{1}$$

where ω is the cyclotron angular frequency, z_{max} is the maximum axial displacement of the electron from the center of the trap, and v_p is the phase velocity of the waveguide mode. The Fourier decomposition of a frequency-modulated signal includes a series of sidebands displaced from the carrier frequency at integer multiples of the frequency of modulation (in our case, approximately 200 MHz). In general, the Fourier amplitude of the nth sideband goes as the Bessel function of the first kind $J_n(h)$. Fig. 3.3-1 illustrates the effect of the Doppler shift at high modulation index. Note that $J_0(2.41) = 0.0$, so the component at the carrier frequency can disappear from the spectrum entirely.

If the signal-to-noise ratio (SNR) is poor in the ^{6}He data, few of the modulation sidebands may stand out above the noise floor. While it is possible to reconstruct the elctron's kinematic parameters from the Doppler-shifted wavetrain, this is a difficult and computationally intensive task[1]. In addition, any biases introduced by a complex event reconstruction algorithm will introduce potential sources of systematic error in the beta-decay spectrum. The problem may be mitigated by decreasing the maximal modulation index for trapped electrons via the magnetic trap depth, but this comes at the cost of a substantial decrease in the rate of detected events.

We intend to utilize a dual-receiver setup to remove the Doppler modulation by digitizing the signals from both ends of the waveguide and multiplying them into a single data train. At any point in time, the signal from one end of the waveguide will

[1]A. Ashtari Esfahani *et al.* (Project 8 Collaboration), arXiv:1901.02844 [physics.ins-det] (2019).

be red-shifted, while the signal from the opposite end will be blue-shifted. The product signal will have components at the sum and difference frequencies of the two wavetrains, so a component at twice the carrier frequency will be present with an amplitude that is independent of the modulation index and free of sidebands.

In the last year we have successfully programmed and tested this dual-receiver algorithm on a field-programmable gate array (FPGA) system designed by the CASPER radio astronomy collaboration. We are now capable of digitizing two wavetrains at 3600 MHz each (with 8-bit resolution), multiplying them and Fourier transforming the product in real time, packetizing the resultant data stream and recording it to disk. While limitations on the FPGA resources and the efficiency of our algorithm prevent us from utilizing the full 5000 MHz sampling rate of the analog-digital converter (ADC) cards, the dual 3600 MHz data stream will be more than sufficient bandwidth for an initial demonstration of the CRES technique in ^{6}He beta-decay. In addition, dealing with data in the frequency domain enables us to average successive spectra in time, improving our expected SNR while allowing us to record continuous data streams, obviating the need for triggering algorithms or data storage architecture that can accommodate 5-10 gigabytes per second.

The primary drawback to this method is the limitations imposed by the Nyquist theorem and a finite sampling rate. Instead of being limited to features less than half the frequency of sampling, we will be able to detect the sum frequency component of cyclotron radiation at less than 1/4 of the ADC sampling frequency. In practice, this means that with a single FPGA and two analog-digital converters sampling at 3600 MHz, we will be able to see only cyclotron radiation less than 900 MHz above the frequency of the analog downmixing oscillator ($\approx$ 18 GHz). Obtaining the full 6 GHz bandwidth supported by the waveguides will therefore require upgrading to a faster analog-to-digital converter and data analysis platform or running multiple FPGAs in parallel, each with its own downmixing oscillator. Given that the ambiguity in analyzing Doppler-shifted CRES waveforms is a considerable technical challenge, the factor of 2 reduction in detection bandwidth is a viable tradeoff.

Future work will involve testing the DAQ system with a realistic GHz-bandwidth calibrated noise source, currently under construction at CENPA. After the experimental apparatus is assembled, we expect to be able to take data immediately.

3.4 ^{6}He-CRES apparatus construction and cryogenic considerations

A. Allen*, J. Amsbaugh, R. Buch, W. A. Byron, D. Combs*, R. Farrell, M. Fertl, A. García, G. T. Garvey, B. Graner, M. Higgins, N. Hoppis, K. Knutsen, P. Mueller†, N. S. Oblath‡, J. Pedersen, G. Savard†, E. Smith, D. Stancil§, H. E. Swanson, J. Tedeschi‡, B. A. VanDevender‡, F. Wietfeldt¶, A. Xiong, and A. R. Young*

With an input signal source of approximately 10^{-15} W (≈ -120 dBm) and a measurement bandwidth on the order of GHz, achieving a reasonable signal-to-noise ratio in a CRES experiment demands ultra low noise input. Attaining input noise levels on the order of -180 dBm/Hz requires the use of cryogenic amplifiers. As mentioned in Section (Sec. 3.2), the amplifiers used in the ^{6}He-CRES experiment have a characteristic noise temperature of 7 K when physically cooled to liquid helium temperature. However, the Gifford-McMahon type cryocooler we intend to use for cooling the amplifiers is capable of absorbing only 1.5 W of heat power at 5 K. Minimizing heat flow onto the amplifiers is therefore critical to the success of the experiment.

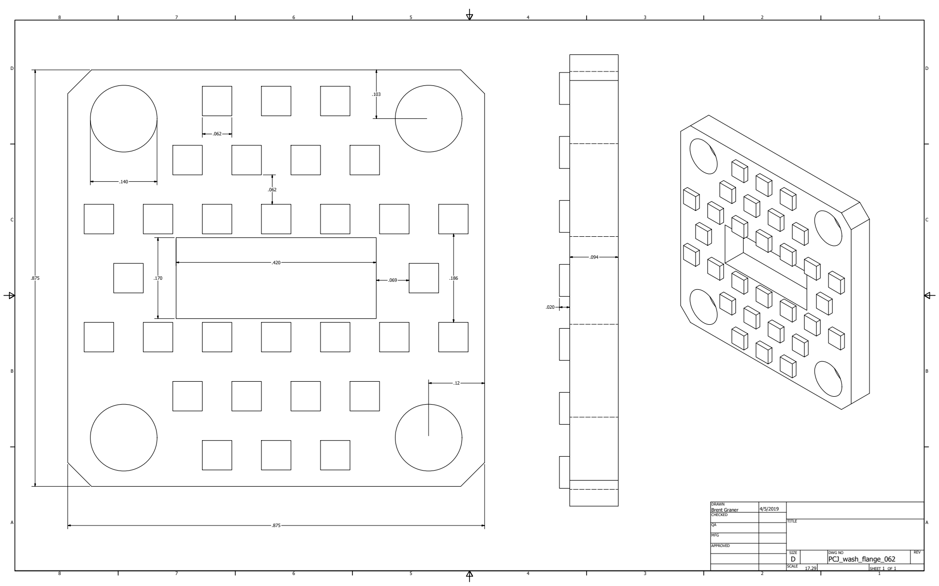

Figure 3.4-1. Scale drawing of the photonic crystal waveguide thermal flanges for thermally isolating the cryogenic waveguide sections. These pices will be stood off from the cold flanges using kapton and nylon washers to prevent metal-on-metal contact and heat transfer.

In the last year we have designed and begun fabricating the cryostat that will house the low-noise waveguide amplifiers. In doing so, we have introduced several unique

*Department of Physics, North Carolina State University, Raleigh, NC.
†Argonne National Laboratory, Lemont, IL.
‡Pacific Northwest National Laboratory, Richland, WA.
§Department of Electrical Engineering, North Carolina State University, Raleigh, NC.
¶Department of Physics, Tulane University, New Orleans, LA.

solutions, including the photonic crystal waveguide flange pieces shown in Fig. 3.4-1. The design of these flanges involves a hexagonal tiling of square posts roughly 1/4 wavelength on each side, designed to cause maximum destructive interference on waves that would otherwise "leak out" of the central aperture if it were not in good contact with the adjoining flange. The use of these photonic crystal flanges allows us to implement a vacuum gap using non-metallic standoffs from the cryogenic pieces of the waveguide, without appreciable loss of RF power. Initial measurements of prototype flanges suggest that millimeter-scale gaps can be introduced without degrading the transmission by more than 0.25 dB, substantially better than two flat flanges separated by a similiar gap.

3.5 Helium absorption in polyimide films

A. Allen*, J. Amsbaugh, R. Buch, W. A. Byron, D. Combs*, R. Farrell, M. Fertl, A. García, G. T. Garvey, B. Graner, M. Higgins, N. Hoppis, K. Knutsen, P. Mueller†, N. S. Oblath‡, J. Pedersen, G. Savard†, E. Smith, D. Stancil§, H. E. Swanson, J. Tedeschi‡, B. A. VanDevender‡, F. Wietfeldt¶, A. Xiong, and A. R. Young*

The ^{6}He CRES decay volume must have windows that are transparent to microwaves, strong enough to hold vacuum, stable across an array of temperatures, and radiation hardy. These considerations make a polyimide film such as Kapton a good candidate. However, the small size of helium results in a relatively large permeability through matter. If ^{6}He has even a modest probability of being absorbed (per collision) this could significantly decrease the pressure in the decay volume and affect the counting rate. There is data on the permeability and solubility of ^{4}He in Kapton but extracting a probability of absorption upon collision from this data is difficult (or impossible). We have designed an experiment to quantify the absorption of ^{6}He into Kapton. We will measure the apparent mean lifetime of ^{6}He in a decay volume with its inner surface area lined with Kapton film. Because the Kapton is at a distance from the two parallel scintillating panels that detect decay electrons, ^{6}He atoms that decay after being absorbed onto the Kapton film will not be detected. This will lead to a decrease in measured (apparent) lifetime.

The relative difference between this apparent lifetime and the lifetime measured without Kapton in the volume is given by:

$$\frac{\tau' - \tau}{\tau} \approx P_{abs} \tau v_z \frac{A}{V} \tag{1}$$

*Department of Physics, North Carolina State University, Raleigh, NC.
†Argonne National Laboratory, Lemont, IL.
‡Pacific Northwest National Laboratory, Richland, WA.
§Department of Electrical Engineering, North Carolina State University, Raleigh, NC.
¶Department of Physics, Tulane University, New Orleans, LA.

Where v_z is the velocity of the gas perpendicular to the film which is given by the temperature of the gas, A/V is the ratio of surface area (of Kapton) to volume of the decay cell, and P_{abs} is the probability of absorption upon collision with the film. In order to scale the effect we measure at room temperature to the temperature relevant to ^{6}He CRES (120 K), we rely on literature which claims that absorption should be greatly diminished as temperature decreases. In May 2018 lifetime data was taken with Kapton in the decay volume and without. Each run was made up of 100-200 14-s cycles. A single 14-s cycle was comprised of 1 s of pumping to clear the volume, 3 s of ^{6}He filling, and 10 s in which the volume was closed and decay data was taken. The histogram of the decay spectra was recorded cumulatively over the course of one run, meaning that a given time bin contains the total counts that occurred at that time over all cycles in the run. Data from a run is shown in Figure Fig. 3.5-1.

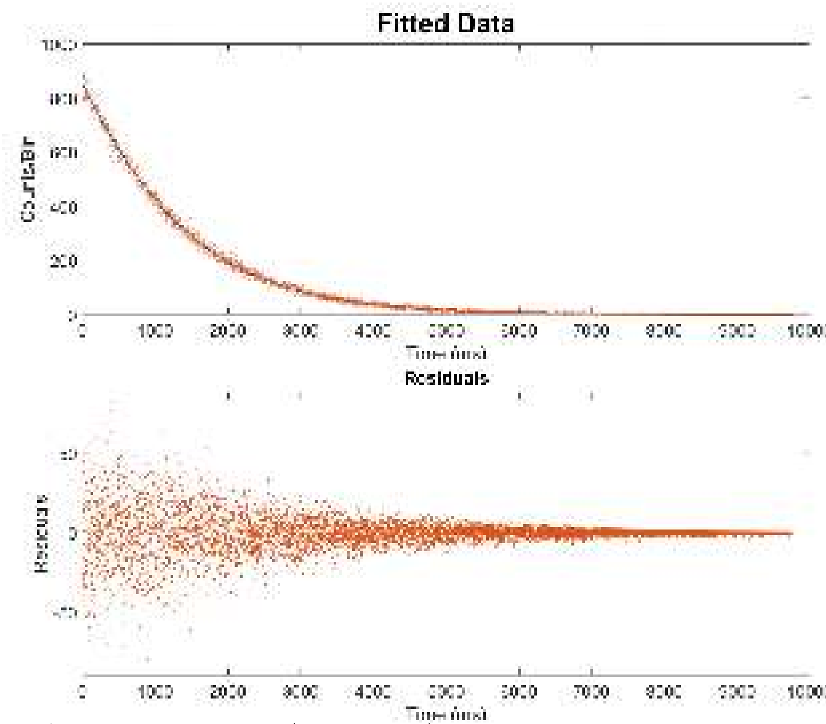

Figure 3.5-1. A histogram of rates (ms bin size) recorded during a run of $\sim$ 200 cycles with Kapton in the volume fit to a dead-time affected exponential.

The decision to histogram cumulatively made the analysis challenging. There was significant deadtime and variability in ^{6}He production between cycles within a given run. The inconsistency in lifetime found between runs with the same run parameters (either with Kapton or without) was of the same order as the difference across runs with different run parameters. The experiment was inconclusive. However, it did indicate that the effect of the absorption is not large. In order to rule out the possibility that Kapton vacuum windows could hurt our ^{6}He CRES statistics and for future experiments in need of Kapton for similar applications we plan to redo the experiment with a few integral improvements. First, we will record the decay spectrum of each individual 14-s cycle. Second, we will measure the dead time independently as opposed to leaving it as a fit parameter. Third, we will resolve an issue regarding an inconsistency in our analog-to-digital converter channel count-rate that was discovered after the May 2018 experiment. We plan to retake data before the end of 2019.

3.6 Magnet assembly and liquid-helium recovery

A. Allen*, J. Amsbaugh, R. Buch, W. A. Byron, D. Combs*, R. Farrell, M. Fertl, A. García, G. T. Garvey, B. Graner, M. Higgins, N. Hoppis, K. Knutsen, P. Mueller†, N. S. Oblath‡, J. Pedersen, G. Savard†, E. Smith, D. Stancil§, H. E. Swanson, J. Tedeschi‡, B. A. VanDevender‡, F. Wietfeldt¶, A. Xiong, and A. R. Young*

Last year, we received a refurbished 7-Tesla AMI superconducting magnet from our collaborators at Argonne National Laboratory.[1] Since its reception, substantial effort has been put into designing and building the infrastructure necessary to operate this magnet and integrate it within the existing design constraints.

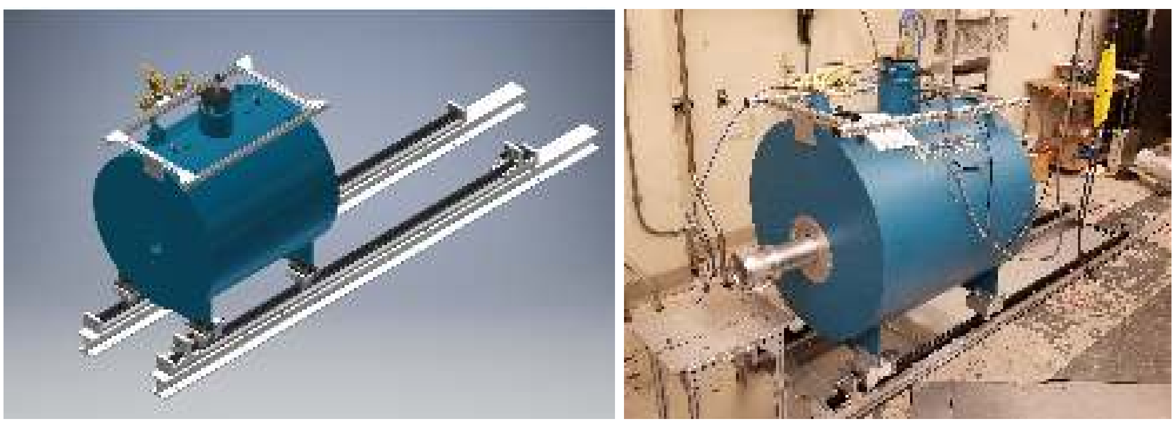

Figure 3.6-1. *Left*: CAD model of the blue 7-Tesla AMI superconducting magnet with its support structure and gas manifold. *Right*: Physical magnet in place on rail support structure with mounted gas manifold and vacuum housing for the experiment insert.

Since the magnet's bore is horizontal and designing a movable insert would prove challenging with the rigid ^{6}He supply line, we opted to put the magnet on a translatable support structure, allowing it to move on-axis in and out of position around a fixed cylindrical insert. In order to get the magnet back to a repeatable position, the final

*Department of Physics, North Carolina State University, Raleigh, NC.
†Argonne National Laboratory, Lemont, IL.
‡Pacific Northwest National Laboratory, Richland, WA.
§Department of Electrical Engineering, North Carolina State University, Raleigh, NC.
¶Department of Physics, Tulane University, New Orleans, LA.

[1]CENPA Annual Report, University of Washington (2018) p. 66.

design uses a ceramic coated aluminum rails with Frelon-lined linear bearings. In addition to being nonmagnetic, The rail and bearing assembly lets us repeatedly slide the magnet back to within 0.0005” of its original position.

We are fortunate to share a facility with the Axion Dark Matter eXperiment (ADMX) (Sec. 5.1), who operates and maintains a helium recovery and liquefaction system for their own superconducting magnet. We are very close to completing construction of a roughly 150-foot helium recovery line from our superconducting magnet to the ADMX system. This line will soon make it possible for us to recover the boil-off helium from the magnet and re-liquefy it, mitigating operating costs while utilizing existing laboratory infrastructure.

As of now, the magnet's vacuum jacket has been pumped out, the liquid nitrogen (LN_2) shield has been filled, and the liquid helium (LHe) space has been pre-cooled with LN_2. We are gearing up to do a full LHe cool-down and initial ramp of the magnet in May.

3.7 Input ^{6}He flux monitoring

A. Allen*, J. Amsbaugh, R. Buch, W. A. Byron, D. Combs*, R. Farrell, M. Fertl, A. García, G. T. Garvey, B. Graner, M. Higgins, N. Hoppis, K. Knutsen, P. Mueller†, N. S. Oblath‡, J. Pedersen, G. Savard†, E. Smith, D. Stancil§, H. E. Swanson, J. Tedeschi‡, B. A. VanDevender‡, F. Wietfeldt¶, A. Xiong, and A. R. Young*

The ^{6}He CRES experiment reconstructs the full beta spectrum by separately measuring different parts of the spectrum. Each part needs to be normalized by the number of beta decays from the ^{6}He atoms. So while the ^{6}He gas is being pumped into the decay volume, a monitor is needed to count the number of decayed betas. The goal of this project is to develop this monitor so that it drifts less than one part-per-thousand over the course of a dataset. Using a constant-intensity ^{90}Sr source, the test results with 3 experimental setups are summarized in this report. The detection schemes tested include a gas chamber + Si detector, two pairs of scintillators (horizontal + vertical), and single Si (PIPS) detector.

The stability can be evaluated by two statistical indicators: χ^2/ndf and σ/μ. We expect the time series counting rate to remain constant except for statistical fluctuations. So in the equation of chi-square, we used the weighted average of count rate as the expectation. The probability (p value) at the upper tail area of chi-square distribution was used to quantify the goodness of fit between the data and the mean

*Department of Physics, North Carolina State University, Raleigh, NC.
†Argonne National Laboratory, Lemont, IL.
‡Pacific Northwest National Laboratory, Richland, WA.
§Department of Electrical Engineering, North Carolina State University, Raleigh, NC.
¶Department of Physics, Tulane University, New Orleans, LA.

count rate. The level of fluctuation for the counting rate measurements is defined as the standard deviation of the rate measurements divided by the mean. To reach 10^{-3} sensitivity, each rate measurement needs to include at least 1 million counts.

Using the statistical indicators mentioned above, the stability can be evaluated by comparing the experimentally calculated statistics to the expected ones. Given a large enough data set with the number of measurements larger than 20, if the fluctuation is small and purely statistical, the counting measurements should follow a normal (Gaussian) distribution and the measured chi-square per degree of freedom (χ^2/ndf) should be around 1. Generally if the ndf is arbitrary, an experimentally calculated χ^2/ndf should always be compared to the theoretical chi-square distribution with the corresponding ndf. The theoretical distributions in Fig. 3.7-2 and Fig. 3.7-4 are generated using simulated data from a normal distribution. A good stability yields a measured χ^2/ndf around the center or to the left of the distribution and the p value should be larger than 5 %. Poor stability leads to a large chi-square with respect to the distribution and small p value.

The first setup we used is a combination of gas counter and Si detector. After several 1 hour measurements done at different times of the day, we observed very poor stability in gas counts over time (eg: 3% variation when 0.1% is needed). Considering the limitations of the gas counter, we turned to using scintillators.

Pairs of horizontally and vertically positioned of scintilltors were tested. For each, the data acquisition was triggered on the coincidence between two scintillators. Fig. 3.7-1 shows 15 hours of count rate data. The level of fluctuation is much larger than the statistical uncertainty marked by error bars, which suggests significant systematic shifts of the detection sensitivity over time. Fig. 3.7-2 confirms this observation because it shows that the experimental χ^2/ndf sit on the far right of the simulated distributions of χ^2/ndf with both scintillators.

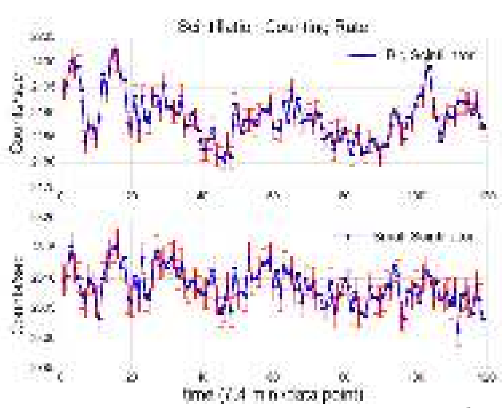

Figure 3.7-1. Time series counting rate with scintillators, each point has around 1 million counts

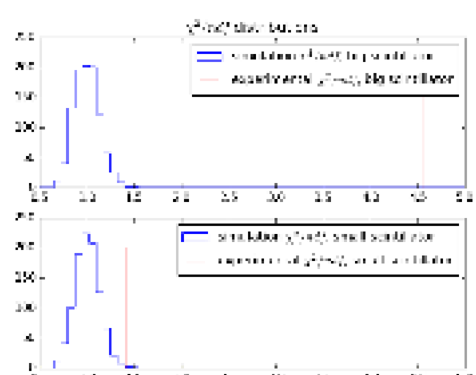

Figure 3.7-2. Simulated Chi- square distributions being compared to experimental values

The large fluctuation of the data motivated us to explore the possible systematics that could shift counting rate:

- **Gain shifting**: Count rate can shift with fluctuation of the gain set on the amplifier. For example, more counts are recorded if the gain shifts up. The spectrum centroid recorded on the data acquisition system was used as an indicator for such shift. We assumed a linear relation between the counting rate and the centroid of the spectrum. After extracting a slope from the linear fit between measured counting rate and the centroid, we performed a linear correction to the rate.

- **ADC dead time**: we recorded data on a pulse generator in parallel with scintillators and performed a dead time correction, calculating the ratio of measured pulser rate to the known frequency, and applying the fraction to our counting rate.

- **Mechanical vibrations**: A nearby vacuum pump to the scintillator test area was causing vibrations in the floor, causing the distance between the source and detector to fluctuate. We placed the source further from the detector to reduce this effect because the change in count is inversely proportional to the distance:

$$\delta\ Counts \propto \frac{d}{dr}\left(\frac{1}{r^2}\right)\delta r \propto \frac{-2}{r^3}\delta r \tag{1}$$

- **High voltage setting**: We adjusted the HV supply of the PMT so that the counting rate fluctuation was minimized.

- **Light leaks on scintillators**: Scintillator paddles were wrapped with extra light blocking material to minimize light leaks from the room into the material.

We apply a gain shifting correction only if the correlation between the centroid and the counting rate is large. Also, the fraction alive correction was not applied if the correction makes little modification on the counting rate. The statistics from the main test runs are summarized in Table 3.7-1. The results from scintillators show that the statistics are close to expectations after applying the adjustments and data corrections.

Considering that using double detector systems might over-complicate the triggering, we tested on a single Si (PIPS) detector. The detection apparatus was placed inside a 24" scattering chamber, pumped by a combination roughing and diffusion pump. Vacuum pumping helps reduce the scattering of betas with air molecules and therefore increased the detection efficiency. This time, we were also more careful on matching impedance when connecting cables from detector to the computer. As shown in the last row of Table 3.7-1 and visually in Fig. 3.7-3 and Fig. 3.7-4, the χ^2/ndf is toward the left side of the simulated theoretical distribution and the level of fluctuation is around 10^{-3}. Both indicate that the current setup has stability close to our requirements.

In summary, we have examined the stability of potential beta monitors using simple detection systems available off-the-shelf at CENPA. We found that scintillators with

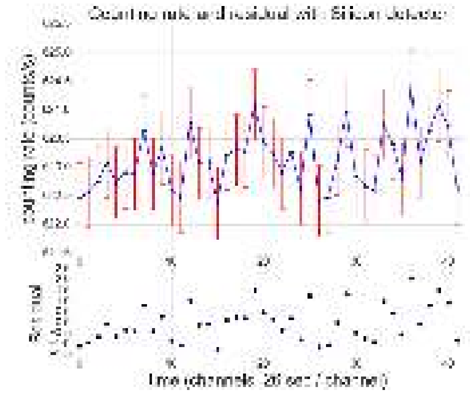

Figure 3.7-3. Time series counting rate with single Si detector(PIPS), each point has around 1 million counts

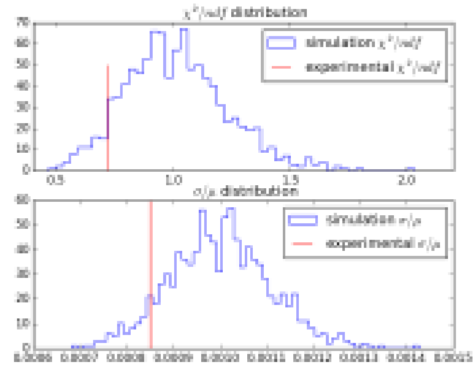

Figure 3.7-4. Simulated distributions of statisticial indicators being compared to experimental values

Data Sample	Total time (hrs)	ndf	Chi per ndf	Stdev	p value
Scint_thin_vertical	15	119	4.540	0.00216	near 0
Scint_thick_vertical	15	119	1.420	0.00106	0.00190
Scint_thin_horiz	15	4	0.447	0.000668	0.775
Scint_thick_horiz	15	4	49.2	0.00742	near 0
Scint_thick_hor_CenCorr	15	4	0.163	0.00424	0.325
Scint_thick_hor_FracCorr	15	4	1.110	0.00100	0.350
single Si (PIPS)	19	42	0.72	0.00085	0.91

Table 3.7-1. Raw and corrected counting rate statistics, p value = Prob($\chi^2 > \chi^2_{measured}$)

PMTs or a proportional gas chamber do not yield enough stability. Using a semiconductor detector and the vacuum condition, on the other hand, showed sufficient stability. However, using one Si detector has the disadvantage of being sensitive to background gamma radiation so more tests are needed to determine whether the sensitivity to gamma rays will preclude its use as a beta monitor. In general, the detection efficiency could also be affected by the distortion of the electron trajectories when this monitor is put close to the magnet. In the future, we would like to test the influence of gamma background. In addition, new detector design is likely to be pursued to avoid the influence from the magnetic field.

3.8 Electron tracking and estimation of systematic uncertainties

A. Allen*, J. Amsbaugh, R. Buch, W. A. Byron, D. Combs*, R. Farrell, M. Fertl, A. García, G. T. Garvey, B. Graner, M. Higgins, N. Hoppis, K. Knutsen, P. Mueller†, N. S. Oblath‡, J. Pedersen, G. Savard†, E. Smith, D. Stancil§, H. E. Swanson, J. Tedeschi‡, B. A. VanDevender‡, F. Wietfeldt¶, A. Xiong, and A. R. Young*

The He6-CRES experiment involves the trapping of beta-decay electrons from ^{6}He within a magnetic trap formed by the combination of a uniform field provided by a superconducting solenoid along with three coils generating fields of approximately 1/1000 of the solenoid field. Only 2–3% of the electrons generated during these decays will be trapped. Whether or not trapping occurs will depend on the initial position of the electron in the trap, the initial pitch angle of the electron's trajectory with the direction of the main axial magnetic field, and the cyclotron radius of the electron due to the possibility of collisions with the RF-guide walls. Thus, although the efficiency of a wall-less magnetic trap is independent of the magnitude of the electron's momentum, the possibility of collisions with the guide walls implies lower trapping efficiency for higher-energy electrons. Due to these considerations, it is important to have a clear picture of what the actual electron trapping rates within the experiment are as a function of energy.

A realistic calculation of these trapping rates requires detailed calculations of both the magnetic fields within the trap and the resulting trajectories of the electrons. Thus, the particle-tracking simulation software Kassiopeia[1] has been employed to attempt to solve this problem by running Monte Carlo simulations of the He6-CRES experiment.

Kassiopeia is an extensible software package written in C++ for running particle tracking simulations in complex geometries and electromagnetic fields, originally designed for use in the KATRIN collaboration.

The first step to using Kassiopeia to simulate the He6-CRES experiment was to program the geometric construction for the three-coil magnetic trap to be used in the He6-CRES experiment. This construction consists of a cylindrical decay tube that will contain the ^{6}He gas along with three coaxial current coils (Fig. 3.8-1). Next, by setting a fixed axial magnetic field everywhere and the appropriate current densities in the three coils, a simulated three-coil magnetic trap within the decay tube was generated (Fig. 3.8-2).

*Department of Physics, North Carolina State University, Raleigh, NC.
†Argonne National Laboratory, Lemont, IL.
‡Pacific Northwest National Laboratory, Richland, WA.
§Department of Electrical Engineering, North Carolina State University, Raleigh, NC.
¶Department of Physics, Tulane University, New Orleans, LA.

[1] D. Furse *et al.* (KATRIN Collaboration), New J. Phys. 19 053012 (2017).

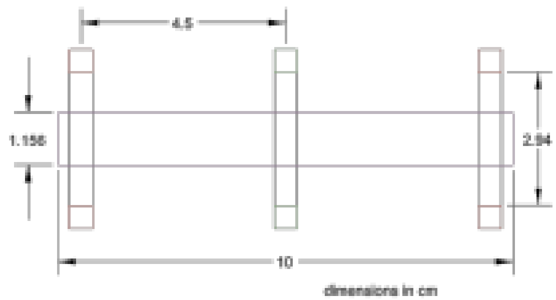

Figure 3.8-1. Geometry of the 3-Coil magnetic trap.

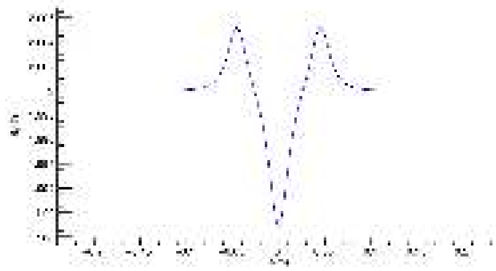

Figure 3.8-2. Axial magnetic field B_z along central axis for 2 T primary field.

Once the initial settings for the trap had been set, $N = 10{,}000$ randomized simulations were run for each electron energy with corresponding cyclotron frequencies 18 GHz, 19 GHz, ... , 24 GHz for axial magnetic field strengths 1 T, 2 T, ... , 5 T, for a total of $N = 350{,}000$ simulations, from which the trapping rates for each energy are determined.

To determine the actual trapping rates one would need to include all possible initial pitch angle trajectories, but with the knowledge determined by running test simulations that no trapping occurs outside the 84.7°–95.3° range, the calculation of the actual trapping rates from the Kassiopeia simulation was determined by considering initial pitch angles between 84.7°–95.3° and azimuthal angles between 0°–360°, calculating the solid angle Ω of the resulting surface as $\Omega = 4\pi - \{2 \times 2\pi\,[1 - \cos(84.7°)]\}$ and multiplying the trapping efficiencies for 84.7°–95.3° by the ratio of said surface's solid angle to the solid angle of a sphere ($\Omega/4\pi$), obtaining the following results (Fig. 3.8-3).

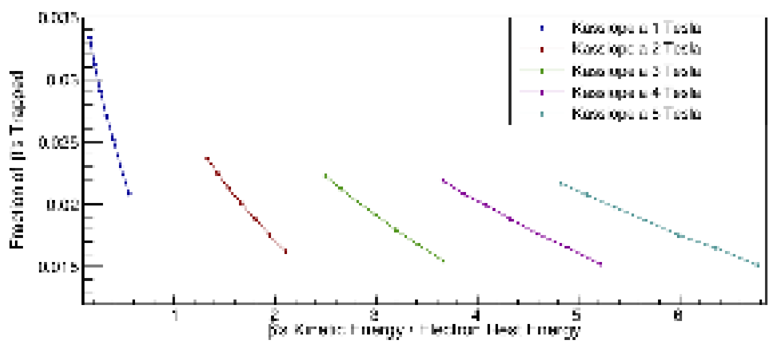

Figure 3.8-3. Trapping of β-decay electrons for 1-5 T fields. Higher-energy electrons have greater cyclotron radii, increasing the chances of a collision with the RF-guide walls and thus lowering the fraction of trapped β's.

In addition to the overall trapping rates, earlier test simulations showed the expected relation between the initial trajectory pitch angles and the initial axial positions of trapped electrons as expected in an adiabatic magnetic trap (Fig. 3.8-5), with the electrons generated away from the center of the trap requiring initial pitch angles closer and closer to 90°.

Consideration of the consequences of these effects on limiting the sensitivity of searches for the Fierz interference are under progress.

Figure 3.8-4. Coordinate system of the trap, p_e being the initial momentum of the β-decay electron.

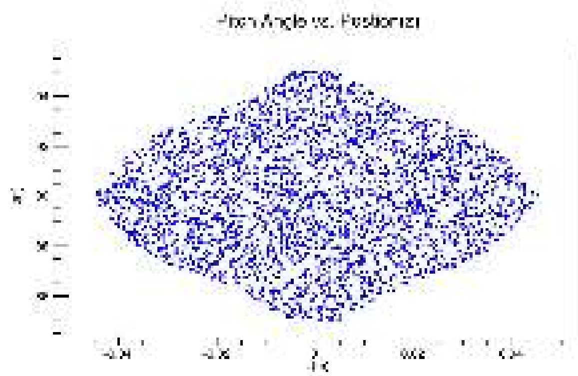

Figure 3.8-5. Trapping as a function of initial pitch angle θ. Each dot represents the initial axial position versus initial pitch angle of a trapped electron.

3.9 Development of a ^{19}Ne source

A. García, M. E. Higgins, N. C. Hoppis, E. B. Smith, and <u>D. W. Storm</u>

Accurate measurements of the beta spectra from ^{6}He and ^{19}Ne could lead to the most sensitive searches for chirality-flipping interactions. This is because the effect of the chirality-flipping interactions shows as a distortion of the beta spectra that has opposite signs for β^- versus β^+ decays.[1] In addition, previous measurements[2] of the angular distribution of electrons from polarized ^{19}Ne in combination with the lifetime imply something is amiss in these measurements or their interpretation. Thus, it would be very interesting to measure the ^{19}Ne beta spectrum.

We plan to use the $^{19}\mathrm{F}(p,n)^{19}\mathrm{Ne}$ reaction with a beam from the Tandem accelerator at somewhat over 11 MeV. The source design is similar to the ^{19}Ne source developed at Berkeley[3,4] and used later at Princeton,[5] but without the difficulties related to getting polarized atoms.

The gas will flow continuously through the target, and the activated gas will pass through a cold trap to freeze out the SF_6, leaving the ^{19}Ne free to be compressed by a

[1] M. Gonzlez-Alonso, O. Naviliat-Cuncic, and N. Severijns, Prog. Part. Nucl. Phys. **104**, 165 (2019).

[2] F. P. Calaprice, S. J. Freedman, W. C. Mead, and H. C. Vantine Phys. Rev. Lett. **35**, 1566 (1975).

[3] D. Dobson, *The beta-decay asymmetry and nuclear magnetic moment of Neon-19,* Ph. D. Thesis, U. C. Berkeley (1963).

[4] D. C. Girvin, *Test of time-reversal invariance in ^{19}Ne beta decay,* Ph. D. Thesis, U. C. Berkeley (1972).

[5] M. B. Schneider, F. P. Calaprice, A. L. Hallin, D. W. MacArthur, and D. F. Schreiber, Phys. Rev. Lett. **51**, 1239 (1983).

turbo pump. The flow rate will exhaust the target volume in well under the 17-s half life of ^{19}Ne, and is expected to fill the cold trap to capacity in a few hours. A pair of cold traps is planned to permit continuous operation.

SF_6 target

The SF_6 will be contained at 2 – 3 bar in an aluminum cylinder 20 cm in length with a volume of $\approx$ 50 cm^3. The gas will be separated from the beamline vacuum by an aluminum foil window and an electric insulating break. Aluminum was chosen both because it is resistant to corrosion by Flourine and because it will not produce long lived radioactivity under neutron or proton bombardment. The target is cooled with a water jacket to remove the 110 W deposited in the gas by a 10-μA, 11-MeV beam.

The ^{19}F$(p,n)^{19}$Ne reaction cross section[1] peaks at $\approx$ 70 mb for 6 MeV. Just below 5 MeV the reaction cross section becomes negligible. Using SRIM[2] to determine the energy profile of the beam as it slows in the gas, we found that ^{19}Ne production rate for a target with uniform SF_6 density is dominated by beam energies between 11 and 5 MeV. Because beam heating in the target gas will reduce target density in the neighborhood of the beam in an unpredictable manner, we chose a target length of 20 cm (a factor of safety of 2 above cold 3-bar SF_6) and will vary target pressure to permit trimming of the low energy tail of the beam. A 10-μA, 11-MeV proton beam, stopping in the gas, should produce 1.0×10^{10} ^{19}Ne atoms/second.

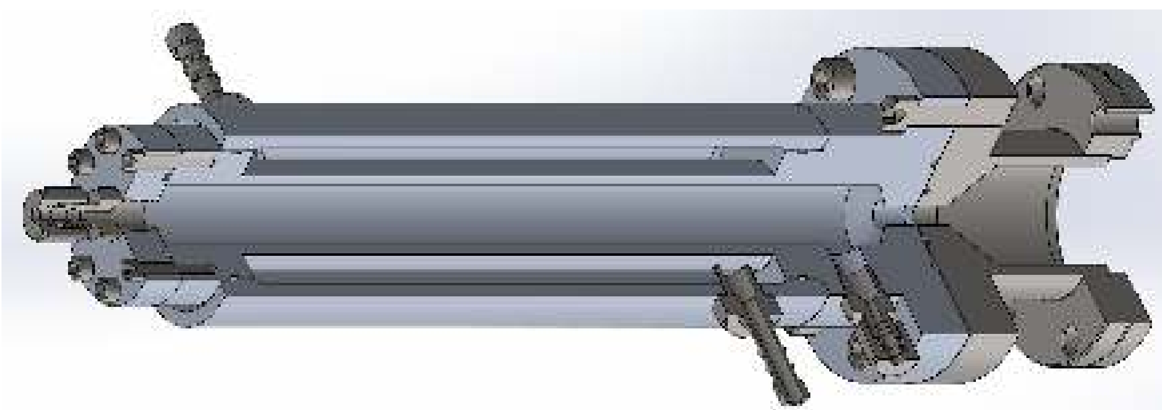

Figure 3.9-1. The SF_6 gas target, 3/4 sectional view. Target body on the right connected to the conflat flange is 304SS. The remainder of the target body is AL6061. The window goes between the stainless and aluminum pieces. The barbed fittings are for the water cooling. Gas enters near the window, and the activated and heated gas exits at the rear (left in the figure).

The window is a 0.002-in thick foil of 1235 Al. Since the expected beam radius

[1] A. J. Koning and D. Rochman, Nuclear Data Sheets **113**, 2841 (2012).
[2] J. F. Ziegler, M. D. Ziegler and J. P. Biersack, Nucl. Instrum. Methods **268**, 1818 (2010).

at the target window will be about 3 mm, the window has an unsupported radius of 6 mm. Calculations indicate that the primary cooling mechanism will be conduction to the edges. Ignoring cooling by the gas, we expect a temperature increase of less than 70K. (108K if the beam is only 2 mm) The window is sealed with viton o-rings. The window has been tested to rupture at a 11.6 bar pressure differential and has held 10.5 bar indefinitely. The beam energy loss is only 1/2 MeV, so although this material is more than sufficiently strong for the anticipated 3-bar pressure, there is no reason to use thinner material.

Gas handling system

The gas handling system is illustrated in Fig. 3.9-2. The gas is stored at up to 8 bar, and delivered through a regulator at a fixed pressure, e.g. 3 bar, to the target cell. The flow rate through the target is set with a needle valve to be, for example, 0.1 g/s, and monitored with the flow meter. The SF_6 is frozen in the cold trap after passing though a length of tubing. Calculations indicate a fraction of a bar pressure drop in the tubing, which will extend from the target location after the 24-inch chamber to the trap located near the ^{6}He production area. The ^{19}Ne which was carried to the cold trap with the SF_6 flow will diffuse from the cold trap to a nearby turbo pump which will send it into the vacuum system attached to the existing ^{6}He production system.

When either the storage tank pressure approaches the regulator setting or the cold trap becomes saturated, we can switch to the second tank or trap. A full trap will be heated to refill the storage tank, enabling continuous operation.

The flow rate of 0.1 g/s was used by Dobsen[3] and must be high enough to exhaust the target cell in under the 17-s half life of ^{19}Ne but low enough that the cold traps do not have to be cycled too often. At 3 bar the cell contains about 1.0 g of gas. The cold traps are about 2 liter, and should hold[3] about 2 kg of frozen SF_6. Thus at 0.1 g/s the cell is exhausted in 0.6 half life, and the cold trap should take a little under 6 hrs to fill. There is reasonable opportunity to vary the flow rate to optimize the process.

Pressure relief valves are located appropriately, to protect against operator error.

We anticipate that the SF_6 will initially have contaminants (air) that will not freeze out, but for the experiment a good vacuum is required for the ^{19}Ne. By pumping on the cold traps we can remove the contaminants and then the sublimated SF_6 should be free of contaminants that don't freeze. In testing using CO_2, we showed that pumping on the frozen gas would produce a good vacuum while the CO_2 stayed frozen.

The traps are made of 1/8-in wall stainless steel tubing with an outer diameter of 4.5 in. End plates are 1/4-in thick. To aid in the freezing of SF_6 they have baffles welded to the bottom. The traps are calculated to withstand over 34 bar, well above the 8 bar expected when the frozen SF_6 is warmed and transferred to the storage tanks.

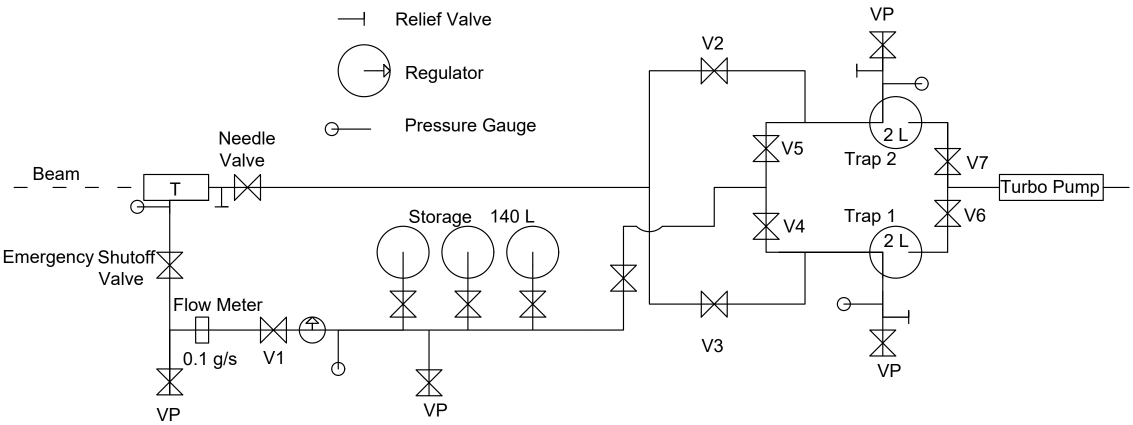

Figure 3.9-2. The Gas Handling System. The turbo pump sends the ^{19}Ne into the transport system for the experiment.

For storage, we will use three gas cylinders, with total volume 150 liters.

The target and one trap have been built and the system is being assembled. The trap was hydrostatically tested to 17 bar without incident. Tests of the gas system, without beam and with one trap, are anticipated before the summer.

4 Precision muon physics

MuSun

4.1 Muon capture and the MuSun experiment

D. W. Hertzog, P. Kammel, E. T. Muldoon, D. J. Prindle, R. A. Ryan, and D. J. Salvat*

Muon capture provides a powerful tool to study properties and structure of the nucleon and few nucleon systems as predicted by effective theories (EFT) founded on Quantum Chromodynamics. Our program focuses on capture from the simplest of all muonic atoms, namely the theoretically-pristine muonic hydrogen (MuCap experiment) as well as muonic deuterium (MuSun experiment). Our collaboration has pioneered a novel active-target method based upon the development of high-pressure time-projection chambers (TPC) filled with hydrogen/deuterium gas, which reduced earlier experimental uncertainties by about an order of magnitude. Two applications of utilizing this precision information are discussed here.

The axial radius is a basic nucleon property, and, furthermore, it plays a dominant role in the momentum dependendence of the axial-vector form factor

$$F_A(q^2) = F_A(0)\left(1 + \frac{1}{6}r_A^2 q^2 + \ldots\right), \tag{1}$$

which is essential for predicting neutrino-nucleus cross sections required for studies of neutrino properties in the next generation of long baseline oscillation experiments. Our MuCap experiment[1] has measured the capture rate $\Lambda_{\text{singlet}}^{\text{MuCap}} = 715.6(7.4)s^{-1}$ in muonic hydrogen with unprecedented precision, with the main goal of determining the induced pseudoscalar nucleon coupling g_P. In the past, the uncertainty in Λ_{singlet} introduced by the momentum dependence of the other weak form-factors was considered negligible. However, a recent determination of the axial-vector charge-radius squared from a new model-independent z-expansion analysis[2] of neutrino-nucleon scattering data determined $r_A^2(z\ \text{exp.}) = 0.46(22)\,\text{fm}^2$, with a more realistic, but 10-fold increased, uncertainty compared to previous model-dependent analyses. In a recent paper[3] we reviewed the axial radius starting from the vantage point of muon capture. Taking into account the current r_A^2 uncertainty, we updated g_P^{MuCap} to 8.23(83), which implies $g_P^{\text{theory}}/g_P^{\text{MuCap}} = 1.00(8)$, confirming theory at the 8% level. If instead, the predicted expression for g_P^{theory} is employed as input, then the MuCap capture rate alone determines $r_A^2(\mu H) = 0.46(24)\,\text{fm}^2$, or together with the independent recent analysis of νd

*Presently at Indiana University, Bloomington, IN.

[1] V.A. Andreev *et al.*, Phys. Rev. Lett., **110**, 012504 (2013).
[2] A S. Meyer *et al.*, Phys. Rev., **D93(11)** 113015, (2016).
[3] R. Hill, P. Kammel, W. Marciano and A. Sirlin, Reports on Progress in Physics **81**, 096301 (2018).

data, a weighted average $r_A^2(\text{ave.}) = 0.46(16)\,\text{fm}^2$. We also examined the possibility of improving the MuCap experiment by roughly a factor of 3 and thereby determining r_A^2 to about $\pm 20\%$. As demonstrated in Fig. 4.1-1 that level of accuracy would nearly halve the uncertainties in neutrino-nucleon scattering cross sections up to several GeV neutrino energy.

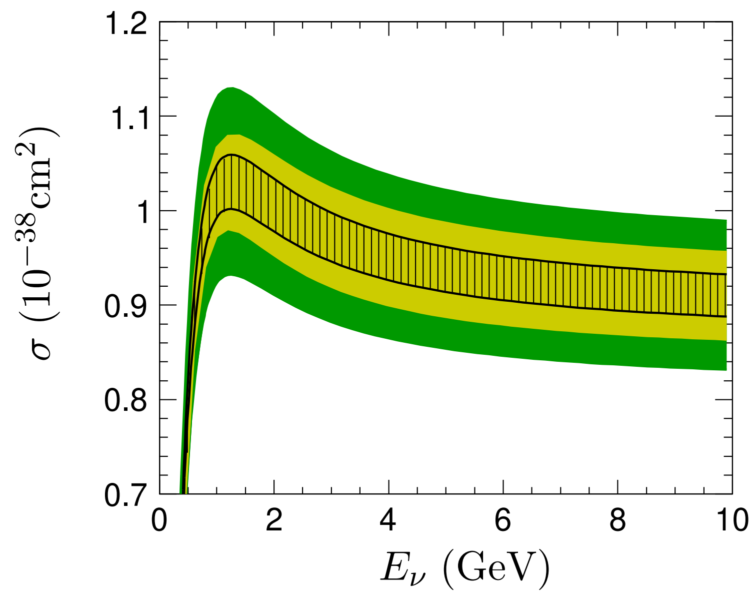

Figure 4.1-1. Quasielastic neutrino-neutron cross section. Outer solid green band shows the current uncertainty. The inner solid yellow band shows the uncertainties independent of r_A^2. The hatched black band shows the uncertainty contribution from r_A^2, if r_A^2 would be known to 20%. In that case, the r_A^2 contribution would be subdominant in the total error.

One of the most interesting topics for muon capture in the few-body sector is the family of two-nucleon weak-interactions processes. In these reactions only a single unknown low energy constant (LEC) enters the description up to the required order, which characterizes the strength of the axial-vector coupling to a four-nucleon vertex, the two-nucleon analog to g_A for the nucleon. This family contains muon capture on the deuteron,

$$\mu + d \to n + n + \nu, \tag{2}$$

together with astrophysics reactions of fundamental interest, in particular, pp fusion, which is the primary energy source in the sun and the main sequence stars, and the νd reactions, which provided the evidence for solar neutrino oscillations at the Sudbury Neutrino Observatory (SNO). The extremely small rates of these processes do not allow their quantitative measurement under terrestrial conditions; they can only be calculated by theory, with information derived from the more-complex three-nucleon system. MuSun plans to determine the rate Λ_d of reaction (2) to 1.5%, where Λ_d denotes the capture rate from the doublet hyperfine state of the muonic deuterium $1S$ state.

Current experiments are at the 6-10% level and the most-precise one disagrees with the latest 1% theory calculation by more than 3-sigma. The LEC will be determined at the 20% level, i.e. 5 times better than what is presently known from the two-nucleon system.

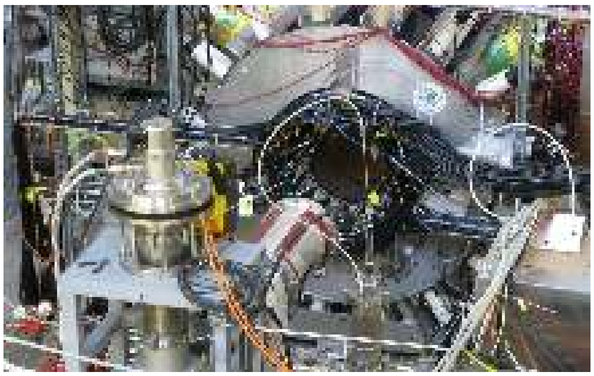

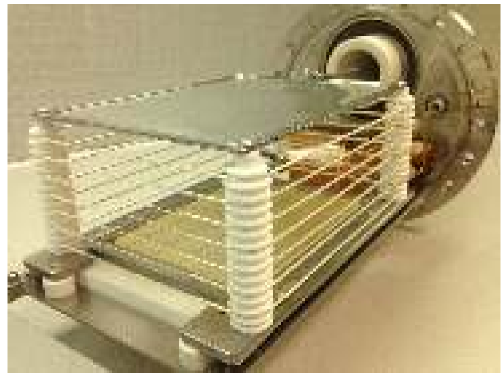

Figure 4.1-2. MuSun detector. Left: detector overview, showing cryosystem, TPC vessel and electron detector. Right: cryogenic-time projection chamber developed at CENPA.

The MuSun experiment, shown in Fig. 4.1-2, uses the so-called "lifetime method". The disappearance rate, $\lambda_{\mu d}$, of negative muons in an active deuterium target is measured. The capture rate is then determined as the difference $\Lambda_d \approx \lambda_{\mu d} - \lambda_{\mu^+}$, where λ_{μ^+} is the precisely-known positive muon decay rate[1]. Muons pass through the entrance detectors to stop in a deuterium target TPC. Decay electrons are detected in two cylindrical wire chambers and a 16-fold segmented scintillator array. The lifetime is determined from the measured time difference between the fast muon entrance detector and the decay electron scintillator array.

A key aspect for achieving the required precision was the development of a new cryogenic high-density TPC operating with ultra-pure deuterium. Tracking in three dimensions in the TPC eliminates most muon-stops in wall material. Muon transfer to impurity elements, where capture occurs with a much higher rate than in deuterium, is suppressed by keeping the gas contamination at the 10^{-9} level. The target conditions (T = 31 K and density 6.5% of liquid-hydrogen density) are optimized to allow an unambiguous extraction of Λ_d, independent of muonic atomic-physics complications that occur after muons stop in deuterium, in particular the numerous dd-fusion reaction catalyzed by the muons[2]. The high gas density implies that the cryo-TPC has to be operated as an ionization chamber without signal amplification in the gas and that drift voltages of 80 kV are required.

After final hardware upgrades MuSun collected the full statistics of 1.4×10^{10} events in two main production runs R2014 and R2015, followed, in 2016, by a shorter systematics run. MuSun is a high statistics/high precision experiment, which needs supercomputer resources to analyze the several hundred TB of primary and processed data

[1]V. Tishchenko et al.,*Phys. Rev.*, D87(5):052003, 2013.

[2]P. Kammel and K. Kubodera, *Ann. Rev. Nucl. Part. Sci.*, 60:327–353, 2010.

(provided by an XSEDE[1] grant). The UW team led the development of the staged-analysis framework and maintains it. We upgraded the MuSun Monte Carlo to a well-tuned and indispensable analysis tool, and run large production sets (D. Prindle). The analysis of the high quality R2014 data is well documented in the Ph.D. thesis of R. Ryan, March 2019, which provides the most comprehensive report on the MuSun experiment. Highlights are a full model of time dependent background structures, anchored on detailed experimental evidence, and a new method to determine one of the most difficult systematics, the interference of muon-catalyzed fusion events with the incoming muon track in the TPC. Data consistency has been verified over a wide range of tests, nearly all sources of systematics have been addressed and a roadmap of remaining tasks towards a final result has been developed. The analysis of run R2016, performed by Ph.D. student Ethan Muldoon, is also well advanced. Ethan developed a comprehensive analysis of capture and fusion neutrons observed in MuSun. The next steps are the comparison of the two data sets and the quantification of remaining systematic issues towards a first physics publication.

4.2 Towards a final analysis of the R2014 dataset

D. W. Hertzog, P. Kammel, E. T. Muldoon, D. J. Prindle, R. A. Ryan, and D. J. Salvat*

The analysis of the R2014 dataset has reached an advanced state. Several crucial quality cuts have been developed to reduce backgrounds and sources of systematic error. A scan of the fitted disappearance rate for each of five sub-datasets, based on running conditions, can be seen in figure Fig. 4.2-1. A linear fit, displayed in red, yields a fit probability and chi squared indicating good consistency within the five datasets. Scans of the lifetime fit stability over several other parameters, including fit start times, location of the muon stop and electron emission direction, demonstrate the consistency and robustness of the analysis.

The main sources of systematic error and their impact on the observed disappearance rate have been studied, and can be seen in table Table 4.2-1. A model of the background sources related to the kicked beam structure was developed and used to characterize impacts on the fitted rate. Extra energy from processes other than the muon stop within the TPC can result in a mis-reconstruction of the muon stop position. The muon track interference resulting from the decay electron was studied using Monte Carlo simulations. A data-driven correction for muon-catalyzed fusion interference was developed using the high resolution TPC to collimate the muon stop distribution. An analysis in which muon captures on nitrogen are measured directly within the TPC was used to make initial estimates on the impact of chemical gas impurities.

---

*Presently at Indiana University, Bloomington, IN.

[1] The Extreme Science and Engineering Discovery Environment is supported by the National Science Foundation.

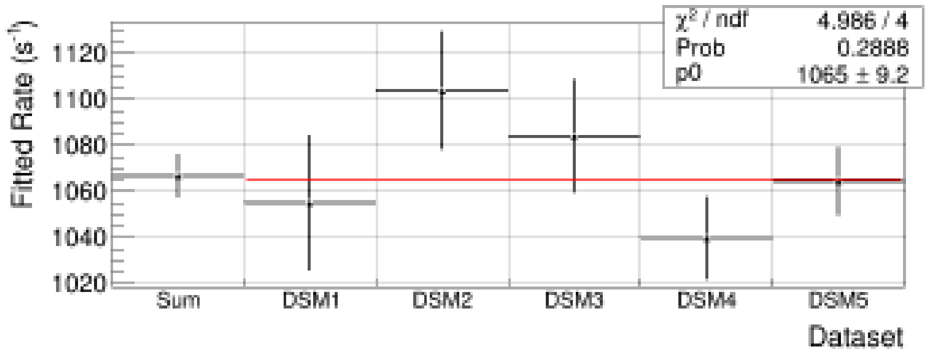

Figure 4.2-1. Fitted disappearance rate for the sum and each of the five R2014 sub-datasets. A linear fit to the five sub-datasets is shown in red.

For the majority of the effects, an upper bound has been determined, and future analyses will yield further quantification and uncertainty estimates. The precision goal of the MuSun experiment is $4\,s^{-1}$ statistical plus $4\,s^{-1}$ systematic uncertainty. For the R2014 dataset, a statistical uncertainty of $9.23\,s^{-1}$ is obtained from the fitted rate starting at $1\,\mu s$, with all standard cuts applied. Although the final systematic uncertainty goal has not yet been reached, the achieved uncertainties already imply at least a two-fold improvement over previous measurements of the muon capture rate.

Systematic		**Rate Shift (s^{-1})**	**Direction**
Backgrounds	Missed Muons	< 1.54	+
	Upstream Muon Stops	< 0.25	+
	Multiple Electrons	< 7.5	−
Muon Track Interference	Electrons	< 5	−
	Fusion Products	10.2±8	−
Gas Purity	Isotopic	0.8±0.2	+
	Chemical	< 6	+
Other	Wall Stops	small	+

Table 4.2-1. MuSun sources of systematic error and the effect of each on the observed rate. For the fusion correction and isotopic purity, an uncertainty in the observed shift is given. For all other systematics, only an upper limit on the size of the effect has been determined. The last column denotes the direction of the shift; positive indicates an increase in the fitted rate.

4.3 Improved detection of neutrons in the MuSun Experiment

D. W. Hertzog, P. Kammel, E. T. Muldoon, D. J. Prindle, R. A. Ryan, and D. J. Salvat*

Direct studies of the MuSun neutrons provide an important constraint on the muon kinetics as well as allowing for detection of wall stop signals. Significant improvements to the neutron analysis have been made, leveraging improved understanding of the signals as well as the upgraded neutron detectors used in the 2015 data production. The analysis has also been expanded to study gamma rays in addition to the neutrons themselves, improving the sensitivity to wall stops. This results in a large number of different signals, so it is helpful to categorize them by their source:

Beam Backgrounds. Upstream muon stops emit both neutrons and gammas, which behave consistently with our beam background model. (Sec. 4.4)

Deuterium Stops. Stops in deuterium may produce neutrons via either muon-catalyzed fusion of dμd $\rightarrow$ n+^{3}He or μ-d nuclear capture.

Wall Stops. Stops in high-Z wall materials emit neutrons from nuclear capture, often followed by gamma emission from the excited daughter nucleus. Atomic muon capture also produces a distinct gamma pulse coincident with the muon stop.

Scattering. Decay electrons may scatter in the walls, emitting bremsstrahlung radiation. Similarly, gamma rays may strike the walls and produce neutrons via photo-disintegration. These effects are difficult to model due to their dependence on the detector geometry.

A fit model to account for these signals is constructed using RooFit. For each signal, the expected time distribution is modeled as a probability density function (PDF). The model adds the PDFs for each component to create combined signals for each detector, and then performs simultaneous fits to the data from all eight detectors. Fits to calibrate the detector efficiencies and muon kinetics parameters are generally performed using either the fiducial volume or the entire TPC. To study wall stops, we then fix the signal shapes and perform scans over the stop position. This produces a map of the wall stop contamination as a function of position, as shown in Fig. 4.3-1.

The wall stop fraction in the fiducial volume is estimated to be $(1.19 \pm 0.03) \times 10^{-4}$. The resulting lifetime correction falls exponentially with increasing fit start time. To avoid the effects of the kicker we often fit starting at 1 μs, in which case we could potentially tolerate up to 10% wall stops and could consider relaxing the fiducial volume. Alternatively, now that the beam backgrounds are well understood we could use an earlier start time. A 300 ns fit start would have an approximately 1 s^{-1} systematic lifetime shift due to the wall stops.

*Presently at Indiana University, Bloomington, IN.

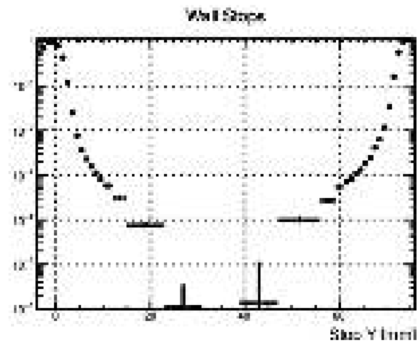

Figure 4.3-1. Estimated wall stop fraction vs reconstructed Y stop position.

4.4 A model of beam background effects

D. W. Hertzog, P. Kammel, E. T. Muldoon, D. J. Prindle, R. A. Ryan, and D. J. Salvat*

To allow a high beam rate while still ensuring only a single muon enters the detector at a time, an electrostatic kicker is used to block the beam once a muon is detected. This setup has allowed us to reach our target statistics, but also introduces time dependent systematic effects on the beam backgrounds. Characterizing these has been an ongoing challenge in the analysis, but a detailed model of the background has now been developed.

The kicker causes the beam to toggle between two states, as shown in Fig. 4.4-1. In the normal state the kicker is idle and the beam is focused on the entrance window, with some background from beam electrons and scattered muons. In the kicked state the kicker diverts the beam into an upstream collimator, reducing the muon rate but introducing backgrounds from reactions in the collimator. These signals are highly dependent the beam tune and collimator alignment, and we often observe increased background rates in the kicked state.

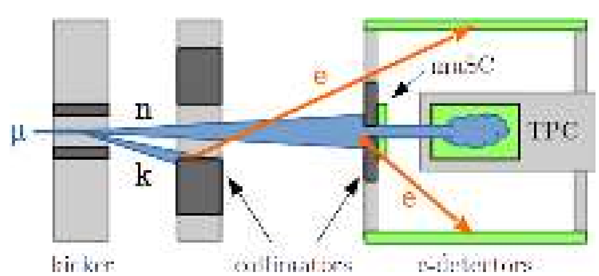

Figure 4.4-1. Simplified sketch of the MuSun beamline, indicating the paths of the kicked (k) and normal (n) beams in blue. Potential background signals are shown in orange.

*Presently at Indiana University, Bloomington, IN.

The entrance scintillator (muSC) signals the kicker to activate when a muon is detected. Signal delay and muon flight time combine to a $t_k \approx 800ns$ delay before the beam is diverted from the target. The kicker remains charged for an event window of $t_w = 25\mu s$ after the trigger. Adjacent kicks are governed by uncorrelated muons, yeilding a probability of seeing the beam which falls exponentially with the beam rate λ_b. A simple background model then requires only normal and kicked hit rates multipled by the corresponding probabilities that the beam was either normal or kicked.

Muons detected by the muSC require special attention because they control the kicker. Therefore there cannot be a muon detected between two adjacent kicks, since it would have been the muon to trigger the kicker in that case. This is equivalent to setting the un-kicked rate to zero before the entrance time. Muons undetected by the muSC are exempt from these considerations and have no such effect.

Two additional complications arise when considering other background signals. First, most backgrounds result from upstream muon stops rather than the beam itself. The resulting distribution is convolved with the muon decay time, with the primary qualitative effect of smoothing the abrupt kicker step into an exponential. Second, non-muons have a time offset due to their time of flight and may even have multiple offsets for different signal sources. Referring back to Fig. 4.4-1, electrons produced upstream travel faster than the muons and pass them in the beam pipe. This produces a transient background spike, as the kick first increases the upstream background and only later reduces the downstream background once the muons are depleted. The data matches this model well, as shown in Fig. 4.4-2.

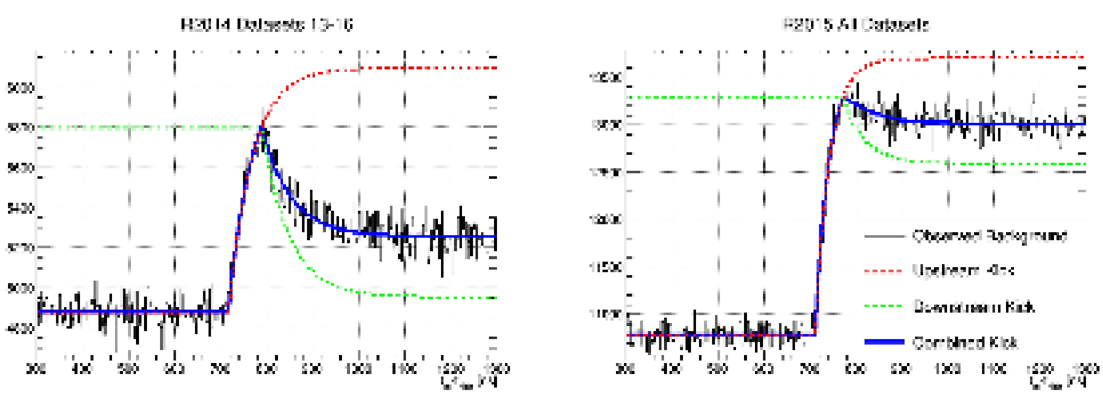

Figure 4.4-2. Kicker steps observed in R2014 and R2015 clock data, fit to an upstream plus a downstream kick. The different beam tunes produce significantly different step sizes.

Finally, a slight slope has been identified in the electron background which has a small effect on the fitted muon lifetime. This may be due to a gradual loss of charge from the kicker, and the effect is currently under investigation.

4.5 Monte Carlo framework and studies

D. W. Hertzog, P. Kammel, E. T. Muldoon, D. J. Prindle, R. A. Ryan, and D. J. Salvat*

We have tuned our scripts for generating Monte Carlo data for cenpa-rocks, the upgraded CENPA linux cluster. The end product of the MuSun Monte Carlo, a tree used for the final lifetime analysis, is produced in a chain of four steps. First we run GEANT with a detailed description of the MuSun detector, then we run a detailed detector response. The third step turns our raw data into physics objects and the fourth step produces physics histograms as well as the lifetime tree and skims of interesting events. Typically we process 2×10^6 μ^- events per chain, running a total of 5000 chains to get a dataset of 5×10^9 fiducial volume μ^- stops. The total intermediate output for a dataset is about 140 TB. We do not have this much storage space at cenpa-rocks so we run all four steps of the chain in sequence in a single process, writing intermediate data to local disks and deleting after the data is used in the next step. We copy the final lifetime event trees, skimmed events and all histograms and log files to permanent disk storage. The final disk space used is about 5 TB for 5×10^9 fiducial volume μ^- stops. We run 800 chains in parallel producing a dataset in less than one week.

We have been using this ability to quickly generate large Monte Carlo datasets to study electron interference. Muons that decay within a μs after stopping add from 50 to 100 keV of ionization energy from the Michel electron to the stopping ionization. Muons that decay later but travel in the drift direction also contribute energy from the Michel to the muon stopping energy. This is a small amount of energy but it may be possible for it to the stop position creating an eSC dependent lifetime. The additional Michel electron energy is observable in data and Monte Carlo by plotting the peak S-Energy versus electron time and eSC, shown in Fig. 4.5-1. The Monte Carlo shows a stronger effect in the S-Energy due to an a small electronics undershoot that lasts for a few μs after the muon stop. In the data this undershoot reduces the Michel electron contribution after the muon pulse. We are currently tuning the detector response in the Monte Carlo to match the data. We will also run the Monte Carlo completely turning off the TPC response to the Michel electron. The eSC dependent lifetime fits to the different Monte Carlo data sets combined with fits to the data will put a strong limit on the effect of electron interference on the lifetime.

*Presently at Indiana University, Bloomington, IN.

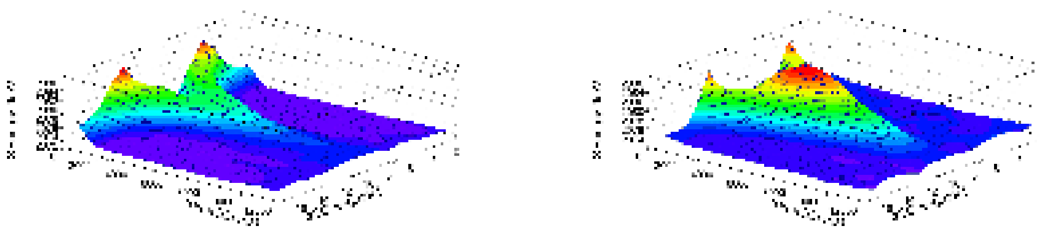

Figure 4.5-1. S-Energy as function of eSC and electron time. Left panel is data, right Monte Carlo. Later decays only contribute to the S-Energy for eSCs in the TPC drift direction.

g-2

4.6 Overview of the Muon $g-2$ experiment

H. Binney, M. Fertl, A. T. Fienberg, N. S. Froemming, A. García, J. B. Hempstead, D. W. Hertzog, P. Kammel, J. Kaspar, K. S. Khaw, J. LaBounty, B. MacCoy, R. E. Osofsky, and H. E. Swanson

The last 12 months have been particularly exciting for the Muon $g-2$ collaborators. In the period from March to July of 2018, the experiment accumulated its first major physics data set: Run 1. Our group has been intensively analyzing these data with the aim that, together with the full $g-2$ collaboration, we will unblind and publish the result in mid-2019. Run 1 data exceeds the entire Brookhaven National Laboratory (BNL) E821 data volume by a factor of approximately 1.5. Our new result should have a precision that betters BNL and, once combined with BNL, might even more strongly hint at new physics; or, of course, point back toward the Standard Model (SM). In either case, it is a highly anticipated result. In parallel to our analysis efforts, we have been busy with the preparation and data-taking phase of Run 2. A data-taking start date planned for late fall 2018 was delayed by various safety improvement considerations, kicker repairs, and various cryogenic system stability issues. Only in mid-spring 2019 did smooth data-taking begin. At the time of this writing, we have again exceeded the BNL statistics benchmark. The UW group continues to be involved in all phases of the experiment, which we briefly describe below. Examples of our work are found in the accompanying articles. We first remind the reader of the physics motivation and basic experimental technique.

Muon $g-2$ is a special quantity because it can be both measured and predicted to sub-ppm precision, enabling the so-called $g-2$ test for new physics defined by $\Delta a_\mu^{\rm New} \equiv a_\mu^{\rm Exp} - a_\mu^{\rm SM}$. As a flavor- and CP-conserving, chirality-flipping, and loop-induced quantity, a_μ is especially sensitive to new physics contributions[1]. The $g-2$

[1] A. Czarnecki and W. J. Marciano, "The muon anomalous magnetic moment: A harbinger for new physics," Phys. Rev. D **64**, 013014 (2001); D. Stockinger, "The Muon Magnetic Moment and Supersymmetry," J. Phys. G **34**, R45 (2007).

test compares measurement to the Standard Model prediction. An example, using a recent SM update[1] gives

$$\Delta a_\mu^{\mathrm{New}} = [270.5 \pm 72.6] \times 10^{-11} \quad 3.7\,\sigma. \tag{1}$$

The persistent discrepancy between experiment and theory fuels speculative models of new physics. Over the past year, tension has increased with respect to many of the most popular interpretations because of continually improved supersymmetry (SUSY) limits from the Large Hadron Collider (LHC) at high-mass, and because of the essential elimination of any possible effect from dark photons at low-mass.

The SM terms are organized in five categories:

$$a_\mu^{\mathrm{SM}} = a_\mu^{\mathrm{QED}} + a_\mu^{\mathrm{Weak}} + a_\mu^{\mathrm{HVP}} + a_\mu^{\mathrm{Had-HO}} + a_\mu^{\mathrm{HLbL}}. \tag{2}$$

The QED, weak, and hadronic higher-order (Had-HO) terms have negligible uncertainties. The hadronic vacuum polarisation (HVP) precision continues to improve; it can be determined from experiment through a dispersion relation that amounts to an energy-weighted integral of $e^+e^- \to hadron$ total cross sections. The hadronic light-by-light (HLbL) effect has been evaluated using models and the quoted uncertainty of 26×10^{-11} is only a consensus estimate reached by comparing a variety of models; it is not a well-defined uncertainty. Lattice prospects are maturing and we expect a new result to be published soon with, for the first time, a predicted value and a competitive uncertainty with respect to the modeling efforts. In parallel, data-driven HLbL efforts are also maturing. Hoferichter *et al.* calculated the leading pion-pole contribution with pure data-based inputs, including uncertainties[2]. They confirmed previous model-driven methods. Additional work is ongoing and updates for this and all other $g-2$ theory efforts are forthcoming at the next global Muon $g-2$ Theory Workshop, to be held at the Institute of Nuclear Theory, here in Seattle[3]. The aim of the group is to produce a white-paper, community-recommended, best value for the entire Standard Model contribution to $g-2$.

Experiment and Collaboration

The muon anomaly is proportional to the ratio ω_a/ω_p, where ω_a is the anomalous precession frequency of the muon spin in a magnetic field and ω_p is a measure of that average magnetic field determined using proton nuclear magnetic resonance (NMR). Both frequency measurements must control systematic uncertainties to 70 ppb. The statistics required to determine ω_a exceed those at Brookhaven by a factor of 18.

[3]INT Workshop INT-19-74W, Hadronic contributions to $(g-2)_\mu$; September 9 - 13, 2019.

[1]A. Keshavarzi, D. Nomura and T. Teubner, "The muon $g-2$ and $\alpha(M_Z^2)$: a new data-based analysis," arXiv:1802.02995 (2018).

[2]M. Hoferichter, B. L. Hoid, B. Kubis, S. Leupold and S. P. Schneider, "Pion-pole contribution to hadronic light-by-light scattering in the anomalous magnetic moment of the muon," arXiv:1805.01471 (2018).

Our UW group is involved in the ω_a and the ω_p measurements, and in critical beam-dynamics studies. We have designed and built a significant array of hardware tools for all three of these efforts as outlined in many previous Annual Report articles.

The highlight of this Annual Report is that the Muon $g-2$ experiment has collected a significant data set, is analyzing it toward a first publication, and is presently collecting Run 2 data. However, our hardware and operations efforts remain vigorous. Brynn MacCoy and Peter Kammel built and installed a new IBMS-3 detector system that resides in the vacuum just downstream of the inflector. Jarek Kaspar has again served in a central role in all aspects of $g-2$ Operations, including much work central to upgrading the storage ring kicker systems and on many of the subtle DAQ/Triggering issues that required improvement. Jason Hempstead is serving as the on-site Detector Coordinator. As one of his first tasks, he had to overcome a water accident[4], which required rebuilding Calorimeter 5. He also greatly improved the overall system reliability, installed some additional detectors, and maintained and calibrated many systems prior to data-taking. Hannah Binney has taken over the online Data Quality Monitor system from Aaron Fienberg and Josh LaBounty has taken leadership of the Nearline Analysis production. Martin Fertl and Jarek Kaspar contributed to the design of new kicker feedthrough components to help eliminate internal sparking; CENPA shops built a number of small parts for this upgrade.

The E989 Collaboration now exceeds 200 collaborators, drawn from 33 institutes in 7 countries. David Hertzog is the Analysis Coordinator. Kim-Siang Khaw is Co-Coordinator of the six Precession Analysis efforts and Eric Swanson is coordinating the two independent Field Tracking Analyses. Aaron Fienberg leads the "West-Coast" UW analysis and Rachel Osofsky leads the "Bloch" Field Analysis. Analysis efforts are grouped by the following names: Beam Dynamics, Field, Precession. Our group is involved all of these teams at various levels.

The work of the Beam Dynamics team begins with understanding the muon beam delivery into the storage ring, then moves to characterizing to the beam's storage properties. Our former Ph.D. student Nathan Froemming continues as an accelerator physics postdoc with the NIU group where he plays a leading role in beam modeling and tuning. His work is now aided by collaboration with Brynn MacCoy and Peter Kammel, who provided three imaging detector systems to help better steer the muon beam into the ring. The beam must then be kicked onto a stable orbit. The kickers have been the biggest problem we have faced and they required significant rebuilding during summer 2018, work which eventually stretched into early 2019. They now operate reliably, and at a higher kicker strength compared to 2018, but work remains before they can reach their full design potential. One topic that has become critical in the analysis is the question of the muon loss systematic uncertainty. Several UW team members contributed to establishing the connection between incoming predicted muon

[4]An unfortunate accident, where a kicker cooling water hose dumped 50 gal of water on Calorimeter 5 during the shutdown period and damaged 20 PbF_2 crystals.

spin phase-momenta correlations and their subsequent impact on time-dependent phase changes during storage. We initiated a study to prove the effect, which involved running the storage ring at a central momentum 0.66% above P_{magic}. Hannah Binney analyzed and presented these results recently to the Collaboration and Aaron Fienberg's model was used to estimate the net systematic uncertainty; this work is still in progress.

The Field team has transitioned to analysis mode now that the full UW-built Fixed Probe NMR system is operational. Rachel Osofsky completed the critical surface coil final dynamic shimming tasks, and the rest of the team completed the absolute field calibrations and trolley relative calibrations. Rachel is now leading the so-called Block Analysis effort. She recently successfully defended her approach in a lengthy review process that compared various proposed methods.

The Precession team consists of six quasi-independent analyses. Four are built from the UW-based West Coast reconstruction products that create positron time and energies from struck calorimeter crystals. Aaron Fienberg leads our group's subsequent extraction of the precession frequency based on his work designing fit functions and developing pileup and gain-correction routines. Many others in our group are contributing to the overall effort. In 2019, the Precession team carried out a relative unblinding of a 60-hour data set, roughly 10% of the Run 1 total. After 1.5 days of intense scrutiny, it was determined that all analyses were sufficiently mature to participate in the unblinding. The result was very positive: all six agreed very well within strict expectations. Based on that, we have pushed hard to complete the analysis of the remaining data sets and hope to finish this work soon.

In the articles that follow, the reader will find a variety of specialized effort team members have led. It is but a small sample of the actual work accomplished. We hope that in next year's Annual Report, we can be proudly discussing the impact of our first physics results.

4.7 Analysis of the precession frequency for Run 1

A. T. Fienberg, J. B. Hempstead, D. W. Hertzog, and K. S. Khaw

With Run 1 data collection complete, the $g-2$ precession frequency team has launched an intensive analysis campaign. The anomalous precession frequency, ω_a, is one of two numbers that must be extracted from the Run 1 data to ultimately determine a_μ. (The other is ω_p, a measurement of the average magnetic field experienced by the stored muons.) For a single muon, ω_a is the rate of change of the angle between the muon's spin and its momentum. The value that can be measured experimentally is this quantity averaged over the stored muon population. After applying the sub-ppm corrections for the so-called electric field and pitch effects, the ratio ω_a/ω_p is fundamental and, when combined with other precisely known fundamental constants, provides a value of a_μ.

The observed decay positron energy spectrum depends on the angle between a muon's spin and its momentum at the time of decay; through this dependence, one can measure ω_a solely through observation of decay positrons. In the $g-2$ experiment, 24 electromagnetic calorimeters measure the time- and energy-dependent decay positron spectrum. This spectrum is then fit to extract ω_a. There are multiple feasible approaches for achieving the extraction of ω_a from the calorimeter data, each with differing strengths and weaknesses. For example, a systematically robust but statistically suboptimal approach—called the T-Method, or threshold method—histograms decay positrons observed above a chosen energy threshold as a function of time and fits an oscillatory model to the resulting one-dimensional spectrum.

To leverage the benefits of varying analysis approaches and as an important consistency check, the $g-2$ collaboration has formed six independent ω_a analysis teams. One of these teams is based at CENPA. Across the six teams there are three independent raw data reconstruction algorithms, and each team has developed its own fitting code and systematic error correction routines.

The Run 1 dataset is divided into a number of subdatasets with stable storage conditions. One of these, the 60-Hour Dataset, served as a testing ground for the six analysis teams to develop their ideas and software. The 60-Hour Dataset contains approximately 1×10^9 high-energy decay positrons, sufficient for a 1.3 ppm ω_a measurement. This level of statistics is enough to observe many of the subtle effects that must be controlled in the ω_a analysis but is still a small subset—less than 10%—of the entire Run 1 dataset.

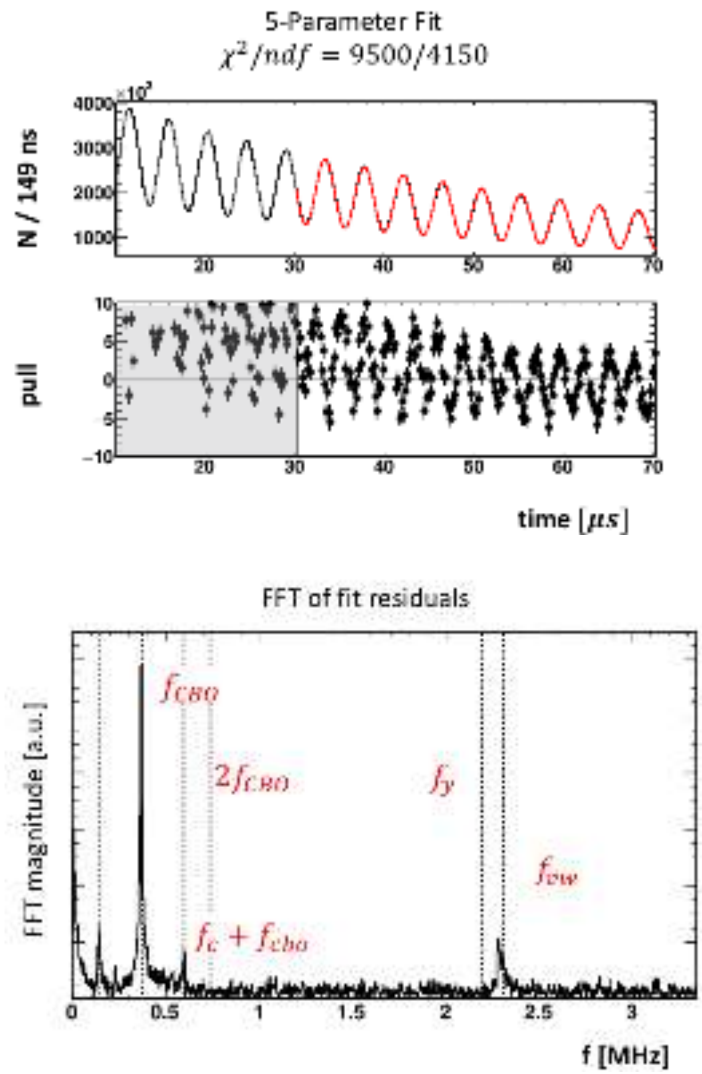

Figure 4.7-1. Five-parameter T-Method fit to the 60-Hour dataset. *Top:* The fit at early times and the fit residuals divided by the bin errors, or pulls. The full fit range is not shown. The grayed-out region shows the pulls extrapolated beyond the fit start time of 30.2 μs after beam injection. *Bottom:* Fourier transform of the fit residuals. Clear peaks are present at the expected beam oscillation frequencies. Notably, the expected coherent radial oscillation frequency, ω_{CBO}, and the expected oscillation frequencies of the first and second moments of the vertical beam distribution, ω_y and ω_{VW}, are marked on the graph. The large χ^2 value and the periodic structures in the fit residuals indicate that a five-parameter fit model does not adequately describe the 60-Hour Dataset.

As shown in Fig. 4.7-1, a five-parameter fit model containing only anomalous precession and muon decay is not adequate to explain the data. To properly fit the data, one must account for beam dynamics, or coherent motion and losses of the stored beam, and undesired detector effects, specifically unresolved overlapping pulses (pileup) and changing calorimeter gains.

Oscillations of the stored beam appear in the calorimeter spectra through acceptance effects. They can be addressed by modifying the fit model accordingly. Muon losses from the ring during the measurement period also distort the observed spectrum. Lost muons can be observed and tagged through their tendency to strike three or four consecutive calorimeters and their characteristic energy deposition in each detector. The spectral distortion from lost muons is removed using an empirical correction derived from the tagged loss candidates.

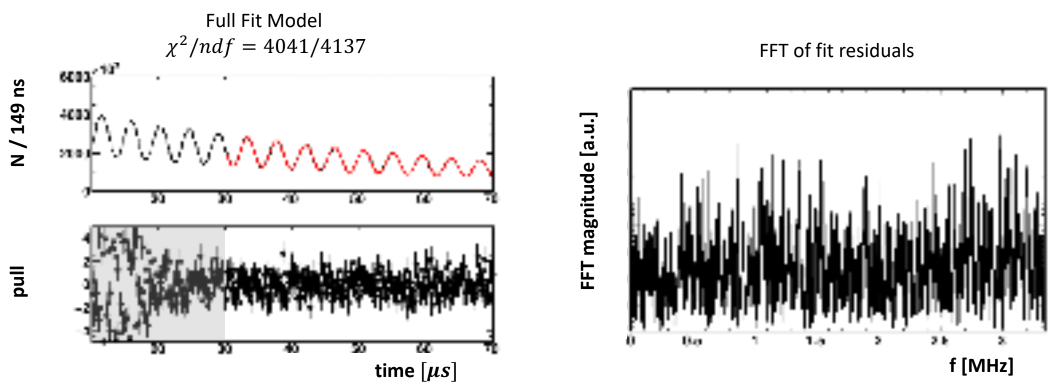

Figure 4.7-2. Similar to Fig. 4.7-1, except with corrections for pileup and gain and a fit model respecting beam dynamics effects, a result of the UW ω_a analysis. The χ^2 value is now within the range expected from purely statistical fluctuations, and no oscillatory structures remain in the fit residuals. The vertical scale of the Fourier spectrum graph has been reduced by a factor of 12 compared to the one in Fig. 4.7-1.

Uncorrected time dependence of the calorimeter response can bias the extracted ω_a value. As the $g-2$ experiment collects data in a fill structure whereby muons are periodically injected and observed, the calorimeter hit rate is time dependent, highest immediately following a muon injection and decreasing by nearly five orders of magnitude across each fill. Thus, rate-dependent effects such as pileup and gain create time-dependent distortions. Gain perturbations are measured in situ using a laser calibration system and then corrected in software. The three calorimeter reconstruction algorithms used by different teams have intrinsically different pileup responses. Pileup remaining after reconstruction is subtracted on average; the details of how this is accomplished differ significantly between analysis teams, making agreement between their results an important check on the correct treatment of systematic effects such as pileup. Fig. 4.7-2 shows the UW team's T-Method fit following corrections for beam dynamics and detector effects.

All ω_a analyses are conducted blindly. In addition to hardware blinding of the digitizer clocks, each analyzer applies a secret frequency offset in software before reporting results. In February 2019, after all analysis teams were satisfied with their independently developed fitting procedures and corrections, a relative unblinding of the extracted 60-Hour Dataset ω_a values was conducted. This was accomplished by applying a common software offset to all analyses. The numbers produced by the six teams were in excellent agreement. In successfully completing this relative unblinding, the precession team has reached a major milestone along the path toward a complete Run 1 analysis.

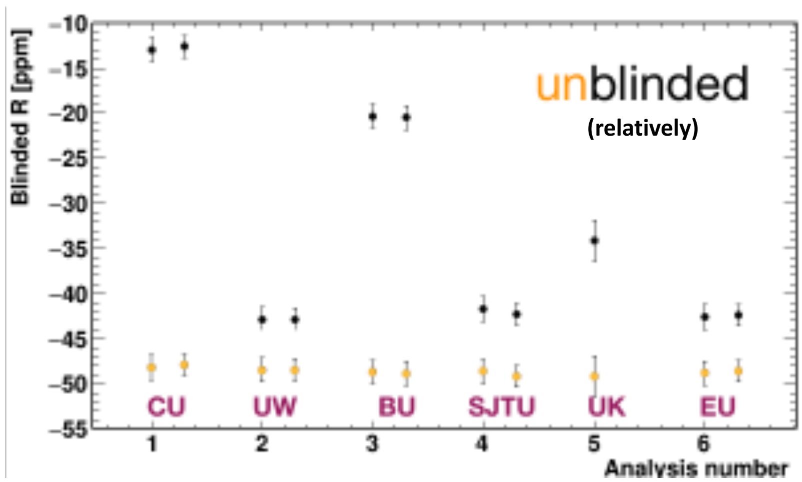

Figure 4.7-3. February 2019 60-Hour Dataset unblinding results. Five of the six teams conducted two separate ω_a analyses using different fitting techniques. The black points are the results before relatively unblinding and the orange points are the results after. With a common software offset, the results are in excellent agreement.

The Run 1 precession frequency analysis effort has now moved beyond the 60-Hour Dataset. Relative unblinding of the majority of the Run 1 data is planned for early summer 2019. Assuming success, final internal reviews and systematic error evaluations will occur in the following months. The $g-2$ precession analysis is on track for a complete Run 1 result by fall 2019.

4.8 Bunch structure of the muon beam: Impact on the ω_a analysis and extraction of the momentum distribution

K. S. Khaw

A beam profile that is narrow in time is essential for the muon beam storage of the Muon $g-2$ experiment. This is due to the requirement that the muon beam bunch has to be kicked by the pulse magnetic kicker within the first turn inside the ring. The average time width of the muon bunch achieved in Run 1 of the experiment is about 40 ns in RMS as shown in Fig. 4.9-1, whereas the cyclotron period T_c of the 3.1 GeV/c beam is about 149 ns. As the muon beam comes with a finite momentum width, it will de-bunch after 10s of μs after injection and spread out in the entire storage ring azimuthally. Such beam time and momentum profiles have important consequences for the analysis of anomalous precession frequency ω_a in the Muon $g-2$ experiment.

Impact on the ω_a fitting analysis

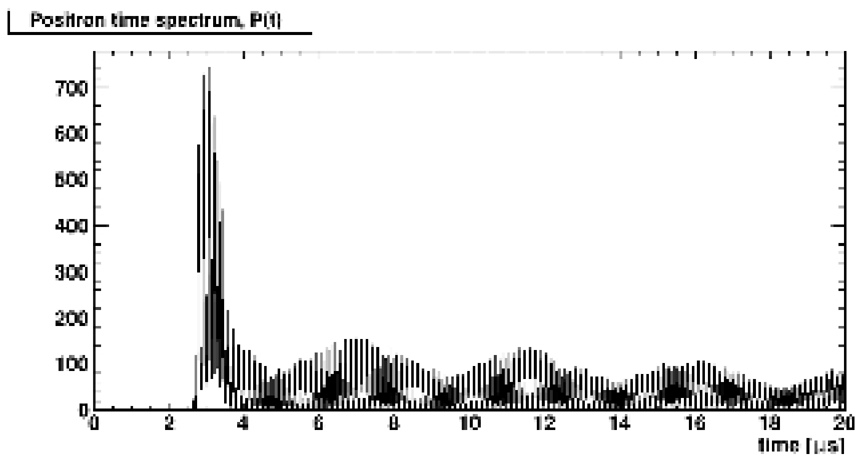

Figure 4.8-1. Number of high-energy positrons as a function of time $P(t)$ from the 60-Hour dataset. The fast oscillation (period ∼149 ns) comes from the cyclotron motion of the muon beam bunch and the slow oscillation (period $\sim 4.37\ \mu$s) is coming from the muon anomalous precession.

Among other beam and detector effects, the muon beam bunch structure causes a distortion to the perfectly exponential and cosine modulation of the positron time spectrum $P(t)$,

$$P(t) = N_0 e^{-t/\gamma\tau_\mu} \left[1 + A\cos\left(\omega_a + \phi\right)\right] \ . \tag{1}$$

as shown in Fig. 4.8-1. This introduces a systematic bias to the fitted value of ω_a, and the size of the bias depends on the relative phase between the (relatively) slow $g-2$ oscillation and fast cyclotron oscillation.

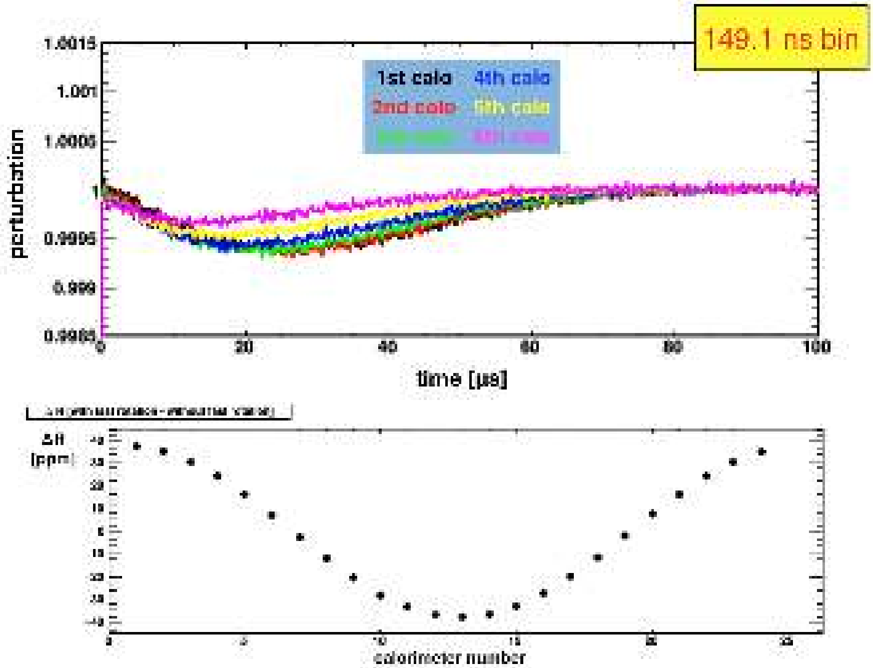

Figure 4.8-2. *Top*: Relative perturbation to the positron time spectra without time randomization. *Bottom*: Bias in the fitted value of ω_a in ppm with minus without the fast cyclotron oscillation. Both plots are based on a toy Monte Carlo simulation.

To reduce the fast rotation effect, two procedures have been applied to the ω_a analysis flow:

1. randomizing positron hit time with a flat distribution between $\pm T_c/2$ before histogramming, and

2. binning the time histogram in the as-measured average cyclotron period.

It is important to note that 2) itself is not sufficient to eliminate the fast rotation effect as the stored muon has a finite momentum distribution. For any chosen time bin size $T_{bin} = 1/f_{bin}$, there will be a beating effect $f_{beat} = f_c - f_{bin}$ between the bin size and the muon with a cyclotron period $T_c = 1/f_c$. A typical beating period is about $30 - 60\,\mu$s, depending on the momentum distribution of the muon. An example of a perturbation to the time spectrum is shown in Fig. 4.8-2 (Top) for the case of a Gaussian momentum distribution. If unaccounted for, this fast rotation effect will cause a periodic bias of the order of $O(10)$ ppm in the fitted ω_a value at the per-calorimeter level, as shown in Fig. 4.8-2 (Bottom).

Extraction of the momentum distribution: Cosine Fourier Method

While this fast rotation effect slightly complicates the ω_a analysis, it can be utilized to extract the momentum distribution of the stored muons in the storage ring. This momentum distribution can then be used to estimate the so-called *E-field correction* to the ω_a, which is caused by the existence of the vertically focusing electric quadrupole field in the storage ring and the *non-magic* muon momentum ($\gamma_{magic} = \sqrt{1 + 1/a_\mu} = 29.3$, $p_{magic} \sim 3.09$ GeV/c). The motional magnetic field seen by a relativistic muon passing through the electric field causes a reduction in ω_a as described by

$$\vec{\omega}_a = -\frac{q}{m}\left[a_\mu \vec{B} - \left(a_\mu - \frac{1}{\gamma^2 - 1}\right)\frac{\vec{\beta} \times \vec{E}}{c}\right] . \tag{2}$$

With some approximations, it can be shown that the E-field correction can be estimated using

$$C_E = \frac{\delta\omega}{\omega} = -2n(1-n)\beta^2 \frac{< x_e^2 >}{R_0^2} \tag{3}$$

where n is the field index of the storage ring, x_e is the equilibrium radius to be determined from the analysis in this section, and $R_0 = 7.112$ m the orbit radius of the magic muon. Two methods are deployed by the Muon $g-2$ experiment to extract the x_e distribution; of these, the *Cosine Fourier Method* will be described herein.

As derived by Orlov et al.[5], the cyclotron frequency distribution of the muon beam in a storage ring can be written as

$$\Phi(f, t_s; t_m) = \int_{t_s}^{t_m} F(t) \cos\left[2\pi f (t - t_0)\right] \, dt \tag{4}$$

where t_s is the analysis start time, t_m the analysis stop time, $F(t)$ the fast rotation signal that is produced by normalizing the positron hit time distribution in Fig. 4.8-1, and t_0 the time at which the center of the beam distribution passes through the calorimeters. In practice, $F(t)$ is represented as a finely binned time histogram and the contents of each of its bins are denoted as T_i. Examples of $F(t)$ for different time ranges are shown in Fig. 4.8-3. Similarly, the reconstructed frequency distribution $\Phi(f)$ is also represented as a frequency histogram and its bin content F_i is given by

$$F_i = \sum_j T_j \cdot \cos\left[2\pi f_j (t_j - t_0)\right] \cdot \Delta t \tag{5}$$

where f_j is the bin center frequency of F_j, t_j the bin center time of T_j and Δt the time bin width.

[5] *Muon revolution frequency distribution from a partial-time Fourier transform of the g-2 signal in the muon g-2 experiment*, NIM A 482, 767-775 (2002)

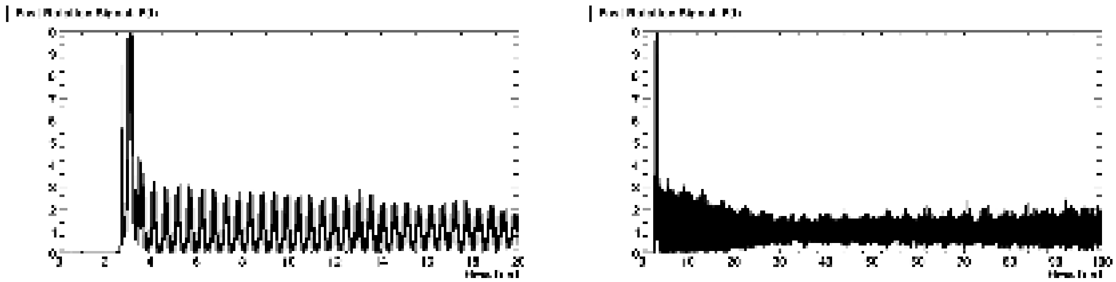

Figure 4.8-3. *Left*: Fast rotation signal $F(t)$ after normalizing $P(t)$ with a 5-parameter function fit $N(t) = N_0 e^{-t/\gamma\tau_\mu}\{1 - A\cos(\omega_a t + \phi)\}$ describing muon anomalous precession ω_a. *Right*: The amplitude goes down to $\sim$1 at 30 μs after injection, indicating that the 5-parameter function can perfectly describe the measured data at late time when the fast rotation effect is gone.

Due to the positron contamination in the beam, typically the first 4 μs of the data is skipped in the analysis. The decay positron data from around 4 μs to 200 μs are used to construct a first approximation of the cyclotron frequency distribution. From the first approximation, the missing part of 0-4 μs is then estimated and corrected for in the second iteration. Finally, the frequency distribution is converted to the equilibrium radius distribution using $\beta c/2\pi f$ as shown in Fig. 4.8-4. Typical correction to ω_a for the Run 1 of Muon $g-2$ using Eq. 3 is about +0.5 ppm. Estimation of systematic uncertainty due to this frequency extraction technique is in progress for the Run 1 result.

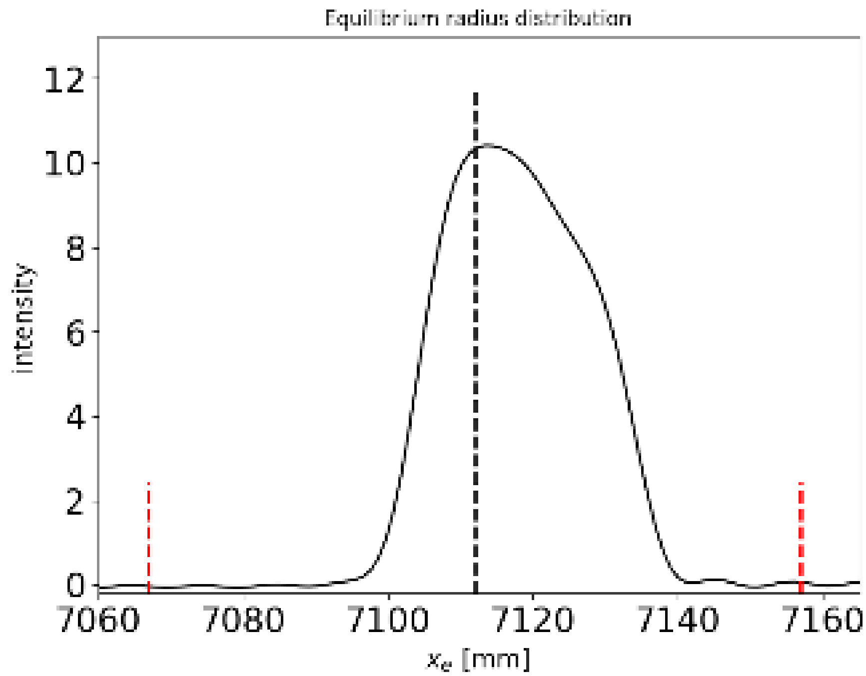

Figure 4.8-4. Equilibrium radius distribution of the 60-Hour dataset extracted using the *Cosine Fourier Method*. The black dotted line denotes the magic radius of $R_{magic} = 7.112$ m and the red dotted lines denote the boundaries $R_{magic} \pm 45$ mm of the storage region.

4.9 T0 and CTAG data quality control for Run 1

H. Binney

Data quality control (DQC) is an essential step in the Muon $g-2$ analysis chain. Because of the complexity of the accelerator, ring, and detector systems, conditions often change in subtle ways during data-taking. This was especially a concern during Run 1, when commissioning of these systems was occurring across data-taking periods. Beam tuning, pulses with extra blips, abnormally small pulses, and systematic studies all occurred with regularity during Run 1 data-taking. The role of DQC is to ensure that only high quality data with consistent conditions are passed down the chain to the final physics analysis. DQC cuts are placed on kicker settings, beam intensity, laser pulses, field behavior, muon storage, etc. to remove bad events. The events that fail the filter remain in the reconstructed data and can be examined for other studies; however, they are not included in the default physics analysis. I will discuss T0 and CTAG data quality here in more detail.

The T0 start-time detector is an especially valuable DQC tool. T0 is the most upstream detector in the magnetic storage ring, and it measures the profile of the muon beam intensity versus time as the muons are injected. It was designed and constructed last year at CENPA and is composed of two photomultiplier tubes coupled via light guides to a thin plastic scintillator. An optical fiber coupled to each channel provides laser pulses to synchronize the T0 detector with the rest of the experiment.

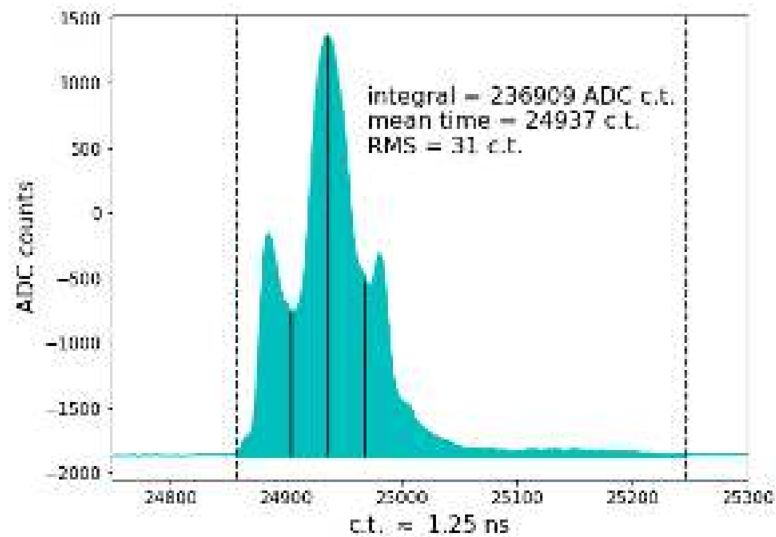

Figure 4.9-1. Sample T0 trace showing the integration limits (dotted lines), mean time (center line), and mean time ± the RMS. The horizontal axis in is clock ticks, where 1 c.t. ≈ 1.25 ns. The vertical axis is in ADC counts, a digitizer measure of voltage.

Because T0 is the first thing that the muons pass through as they enter the ring, placing a cut on T0 metrics ensures that the beam is high quality and arriving as normal from the accelerator. A sample reconstructed trace from a single fill is seen in Fig. 4.9-1. Each muon fill has a T0 beam pulse and an associated T0 laser sync pulse. To ensure that the event is high quality, we cut on five T0 metrics: the beam pulse integral, time, and RMS; and the laser pulse integral and time.

The T0 pulse integral scales linearly with beam intensity, so we can assume that any beam pulse with a very low T0 integral is abnormal and should not be included in the physics analysis. A histogram of T0 integrals as a function of run number (chronological) for one of the Run 1 datasets is shown in Fig. 4.9-2. There is a band of high intensity events with an integral of > 300,000; a band of medium intensity events; and then a few events with an integral close to 0. These 0 integral events are those where no beam arrives from the accelerator. From looking at the traces in the medium intensity events, I determined that the pulses are smaller in size but similar in shape, and therefore should pass the filter. I decided to only cut out the events with very low integrals.

Similar decisions can be made for the other T0 metrics. The beam pulse is expected to arrive at the same time for every event, and initially it seemed unimportant to place tight boundaries on the timing. However, by placing cuts on the beam time, we found

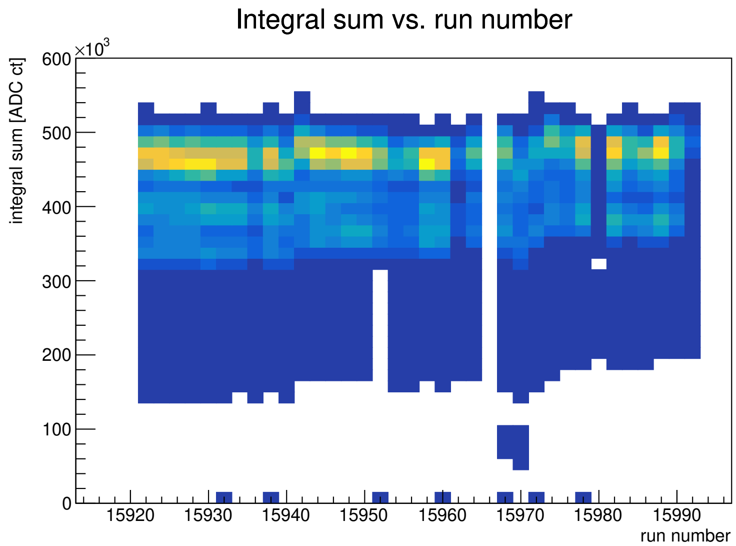

Figure 4.9-2. T0 integral distribution from the 60-Hour dataset. The data quality cut is placed at 20,000 ADC c.t. (where c.t. is clock ticks.)

that some systematic studies with different timings remained in the main dataset even though they should have been removed. We were able to identify these events using the DQC filter. The beam pulse RMS is a basic measure of the pulse shape, which is expected to have a standard "W"-shaped time profile as it enters the ring. Placing cuts on the beam RMS removed, for example, events with extra beam blips coming through before the main pulse. Finally, the cuts on laser pulse time and integral ensure that the laser pulse exists in the event. This is essential in order to synchronize the T0 detector with the rest of the experiment.

I also worked on DQC relating to a metric called CTAG, which is defined as a calorimeter hit with a certain minimum energy. CTAGs are a measurement of decay positrons detected in the calorimeters. The number of CTAGs in the fill acts as a proxy for muon storage. If the incoming beam is normal and the ring systems (e.g. kickers, quads) are working properly, the muon storage will be high, and therefore there will be more decay positrons hitting the calorimeters. If the beam intensity (measured by T0 integral) is low or the ring systems are malfunctioning, the number of CTAGs will be low. For example, we had many quadrupole sparks (and subsequently quad spark recoveries) during Run 1 data-taking, and these events caused the muons in the ring to be lost. Changing quad conditions affect the beam dynamics, so these events should be removed from the physics dataset. We check both the absolute number of CTAGs and the CTAG value normalized to the incoming beam intensity (normalized CTAGs shown in Fig. 4.9-3).

These DQC cuts along with many others have been implemented for most of the Run 1 datasets and have ensured that the data used for physics is consistent and high quality.

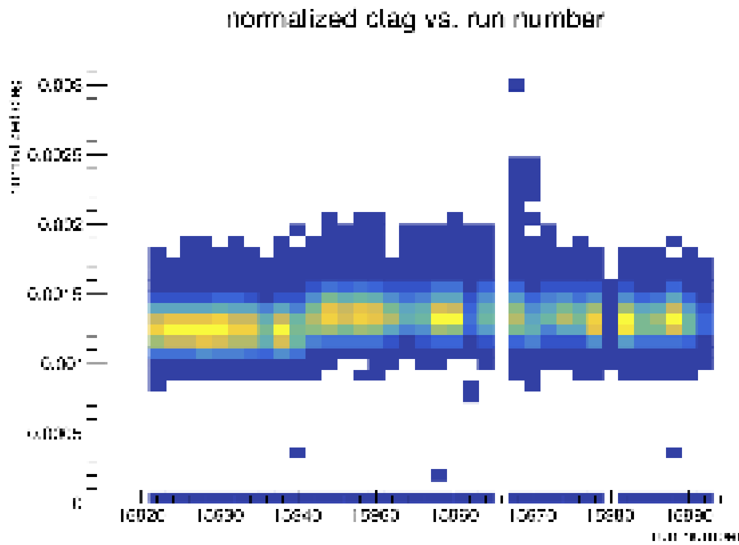

Figure 4.9-3. CTAG normalized to T0 integral from the 60-Hour dataset. The data quality cut is placed at 0.0005.

4.10 Comparison of reconstruction algorithms

J. LaBounty

Quasi-independent reconstructions of the Run 1 $g-2$ calorimeter data are carried out by the 'Recon East' and 'Recon West' teams. The goal of the two reconstruction algorithms is the same: to fit individual calorimeter crystal pulses, calibrate them consistently in time and energy, and cluster them appropriately to represent the energy, time, and position of an impacting positron. The two reconstruction efforts made a number of different design decisions, which can naturally lead to different reconstructed clusters.

We made an effort to compare the East- and West-based algorithms at the individual cluster level in order to test for errors or biases in either approach. This analysis was presented alongside the relative unblinding effort described in (Sec. 4.6), and no changes were made to either analysis based on these results before the relative unblinding was completed.

One example of a comparison that was made is that, for the same raw waveform digitizer traces, we compare the number of clusters found in each reconstruction. Were they to be identical algorithms, we would expect an exact 1:1 correspondence. In Fig. 4.10-1 we see this is not the case. Instead we see a number of off-diagonal islands, in which n clusters are present in one reconstruction and m clusters are present from the other, for some $n \neq m$. The differences here are largely due to temporal and spatial pileup choices employed at this stage in the analysis. They are understood and rectified at a later stage in the analysis chain.

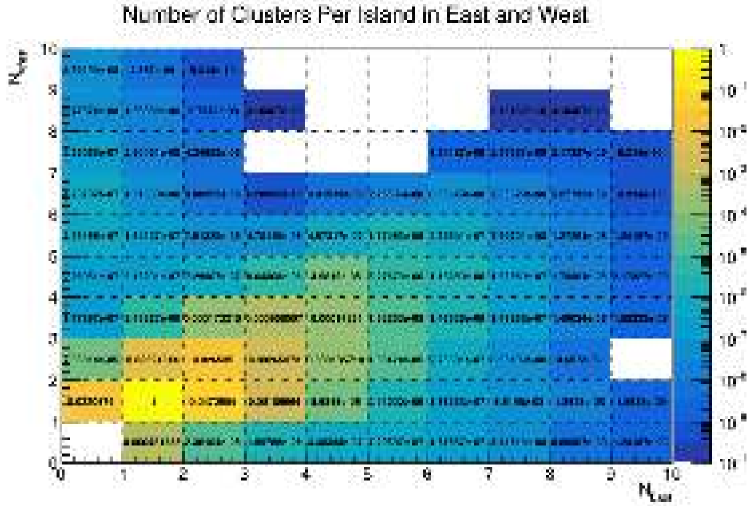

Figure 4.10-1. Number of clusters from Recon West and Recon East per island, normalized to the number of 1:1 islands. The high-n values predominantly occur early in the fill when the pileup is more pronounced.

To compare the reconstruction algorithms directly, we attempt to identify pulses that are coming from the same physics sources, for example by only examining events having only 1 cluster from each reconstruction within a $\pm 19\,\mathrm{ns}$ time window. This time cut is overly conservative in order to ensure a pure sample. The largest differences between these '1:1' clusters come from the reconstructed energies. Looking at Fig. 4.10-2, we see that the slope of E_{west} vs. E_{east} is not 1.0. This does not present a problem, as the definition of an MeV in East and West is allowed to slightly differ (there being no trivial absolute calibration metric). As long as the analyses are internally consistent (i.e. all calorimeter crystals are calibrated consistently with respect to one another within each analysis) then there will be no bias from one to the other. The second feature evident in the is the 'banding' that is present above the main slope. This is due to specific crystals that have particularly poor relative energy calibrations. Some of these were known issues in advance, but some other discrepancies were revealed in this analysis. These crystals have been identified, and much work has been done to improve this going forward for Run 2.

We also evaluated whether there exist any relative shifts between the two reconstructions from early to late in the fill. The most concerning of these shifts would be a relative change in the timing of the reconstructions. Were this to happen, it would appear as a linear shift in the value of ω_a seen by one reconstruction relative to the other. Other than a simple oscillatory behavior due to pileup, which is addressed by the pileup corrections in Recon West and Recon East later in the analysis chain, the overall shift in ω_a is less than 0.24 ppb. This, combined with independent checks of the time stability of both Recon West and Recon East, provides good evidence that both reconstructions are stable in time.

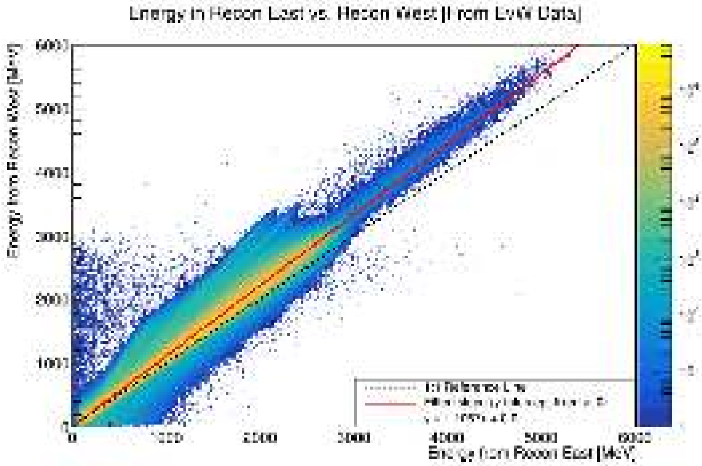

Figure 4.10-2. Reconstructed energies for E_{west} vs. E_{east}. While the reconstructions are internally consistent, the definition of an 'MeV' can differ between reconstructions (see text for details). This difference leads to the non-unity slope seen here.

Because of the differences between the two reconstructions, different subsets of the collected positrons will enter into our analyses for what is nominally the same dataset. Thus, when the analyses are recombined into one final result, the allowed statistical differences from these set-subset differences should be taken into account. We use this study to provide a first estimate of the set-subset differences that would be present in a typical T-Method analysis. In such an analysis, all positrons above a certain energy threshold are histogrammed vs. time, and this histogram is fitted to extract ω_a. For the example below, we used the thresholds provided by two of the main analyzers of the Run 1 data. The Recon West threshold was fixed at 1730 MeV for every calorimeter and the threshold for Recon East was varied on a per-calorimeter basis (ranging from $1350 - 1600$ MeV).

Using these thresholds, we quantify the percentage of identified clusters that are unique between the two reconstructions. The results of this calculation are shown in Fig. 4.10-3. We find that for these thresholds the overall percentage of clusters that are unique to one reconstruction or the other falls between 2 and 5% (Fig. 4.10-3).

4.11 Preparing the calorimeters for Run 2

J. B. Hempstead and J. Kaspar

In order to measure the precession frequency ω_a for the Muon $g-2$ experiment, 24 electromagnetic calorimeters are equally spaced around the inside of the muon storage region. The direction of the muons' spins is imprinted on the number of high-energy positron decays in a particular direction. When a stored muon decays, the lower mass positron curls inward in the magnetic field. By recording the hit times and energies of

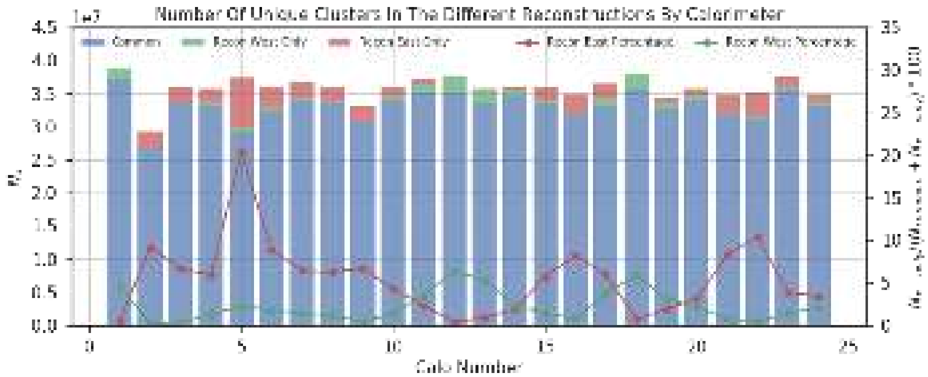

Figure 4.10-3. Percentage of unique clusters for each calorimeter in an example analysis. Overall, the percentages of unique clusters in Recon West and Recon East are 2.32% and 5.47%, respectively.

positrons, ω_a can be extracted by fitting a histogram of positrons above a particular energy.

Each calorimeter consists of 54 lead fluoride (PbF_2) crystals arranged in a 9 wide by 6 tall grid. The crystals are individually read out by silicon photomultipliers (SiPMs) attached to the back faces of the crystals. The response of the SiPMs is governed by the applied bias voltage V_a and the programmable gain amplifier in the signal output circuit. More specifically, each SiPM has a characteristic breakdown voltage V_{bd} that is temperature dependent. The gain of the SiPM is proportional to the over-voltage $V_{ov} = V_a = V_{bd}$. Thus, if a constant bias voltage is applied, temperature drifts will cause a change in the over-voltage and, therefore, gain.

A typical over-voltage for the SiPMs in Run 1 was about 1 V. Lab tests indicate that the change in the breakdown voltage of the SiPMs with temperature to be $\sim$0.07 V/°C. Temperature swings of $\pm 2\,^{\circ}$C correspond to a spread in gains on the order of 30%. While the laser system employed in the experiment can adequately track these changes, better hardware stability is preferable.

Additionally, 160 MHz noise was prevalent in the Run 1 data. The width of the peaks created by a signal at this frequency is very similar to that of the width of the peaks of the SiPM pulses used to detect particles, so the noise passes through the frequency filters in the readout electronics. It has been demonstrated that the noise is amplified by the programmable gain amplifiers but is unaffected by the bias voltage. Therefore, the amplification can be reduced to lessen the impact of the noise while the bias voltages can be raised to compensate, and this improves the physics-related performance. This also has the benefit of increased robustness to temperature fluctuations. Based on these considerations, the bias voltages of all 1296 SiPMs were raised 0.2 V for Run 2 data-taking.

SiPM gain equalization

Following the voltage change to all channels, the programmable gain settings for all of them had to be recalculated. The driving constraints are that each channel must simultaneously have a gain large enough to resolve the energy peak of an incident muon at 170 MeV and small enough that two simultaneous 2 GeV positrons (in one channel, a very rare occurrence) do not saturate the readout electronics or digitizers.

The laser system can be used to simultaneously probe the gain of all channels by using a series of filters to attenuate the amount of light reaching each SiPM. For each scan, a measure of the gain is calculated and the amplifier setting for each channel is adjusted to reach a target value. The results of this process can be seen in Fig. 4.11-1.

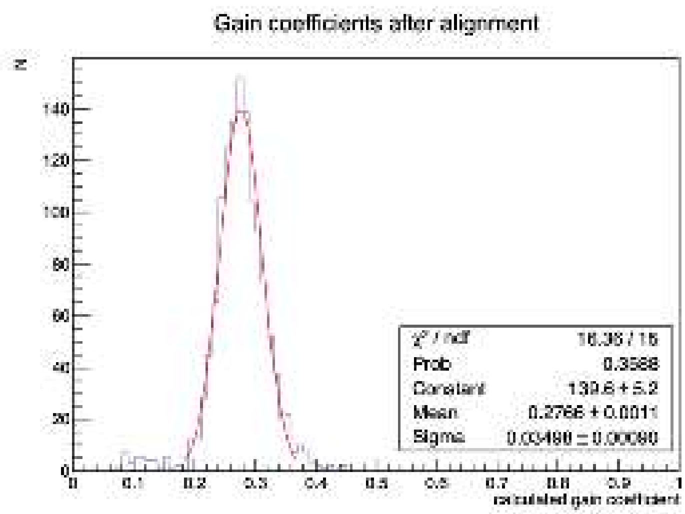

Figure 4.11-1. Gain coefficients following alignment. The gain coefficient is the inverse of the gain measured in a scan of laser filters of varying transmittance. The non-Gaussian tails arise from channels for which the desired amplifier setting is outside the allowed range of the hardware.

Calibration and timing alignment

Since the calorimeters are primarily responsible for measuring a frequency, the channels must be well aligned in time. A single laser pulse sent to every channel at the beginning of each 700 μs muon fill is used to coarsely align the SiPMs. However, due to differing electronics-related and laser-fiber-related delays, constant offsets must be applied to each channel. To calculate the calorimeter-dependent offsets, the time of flight of muons that are lost from the storage region before decaying can be measured by finding coincidence events in consecutive calorimeters. The results of using this process can be seen in Fig. 4.11-2. To calculate the channel-by-channel offsets necessary within a calorimeter, the time difference of decay positron showers in adjacent crystals is set to

0.

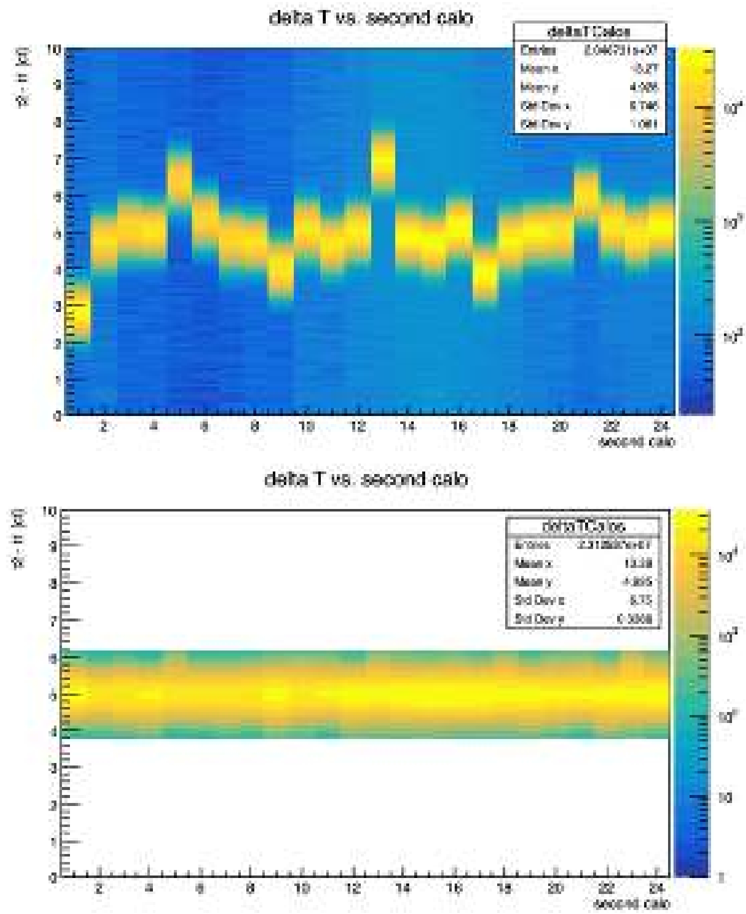

Figure 4.11-2. Muon time of flight between consecutive calorimeters (*top*) uncorrected and (*bottom*) corrected. By constructing coincidences between consecutive calorimeters, the time of flight of muons can be used to calculate necessary calorimeter timing offsets. Following alignment, the measured time of flight between separate pairs of calorimeters is consistent at the expected value of ~5 clock ticks (6.25 ns).

To align the energy scales of every channel, the same lost muon events referenced for calculating calorimeter-dependent timing offsets are used. The muons pass relatively unimpeded through the calorimeters and typically deposit energy in only one channel. The peak of this energy deposition in the coincidence events is equalized at a value of 170 MeV. Once this is done, the maximum figure of merit for a fit to extract ω_a falls at the predicted value of 1.7 GeV and the endpoint of the decay positron energy spectrum lies at the expected 3.1 MeV. The results of this procedure can be seen in Fig. 4.11-3.

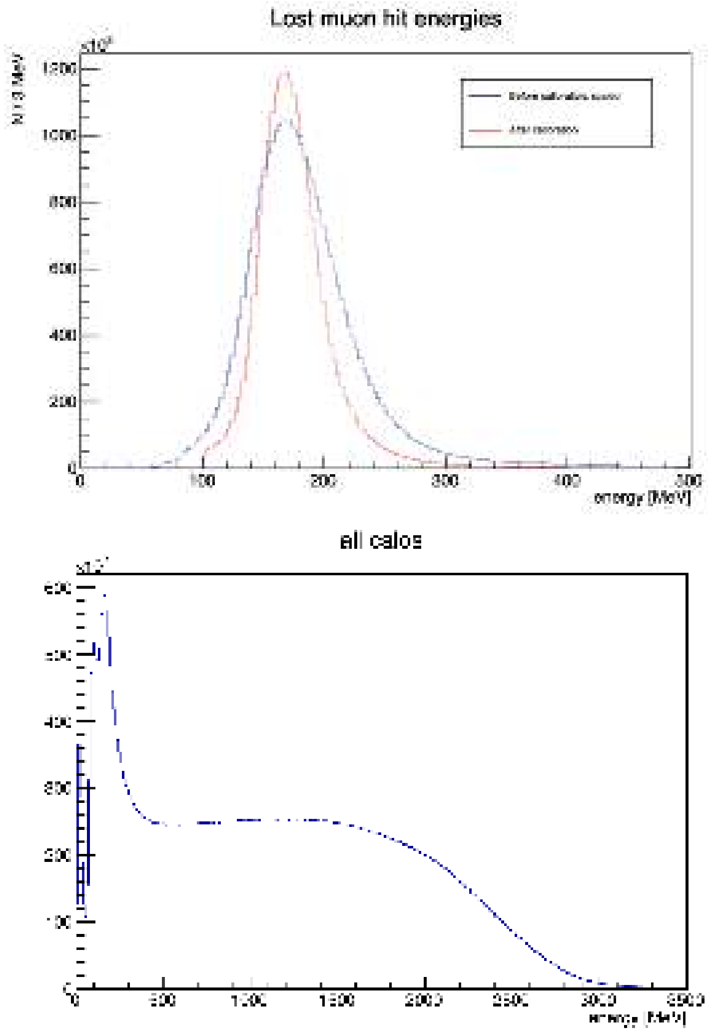

Figure 4.11-3. Energy spectra for (*top*) lost muons before and after calibration and (*bottom*) all calorimeter hits. The tendency for lost muons to deposit energy in only one channel is leveraged to align the measured energy values for all channels. Following alignment, the endpoint of the energy spectrum for decay positron events falls naturally at the expected value of 3.1 GeV.

4.12 Nearline and DQM processing for Run 2

H. Binney, J. LaBounty, and K. S. Khaw

When the Muon $g-2$ experiment is receiving beam, the data acquisition system (DAQ) produces about one 1.5-2.0 GB 'subrun' of data every 6 seconds. Processing all of this to physics-results level quality in real time is unrealistic, but we still require rapid feedback in order to assess the quality of the data in (close to) real time. Thus we have developed three tiers of data analysis—the DQM, Nearline, and Offline—each with their own characteristic turnaround time.

The first, and fastest, of these tiers is the Data Quality Monitor (DQM). This processes a small fraction of the data as it comes in. It reports on instantaneous trends, such as the intensity of the muon beam entering the ring through the T0 detector, the number of decay positrons hitting each calorimeter, and the magnetic field. This information is useful at a glance to the shifters running the experiment, and is often used for fast feedback when tuning beam/experimental parameters. Where the DQM falters, however, is with volume: only a few minutes of data are stored at a time. Therefore, to examine longer term trends, or to examine small effects that require increased statistics to see, we turn next to the Nearline.

The Nearline processes the data on a subrun-by-subrun basis and stores its output indefinitely, so long-term trends can easily be seen and analyzed. The Nearline primarily uses the same analysis software as the full offline analysis. Some modifications were made in order to increase the speed of the software, at the expense of some analysis fidelity. These include removing the tracking detectors from the analysis chain, only running a single reconstruction (Recon West), and doing gain corrections using sync pulses rather than out-of-fill pulses. The Offline also has an extensive system of data quality control which is not present in the Nearline, as it requires database checks which are impossible on the rapid timescales required. This means that many of the same sophisticated analysis modules that were developed for the full analysis can be run on the Nearline. However, it takes approximately 30-45 seconds to process each subrun, and so the Nearline can still only process a fraction of the data being taken in. Significant improvements over Run 1 have been undertaken to improve this fraction from $\sim$20% to $\sim$40%.

The final data analysis tier is the full offline reconstruction (mentioned here for completeness), which processes 100% of the data with the most stringent data quality control. This is the analysis which is used by the final analyzers. The characteristic turnaround time for this is on the order of greater than one month, and thus motivates the rapid response found in the Nearline and DQM.

DQM

The DQM has continued to run smoothly through Run 1 and Run 2 without major overhaul. A few recent updates have been implemented. The DQM has been modified to run with the IBMS3 detector, which is newly installed for Run 2. Additionally, we have implemented timing corrections in the DQM. In the offline analysis, the experiment systems are aligned in time by the use of a laser synchronizing pulse, and each calorimeter crystal is further time aligned with respect to the others. These timing alignment steps are necessary to extract the physics result; however, they were previously deemed unnecessary for DQM purposes. However, we added them for this run so that beam injection would occur more intuitively at 0 and so the timing windows on certain plots could be tightened. There have also been several accelerator changes that have prompted DQM updates. First, the accelerator system now delivers a 16-pulse train to the experiment instead of an 8-pulse train, so we altered the DQM accordingly. Second, the accelerator now sometimes delivers beam to the test beam facility, during which time we use internal triggers to continue firing the kickers while no beam is arriving. However, averaging these events into the DQM causes certain metrics (specifically CTAGs, a proxy for muon storage) to seem artificially low. We have been working on excluding these events from certain DQM pages. The DQM is expected to run reliably though Run 2 data taking and beyond, with smaller updates implemented as necessary.

Nearline

The Nearline consists of two machines that process data semi-independently. We have tuned them such that the first machine is always attempting to process the latest few files, while the second catches as many as possible that are skipped by the first. Log files are used to ensure that each file is only processed once.

The first task of the Nearline is to determine the preliminary gain correction factor for each calorimeter crystal. As the temperature of the environment, changes the gain of our detectors can drift. Laser pulses of a known intensity are used to calibrate the response of each SiPM relative to a known reference run. This is less sophisticated than the procedure used in the final offline analysis, which incorporates a number of additional corrections, but comes with a significant increase in speed. After this is done, the Nearline runs a number of different analysis modules. Modules are included that store the output from the various beam profile monitors (T0 and IBMS1-3). Other modules track the positron hits in the calorimeters, and run the same reconstruction and clustering algorithms present in the offline in order to produce energy/time spectra. A subset of the plots produced for each run of the data can be seen in Fig. 4.12-1.

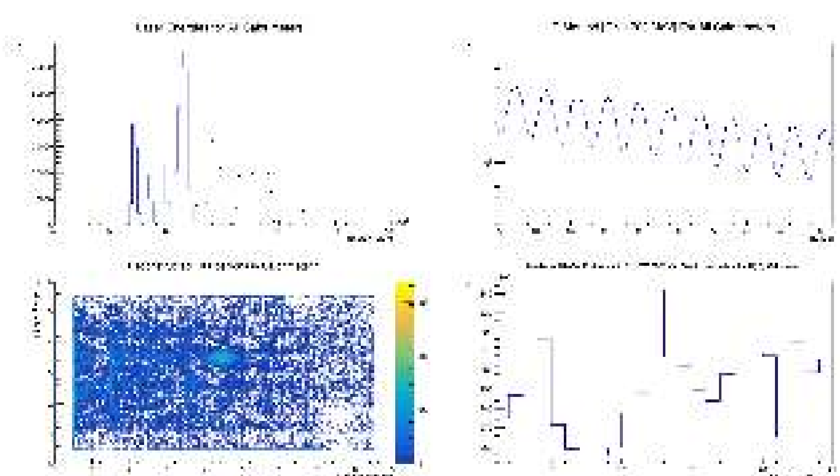

Figure 4.12-1. Example plots produced from a single run of Nearline data. This represents approximately one hour of normal data taking (approximately 500 subruns).

A number of upgrades were made to the Nearline for Run 2 in order to improve its overall performance. A custom C program was written to identify the newest files in a directory, rather than relying on the Linux `find` command. Because the directory in which the subrun files are saved is constantly being written to, often there isn't a reliable index. This was often a bottleneck for identifying files in Run 1. The C program first gets the names of the files present, a very fast operation, and then only runs `stat()` (the limiting factor in determining which files are newest) to identify when they were produced if their names match a certain known pattern. Another speed improvement was achieved by streamlining the template fitting code. Every single crystal has a beam and a laser pulse template, which previously were stored in separate files. By combining all of the templates for each calorimeter into a single file and modifying the template fitter to accommodate this change, we decreased the initialization time for the Nearline fitter from 20 seconds to <1 second. These improvements, combined with other miscellaneous changes, were what made it possible to increase the fraction of events processed by the nearline from ∼20% to ∼40%. As we did with the DQM, we also modified the Nearline to analyze data from the newly installed IBMS3 detector (Sec. 4.13).

4.13 Completion and performance of the inflector beam monitoring system

T. Burritt, P. Kammel, B. K. H. MacCoy, D. A. Peterson, and T. D. VanWechel

The muon injection into the $g-2$ storage ring is one of the most critical and complex elements in the muon delivery concept. The entering muon beam has to pass through strong fringe fields and the narrow inflector apertures (18 mm × 56 mm), which results in a mismatch between transmitted beam phase space and the ring acceptance. The Inflector Beam Monitoring System (IBMS) was designed and constructed at CENPA. It is the primary diagnostic tool to verify the beam profile at injection, and is being used as a continuous monitor of beam properties. Two IBMS modules (IBMS1 and IBMS2) were installed for operation starting in the 2018 commissioning Run (Run 1). A third module (IBMS3) was built, tested, and installed for the 2019 Run (Run 2).

IBMS1 and IBMS2 consist of two planes of 16 scintillating fibers (SciFis) each, oriented in the horizontal and vertical directions. IBMS3 consists of just one plane of 16 vertically-oriented SciFis. Each 0.5 mm diameter, double-cladded fiber (SCSF-78 from Kuraray) is coupled to a silicon photomultiplier (SiPM) (S12571-010P from Hamamatsu). These 1 mm^2 area SiPMs were selected for their large dynamic range (10,000 pixels) and fast recovery time. Detector geometry was optimized for the expected beam profile at each position. The readout electronics are based on low-noise programmable gain amplifiers followed by line drivers that transport the analog signals via micro-coax cables to the receiving CAEN V1742 waveform digitizers. Each 16-SiPM-channel board fits onto one 16-fiber detector plane, with each channel reading out one SciFi.

A Sr beta source, along with a special high-gain amplifier board, was used to characterize the detector response to minimum ionizing particles (MIPS). Neutral density filters placed in front of the SiPMs then set the detector response within the linear SiPM operating range for the expected 700,000 muons per 120 ns beam pulse.

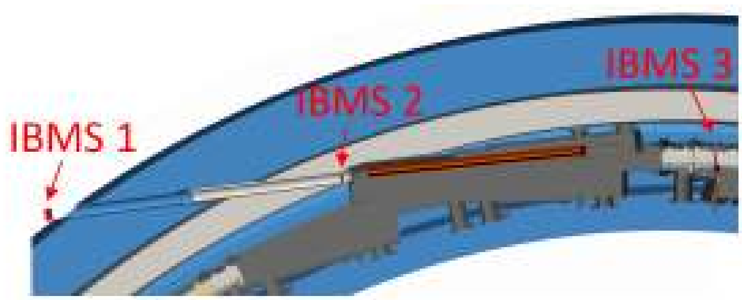

Figure 4.13-1. IBMS1/2/3 locations are shown in a top view segment of the ring.

IBMS1&2: IBMS1 is the upstream-most IBMS module, positioned just outside the yoke hole bore into the ring magnet. IBMS1 is mounted on an X-Y translation stage for fine position adjustments and repeatable displacements for in-beam detector calibration. Readout electronics feature modular SiPM and amplifier boards for easy maintenance access. The fiber pitches are 5.5 mm (X plane) and 2.7 mm (Y plane), for an 88 mm $\times$ 43.2 mm active area.

IBMS2 is positioned inside the yoke hole bore, just upstream of the inflector. A linear rail and carriage system installed in the 100-mm-diameter bore carries the IBMS2 detector assembly to its operating position 2 m downstream of the yoke hole entrance. Readout boards include SiPMs and amplifier electronics mounted together due to space constraints. The fiber pitch is 3.25 mm on both the X and Y planes, for a 52 mm $\times$ 52 mm active area.

A light injection system directs pulsed LED light into each SciFi of IBMS1&2 for real-time detector stability monitoring. Electronic test pulses monitor the amplifier stability. IBMS1&2 have been installed and operating stably since Run 1.

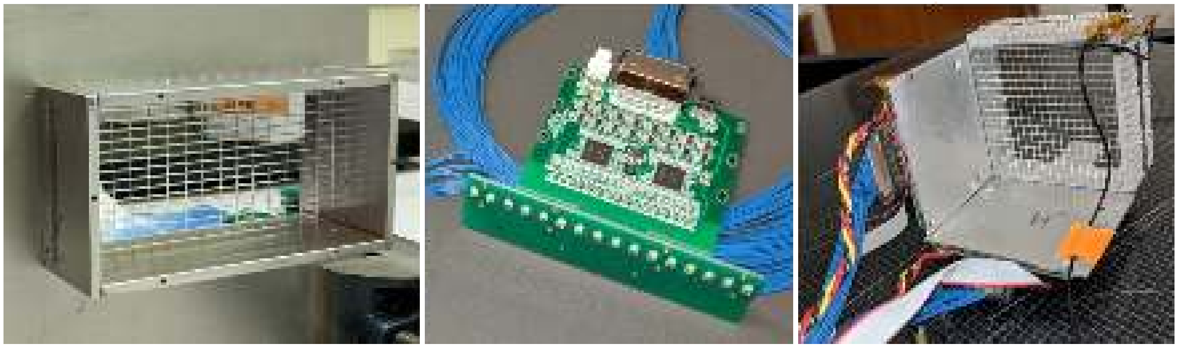

Figure 4.13-2. IBMS1 (*left*) and IBMS2 (*right*) each consist of 16 × 16 SciFis read out by two 16-channel amplifier and SiPM boards. IBMS1 readout electronics are modular with independent SiPM and amplifier boards (*center*).

IBMS3: IBMS3 is the downstream-most IBMS module, positioned 8.3° or 1 m downstream of the injection point (inflector exit aperture). It is located inside the storage ring vacuum chamber at the upstream port of tracker station 1. The assembly was built with a modified tracker port flange and is mounted in an unused tracker port. The fiber pitch is 3 mm with a 48 mm active width; the vertical fibers provide horizontal beam profiles, which contains the most important injected beam information. The SiPM board is mounted directly to the fiber frame in the vacuum, and microcoax cables carry the signals out through a vacuum feedthrough connector to an independent amplifier board on the air side.

Its location in the vacuum and in the ring field imposes several constraints which required design and testing before installation. The entire assembly must be non-magnetic to avoid perturbing the field above the few-ppm level. To verify this, the full assembly was transported to Argonne National Lab (ANL) to measure the field perturbation on a 1.45 T magnet test stand with an NMR probe, with support from the ANL team. The largest measured perturbation was 3.5 ppm, well within safe limits. All in-vacuum components must be low outgassing for the $< 10^{-6}$ torr vacuum of the ring. The rate of rise (ROR) of all in-vacuum components was measured in an in-house customized vacuum test chamber. Once cleaning procedures were optimized, all components had ROR well below 10^{-5} torr L/sec (the tracker station specification used here for reference). The custom-built IBMS3 flange was leak checked with a He leak checker, and no leaks above $\sim 10^{-9}$ torr L/sec were found. The assembly must not interfere with muon storage during production running, and it must clear the path of the field probe trolley travelling through the storage region as well as the trolley rails. The detector is mounted on a vacuum feedthrough linear micrometer. For normal physics running and trolley runs, IBMS3 is retracted out of the way of the storage region. For dedicated beam studies, IBMS3 is manually inserted into the injected beam.

To simulate beam profiles and fiber hits and check for scattering effects such as calorimeter shadowing, the simulation team incorporated the detailed IBMS3 model into the $g-2$ Geant4-based Monte Carlo software. The simulation showed a reasonable beam distribution hitting the IBMS3 fibers, and very little effect on calorimeter positron hits.

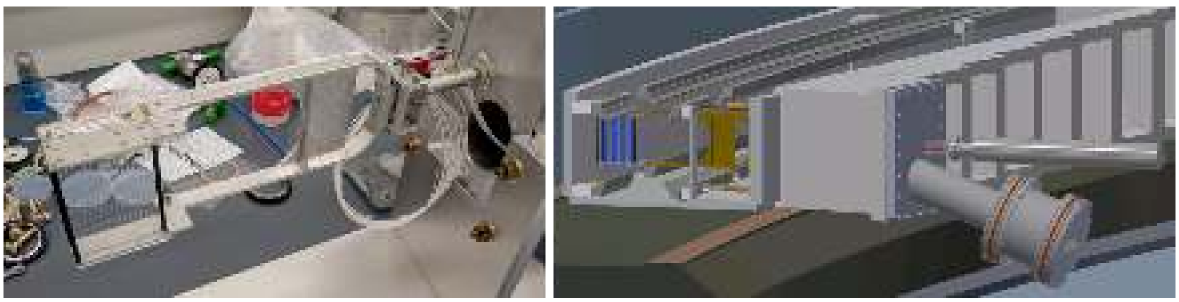

Figure 4.13-3. IBMS3 consists of 16 vertical SciFis (for horizontal profiles only) on a 3 mm pitch read out by SiPMs mounted to the fiber frame (*left*); signals are fed out of the vacuum on microcoax cables to a 16-channel amplifier board. The detector is located 8.3° downstream of the injection point inside the storage ring vacuum chamber, mounted in an unused tracker port (*right*).

IBMS3 was installed in early 2019, and recorded its first beam profiles with commissioning in the 2019 Run. Two challenging aspects in particular could not be verified until full commissioning: 1) Some noise pickup on the SiPM signal cables was present during lab testing, but possible effects from the pulsed kicker magnets and electrostatic quadrupoles combined with RF shielding of the vacuum chamber were unknown. 2) The detector dynamic range, set with a neutral density filter, was selected based on beam injection simulations, measured IBMS1&2 intensities from Run 1, and MIPS calibration. However, the true response could not be verified until IBMS3 was commissioned in the injected beam.

IBMS3 performed very well during commissioning. Noise pickup was lower than expected, <5 mV on a full-scale signal range of 0.8 V. The dynamic range was optimal; with IBMS3 inserted into the injected beam, the SiPM response was well within the linear range. IBMS3 was also exposed to the lower-intensity stored beam by positioning it in the muon storage region, and the beam profile clearly showed several 150 ns turns of the beam around the ring within the 1 μs digitized waveform.

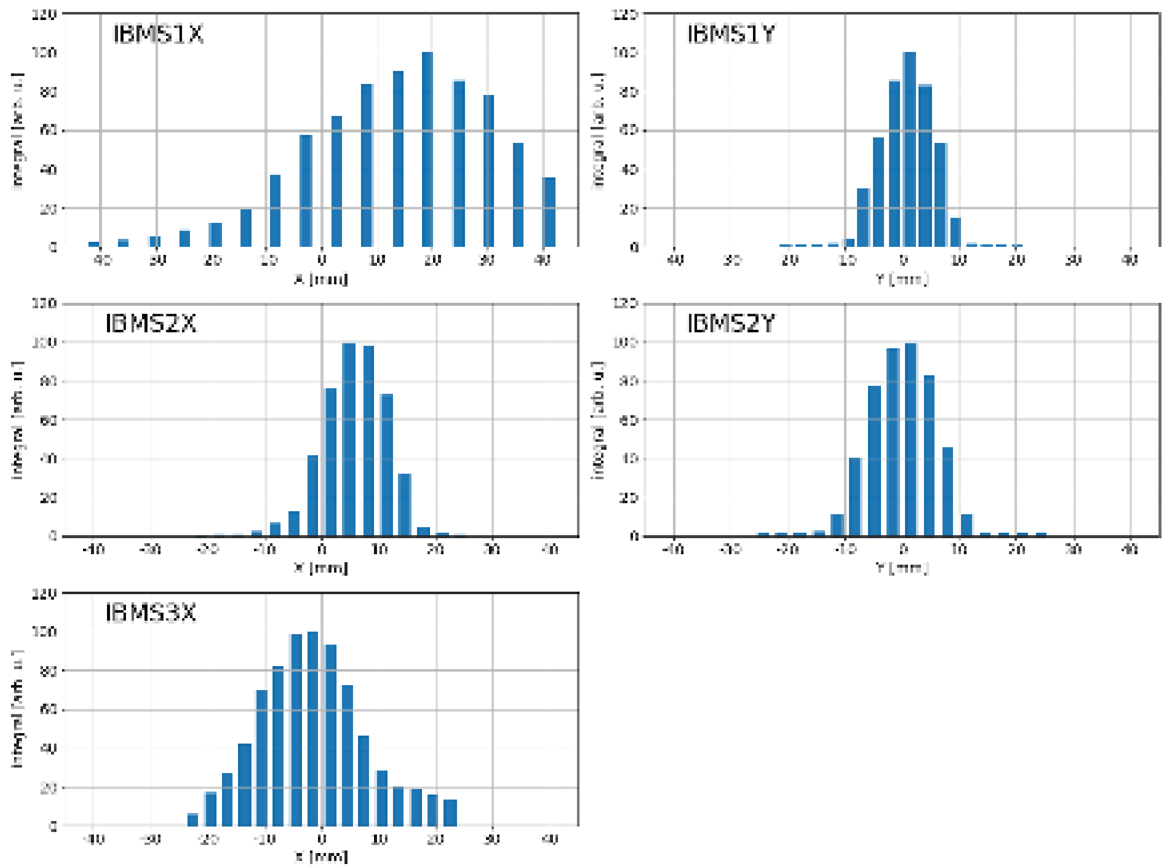

Figure 4.13-4. Spatial beam profiles for IBMS1, 2, & 3 during Run 2, as seen by incident beam. X (left) corresponds to radial profiles (+X = radially in) and Y corresponds to vertical profiles (+Y = up). Average spatial beam profiles are given by time integrals of the beam pulse for each fiber.

4.14 Temporal magnetic field tracking in the $g-2$ storage ring

M. Fertl, A. García, R. Osofsky, and H. E. Swanson

An important component of the $g-2$ calculation is understanding the magnetic field experienced by muons in the storage ring. The magnetic field in the storage ring is mapped using a suite of nuclear magnetic resonance (NMR) probes. An array of 17 probes is pulled around the ring in the "trolley" while a suite of 378 "fixed probes" are installed in the outer walls of the vacuum chambers, split between 72 evenly spaced locations ("stations") around the ring. The fixed probes are constantly monitoring the magnetic field, with every probe being read out approximately every 1.7 seconds. The trolley is pulled through the storage region, typically every three days, while reading out all probes every 0.5 seconds. Because the trolley cannot be present in the muon storage region while muons are present, the fixed probes must be used to track changes of the magnetic field (we call this "magnetic field interpolation").

As the trolley passes underneath each fixed probe station, the 17 trolley probes and 4 or 6 fixed probes sample the magnetic field at the same time and azimuthal location, and a calibration can be done, relating the fields measured by the two sets of probes. After this time, only the fixed probes can be used to track the field evolution at that location until the trolley passes underneath the station during the next full trolley run.

The basic magnetic field interpolation process is as follows:

1. Determine the time at which the sensitive regions of the trolley NMR probes are directly underneath the sensitive regions of the fixed probes at all stations.

2. Determine the magnetic field components measured by the trolley at this time.

3. Determine the magnetic field components measured by the fixed probes at this time.

4. Begin tracking changes of the magnetic field using only the fixed probes.

5. Make magnetic field predictions up until the time of the next trolley passing, when the prediction can be evaluated against the new measurement.

Interpolation is done for each fixed probe station individually, and then an azimuthally averaged magnetic field is predicted.

The magnetic field is described in terms of magnetic field multipoles. While the trolley is well suited to this type of expansion, the fixed probes are not. Instead, sums and differences must be used to track similar magnetic field moments. Additionally, the fixed probes, located at their 72 azimuthal locations, are not sensitive to local magnetic field changes throughout the full 360 degrees of the ring, but still must be used to track azimuthally averaged changes. Because the trolley measures the actual magnetic field in the storage region, times close to a trolley run have smaller associated uncertainties, whereas times directly between the trolley runs have the largest uncertainty.

For run 1 analysis, we concentrate on magnetic field tracking of the azimuthally averaged magnetic field components. Fig. 4.14-1 shows the tracking of the azimuthally averaged dipole magnetic field (the dipole field is the average magnetic field in the ring) between two trolley runs that were separated by 73 hours. The purple points represent the trolley measurements while the green points are predictions made using the fixed probes. The maximum uncertainty on the magnetic field is 135 parts per billion, while the average error is 105 parts per billion. As more data becomes available and we are better able to study how the field typically evolves, we expect the uncertainties to decrease, eventually to the 70 parts per billion level.

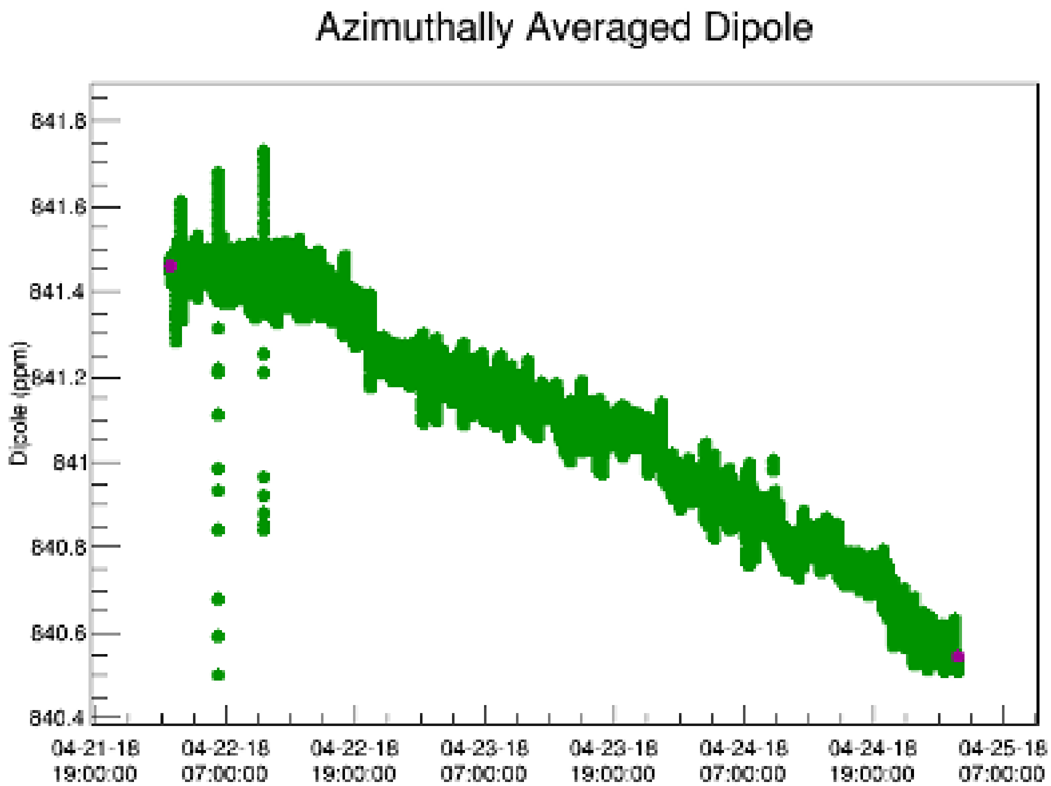

Figure 4.14-1. The magnetic field in the muon storage region is mapped approximately every 3 days by a "trolley" carrying an array of 17 NMR probes. The trolley is not allowed to be present in the storage ring at the same time as muons, so NMR probes embedded in the vacuum chamber walls are instead used to track magnetic field changes. Trolley measurements are shown in purple, while tracking using these external probes is shown in green. The spikes are real changes of the magnetic field, caused by improper usage of magnetic field hardware.

4.15 Monitoring the $g-2$ storage ring magnetic field with fixed probes

M. Fertl, A. García, R. Osofsky, and H. E. Swanson

The storage ring magnetic field is monitored by pulsed proton Nuclear Magnetic Resonance (NMR). The fixed probe system consists of 378 individual NMR probes located above and below the muon storage volume. They are spaced uniformly around the ring in 4 and 6 probe groups centered about the "magic" radius[1]. The probes and readout electronics follow the function and form used in the Brookhaven experiment E821 but were completely redesigned and constructed at the CENPA and Physics department

[1]Motional B fields from electrostatic focusing elements are cancelled for muons with momentum corresponding to this radius.

shops for the Fermilab measurement[1,2,3].

The system was operational for the entire Run 1 data set. Waveforms from all probes were acquired every 1.6 seconds and extracted frequencies were available in real time. This has since been reduced to 1.4 seconds and in subsequent runs we will make complete field measurements for each accelerator beam cycle. Individual probe resolutions depend on local field gradients but in most cases probes had fractional resolutions better than 70 parts per billion (ppb). A subset of probes is used to hold the dipole field constant by applying feedback to the magnet power supply.

The purpose of the fixed probes is to continuously track the storage ring field governing muon spin precession. Ideally, power supply feedback maintains the field average within its 15 ppb control band. However, the storage ring's response to the temperature environment and other drivers is not uniform and individual probes show large variations from the average as seen in Fig. 4.15-1.

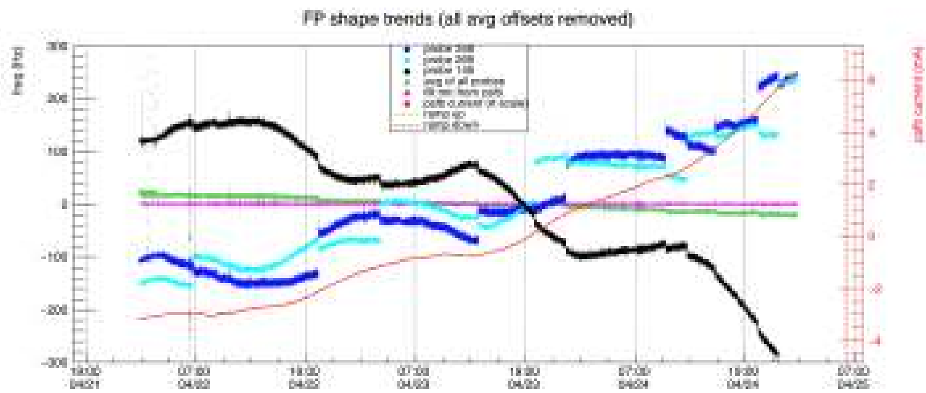

Figure 4.15-1. Field trends over the period of the 60-Hour data set. Magenta curve: feedback probe subset average, green curve: all probe average, red curve: power supply feedback to hold subset probe average constant, individual probe curves: from different azimuthal positions showing spontaneous field jumps. The full range of the plot is about ±5 ppm.

Run 1 was divided into a series of data sets. The 60-Hour data set coincided with a period of rapid warming of outside air temperatures, exceeding the capacity of the hall air conditioning to maintain a constant temperature. In Fig. 4.15-1 the red curve shows the power supply feedback current compensating for rising temperatures in the hall. The magenta curve at the center shows the constant average field from probes used for the power supply feedback. A malfunction in one of the ring subsystems resulted in spurious triggers for some of the probes and they had to be removed from the feedback subset. This skewed the azimuthal coverage, as shown by the slope of the green curve, which comes from the change in the average of all probes as temperature increases. To improve our immunity to these kind of events in the future we shielded the cable

[1]CENPA Annual Report, University of Washington (2018) p. 105.
[2]CENPA Annual Report, University of Washington (2017) p. 108.
[3]CENPA Annual Report, University of Washington (2016) p. 78.

carrying the trigger signals. The black and blue curves are fields from individual fixed probes in different parts of the ring that contribute to the green average. They also show spontaneous step changes in the field that vary in size around the ring.

Fig. 4.15-2 shows the magnitude of these field steps seen by the different fixed probes plotted against their azimuthal locations. Vertical lines correspond to positions of radial stops that constrain the geometrical shape of the superconducting coils. We believe stick-slip motion at these stops to be responsible for the field jumps. We have since enclosed the storage ring in an insulating blanket and are working to add additional cooling in the experimental hall to mitigate thermal effects as the summer season approaches. Field steps are still observed in the better insulated magnet.

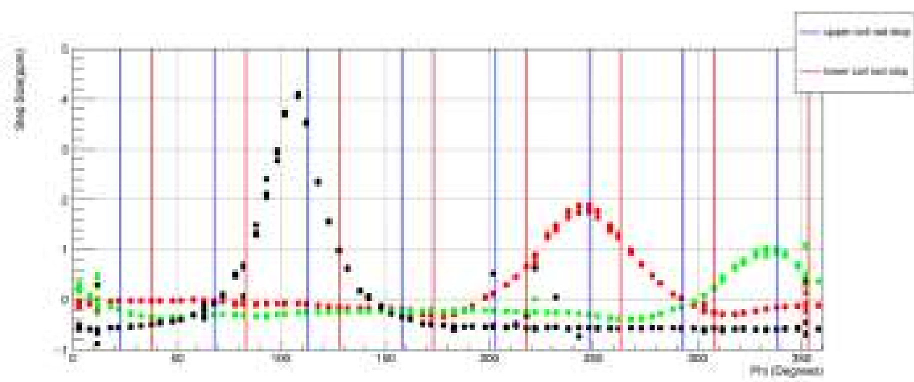

Figure 4.15-2. Spontaneous field jump magnitudes observed by the fixed probes are plotted vs. the azimuthal location of the probe. Vertical lines show the locations of radial stops associated with mounting fixtures for the superconducting coils. Epicenters of these step events occurred at 3 different azimuthal locations shown in different colors.

Field jumps are isolated events and their immediate regions can be cut from the measurement timeline. Other effects like field oscillations that come and go with time add to the noise in our measurement. Fig. 4.15-3 shows a typical example from one of the probes. They are observed at all azimuthal locations and would be even larger except for power supply feedback which reduces their amplitude to that seen here. We have not yet identified the source but they are well resolved with our measurement precision and contribute to our field measurement uncertainty.

Overall the fixed probe system has performed reliably over the first running period. We had to repair a few of the multiplexer units that switch between individual probes in the measurement sequence. This was done with in-house spares requiring very little down time in the measurement.

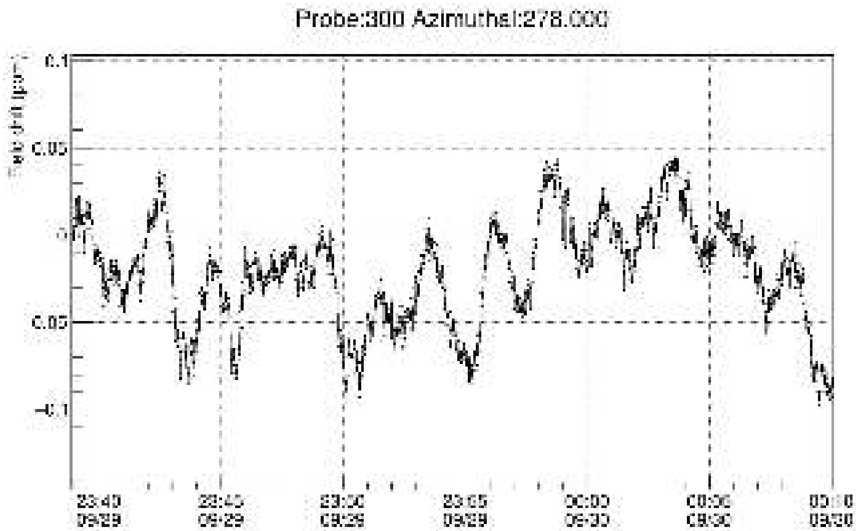

Figure 4.15-3. Field oscillations with an approximate 2 minute period are seen by all fixed probes. The figure shows the field from a typical NMR probe with peak-to-peak oscillations of 100 ppb.

4.16 Synchronizing magnetic field measurements with accelerator beam spills

D. A. Peterson, H. E. Swanson, and T. D. Van Wetchel

The storage ring magnetic field is continuously monitored by the fixed-probe system as described elsewhere in this report (Sec. 4.15). Hardware magnetometers generate $\pi/2$ excitation pulses and down-convert free induction decay (FID) waveforms to frequencies compatible with the waveform digitizers (WFDs). We designed and constructed a trigger module to control measurement sequences and interface with the data acquisition computer (DAQ). Latency in the computer's operating system does not permit precise measurement timing using only data acquisition code. The trigger module provides hardware equivalent timing precision and allows synchronization with an external clock, such as the super cycle start signal. Field measurements are sequenced using a Moore state machine implemented in an ACROMAG IP-201 FPGA module. A Moore state machine changes state on the rising edge of an internal 1 MHz clock, which determines the timing precision. Fig. 4.16-1 shows the state machine as a block diagram where each outlined block is one of the machine states.

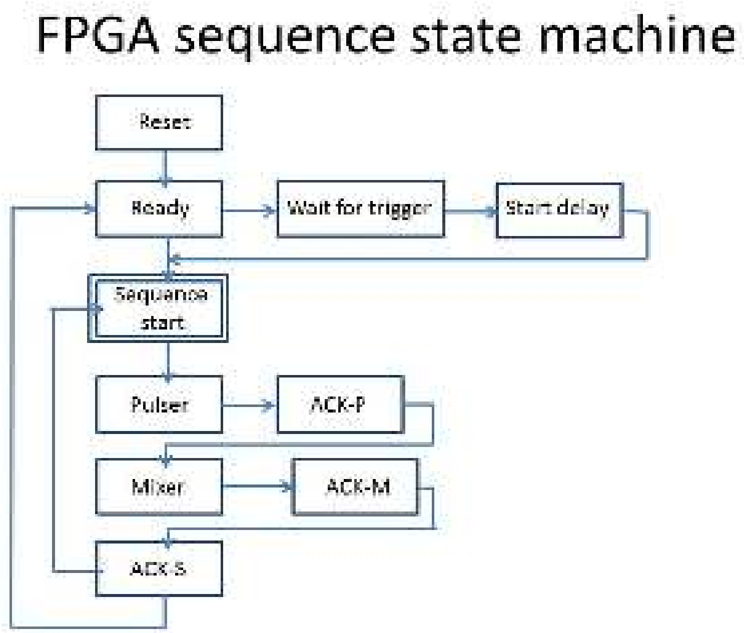

Figure 4.16-1. Diagram representing state machine for sequencing measurement triggers.

RESET	Starting state, initializes internal variables
READY	Branch decision point
*	Branch when an external trigger mode selected
WAIT FOR TRIGGER	Waits for external clock edge to proceed
START DELAY	Waits specified number of clock tics to proceed
*	Branch for measurement sequence
SEQUENCE START	Requires DAQ grant permission to proceed
PULSER	Issues $\pi/2$ and WFD trigger pulses
ACK-P	Acknowledge completion
MIXER	Waits specified number of clock tics to proceed
ACK-M	Acknowledge completion
ACK-S	Branch decision point repeat sequence or wait for external trigger

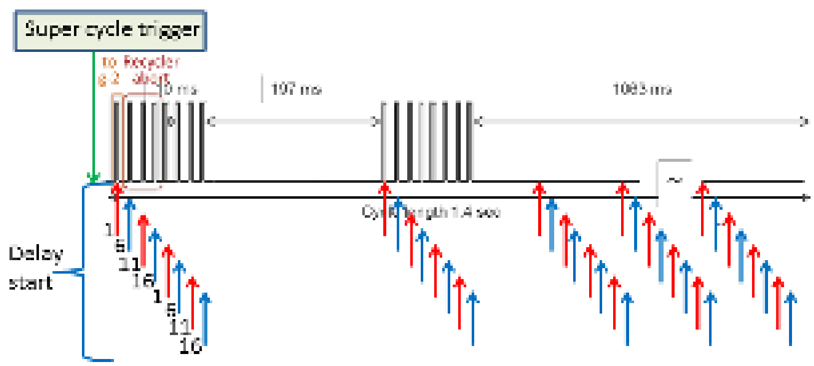

Figure 4.16-2. Timeline of the 1.4 second accelerator super cycle where muons come in two groups of 8 bunches shown by vertical black lines. The sequence in this mode starts after a specified delay and makes 5 equally spaced measurements coinciding with the first bunch in each group as shown by red and blue arrows. Each subsequent set of 5 measurements starts 10 msecs later in time coinciding with the next bunch in each group. This sequence continues for 8 cycles and repeats for the duration of the data run.

In a typical measurement scenario, the DAQ selects individual probes and grants permission to start a measurement sequence. The module sends trigger signals to the magnetometer hardware and WFDs to start a measurement. A timer pauses the sequence to wait for completion of the free induction decay. After digitizing the FID the DAQ reads out the waveforms and repeats the process for the next probe. The trigger module's timer is set for a period longer than it takes for the DAQ to complete this cycle so the measurement rate is determined by the trigger modules clock and not the DAQ. The module has 3 different operating modes that are selected from the DAQ.

Mode 1: the measurement sequence runs asynchronously with respect to the accelerator beam cycle, requiring only coordination with the DAQ for probe selection.

Mode 2: measurement sequences are synchronized with the accelerator beam cycle. The purpose of this mode is to make field measurements as muons are injected in the ring. Fig. 4.16-2 shows the supercycle timeline and the group structure of injected muons. The measurement sequence starts after a specified delay and makes 5 equally spaced field measurements coinciding with the first bunch in each group of 8 as shown by red and blue arrows. After completion of these 5 measurements, control returns to the ready state to wait for the next accelerator trigger. Each external trigger starts the measurement 10 msec later in time and coincides with the next bunch in each group. This sequence continues for all 8 bunches. All probes are sampled in 4 accelerator cycles and all bunches in 8.

Mode 3: as in mode 2, the measurement sequence is synchronized with the accelerator beam cycle. The sequence starts after a specified delay and continues until all probes are read. Data acquisition is fast enough to complete the process within a single accelerator supercycle.

Field measurements need to be made whether or not accelerator muons are in the ring in order to maintain a constant field through feedback of these measurements to the magnet's power supply. For synchronized modes, an internal clock with this same supercycle period triggers measurements in the absence of external accelerator triggers. In this case, measurements proceed by internal clock triggers until external triggers are available. The phase of the internal clock is then slowly shifted until it coincides in time with the external trigger at which point measurements proceed triggered externally.

5 Dark matter searches

ADMX (Axion Dark Matter eXperiment)[1]

5.1 Overview of ADMX

C. Bartram, T. Braine, R. Cervantes, N. Crisosto, N. Du, N. Force*, G. Leum, R. Khatiwada†, S. Kimes, B. LaRoque‡, L. J. Rosenberg, G. Rybka, and D. I. Will

The Axion Dark Matter eXperiment (ADMX) is a search for dark matter axions in the galactic halo via an implementation of Pierre Sikivie's axion haloscope.[2] The ADMX collaboration has operated a series of axion searches since the mid-1990s. The experiment has been located at CENPA since 2010. Since 2014, ADMX has undergone a series of upgrades, most notably the addition of a dilution refrigerator, to enter its "Gen-2" phase. As of April 2019, ADMX Gen-2 has completed and released the preliminary results of its second science run. The second run maintained its level of sensitivity to dark matter axions with the first run and showed improved operational performance of the refrigerator and other components. ADMX Gen-2 is preparing for a third science run in the next month using new quantum amplifiers and tuning rods to probe its next frequency range of axions, 780-1200 MHz.

The axion first emerged in the late 1970s as a consequence of a solution to the "strong CP problem." This problem arises from the need to unnaturally fine tune the Standard Model to account for an seemingly unnecessary conservation of the discrete symmetry CP (charge times parity) within Quantum Chromodynamics (QCD). The amount of CP violation in QCD is encoded in a phase θ which appears in the QCD Lagrangian. When θ differs from zero, QCD violates CP. Since the strong interactions appear to be CP conserving in the laboratory, θ must be very small. From measurements of the upper limit on the neutron electric-dipole moment, it is required $\mid \theta \mid < 10^{-10}$. However, in the Standard Model, CP-violation by weak interactions feeds into the strong interactions so that the predicted value of θ is of order unity. Peccei and Quinn put forward a solution to this problem in which the Standard Model is modified so that θ becomes a dynamical field and relaxes to zero, thus conserving CP in a more natural way.[3] The theory's underlying broken continuous symmetry dictates existence of a particle: the axion. The axion is the quantum of oscillation of this θ field

*Presently employed at Cytek Biosciences, Seattle, WA.
†Presently at Fermilab, Evanston, IL.
‡Pacific Northwest National Laboratory, Richland, WA.

[1] ADMX is supported by the DOE Office of High-Energy Physics and makes use of CENPA resources by recharge to the cost center.
[2] P. Sikivie, Phys. Rev. Lett. **51**, 1415 (1983).
[3] R. D. Peccei and H. R. Quinn Phys. Rev. Lett. **38**, 1440 (1977).

and has zero spin, zero electric charge, and negative intrinsic parity, allowing the axion to decay into two photons. The axion was then realized to be an ideal dark matter candidate over a certain mass range due to its weak couplings, long decay times, and other properties.

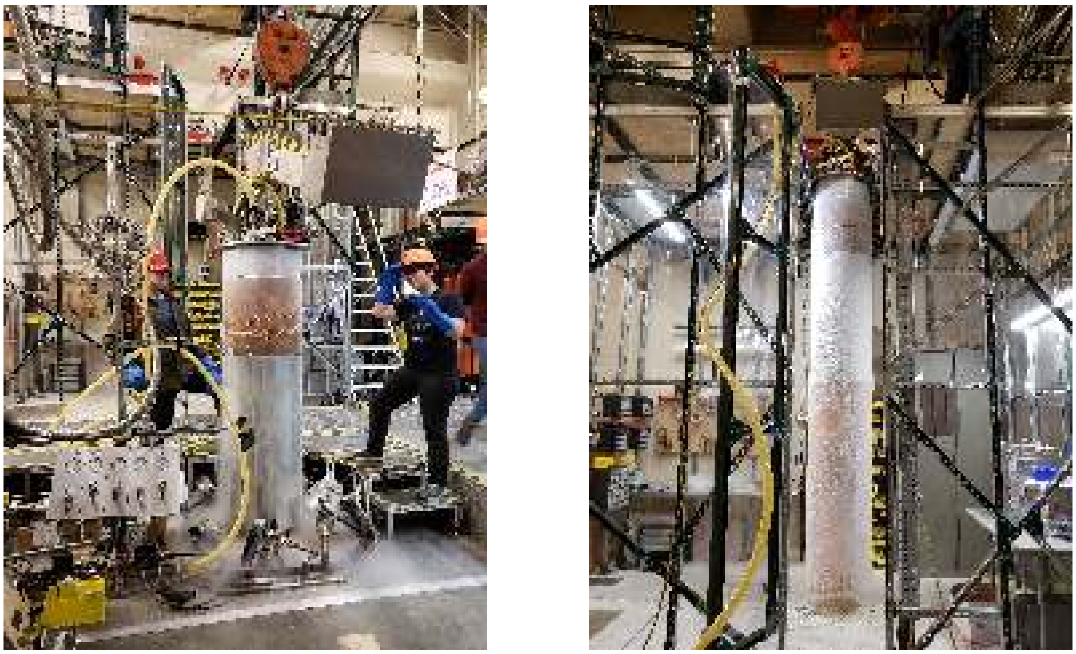

Figure 5.1-1. *Left*: The Cavity Insert being extracted after Run 1B November 2018. *Right*: The insert mounted in clean room after extraction.

ADMX operates by stimulating the conversion of local dark matter axions into photons via Primakoff conversion and detecting the resulting photons. Experiments and astronomical observations have since constrained the axion's mass to within a range in which the axion contributes a significant portion of dark matter. This mass range corresponds to microwave photons being produced in its decay. The aparatus consists of a large tunable microwave cavity, immersed in a static magnetic field (Fig. 5.1-1). The resonance of the cavity is tuned to search for axions of varying mass, enhancing conversion to photons within its resonant range. An RF receiver records the power spectrum of the cavity for each tuning configuration as ADMX scans in frequency. These power spectra are combined to reduce noise and probed for axion-like signals. Because of the axions' extremely weak electromagnetic coupling, the expected signal power is extraordinarily weak, around 10^{-22} W for the ADMX apparatus. The present ADMX collaboration is operating the first, and presently only, experiment sensitive to the DFSZ theoretical model of QCD dark matter axions.

ADMX is essentially an extraordinarily low-noise radio receiver with a tunable RF cavity forming a tuned resonance circuit. A short electric-field probe, an 'antenna', couples power from the cavity into a cryogenic quantum amplifier which is cooled to near the cavity temperature.

The dominant background in ADMX comes from thermal Johnson-Nyquist noise; the system noise temperature is the noise temperature of the amplifiers plus the temperature of the cavity. The motivation for lowering the system noise temperature is two-fold: (i) for a given axion-photon coupling, the frequency scan rate decreases by the square of the system temperature and (ii) for a given scan rate, the power sensitivity increases as the system temperature drops. To reduce the amplifier noise temperature, ADMX collaboration members developed superconducting quantum interference device (SQUID) amplifiers in the 100-1000 MHz range specifically for ADMX. This development allowed for more than an order-of-magnitude reduction in the system noise temperature. To reduce cavity temperature, as part of the fall 2014 Gen-2 upgrade, a dilution refrigerator was installed to reduce the cavity temperature to 100 mK over the previous 1.2 K pumped liquid helium system. The major Gen-2 upgrades were: the installation of a dilution refrigerator and supporting plumbing and infrastructure, a redesigned RF system including Josephson Parametric Amplifier, Traveling-Wave Parametric Amplifiers, and SQUID amplifiers, and substantial redesign of the thermal linkages and connections in the experiment to achieve the lowest possible operating temperature.

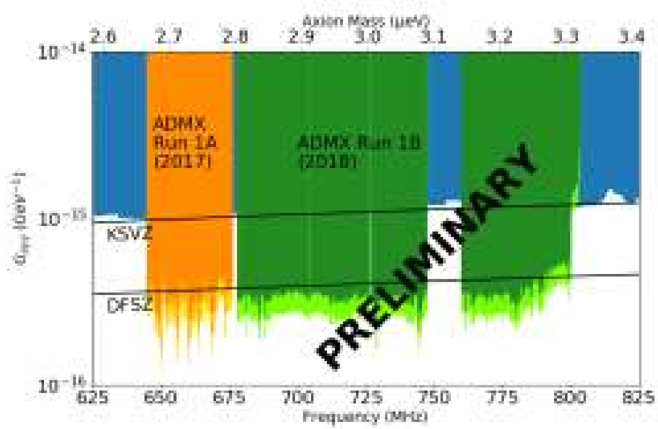

Figure 5.1-2. The preliminary limits of axion-photon couplings set by ADMX Gen-2 in its second science run in 2018 (Run 1B) and the official limits of 2017 Run 1A published March 2018. The limits were made assuming that axions composed 100% of dark matter in the universe. Four mode crossings were skipped over in Run 1B and can be seen as gaps in the plot, first in between Run 1A and Run 1B, the larger at 750 MHz, and the two small gaps around 700 and 725 MHz.

ADMX Gen-2 concluded its first science run in June 2017, searching for axions in a 645-680 MHz range with SQUID micro-strip amplifiers. In that range, axion-like signals were not observed, so instead, 90 % upper confidence limits were placed on the axion-photon coupling over the search range (Fig. 5.1-2). These limits excluded DFSZ axions between 645-676 MHz, representing the first time an axion haloscope has excluded axion couplings with DFSZ sensitivity. ADMX has become the only operating experiment to probe the DFSZ grand unified theory coupling for the axion[1].

ADMX finished its second data taking run in November 2018 using a combination of a Josephson parametric amplifier and SQUID amplifier to search a much larger range from 680-890 MHz. No axion-like signals were observed either, but the same upper confidence limits were placed and preliminary exclusion plots are including in this report (Fig. 5.1-2). The collaboration is in the process of getting these results published. It is worth noting, the magnet operated at a higher field of 7.6 T compared to 6.8 T in the first run. In addition, changes to the plumbing of the dilution refrigerator and the thermal linkages of the experiment allowed it to run with the mixing chamber at 100 mK, compared to 150 mK in the previous run. Together, these improvements enabled the experiment to probe for axions at a faster rate with more consistent sensitivity as seen in the plot. This was further demonstrated by several detections of synthetically injected axion signals by our operations team; the injections were blind, being coordinated behind the scenes by our blindness "Czar."

Currently, ADMX is preparing to begin a third data taking run using a combination of a Josephson parametric amplifier and traveling wave parametric amplifiers to search an even larger range from 780-1200 MHz. The dilution refrigerator and magnet will continue to operate with improved performance, however, because larger tuning rods will be used to shift the cavities' resonance to higher frequencies, volume contributions to the power signal will be reduced. We will still achieve DFSZ sensitivity levels this next run, but as the experiment approaches higher frequencies, multi-cavity arrays will be implemented to circumvent this issue. The current experiment in progress will tune up to 2 GHz, while development of systems up 4 GHz and R&D projects up 10 GHz are currently underway (Fig. 5.1-3). We emphasize that the collaboration is still in a position to discover the axion at any moment.

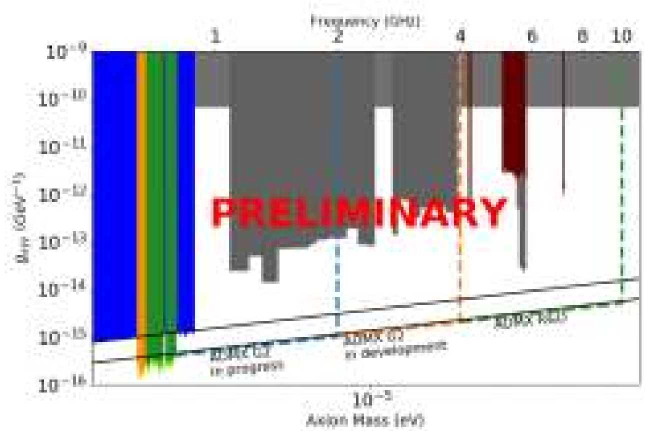

Figure 5.1-3. ADMX Gen-2 discovery potential limits compared to Run 1A (orange) Run 1B (green) and ADMX Gen-1 (Blue) limits on axion-photon coupling.

[1] N. Du et. al., Phys. Rev. Lett. **120**, 151301 (2018).

5.2 Higher-frequency axion searches with Orpheus

R. Cervantes, S. Kimes, P. Mohapatra, Y. Park, and G. Rybka

The ADMX Orpheus experiment aims to search for axion-like particles with masses approaching 100 μeV$/c^2$. Orpheus consists of a dielectric-loaded Fabry-Perot resonator. It operates at a high-order mode to increase the mass range while keeping the detection volume high. The open design reduces dissipation in the cavity walls, thus increasing the quality factor. Alumina lenses are placed every fourth half-wavelength in order to suppress the electric field that is anti-aligned with the magnetic field, increasing the resonator's coupling to the axion.

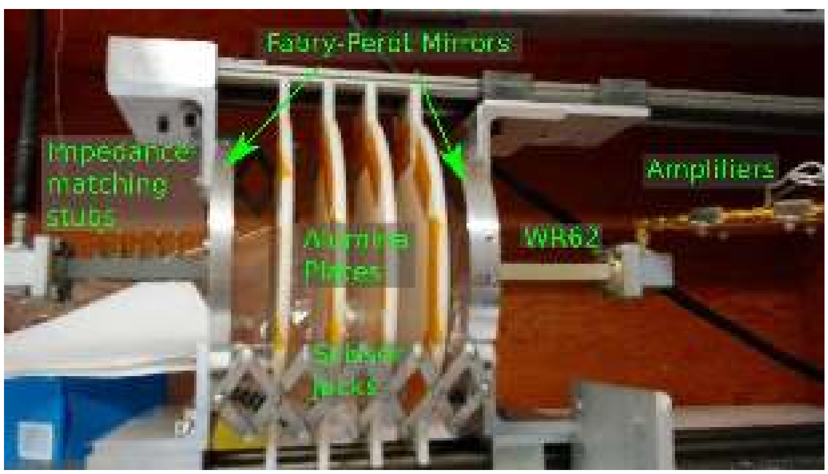

Figure 5.2-1. The table-top room-temperature Orpheus prototype. Four alumina plates sit between the Fabry-Perot mirrors. The scissor jacks adjust the alumina plates so that they are evenly spaced inside the resonator.

This year, we built a room-temperature, table-top prototype, as shown in Fig. 5.2-1. The resonator is designed so that the TEM_{00-18} mode (a fundamental gaussian mode with 19 half-wavelengths) couples to the axion. Each dielectric is placed at every fourth half-wavelength. Jack-scissors keep the dielectrics evenly spaced throughout the entire resonator while the resonator's length changes. Rectangular waveguides are attached to small apertures in the mirrors to allow coupling to the resonator.

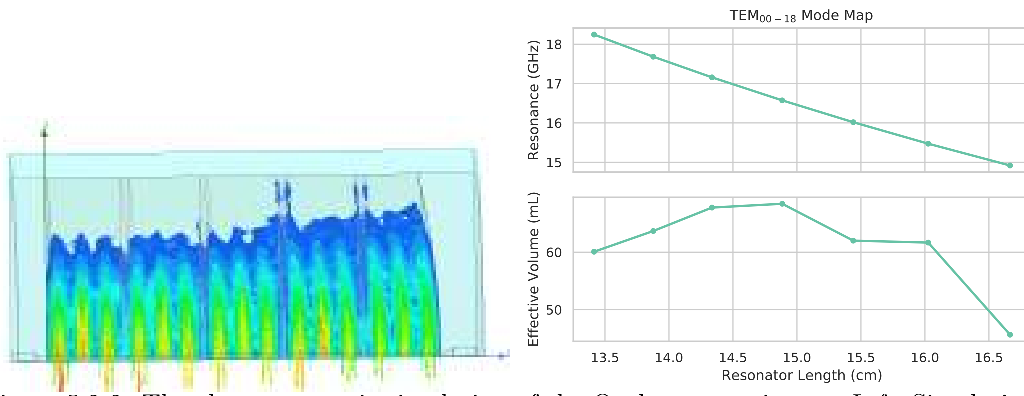

Figure 5.2-2. The electromagnetic simulation of the Orpheus experiment. *Left:* Simulation of the TEM$_{00-19}$ mode. An alumina plate sits at every fourth half-wavelength. *Right:* The resonant frequency of the simulated TEM$_{00-19}$ mode. The simulation is compared to an analytical prediction based on the resonances of an empty resonator, but with the physical length replaced by the optical length. For each simulated mode, the effective volume is calculated.

The TEM$_{00-18}$ mode of Orpheus was simulated using finite element analysis software (ANSYS HFSS). Both the resonant frequency and effective volume of the TEM$_{00-18}$ mode were simulated as a function of resonator length (Fig. 5.2-2). The effective volume is found to be about 60 mL. While 60 mL is about 2% of the resonator's physical volume, this is about 40 times the effective volume of a right-cylinder cavity with a 2-to-1 aspect ratio resonating at 15 GHz.

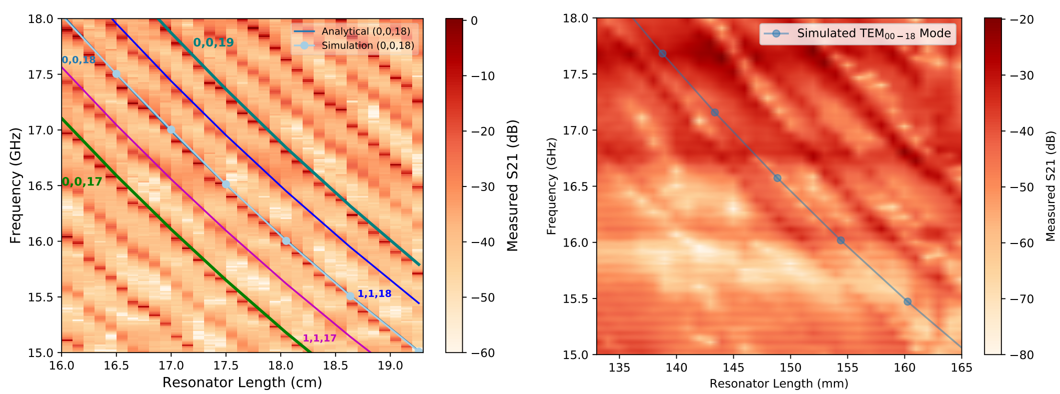

Figure 5.2-3. The transmission coefficient S_{12} vs the resonator length when the resonator is empty (*left*) and when there are four evenly-spaced alumina plates (*right*). Evidently, the resonant frequencies increase with decreasing resonator length, as expected. The resonant modes of the empty resonator agree well with those predicted from Gaussian modes. The Q of the modes fall between 2,000 and 10,000. The mode frequency of the dielectric-loaded resonator (*right*) do not agree with simulation, possibly due to a mismatch of dielectric constants. The Q of the modes are between 200 and 300.

We measured the transmission through the prototype to measure resonant modes vs.length (Fig. 5.2-3). The measured modes of the empty resonator agree with the analytical prediction and have a Q between 5,000 and 10,000. The modes of the dielectric-loaded resonator behave similarly to those of an empty resonator; the frequency tunes down with increasing resonator length. Unfortunately, the quality factors are about 300, making the transmission messier. The simulated TEM_{00-18} agrees with a resonance, although that resonance is faint.

Work is underway to improve the quality factor of the resonator. This goal can be achieved by more precise alignment of the dielectric plates and by cryogenically cooling the components.

DAMIC

5.3 WIMP search with DAMIC at SNOLAB

A. E. Chavarria, P. Mitra, and A. Piers

DAMIC at SNOLAB employs seven 16-megapixel, 40-g, $675-\mu m$ thick, scientific grade, silicon charge-coupled devices (CCDs) cooled to cryogenic temperatures and stored in a radio-pure environment (see Fig. 5.3-1). The low readout noise ($\sim$1.7 e^- per pixel) of the devices makes them sensitive to ionization signals caused by low mass (<10 GeV c^{-2}) Weakly Interecting Massive Particles (WIMPs) that recoil off of electrons or the Si nucleus. In December 2018, after a year of collecting data, we completed a 13 kg-day exposure of the DAMIC experiment. The analysis of this data expands on the previous DAMIC 0.6 kg day exposure presented in 2016[1].

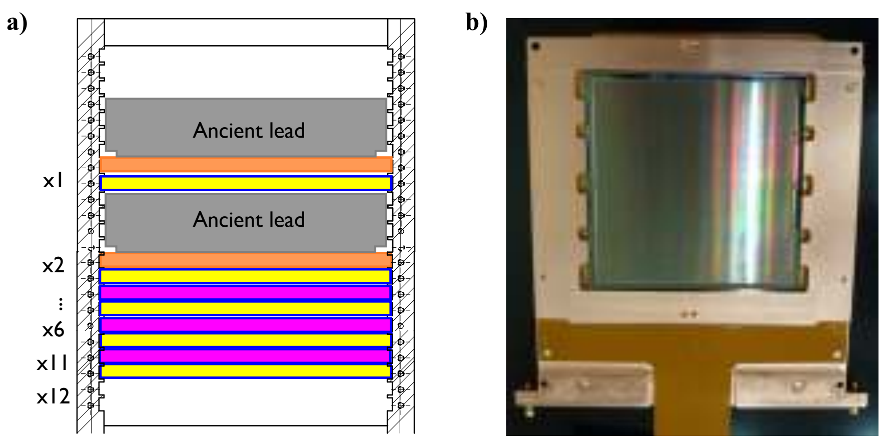

Figure 5.3-1. a) Arrangement of CCDs in DAMIC at SNOLAB. Each extension number (shown on the left) represents an individual CCD. b) Extension 1 CCD in an electroformed copper module.

[1] A. Anguilar-Arevalo, et al. Phys. Rev. D **94**, 082006 (2016).

In February, 2019, UW and CENPA hosted a two-week analysis workshop for the DAMIC Collaboration; researchers (pictured in Fig. 5.3-2) from the University of Chicago (USA), Laboratoire de Physique Nucléaire et de Hautes Energies (France), Subatech/IN2P3 (France), and the University of Washington (USA) attended the event.

During the workshop, we improved and unified the analysis chain on a subset of the SNOLAB data. We finalized the necessary data cuts, extended the radioactive background simulations to include additional species and locations of contaminants in line with the CCD manufacturing process, developed a robust spectral background mode, and integrated the individual analysis components to form a coherent and functioning analysis pipeline. With promising initial results from this dataset, we are working towards a final analysis of the fully unblinded data; this result will be presented in the summer of 2019.

Figure 5.3-2. DAMIC at SNOLAB Analysis Meeting. Clockwise from bottom: Alex Piers (UW), Dan Baxter (UC), Karthik Ramanathan (UC), Ryan Thomas (UC), Joao Da Rocha (LPNHE), Alvaro Chavarria (UW), Mariangelo Settimo (Subatech), and Roman Gaior (LPNHE).

5.4 DAMIC CCD testing and characterization

A. E. Chavarria, M. Kallander, P. Mitra, D. Peterson, A. Piers, and T. D. Van Wechel

DAMIC-M is the successor experiment of DAMIC at SNOLAB. Unlike its predecessor, DAMIC-M will use skipper charge-coupled devices (CCDs). These devices employ a different output stage to repeatedly, non-destructively measure electron-hole pairs in the silicon to achieve an unprecedented single electron-hole pair resolution. While the concept of a skipper CCD is not new, it has rarely been used. DAMIC-M will be the first experiment to use thick (675 μm) skipper CCDs with single-electron resolution and a very low dark current. It is the responsibility of the DAMIC team at CENPA to package the devices and to engineer the operational parameters to reach the target sensitivity and noise levels.

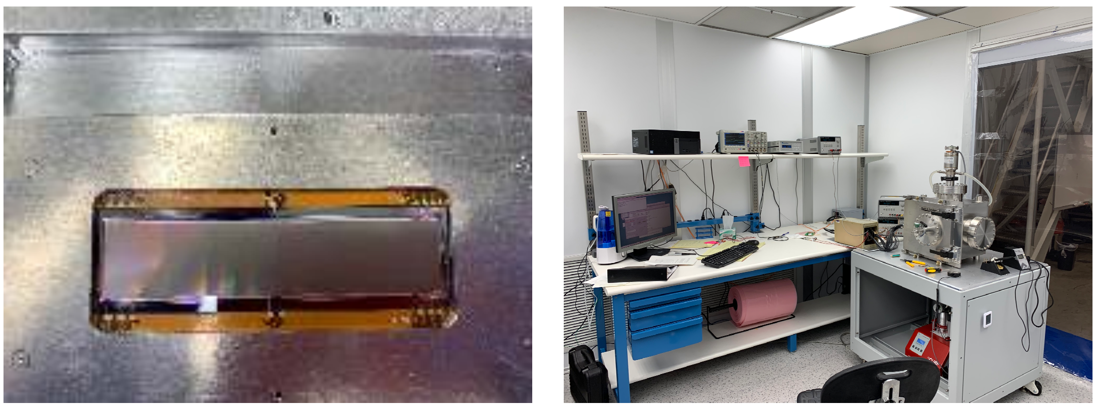

Figure 5.4-1. *Left*: A packaged skipper CCD. *Right*: The CCD testing station.

A laboratory in a cleanroom environment was set up at CENPA to fabricate, test and characterize CCDs. To package skipper CCDs, a station was set up inside the lab, complete with a wire bonding facility. A process was developed based on prior knowledge that had been refined and validated with CCDs from DAMIC at SNOLAB. The procedure was then tailored to the skipper CCDs, and four prototype skipper CCDs were packaged and tested. Fig. 5.4-1 (left) shows a packaged skipper CCD.

A test chamber was built to characterize the CCDs. The chamber consists of a cryostat from Kurt Lesker, a cryocooler from Ametek, and a CCD electronics control system from Leach. The test setup is shown in Fig. 5.4-1 (right). Second stage amplifier electronics boards were developed by David Peterson and Tim van Wechel at CENPA. The test setup is fitted with two resistance-temperature devices (RTD sensors). A control algorithm was developed to cool or heat a CCD package at 3°C per minute to bring a CCD down to the cryogenic conditions essential for its operation or up to room temperature for maintenance. The system is now operational and fully automated.

The first skipper CCD for DAMIC-M was installed in December 2018. A new algorithm to drive this type of CCD was developed, implemented and tested. The Leach system was re-programmed to automatically control the CCD readouts. Presently, a working skipper CCD, with serial number UW-1404S, is installed and is being used to test and improve the control algorithms, to study the dark current and noise patterns, and to take data with the aim of achieving a better understanding of these relatively new devices. A picture of particle tracks taken with a skipper CCD is shown in Fig. 5.4-2.

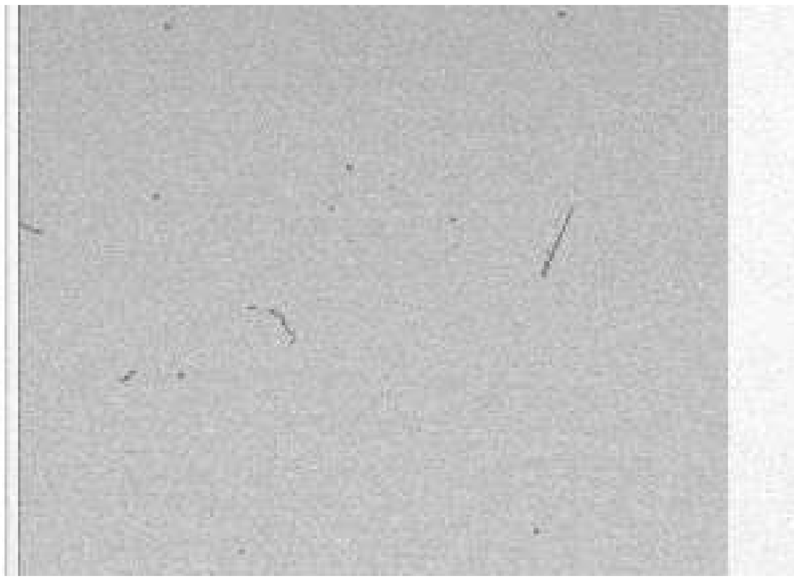

Figure 5.4-2. An image of particle tracks taken using a skipper CCD. The long track is a muon. The squiggly track is an electron. The dots are gamma-rays from a ^{241}Am calibration source nearby.

5.5 DAMIC-M detector design

J. Amsbaugh, A. E. Chavarria, M. Kallander, and A. Vellozzi

DAMIC-M is the next stage of the DAMIC program and will feature a tower of fifty CCDs with single-electron resolution to search for the interactions between dark matter particles and ordinary silicon atoms with unprecedented sensitivity. CENPA leads the design of the CCD tower and the prototyping of the CCD package, i.e., the support structure and cabling that service each of the CCDs. Fig. 5.5-1 shows a preliminary design of the CCD tower. Each CCD rests on a copper tray designed such that the devices can be stacked up. For mechanical and cryogenic testing, we are fabricating prototypes of the copper trays, including following the procedure of unrolling and flattening the copper that will be used for the ultra low-radioactivity electroformed copper of the final detector. We are also responsible for developing the procedure to package each of the CCDs, which must be shown to not introduce radioactive contaminants. We are in the process of evaluating the cleanliness of the procedure, and of implementing improvements to minimize the packaging time and mitigate the deposition of radon daughters on the CCD surfaces.

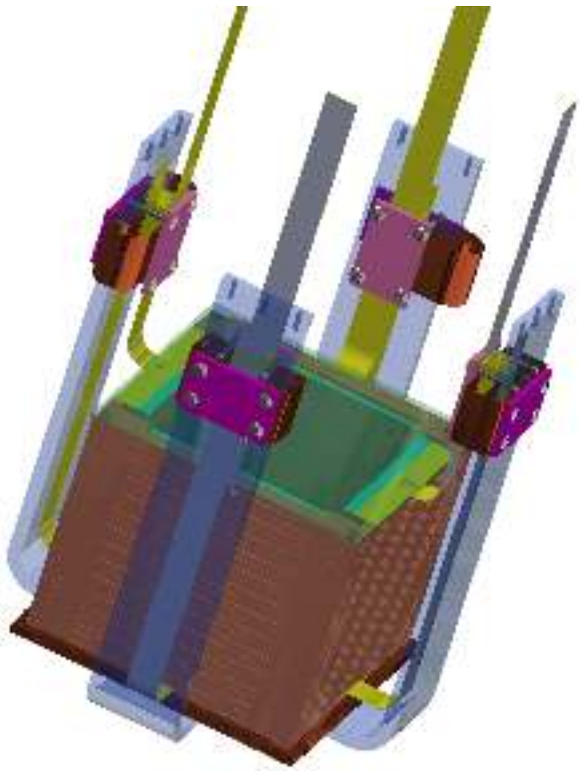

Figure 5.5-1. Evolving design of the DAMIC-M CCD tower.

5.6 Measurement of the activation rate of cosmogenic ^{3}H in silicon on the surface

J. Amsbaugh, R. Bunker*, A. E. Chavarria, S. Elliott†, A. Matalon‡, P. Mitra, A. Piers, P. Privitera‡, R. Saldanha*, R. Thomas‡, and H. M. Tsang*

Tritium (^{3}H) is produced as a spallation product in the interaction of cosmic-ray secondaries (mostly neutrons) with silicon nuclei in the CCDs. Due to its 12.5-year half-life, ^{3}H will accumulate in the CCD bulk during exposure to cosmic rays and then slowly decrease once the devices are deployed underground, with its decay producing low-energy electrons (Q-value = 18.6 keV). To mitigate this background, exposure to cosmic rays must be minimized. Preliminary estimates suggest that the total ground-level equivalent exposure of the silicon (including CCD fabrication) must be kept under two months to meet the radioactive background requirements for DAMIC-M. However, these estimates rely on an assumed activation rate of 80 atoms per kg of Si per day at ground level [1], which is highly uncertain. A more precise measurement of the surface activation

*Pacific Northwest National Laboratory, Richland, WA.
†Los Alamos National Laboratory, Los Alamos, NM.
‡University of Chicago, Chicago, IL.

[1] C. Zhang, D.-M. Mei, V.A. Kudryavtsev, and S. Fiorucci, Astropart. Phys. 84, 62 (2016).

rate of cosmogenic ^{3}H is necessary to properly plan for DAMIC-M.

The beamline at Los Alamos Neutron Science Center (LANSCE) provides a high neutron flux with an energy spectrum that reproduces the cosmic neutron flux but with an intensity 10^{8} times greater. Three 8-megapixel CCDs, identical to the ones used by DAMIC at SNOLAB, were successfully irradiated at LANSCE in September 2018 with 10^{12}–10^{13} neutrons through the CCD plane. Such neutron fluence should activate ^{3}H in the bulk of the CCD to a level of a fraction of a becquerel (Bq), which can be measured in the surface laboratory and then scaled by the relative neutron fluence to obtain the cosmogenic activation rate. Fig. 5.6-1a shows a CCD storage box in the LANSCE beamline prior to irradiation. Fig. 5.6-1b is an image acquired with one of the irradiated CCDs. The lighter background in the middle of the image corresponds to significantly higher leakage current in the irradiated region of the device, while the visible tracks are electrons from the β decay of activated isotopes or environmental γ radiation. Preliminary spectral analysis shows a significant excess above background in the irradiated region, consistent with the presence of activated ^{3}H and ^{22}Na isotopes. We are currently finalizing the analysis with data from the three CCDs to accurately estimate the surface activation rate of cosmogenic isotopes in silicon.

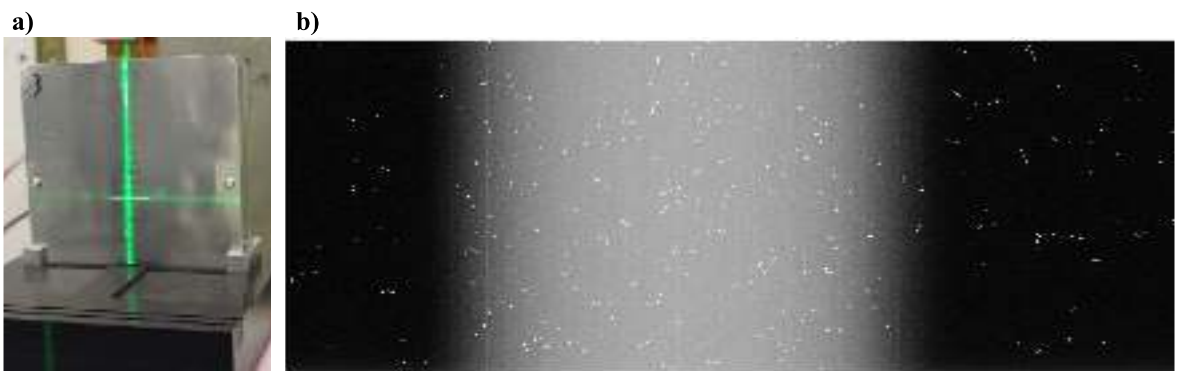

Figure 5.6-1. a) CCD storage box in the LANSCE beamline prior to irradiation. The green laser matches a cross on the CCD cover for alignment. b) Image acquired with one of the irradiated CCDs. Lighter background color corresponds to higher leakage current across the device. The white objects on the image are the ionizing tracks from fast electrons.

5.7 Search for photon emission following fast neutron-nucleus scattering at low energies

A. E. Chavarria, M. Kokoris, and X. Tang

The traditional approach to searching for weakly interacting massive particles (WIMPs) is to look for the signal of a recoiling atom following the elastic scattering of a WIMP with the atomic nucleus. Although this interaction mechanism is expected to dominate, kinematic considerations impose a maximum kinetic energy that can be transferred from the WIMP to the atom, which limits the strength of the observable signal, often driving it below the detection threshold for small WIMP masses. Recently, exotic subdominant interaction channels have been noted where either a photon or an electron is emitted together with the recoiling atom following the interaction [1]. In these cases, it is possible for the WIMP to transfer a much larger fraction of its kinetic energy to the target, leading to a stronger signal that can be detected.

We are looking at past neutron calibration data [2] to search for the emission of a photon following an interaction of a low-energy (<24 keV) fast neutron with a silicon atom. The goal is to determine if there is a statistically significant excess of spatially correlated events in the CCD images arising from this subdominant process. The first ionization event would be the signal of the atomic recoil and the second event, a few pixels away, would correspond to the photoelectron from the absorption of the photon. Fig. 5.7-1a shows the pattern expected in the CCD image from the subdominant process outlined in Fig. 5.7-1b. We considered the energies (E_1 and E_2) and spatial separation (s) between low-energy events in the images with and without the neutron flux. For each data set, we also generated the expected energies and spatial separations for uncorrelated events by constructing E_1, E_2 and s distributions after randomly redistributing the observed events throughout the images. We validated our analysis by restricting the energy of one of the events to the range 1.6 to 1.8 keV to select the silicon fluorescence K x-ray at 1.7 keV. In this case, the distribution of spatial separations showed a large excess at small values, consistent with fluorescence emission following a primary ionization event as outlined in Fig. 5.7-1c. We then performed the search for the subdominant neutron scattering channel by restricting the energy of one of the events to the range 0.1 to 0.5 keV, which corresponds to the observed energy of most atomic recoils [2]. A slight excess for distances of $\sim$5 pixels between events was observed. We are currently investigating its origin, including possible sources of instrumental noise and misidentification of event clusters by the image analysis code.

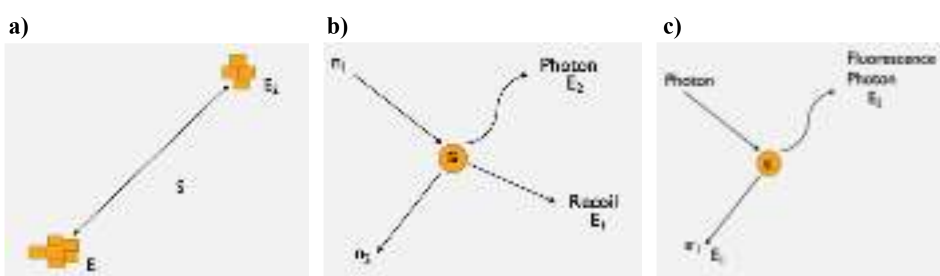

Figure 5.7-1. a) Events with energies E_1 and E_2 separated by distance s in the CCD images. b) Proposed subdominant channel where the scattering of a fast neutron off a silicon atom produces a photon. c) Known process of atomic fluoresce, which exhibits a similar topology to the subdominant channel of interest.

[1] C. Kouvaris, and J. Pradler, Phys. Rev. Lett. 118, 031803 (2017); M. Ibe *et al.*, J. High Energ. Phys. 03, 194 (2018).

[2] A. E. Chavarria *et al.*, Phys. Rev. D 94, 082007 (2016).

6 Education

6.1 Use of CENPA facilities in education and coursework at UW

J. R. Pedersen

CENPA continues to maintain a prominent role in a broad range of practical, hands-on training and education for both undergraduate and graduate students at the University of Washington. We provide a unique opportunity for students to participate in ongoing research and engineering, resulting in contributions to both local and off-site experiment collaborations.

Once trained, students utilize our experimental laboratories, electronics shop, student machine shop, and chemistry laboratories for their education and collaborative contributions. Complimented by mandatory safety training, students acquire a broad range of practical laboratory skills and knowledge, giving them an significant edge in both academia and industry (Sec. 6.3).

We've also sustained a continued presence in the UW curriculum since 2011, and currently offer an accelerator-based laboratory course in nuclear physics (Phys 575/576), titled "Nuclear Physics: Sources, Detectors, and Safety" (Sec. 6.2).

In addition to training and coursework, CENPA provides educational group tours for various classes, organizations, and schools. Most notable for this reporting period were tours given to participants of the Conference for Undergraduate Women in Physics (CUWiP) at the UW in January 2019 (Fig. 6.1-1).

Figure 6.1-1. CUWiP tour group visiting the TRIMS experiment (Sec. 1.5).

6.2 Accelerator-based lab class in nuclear physics

A. García, J. R. Pedersen, E. B. Smith, and D. I. Will

To provide accessible, hands-on education for working professionals, we have developed an evening graduate-level lecture and laboratory class to bolster nuclear physics knowledge in our local workforce[1] (Fig. 6.2-1). Focusing on relevant nuclear theory and practical techniques in nuclear physics experimentation, this class supplies both professional development for the growing aerospace and tech sectors, as well as a unique, hands-on learning environment for working professionals wishing to advance their careers.

Figure 6.2-1. Home page for CENPA's Phys 575 class.

Each student receives hours of experience using real nuclear physics equipment, utilizing our tandem Van de Graaff accelerator, an array of particle detectors, nuclear instrumentation electronics, and data acquisition systems (Fig. 6.2-2).

[1] Phys 575, Nuclear Physics: Sources, detectors, and Safety, http://faculty.washington.edu/agarcia3/phys575.

Figure 6.2-2. *Left*: Students viewing the gamma spectrum of a mystery radioactive source analyzed via a HPGe solid-state detector. *Right*: Students collecting RBS data from a 2 MeV proton beam scattering off of a mystery foil.

The class meets twice a week when offered, once for a 1.5 hour lecture and again in groups for a 1.5 hour lab session. The list of subjects covered are:

1. Atomic nucleus. Basics of nuclear physics, nuclear energy, orders of magnitude.
2. Attenuation of photon radiation. Solid-state detectors (Ge and Si).
3. Ranges of ions and electrons. The weak interaction. Radioactivity, radiation damage, and health risks (α, β, γ, and neutron activity).
4. Deciphering a mystery γ spectrum measured using a Ge solid-state detector. Gauging the level of radioactivity and assessing health risks.
5. 9 megavolt tandem accelerator function, duoplasmatron ion source function, and ion beam optics. Tuning beam through tandem accelerator.
6. Rutherford back-scattering (RBS) spectra measured by scattering accelerated protons off of foil targets and into Si solid-state detectors. Deciphering a mystery spectrum to determine the material contents of a mystery foil (Fig. 6.2-3 *Left*).
7. Fission and fusion. Basics of nuclear reactors.
8. Nuclear astrophysics: nucleosynthesis in stars.
9. Sources of positrons for positron emission tomography.
10. Resonance energy of ^{27}Al(p,γ)^{28}Si nuclear reaction determined by irradiating an aluminum target with accelerated protons and detecting the resulting γ's in a high purity germanium (HPGe) solid-state detector (Fig. 6.2-3 *Right*).

Figure 6.2-3. *Left*: RBS setup indicating 2 MeV protons (orange) incident on a thin foil target yielding back-scattered protons (green) detected in Si solid-state detectors. *Right*: ^{27}Al(p,γ)^{28}Si nuclear resonance setup indicating 1 MeV incident protons (orange) incident on Aluminum target yielding in resonance emission γ's (green) detected in an HPGe solid-state detector.

6.3 Student training

J. F. Amsbaugh, G. T. Holman, D. R. Hyde, J. R. Pedersen, D. A. Peterson, E. B. Smith, T. D. Van Wechel, and D. I. Will

CENPA provides students with training on equipment and best practices in our shops, chemistry laboratories, and experimental laboratories. Prior to that, students receive specific training in laboratory safety, which includes required UW provided in-person and online classes.

CENPA faculty and staff also provide hands-on student instruction in an array of laboratory technical skills and safety on topics ranging from CAD design, electrical power, compressed gases, cryogenic fluids (liquefaction, dispensing, delivery, and transport), lifting and rigging, vacuum technology, high voltages, high currents, high magnetic fields, nuclear instrumentation, radiation detection and measurement, and radioactive sources (Fig. 6.3-1). Completion of available UW provided online safety training is also required.

Figure 6.3-1. Undergraduate students Kate Evans and Axl O'Neal using one of CENPA's High-Purity Germanium (HPGe) gamma ray detectors to identify an unknown radioactive sample for their research project with the Institute for Nuclear Materials Management (INMM). The electronics, computer, and software used were recently acquired through a UW Student Technology Fee grant.

Our electronics shop is available for use by any trained students wanting to learn electronic design and assembly. Highly experienced staff members are available on-site to provide instruction in soldering, wiring, and the use of basic electrical and electronic components. Assistance in the use of Electronic Design Automation software for producing prototype Printed Circuit Boards (PCBs) is also available upon request. Additionally, training in the use of our UV ProtoLaser (purchased with UW Student Technology Fee funds) is given to any UW student wanting to fabricate prototye PCBs for research projects (Fig. 6.3-2 *Left*).

The CENPA student shop facilitates and encourages training for faculty, staff, and students in machine tool operation and safety. David Hyde provides instructional machining classes on a biweekly basis for all those interested. Faculty, staff, and students learn how to safely operate a variety of shop equipment, including lathes, milling machines, drill presses, saws, grinders, a metal sheer and breaker, hand tools, and various power tools (Fig. 6.3-2 *Right*). Additional instruction is provided for the use computer-aided fabrication machines for more complicated parts; namely our Southwestern Industries CNC milling machines (a TRAK KE 2-Axis and a TRAK DMPSX2P 3-Axis), along with our KERN HSE large format laser cutter system (also purchased with UW Student Technology Fee funds).

Figure 6.3-2. (*Left*): Undergraduate student Cedric Kong using CENPA's UV ProtoLaser for prototype PCB fabrication. (*Right*): Undergraduate student MinJung Sung using CENPA's TRAK KE 2-Axis CNC milling machine.

The long-standing unique history of teaching students how to operate our accelerator and ion sources remains a vital part of CENPA today. Graduate and undergraduate students receive instruction in the theory and practicalities of running our duoplasmatron ion source and 9-MegaVolt FN Tandem Van de Graaff accelerator (Sec. 7.2). This training incorporates both laboratory technical skills and safety through direct hands-on operation of the accelerator's equipment (Fig. 6.3-3). Students practice generating an ion beam, charging the Van de Graaff terminal to multi-MegaVolt potentials, tuning the ion beam through the accelerator, and transporting the beam to an experimental target. After receiving this accelerator operations training (a.k.a. "crew training"), these students are qualified to operate the ion source and accelerator for their research. They may also be called upon to serve as crew operators during 24-hour accelerator operations for other research experiments.

Figure 6.3-3. Undergraduate student Michael Huehn operating the tandem accelerator from the CENPA control room.

6.4 High-purity germanium detector

E. B. Smith

A high-purity germanium (HPGe) gamma detection system is now operational in RM 123A resulting from the culmination of multiple efforts at CENPA. The setup is shown in Fig. 6.4-1. The removal of hazardous wastes from RM 123A (formerly a photography dark room, and then PCB metal etching room), during the CENPA waste disposal event in January 2018[1], allowed for the wrecking out of all dilapidated counters and cabinets. Cleaning the walls and floors, painting the walls, and repairing the room exhaust ventilation fan, allowed for the relocation of a HPGe gamma detector, lead brick shielding “castle”, and electronic instrumentation cabinet previously in RM 106.

In parallel with the above work, a proposal was presented to the the Student Technology Fund (STF) committee for upgraded instrumentation and software for use with the HPGe gamma detector. The STF committee generously awarded the proposal[2]. the newly purchased instrumentation and software were installed in RM 123A in the FALL 2018 quarter.

Students from the UW Chapter of the Institute for Nuclear Materials Management (Sec. 6.3), CENPA undergraduate student research associates (CENPA hourlies), and CENPA engineering staff and faculty have been making use of the new RM 123A HPGe gamma detector system. The CENPA Atmospheric Monitoring group is now using this system for their surveying of air filters.

Figure 6.4-1. Images of HPGe setup, instrumentation, and display.

[1] CENPA Annual Report, University of Washington (2018) p. 127.

[2] `https://uwstf.org/proposals/2018/68`.

7 Facilities

7.1 Laboratory safety

B. W. Dodson, G. T. Holman, J. R. Pedersen, E. B. Smith, and D. I. Will

This year we have made significant improvements with safety, safety compliance tracking and facility access policy.

We manage our current users (we generally have 150 active staff, faculty, students, postdocs, visitors, etc.) in our online user list (also known as "telephone list"). Once added to the telephone, the use will gain access to training and access to facility via door code. General visitors, collaborators, etc. sign in/out at the front office and must be escorted. The following is the general order of events:

1. Safety orientation - prior to adding user to telephone list (and hence gaining door code), the supervisor must walk the new user around the facility pointing our evacuation, personal protection equipment (PPE), first aid, fire extinguishers, automated external defibrillator (AED) - mounted in front lobby, etc.
2. Both user and supervisor will then sign the orientation paperwork and we file that paper copy in front office.
3. Front office administrator then adds user (with photo) to telephone list on website. In addition, the signed orientation document is saved in the users personnel file.
4. All CENPA users must complete generalized training, while others need specific based on their lab hazards. These training requirements are selected on the web page for each user.
5. A scheduled weekly task checks safety completion compliance as follows.
    - For each user/uwnetid, a required-training user array (user_array)is created based on the per-user safety requirements.
    - The EH&S database is queried directly for uwnetid and pushed onto array stack (training_array).
    - For each entry (based on EH&S unique Master CourseID key) in (training_array), if it is in (user_array) that entry is removed from (user_array).
    - There is some data massaging, for example training is checked "if current".
    - The resultant array, is that user's required training still outstanding.
    - If (user_array) is not empty, an email is generated to user with list of outstanding training requirements.
    - If (user_array) is empty, training is completed and no email is sent to user.

Tunnel safety improvements

ADMX site operational safety has been recently upgraded based on recommendation from Fermi National Accelerator Laboratory (FNAL) and CENPA engineering personnel.

In preparation for ADMX magnet pull-out and the conclusion of "run 1B", the structural integrity of the clean room was assessed by a University of Washington structural engineer. Based on recommendations, the following reinforcements and precautions were implemented:

- Retrofitted clean room: increased number cross-braced channel struts, increased usage of corner brackets, and increased usage of bolts in diamond plates to clean room.
- OSHA rated roof anchors and signage for fall arrest lifelines were purchased and mandatory training completed by key personnel.

Cryogenic, pressure relief, and oxygen deficiency hazards (ODH) were assessed and appropriate signage was implemented in main entrances to Room 151 (tunnel) and ADMX site, tunnel-pit service alley, and ADMX compressor shed. Additional cyrogenic and pressure relief signage was added to room 151 liquid nitrogen fill stations, main ADMX magnet burst disk and vent chimney, and ADMX gas bag relief in the compressor shed.

Additional PureAire (part number: 99016) oxygen monitors were installed in the following locations:

1. Tunnel liquid nitrogen fill stations.
2. Tunnel-pit service alley near main magnet.
3. ADMX compressor shed.
4. Portable oxygen monitor used by personnel when working on top of clean-room (e.g. during ADMX pull-out and insert procedures).

A 90 dB alarm wired to several monitors (to be interfaced with ADMX cryogenic control panel for remote indication of ODH alarm) was installed with a 1-hour UPS battery backup in case of power disruption.

7.2 Van de Graaff accelerator and ion-source operations and development

B. W. Dodson*, H. T. Gorell, M. A. Huehn†, G. H. Leum, J. R. Pedersen, D. A. Peterson, S. S. Sexton‡, E. B. Smith, T. D. Van Wechel, D. I. Will, and S. P. Zaid§

This annual reporting period saw development, learning, and use of the duoplasmatron direct-extraction-ion source (DEIS) accompanied with an upgrade of the Tandem accelerator TERMINAL COMPUTER. We successfully implanted $^{21}Ne^{+}$ into Ta targets, learned important information about DEIS positive ion extraction, and presented all this information at SNEAP 2018 at the University of Wisconsin, Madison. The only entry into the Tandem accelerator allowed for the upgrading of the terminal computer, which is necessary for a temporary reconfiguration of the accelerator in 2019.

Much effort was spent understanding how to operate the DEIS in a positive ion extraction mode with the aim of not only implanting Ta targets of with $^{21}Ne^{+}$ for $^{21}Ne(p,g)$ experiment (reference Ne-21(p,g) article here), but of producing a body of knowledge about positive ion extraction that could aid and inform our efforts in the future. Using the same Intermediate Electrode (IE) (formerly called "plasma bottle nose") #3 (which was used for 2013 implants of $^{36}Ar^{+}$), a 50 mil diameter anode aperture, and +50 kV bias of the DEIS we achieved sustained $^{21}Ne^{+}$ implant currents of 44 nA for a 0.33"-diameter implant spot size. This setup was used to implant targets with 50 keV Ne-21+ to a density approximately 15% of the Ta atomic density. We developed a great deal of insight concerning positive ion extraction, which was presented at SNEAP 2018 and further summarized in the article by Brittney Dodson (Sec. 7.3).

The Tandem was opened for entry on November 11, 2018, and closed on April 16, 2019. This entry allowed for a complicated process of learning and new hardware testing that finally solved an issue in the TERMINAL COMPUTER (i.e. two Device Interface (DI) boxes with GROUP3 signal control/readback boards) with a failed ADC channel #1 on type C2 8-channel ADC board (S/N C2004) in DI0 (i.e. DI box at address 0) (see this section in 2018 Annual report). The replacement type C2 board (S/N C21029) could only be communicated with by DI Processor (PR) boards using newer revision EEPROM firmware than was presently installed in our system. Additionally, PR boards with newer revisions EEPROM do no support the legacy "Ninth Bit Binary" mode of fiber optic loop communication used by our system, but rather use the new SDLC mode. Fiber optics being necessary for LE GORDO computer outside the Tandem to communicate to TERMINAL COMPUTER inside the Tandem.

*Arrived July, 2018.
†Arrived November, 2017.
‡Departed August, 2018.
§Arrived June, 2017.

Full functionality of the TERMINAL COMPUTER was finally achieved by doing the following:

1. Install new C2 board (S/N C21029) in DI0 box.
2. Install new version "DI V5.0i 17-DEC-2018" EEPROM in DI0 PR board (S/N PR030) and DI1 PR PR board (S/N PR093).
3. Obtain and install a new GROUP3 fiber optic loop control board (LC1-ISA) (S/N LC1011) with newer revision "LC V5.0d 09-NOV-2001" EEPROM in the LE GORDO computer in place of the previous LC1-ISA (S/N LC1009).
4. Remove the version "S2" processor chip from the previous LC1-ISA (S/N LC1009) and install it on DI1 PR board (S/N PR093) in place of the "pre S2" version processor chip, because newer PR board EEPROM (step 3) requires version "S2" processor chip.
5. Set the COMM mode of PR boards in DI0 (S/N PR030) and DI1 (S/N PR093) to SDLC to match LC1-ISA (S/N LC1011) in the LE GORDO computer.
6. Edit LE GORDO MS-DOS based Turbo C++ control program, HOWE.EXE, to select COMM mode=0 for SDLC and recompile (The baud rate was left at 288K, which was needed for "pre S2" processor chip, but not really needed anymore).

TERMINAL COMPUTER full functionality allows for the upcoming reconfiguration of the Tandem to TERMINAL Ion Source (TIS) mode, so the Tandem remains open for that procedure.

During the annual reporting period from April 1, 2018, to March 31, 2019, the tandem pelletron chains operated 126 hours, the sputter-ion-source (SpIS) operated 0 hours, and the DEIS operated 491 hours. Additional statistics for accelerator operations are given in Table 7.2-1. Tandem accelerator produce beams of ions originating from the DEIS included 17.8 MeV $^{2}H^{+}$ for the ^{6}He experiment, 1.0 MeV $^{1}H^{+}$ for the $^{21}Ne(p,g)$ experiment, and 15.2 MeV $^{2}H^{+}$ for visiting experimenters.

ACTIVITY SCHEDULED	**DAYS SCHEDULED**	**PERCENT of TIME**
Nuclear-physics research, accelerator	15	4.1
Ion implantation	5	1.4
Development, maintenance, or crew training	54	14.8
Grand total	74	20.3

Table 7.2-1. Tandem Accelerator Operations April 1, 2018, to March 31, 2019.

7.3 Extracting $^{21}Ne^+$ ions from a duoplasmatron for target implantation

B. W. Dodson, J. Pedersen, E. Smith, and M. Sung

$^{21}Ne^+$ ions extracted from the duoplasmatron direct extraction ion source (DEIS) (Fig. 7.3-1) were implanted into tantalum targets (Fig. 7.3-2) for an experiment studying the angular distribution of $2_1^+ \rightarrow 3_1^+$ photons from the $^{21}\mathrm{Ne}(p,\gamma)^{22}\mathrm{Na}$ resonance reaction[1]. Additionally, in an effort to reduce intermediate electrode (IE) canal sputtering caused by such heavy ions, an IE with a molybdenum-lined canal was fabricated, and its affect on extracted ion source current measured and analyzed.

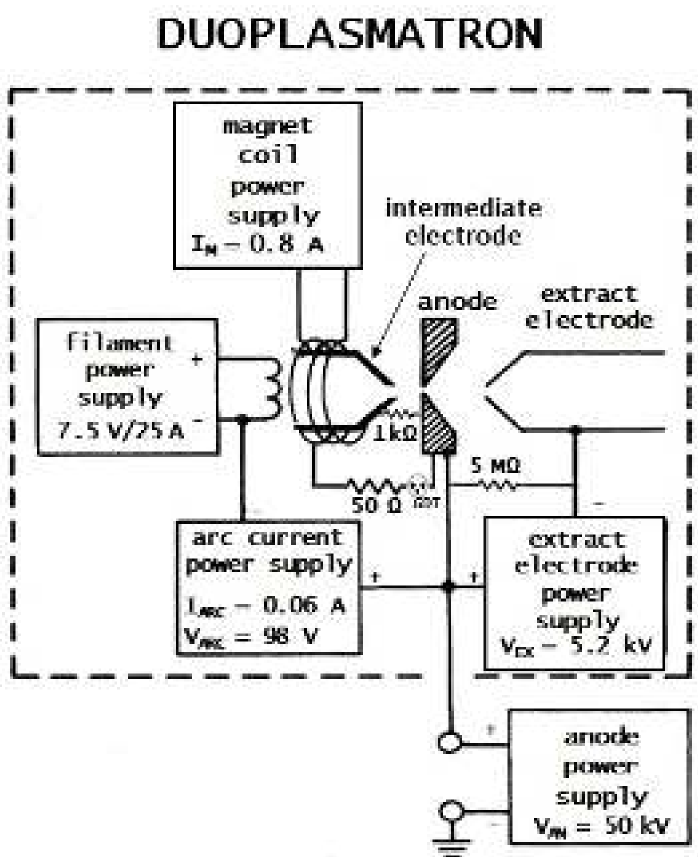

Figure 7.3-1. Duoplasmatron DIES schematic.

[1] CENPA Annual Report, University of Washington (2018) p. 53.

Figure 7.3-2. $^{21}Ne^{+}$ion implanted target.

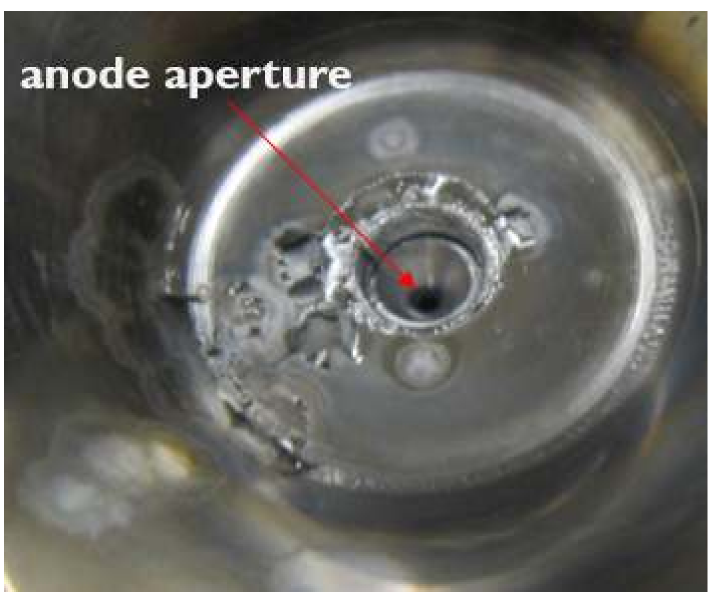

Figure 7.3-3. Back side of anode electrode with aperture indicated, and showing re-deposited steel (flaking metal) sputtered from IE canal.

Initially, we were unable to obtain sufficient beam current for ion implantation to the desired density within a reasonable time. Simply increasing the anode aperture diameter (Fig. 7.3-3) from 0.035” to 0.050” produced 15X increase in beam current. Ultimately, through carefully documented parameter tuning, a $^{21}Ne^{+}$ beam current of 45 nA at 50 keV produced implantation of two targets, each to 15% of tantalum atomic density. The steel IE used during these implants had a 120 mil diameter canal that was not molybdenum-lined.

The steel of the IE 120 mil diameter canal walls is sputtered by the extracted ions and re-deposited throughout the DEIS system. The deposits on the back side of the anode electrode, which faces the extract electrode, can produce metal flaking (Fig. 7.3-3) and electrical shorting of the anode and extract electrodes. To combat this, we fabricated a steel IE with the standard 120 mil diameter canal opening with a 10 mil thick molybdenum (Mo) lining (inner diameter of the molybdenum lining in still the standard 120 mil) which should reduce canal sputtering, since molybdenum is know to be more resistant to sputtering than steel.

However, molybdenum is non-magnetic, so we performed detailed study of the positive ion beams produced by all-steel IE (i.e. canal not lined with Mo) and the steel IE with 10 mil thick Mo lining. First, we measured extracted beam current versus DEIS plasma ARC current for various magnet coil currents (Fig. 7.3-4), which demonstrated the position of maximum extracted beam current for a given magnet coil current moved to higher ARC currents as the magnet coil current was decreased. This behavior agrees with duoplasmatron ion source theory and other researchers’ results when it is understood that the magnet coil current is directly proportional to the magnetic field in the canal, and in the region between the canal and anode.

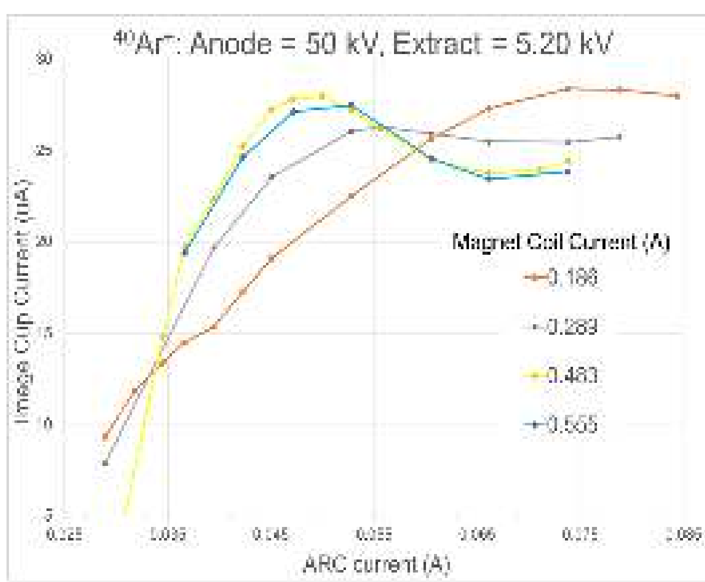

Figure 7.3-4. Maximum beam current occurs at higher ARC currents for decreased magnet coil currents (i.e. decreased plasma magnetic field).

Next, we measured the maximum beam current versus ARC current at various magnet coil currents while using the all-steel IE ("IE w/o Mo insert") and the Mo-lined canal ("IE w/ Mo insert") (Fig. 7.3-5). The position in ARC current where maximum beam current occurs for a given magnet coil current occurs at increased ARC current for "IE w/ Mo insert" compared to "IE w/o Mo insert". Therefore, the "IE w/ Mo insert" demonstrates a reduced magnetic field in the canal and in the region between the canal and the anode, which makes physical sense.

It appears that similar amounts of beam current can be extracted with both "IE w/ Mo insert" and "IE w/o Mo insert" while expecting less sputtering of the "IE w/o Mo insert" canal. Reduced sputtering would allow an IE to be used longer before any shorting issues occur, so the "IE w/o Mo insert" may be better to use for heavy ion implants such as Ar and Ne.

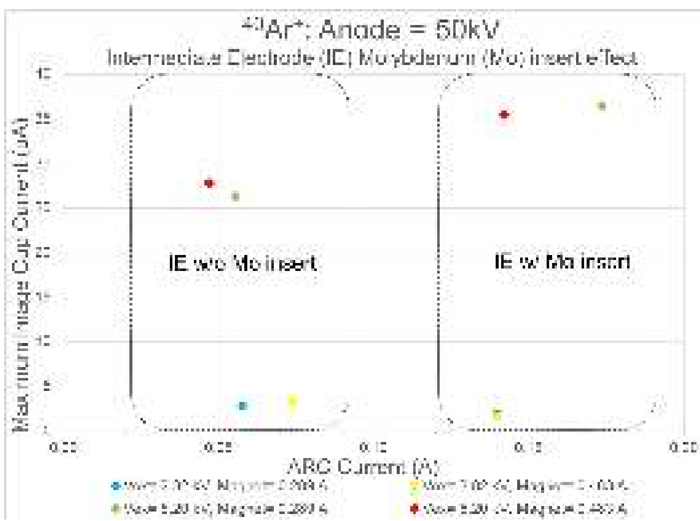

Figure 7.3-5. Maximum beam current occurs at higher ARC currents for "IE w/ Mo insert".

7.4 Laboratory computer systems

G. T. Holman

CENPA is a mixed shop of Windows 7, 10, Mac OS X, and various Linux distributions. Windows 10 is installed on new workstations, but we are still running some Windows XP systems for data acquisition, DOS 6 on accelerator controllers, and an embedded Win 98 for a mechanical shop mill. As with every year, the IT focus was directed toward server consolidation, network security, process documentation and removal of redundant processes. We continue to utilize Xen virtualization for Autodesk Vault versions, ELOGs, wikis, collaboration calendars, and document servers. The CENPA website and research group web pages run on a Drupal 7 web framework. The NPL mail server still provides NPL presence but all email is relayed to UW e-mail hardware.

Workstations connect to the UW delegated organizational unit (OU), which mostly removes the need to run a dedicated domain or LDAP server.

Two Dell 510 20-TB servers (Lisa and Marie) continue to offer user storage, print server capability, and improved backup policy. Linux, Windows, and Mac workstations are backed up to the 20-TB Marie raid farm, which is backed up offsite using UW Trivoli backup service. Lisa runs the Crash Plan Pro backup application which supports all operating systems and provides differential and encrypted backups. Whereas workstations rely on Crash Plan Pro for backups, all servers utilize rsnapshot. Marie provides 20 TB for research, user, and shared group data.

The NPL Data Center (NPLDC) provides legacy infrastructure supporting high-performance scientific-computing applications.

The Athena cluster was upgraded to Rocks 7 with new hardware acquired new servers from the National Energy Research Scientific Computing Center (NERSC) (Sec. 7.5).

7.5 Athena metamorphosis to cenpa-rocks

G. T. Holman and D. J. Prindle

We have incorporated the old PDSF hardware donated to us by NERSC into our rocks cluster. Before adding the new nodes we upgraded the cluster management software to rocks 7.0 and we renamed the cluster cenpa-rocks. The new compute nodes came in two configurations. The first set of 35 nodes have 12 cores and 48 GB of RAM per node. The second set of 55 nodes have eight cores and 24 GB of RAM per node. We have kept 47 nodes from the Athena cluster. These have eight cores per node and had 8 GB per node but we transfered memory from retired nodes so now they all have 16 GB of RAM per node. Some of the Athena nodes are showing memory issues and typically are dropped from the SGE batch management. A few of the eight core nodes from NERSC are also failing with various issues. We can recover some of these nodes but typically we have about 15% of possible cores down. Still we usually have over 1000 cores available, with two, three or four GB of RAM per core.

We did not get any hard drives from NERSC, we managed to find enough hard drives at UW to put at least one into each compute node, which is required by rocks. The majority of these drives are 136 GB. The operating system takes about 30 GB leaving 100 GB of local storage for compute jobs. We have several TB of extra disks which we plan to distribute among the compute nodes and install an xrootd server to manage them.

In addition to compute nodes we recieved four DELL R710 servers with hardware raid cards that control MD1200 storage enclosures. Each of these enclosures has space for 12 hard disks (we have 16 of these enclosures). Currently we have two raid 6 systems with eight 8 TB drives each. To be able to use 8 TB drives we had to upgrade the firmware of the hardware raid controllers. We have managed a transfer rate of 300 GB/s from the raid disks to the compute nodes. This is adequate for analysis jobs that do heavy processing but for some of our jobs this data transfer rate limits the number of useful nodes.

We have installed software packages requested by users, including GEANT, root, cmake, the GNU Scientific Library and python 3.6. The nodes that drop out because of hardware issues have all been automatically dropped by SGE so they have not been causing problems for batch jobs and overall the cluster has been running stably. We have had to shut the cluster down a few times, once for power issues and once for cooling issues. Both times the cluster has restarted with minimal intervention.

7.6 Electronic shop

D. A. Peterson and T. D. Van Wechel

The electronics shop is responsible for the design and construction of new laboratory electronic equipment as well as the maintenance and repair of existing CENPA electronics. Some highlights of projects undertaken by the electronics shop in the past year include the following:

1. The design and construction of custom electronics for the CAGE detector (Sec. 1.13) that is being assembled for the LEGEND collaboration has begun.
2. Continued development and testing of a charge sensitive preamplifier with forward biased reset for the LEGEND collaboration. This is now referred to as the Forward-biased JFET-based Option for Research and Development (FJORD) (Sec. 1.14).
3. The electronics shop assisted in the design and construction of amplifier boards used for the characterization of silicon photomultipliers (Sec. 1.15) for LEGEND.
4. The design and construction of electronics for the Project 8 collaboration (Sec. 1.18), including an nuclear magnetic resonance (NMR) Probe multiplexer, an adjustable-current source and a cold-head supervisory unit.

Figure 7.6-1. Project 8 cold-head supervisory unit board.

5. For the ^{6}He-CRES experiment a shim heater controller has been constructed for the AMI magnet (Sec. 3.1).

Figure 7.6-2. ^{6}He-CRES shim heater controller.

6. Completion of the design and construction of the silicon photomultiplier (SIPM) amplifier boards and other support electronics for the third inflector beam monitoring system (Sec. 4.6) (IBMS3), for the $g - 2$ experiment.

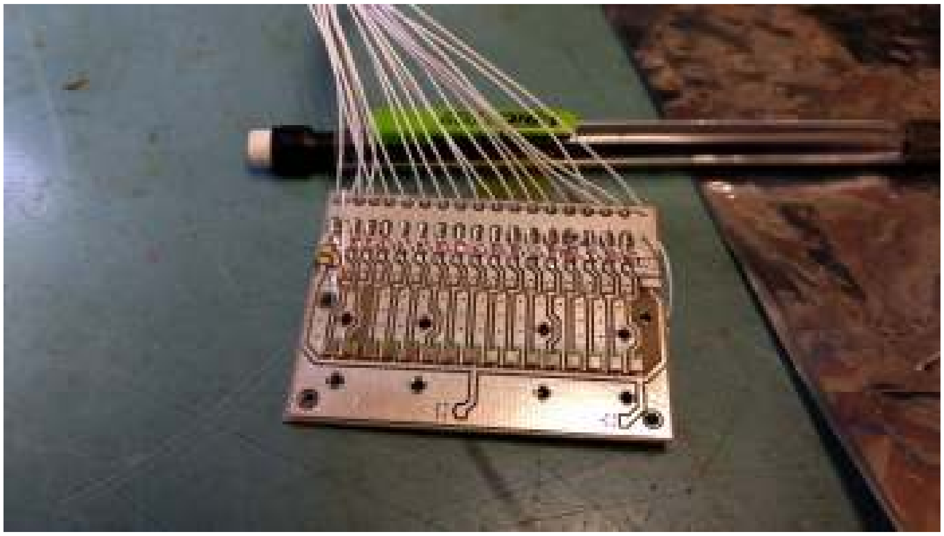

Figure 7.6-3. IBMS3 SiPM board.

7. The design has been completed and construction is underway of the angular encoder readout electronics for the gravitational calibrator (Sec. 2.1) for deployment at the LIGO Hanford Observatory.
8. Amplifier boards were designed and constructed for the testing and characterization of CCDs for DAMIC-M (Sec. 5.5).

Figure 7.6-4. DAMIC SiPM board.

7.7 Instrument Shop

T. H. Burritt and J. H. Elms

The CENPA Instrument shop is manned by highly skilled instrument makers with decades of experience working in the research environment. Tom Burritt supports faculty, staff and students, give advice and suggestion and make sure what they want is feasible and cost effective. Designing and fabrication of ultrahigh vacuum systems cryogenic components equipment operating in high magnetic fields, high and low voltage applications, hydraulics, gas handling systems and mechanical devices. Jim Elms is primary CNC operator wizard, welder and mechanical genius. Together we solve mechanical problems and give CENPA the ability to be a leading force in Physics. In addition to supporting CENPA we also machine parts for other groups at the University the Astronomy department has asked for our help to get parts made for them. This year we purchased a vacuum chuck to hold down material for thin part machining. Some notable fabrications are shown in the images below.

DAMIC

Figure 7.7-1. *Left:* Detector fixtures machined with mirror finish. *Right:* Detector boxes and covers.

$g-2$

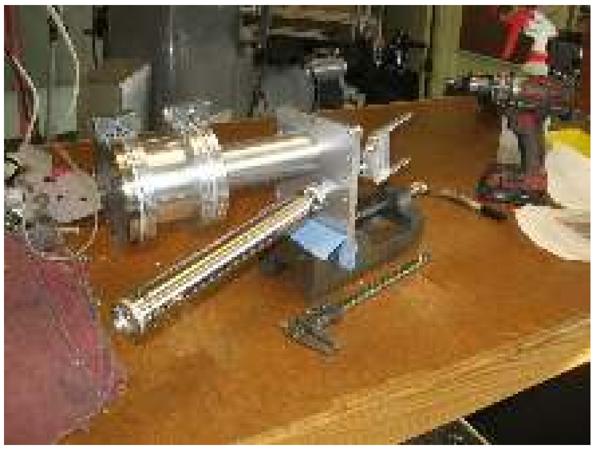

Figure 7.7-2. Designed and fabricated non-magnetic linear-vacuum flange.

Project 8

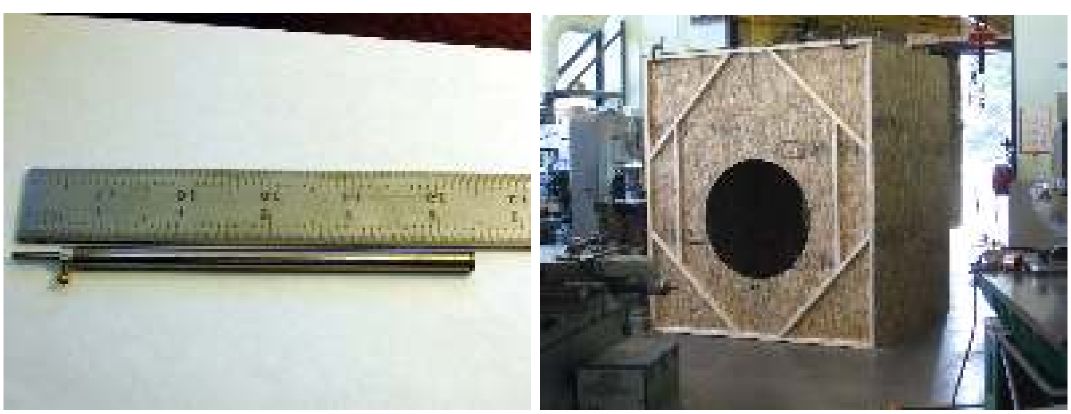

Figure 7.7-3. *Left:* We researched e-beam welding of pure tungsten rods. *Right:* Sound containment box constructed using non-magnetic materials to be installed around the MRI setup of the super-conducting magnet.

^{6}He-CRES

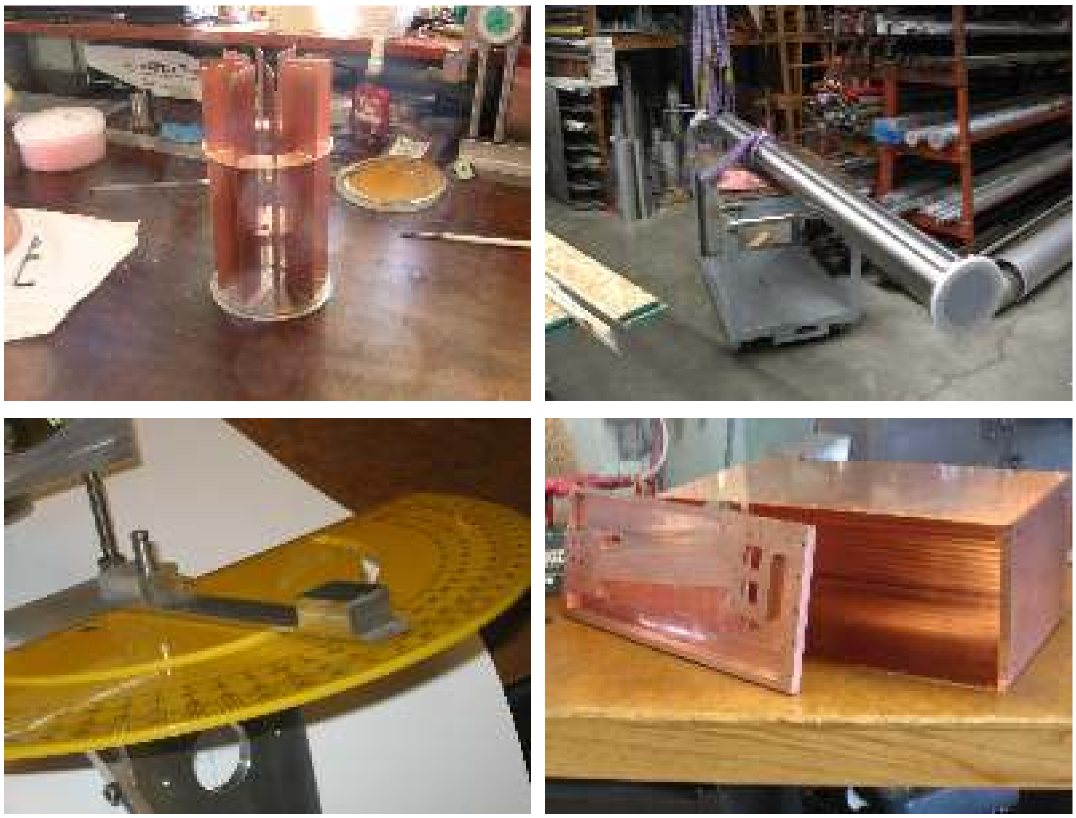

Figure 7.7-4. *Top left:* Machined and soldered helium return cooler assembly. *Top right:* 6” diameter helium return line section with 8” leak-tight coflat flange.*Bottom left:* Laser-pointer protractor for detector alignment. *Bottom right:* Thin-wall copper plate machine using new vacuum chuck.

LEGEND

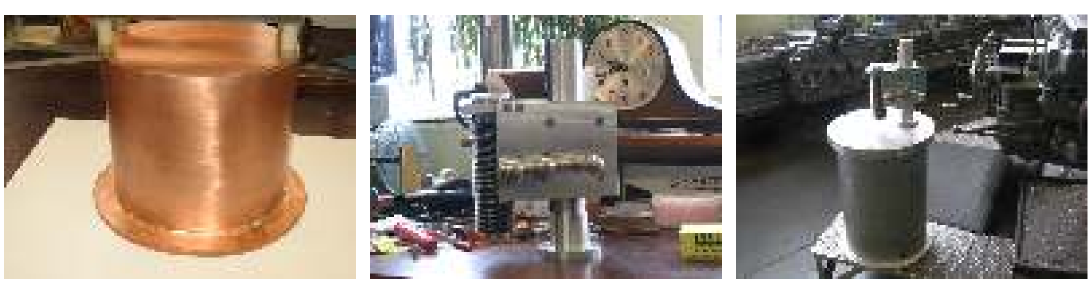

Figure 7.7-5. *Left:* Infrared copper shield. *Middle:* Exterior linear-drive strong enough to lift components for detector scanning.*Right:* Leak-tight vacuum chamber and linear-drive.

7.8 Building maintenance, repairs, and upgrades

I. Boeckstiegel, B. W. Dodson, J. R. Pedersen, E. B. Smith, and D. I. Will

During the 2018 calendar year 173 work orders (WOs) were placed for the North Physics Laboratory buildings which house the CENPA research facility. For the Van de Graaff Accelerator Building 54 total WOs included the following: 31 Preventive Maintenance/Repair/Alterations WOs (PM/R/Alts) by Facilities Services; 19 Service/Repair WOs (S/R) by CENPA staff; and 5 Alterations WOs (Alts) by CENPA staff. For the Cyclotron Building 53 total WOs included the following: 26 PM/R/Alts WOs by Facilities Services, 26 S/R WOs by CENPA staff, and 1 Alts WOs requested by CENPA staff. For the CENPA Instrument Shop 26 total WOs included the following: 17 PM/R/Alts WOs by Facilities Services, 9 S/R WOs by CENPA staff, and 0 Alts WOs by CENPA staff. For the aggregate of these three buildings 10 total WOs included the following: 4 PM/R/Alts WOs by Facilities Services, 4 S/R WOs by CENPA staff, and 2 Alts WOs by CENPA staff.

In mechanical room 115, the direct steam air handler for the lower Cyclotron Building offices did not work after replacement. Facilities Services mechanics were called back to connect the pneumatic drive to steam control valve.

In high bay room 163 the replacement of stuck louvers (allowing cold air intrusion) on a roof vent fan has finally been completed. After the fan housing was rebuilt but without louvers, a commercial set of draft-driven louvers was retrofitted. The direct steam heating units in this same area have a new condensate trap, but re-lagging of the steam and condensate lines is incomplete.

For some years now, there has been a water hammer in the hydronic heating system for the Van de Graaff Accelerator Building high bay setup area and adjacent offices. This problem still has not been solved.

The old darkroom and circuit etching lab, room 123, has been cleared for a reuse and is now the general-lab-use High Purity Germanium (HPGe) detector system lab. Evaluation of temperature stability in this room is ongoing.

The second row of cryostats from the decommissioned, and partially surplused, superconducting booster linac has been disassembled in preparation for new experiments. Several additional prefabricated concrete supports (for the cryostats) still remain in the back parking lot awaiting pickup for reuse or recycling by facilities outside zone. Several additional tons of 3-inch-thick steel x-ray shielding plates (from the linac) are stacked along the courtyard drive awaiting pickup for steel recycling.

During the past year both city water mains (a 6” and an 8” main, both ductile iron) supplying CENPA began leaking and eroding their hillsides below the lab. The longer main on the steeper hillside was abandoned. The shorter main was replaced with a new high density polyethylene main and new valving.

Compressed gas cylinders storage improvement

The storage of compressed gas cylinders at CENPA has been improved together with the removal of many unused or empty cylinders. The CENPA waste disposal initiate in January 2018[1] brought RM 164 east wall from state of clutter and congestion to an cleared state (Fig. 7.8-1), which was able to safely accommodate storage racks for a large number of compressed cylinders of inert and oxidizing gases. Likewise, the cleared west wall was able to support storage of flammable gas cylinders at a distance from oxidizers that satisfies safety requirements.

After a detailed inventory of compressed gas cylinders at CENPA, we identified many cylinders that were empty. Rigorous attempts were made to contact all identifiable vendors associated with the cylinders to request their removal, which resulted in some cylinders being claimed and removed. The remaining cylinders were processed through a safe purging and valve removal procedure. The decommissioned cylinders were sent to UW Recycling.

Figure 7.8-1. Room 164 - East wall showing (*left*) before cleanup, (*middle*) post cleanup, and (*right*) gas storage area with cylinders in installed racks and signage.

[1]CENPA Annual Report, University of Washington (2018) p. 127.

8 CENPA Personnel

8.1 Faculty

Eric G. Adelberger[1]	Professor Emeritus
Hans Bichsel[1,2]	Affiliate Professor
Alvaro Chavarria[1]	Assistant Professor
John G. Cramer[1]	Professor Emeritus
Jason Detwiler	Assistant Professor
Peter J. Doe	Research Professor
Sanshiro Enomoto	Research Assistant Professor
Martin Fertl	Research Assistant Professor
Alejandro García	Professor
Gerald Garvey[1]	Affiliate Professor
Jens H. Gundlach[1]	Professor
Blayne R. Heckel[1]	Professor; Chair
David W. Hertzog	Professor; Director
C. D. Hoyle[1,3]	Affiliate Assistant Professor
Peter Kammel	Research Professor
Jarek Kaspar	Research Assistant Professor
Michael L. Miller[1]	Affiliate Research Assistant Professor
Peter Mueller[1]	Affiliate Professor
Diana Parno[1,4]	Affiliate Assistant Professor
R. G. Hamish Robertson	Emeritus Professor
Leslie J Rosenberg[1]	Professor
Gray Rybka[1]	Research Assistant Professor
Kurt A. Snover[1]	Research Professor Emeritus
Derek W. Storm[1]	Research Professor Emeritus
Thomas A. Trainor[1]	Research Professor Emeritus
Robert Vandenbosch[1]	Professor Emeritus
Krishna Venkateswara[1]	Acting Assistant Professor
William G. Weitkamp[1]	Research Professor Emeritus
John F. Wilkerson[1,5]	Affiliate Professor

[1]Not supported by DOE CENPA grant.
[2]Passed away November 24, 2018.
[3]Affiliated faculty, Humboldt State University, Arcata, CA.
[4]Affiliated faculty, Carnegie Mellon University, Pittsburgh, PA.
[5]Affiliated faculty, University of North Carolina, Chapel Hill, NC.

8.2 CENPA external advisory committee

Robert McKeown[1]	Jefferson Laboratory
Daniel McKinsey[1]	UC Berkeley
Michael Ramsey-Musolf[1]	University of Massachusetts, Amherst

8.3 Postdoctoral research associates

Chelsea Bartram[2,3]	Nicole Crisosto[2,4]
Brent Graner	Mathieu Guigue[2,7,5]
Charlie Hagedorn[2]	Megan Ivory
Rakshya Khatiwada[2,6]	Kim Siang Khaw
Benjamin LaRoque[2,7]	Elise Novitski[8]
Pitam Mitra[2]	Walter Pettus
Menglei Sun[4]	Clint Wiseman[9]

8.4 Predoctoral research associates

Yelena Bagdasarova	Hannah Binney
Thomas Braine[2]	Micah Buuck
William (Drew) Byron	Raphael Cervantes[2]
Nick Du[2]	Ali Ashtari Esfahani[2]
Aaron Fienberg[10]	Ian Guinn
Madeleine Hanley[11]	Jason Hempstead
Alexandru Hostiuc	Luke Kippenbrock[12]
Joshua La Bounty[13]	John Lee[2]
Ying-Ting Lin	Brynn MacCoy
Eric Machado	Ethan Muldoon
Rachel Osofsky	Alexander Piers[2,14]
Michael Ross[2]	Nicholas Ruof
Rachel Ryan	Erik Shaw[2]

[1]CENPA External Advisory Committee formed January 2014.
[2]Not supported by DOE CENPA grant.
[3]Arrived April, 2019.
[4]Arrived October, 2018.
[5]Departed August, 2018.
[6]Departed July, 2018.
[7]Pacific Northwest National Laboratory, Richland, WA.
[8]Arrived January, 2018.
[9]Arrived August, 2018.
[10]Graduated January, 2019.
[11]Arrived July, 2018.
[12]Graduated March, 2019.
[13]Arrived June, 2018.
[14]Arrived March, 2018.

8.5 Undergraduates

Robert Adams	Rybka, Advisor
Yifei Bai	Hagedorn, Advisor
Jeff Capoeman, Jr	Hagedorn, Advisor
Jameson Doane	Rybka, Advisor
Katherine Evans	Smith, Advisor
Callum Farrell	Detwiler, Advisor
Roland Farrell	García, Advisor
Jonathan Gort	Pettus, Advisor
Kezhu Guo	García, Advisor
Joshua Handjojo	Fertl, Advisor
Keira Hansen	Detwiler, Advisor
Michael Higgins	García, Advisor
Brandon Iritani	Hagedorn, Advisor
Jacob Johnson	Rybka, Advisor
Jared Johnson	Hagedorn, Advisor
Megan Kokoris	Chavarria, Advisor
Alyssa Lee	Rybka, Advisor
Jeremy Lu	García, Advisor
Parashar Mohapatra	Rybka, Advisor
Julian O'Leary	Detwiler, Advisor
Axl O'Neal	Smith, Advisor
Nicholas Orndorff	Hagedorn, Advisor
Maurice Ottiger	Fertl, Advisor
Elliott Phillips	Fertl, Advisor
Daniel Primosch	Rybka, Advisor
Spencer Pruitt	Detwiler, Advisor
Matthew Stortini	García, Advisor
MinJung Sung	García, Advisor
Zhizhong Tao	García, Advisor
Andrew Thornberry	Rybka, Advisor
Jessica Thwaites	García, Advisor
Alexander Vellozzi	Chavarria, Advisor
Colin Watson	Detwiler, Advisor
Sierra Wilde	Fertl, Advisor
Kassandra Weber	Hagedorn, Advisor
Anni Xiong	García, Advisor
Zining Zhu	Rybka, Advisor

8.6 Visitors and volunteers

Bernadette Maria Rebeiro	Visiting RA, Ne21pg
Manuja Sharma	user, LPKF laser
Perry Forsyth	Vistor, Gravity
Edward Wang	user, LPKF laser
Thomas Braine	ADMX, Volunteer RA
Alexandru Hostiuc	Volunteer RA, LEGEND/Majorana
Joshua La Bounty	Volunteer RA, Muon g-2
Francis Walsh	Volunteer RA, He6
Thomas Lopez	Visiting RA, He6-CRES
Christine Claessens	Visiting RA, Project 8
Nathan Woollett	Visitor, ADMX
Lisa Pellerin	user, LPKF laser
Shanti Garman	user, LPKF laser
Nathan Yang	user, LPKF laser
Joshua Johnson	user, LPKF laser
Alexander Cable	Visitor, LPKF
Christian Boutan	Visitor, ADMX
Aaron Chou	Visitor, ADMX
David Tanner	Visitor, ADMX
Smarajit Triambak	Visiting Professor, Ne21pg
Jihee Yang	Visiting Research Associate, ADMX
Raahul Buch	He6, Volunteer RA
Yu-Hao Sun	Visiting RA, Project 8
Nicholas Buzinsky	Visiting RA, Project 8
Bhivek Singh	Visitor, Ne21pg
Yasuo Kuga	user, LPKF laser
Jeff Chrisope	user, LPKF laser
James Whitehead	user, LPKF laser
Gulden Othman	Visiting RA, LEGEND

8.7 Administrative staff

Ida Boeckstiegel	Office Administrator
Nerissa Pineda[1]	Fiscal Specialist
Libby Wang[2]	Fiscal Specialist

[1]Departed June, 2018.
[2]Arrived August, 2018.

8.8 Professional staff

John F. Amsbaugh	RS/E	Engineering, vacuum, cryogenics design
Tom H. Burritt	RS/E Sr.	Precision design, machining
Nick Force[1]	RS/E	ADMX
Gary T. Holman	Associate Director	Computer systems
Matthew Kallander[2]	RS/E Asst.	TRIMS, DAMIC and Project 8
Seth Kimes	RS/E	ADMX Dilfridge, Liquifier
Grant Leum[2]	RS/E	ADMX Liquifier
Joben Pedersen	RS/E	Accelerator, ion sources
Duncan J. Prindle, Ph.D.	RS/E Scientist	Heavy ion, muon research
Eric B. Smith	RS/E	Accelerator, ion sources
H. Erik Swanson, Ph.D.	RS/E Physicist	Precision experimental equipment
Timothy D. Van Wechel	RS/E	Analog and digital electronics design
Douglas I. Will	RS/E Sr.	Cryogenics, ion sources, buildings

8.9 Technical staff

James H. Elms	Instrument Maker
David A. Peterson	Electronics Technician

8.10 Part-time staff and student helpers

David R. Hyde	Student shop manager
Michael Huehn	Hourly
Greg Harper	Accelerator engineering, consultant
Daniel Garratt[3]	Hourly
Henry Gorrell	Hourly
Hendrik Simons	Instrument maker
Santos Zaid	Hourly
Yadi Yang	Hourly

[1] Departed September, 2018.
[2] Promoted January, 2019.
[3] Departed January, 2019.

9 Publications

Publications and presentations with a date of 2018 or 2019 are included below. Some entries from early 2019 may therefore also appear in the 2018 Annual Report.

9.1 Published papers

[1]A. A. Esfahani, V. Bansal, S. Böser, N. Buzinsky, R. Cervantes, C. Claessens, L. de Viveiros, P. J. Doe, M. Fertl, J. A. Formaggio, L. Gladstone, M. Guigue, K. M. Heeger, J. Johnston, A. M. Jones, K. Kazkaz, B. H. LaRoque, M. Leber, A. Lindman, E. Machado, B. Monreal, E. C. Morrison, J. A. Nikkel, E. Novitski, N. S. Oblath, W. Pettus, R. G. H. Robertson, G. Rybka, L. Saldaña, V. Sibille, M. Schram, P. L. Slocum, Y.-H. Sun, J. R. Tedeschi, T. Thümmler, B. A. VanDevender, M. Wachtendonk, M. Walter, T. E. Weiss, T. Wendler, and E. Zayas, "Electron radiated power in cyclotron radiation emission spectroscopy experiments", Phys. Rev. C **99**, 055501 (2019).

[2]D. L. Danielson, A. C. Hayes, and G. T. Garvey, "Reactor Neutrino Spectral Distortions Play Little Role in Mass Hierarchy Experiments", Phys. Rev. **D99**, 036001 (2019).

[3]A. A. Aguilar-Arevalo et al., "Dark Matter Search in Nucleon, Pion, and Electron Channels from a Proton Beam Dump with MiniBooNE", Phys. Rev. **D98**, 112004 (2018).

[4]A. A. Aguilar-Arevalo et al., "Significant Excess of ElectronLike Events in the MiniBooNE Short-Baseline Neutrino Experiment", Phys. Rev. Lett. **121**, 221801 (2018).

[5]R. J. Hill, P. Kammel, W. J. Marciano, and A. Sirlin, "Nucleon axial radius and muonic hydrogen - a new analysis and review", Reports on Progress in Physics **81**, 096301 (2018), DOE Supported.

[6]V. Ganzha, K. Ivshin, P. Kammel, P. Kravchenko, P. Kravtsov, C. Petitjean, V. Trofimov, A. Vasilyev, A. Vorobyov, M. Vznuzdaev, and F. Wauters, "Measurement of trace impurities in ultra pure hydrogen and deuterium at the parts-per-billion level using gas chromatography", Nuclear Instruments and Methods in Physics Research Section A: Accelerators, Spectrometers, Detectors and Associated Equipment **880**, 181–187 (2018), DOE Supported.

[7]C. E. Aalseth et al., "Search for Neutrinoless Double-β Decay in ^{76}Ge with the Majorana Demonstrator", Physical Review Letters **120**, 132502 (2018), DOE Supported.

[8]S. I. Alvis, I. J. Arnquist, F. T. Avignone, A. S. Barabash, C. J. Barton, F. E. Bertrand, V. Brudanin, M. Busch, M. Buuck, T. S. Caldwell, Y.-D. Chan, C. D. Christofferson, P.-H. Chu, C. Cuesta, J. A. Detwiler, C. Dunagan, Y. Efremenko, H. Ejiri, S. R. Elliott, T. Gilliss, G. K. Giovanetti, M. P. Green, J. Gruszko, I. S. Guinn, V. E. Guiseppe, C. R. Haufe, L. Hehn, R. Henning, E. W. Hoppe, M. A. Howe, S. I. Konovalov, R. T. Kouzes, A. M. Lopez, R. D. Martin, R. Massarczyk, S. J. Meijer, S. Mertens, J. Myslik, C. O'Shaughnessy, G. Othman, W. Pettus, A. W. P. Poon, D. C. Radford, J. Rager, A. L. Reine, K. Rielage, R. G. H. Robertson, N. W. Ruof, B. Shanks,

M. Shirchenko, A. M. Suriano, D. Tedeschi, R. L. Varner, S. Vasilyev, K. Vorren, B. R. White, J. F. Wilkerson, C. Wiseman, W. Xu, E. Yakushev, C.-H. Yu, V. Yumatov, I. Zhitnikov, B. X. Zhu, and Majorana Collaboration, “First Limit on the Direct Detection of Lightly Ionizing Particles for Electric Charge as Low as e /1000 with the MAJORANA DEMONSTRATOR”, Physical Review Letters **120**, 211804 (2018), DOE Supported.

[9]S. I. Alvis, I. J. Arnquist, F. T. Avignone III, A. S. Barabash, C. J. Barton, F. E. Bertrand, B. Bos, V. Brudanin, M. Busch, M. Buuck, T. S. Caldwell, Y. Chan, C. D. Christofferson, P.-H. Chu, C. Cuesta, J. A. Detwiler, Y. Efremenko, H. Ejiri, S. R. Elliott, T. Gilliss, G. K. Giovanetti, M. P. Green, J. Gruszko, I. S. Guinn, V. E. Guiseppe, C. R. Haufe, R. J. Hegedus, L. Hehn, R. Henning, D. Hervas Aguilar, E. W. Hoppe, M. A. Howe, K. J. Keeter, M. F. Kidd, S. I. Konovalov, R. T. Kouzes, A. M. Lopez, R. D. Martin, R. Massarczyk, S. J. Meijer, S. Mertens, J. Myslik, G. Othman, W. Pettus, A. Piliounis, A. W. P. Poon, D. C. Radford, J. Rager, A. L. Reine, K. Rielage, N. W. Ruof, B. Shanks, M. Shirchenko, D. Tedeschi, R. L. Varner, S. Vasilyev, Vasundhara, B. R. White, J. F. Wilkerson, C. Wiseman, W. Xu, E. Yakushev, C.-H. Yu, V. Yumatov, I. Zhitnikov, and B. X. Zhu, “Search for Tri-Nucleon Decay in the MAJORANA DEMONSTRATOR”, Physical Review Letters **99**, 072004 (2019), DOE Supported.

[10]G. Adhikari, P. Adhikari, E. B. de Souza, N. Carlin, S. Choi, W. Q. Choi, M. Djamal, A. C. Ezeribe, C. Ha, I. S. Hahn, A. J. F. Hubbard, E. J. Jeon, J. H. Jo, H. W. Joo, W. G. Kang, W. Kang, M. Kauer, B. H. Kim, H. Kim, H. J. Kim, K. W. Kim, M. C. Kim, N. Y. Kim, S. K. Kim, Y. D. Kim, Y. H. Kim, V. A. Kudryavtsev, H. S. Lee, J. Lee, J. Y. Lee, M. H. Lee, D. S. Leonard, K. E. Lim, W. A. Lynch, R. H. Maruyama, F. Mouton, S. L. Olsen, H. K. Park, H. S. Park, J. S. Park, K. S. Park, W. Pettus, Z. P. Pierpoint, H. Prihtiadi, S. Ra, F. R. Rogers, C. Rott, A. Scarff, N. J. C. Spooner, W. G. Thompson, L. Yang, and S. H. Yong, “Initial performance of the COSINE-100 experiment”, European Physical Journal C **78**, 107 (2018).

[11]Cosine-100 Collaboration, G. Adhikari, P. Adhikari, E. Barbosa de Souza, N. Carlin, S. Choi, M. Djamal, A. C. Ezeribe, C. H. Ha, I. Hahn, A. J. F. Hubbard, E. Jeon, J. H. Jo, H. Joo, W. G. Kang, W. Kang, M. Kauer, B. Kim, H. Kim, H. Kim, K. Kim, N. Y. Kim, S. K. Kim, Y. Kim, Y.-H. Kim, Y. J. Ko, V. Y. Kudryavtsev, H. S. Lee, J. Lee, J. Lee, M. H. Lee, D. S. Leonard, W. A. Lynch, R. H. Maruyama, F. Mouton, S. L. Olson, B. Park, H. K. Park, H. Park, J. Park, K. Park, W. C. Pettus, H. Prihtiadi, S. Ra, C. Rott, A. Scarff, K. A. Shin, N. J. C. Spooner, W. G. Thompson, L. Yang, and S. H. Yong, “An experiment to search for dark-matter interactions using sodium iodide detectors”, Nature **564**, 83–86 (2018).

[12]P. Adhikari, G. Adhikari, E. B. d. Souza, N. Carlin, S. Choi, W. Q. Choi, M. Djamal, A. C. Ezeribe, C. Ha, I. S. Hahn, A. J. F. Hubbard, E. J. Jeon, J. H. Jo, H. W. Joo, W. G. Kang, M. Kauer, W. S. Kang, B. H. Kim, H. Kim, H. J. Kim, K. W. Kim, M. C. Kim, N. Y. Kim, S. K. Kim, Y. D. Kim, Y. H. Kim, V. A. Kudryavtsev, H. S. Lee, J. Lee, J. Y. Lee, M. H. Lee, D. S. Leonard, W. A. Lynch, R. H. Maruyama, F. Mouton, S. L. Olsen, H. K. Park, H. S. Park, J. S. Park, K. S. Park, W. Pettus, H. Prihtiadi, S. Ra, C. Rott, A. Scarff, N. J. C. Spooner, W. G. Thompson, L. Yang, and S. H. Yong,

"Background model for the NaI(Tl) crystals in COSINE-100", European Physical Journal C **78**, 490 (2018).

[13]G. Adhikari, P. Adhikari, E. Barbosa de Souza, N. Carlin, S. Choi, W. Choi, M. Djamal, A. C. Ezeribe, C. Ha, I. S. Hahn, A. J. F. Hubbard, E. J. Jeon, J. H. Jo, H. W. Joo, W. G. Kang, W. S. Kang, M. Kauer, H. Kim, H. J. Kim, K. W. Kim, M. C. Kim, N. Y. Kim, S. K. Kim, Y. D. Kim, Y. H. Kim, V. A. Kudryavtsev, H. S. Lee, J. Lee, M. H. Lee, K. E. Lim, D. S. Leonard, R. H. Maruyama, F. Mouton, S. Na, S. L. Olsen, H. K. Park, H. S. Park, J. S. Park, K. S. Park, W. Pettus, H. Prihtiadi, C. Rott, A. Scarff, N. J. C. Spooner, W. G. Thompson, and L. Yang, "The COSINE-100 data acquisition system", Journal of Instrumentation **13**, P09006 (2018).

[14]M. Arenz et al., "The KATRIN Superconducting Magnets: Overview and First Performance Results", JINST **13**, T08005 (2018), DOE Supported.

[15]K. Altenmueller et al., "Muon-induced background in the KATRIN main spectrometer", Astropart. Phys. **108**, 40–49 (2019), DOE Supported.

[16]M. Arenz et al., "Reduction of stored-particle background by a magnetic pulse method at the KATRIN experiment", Eur. Phys. J. **C78**, 778 (2018), DOE Supported.

[17]M. Arenz et al., "Calibration of high voltages at the ppm level by the differences of 83mKr conversion electron lines at the KATRIN experiment", Eur. Phys. J. **C78**, 368 (2018), DOE Supported.

[18]M. Arenz et al., "First transmission of electrons and ions through the KATRIN beamline", JINST **13**, P04020 (2018), DOE Supported.

[19]B. Aharmim et al., "Constraints on Neutrino Lifetime from the Sudbury Neutrino Observatory", Phys. Rev. **D99**, 032013 (2019), DOE Supported.

[20]B. Aharmim et al., "Tests of Lorentz invariance at the Sudbury Neutrino Observatory", Phys. Rev. **D98**, 112013 (2018), DOE Supported.

[21]A. A. Esfahani, V. Bansal, S. Böser, N. Buzinsky, R. Cervantes, C. Claessens, L. de Viveiros, P. J. Doe, M. Fertl, J. A. Formaggio, L. Gladstone, M. Guigue, K. M. Heeger, J. Johnston, A. M. Jones, K. Kazkaz, B. H. LaRoque, M. Leber, A. Lindman, E. Machado, B. Monreal, E. C. Morrison, J. A. Nikkel, E. Novitski, N. S. Oblath, W. Pettus, R. G. H. Robertson, G. Rybka, L. Saldaña, V. Sibille, M. Schram, P. L. Slocum, Y.-H. Sun, J. R. Tedeschi, T. Thümmler, B. A. VanDevender, M. Wachtendonk, M. Walter, T. E. Weiss, T. Wendler, and E. Zayas, "Electron radiated power in cyclotron radiation emission spectroscopy experiments", Phys. Rev. C **99**, 055501 (2019), DOE Supported.

[22]M. W. Coughlin, J. Harms, J. Driggers, D. J. McManus, N. Mukund, M. P. Ross, B. J. J. Slagmolen, and K. Venkateswara, "Implications of dedicated seismometer measurements on newtonian-noise cancellation for advanced ligo", Phys. Rev. Lett. **121**, 221104 (2018).

[23]Brown, M. A.-P. and Dees, E. B. and Adamek, E. and Allgeier, B. and Blatnik, M. and Bowles, T. J. and Broussard, L. J. and Carr, R. and Clayton, S. and Cude-Woods, C. and Currie, S. and Ding, X. and Filippone, B. W. and García, A. and Geltenbort, P. and Hasan, S. and Hickerson, K. P. and Hoagland, J. and Hong, R. and Hogan, G. E. and Holley, A. T. and Ito, T. M. and Knecht, A. and Liu, C.-Y. and Liu, J. and Makela, M. and Martin, J. W. and Melconian, D. and Mendenhall, M. P. and Moore, S. D. and Morris, C. L. and Nepal, S. and Nouri, N. and Pattie, R. W. and Pérez Galván, A. and Phillips, D. G. and Picker, R. and Pitt, M. L. and Plaster, B. and Ramsey, J. C. and Rios, R. and Salvat, D. J. and Saunders, A. and Sondheim, W. and Seestrom, S. J. and Sjue, S. and Slutsky, S. and Sun, X. and Swank, C. and Swift, G. and Tatar, E. and Vogelaar, R. B. and VornDick, B. and Wang, Z. and Wexler, J. and Womack, T. and Wrede, C. and Young, A. R. and Zeck, B. A., “New result for the neutron β-asymmetry parameter A_0 from UCNA”, Phys. Rev. C **97**, 035505 (2018).

[24]Sun, X. and Adamek, E. and Allgeier, B. and Blatnik, M. and Bowles, T. J. and Broussard, L. J. and Brown, M. A.-P. and Carr, R. and Clayton, S. and Cude-Woods, C. and Currie, S. and Dees, E. B. and Ding, X. and Filippone, B. W. and García, A. and Geltenbort, P. and Hasan, S. and Hickerson, K. P. and Hoagland, J. and Hong, R. and Hogan, G. E. and Holley, A. T. and Ito, T. M. and Knecht, A. and Liu, C.-Y. and Liu, J. and Makela, M. and Mammei, R. and Martin, J. W. and Melconian, D. and Mendenhall, M. P. and Moore, S. D. and Morris, C. L. and Nepal, S. and Nouri, N. and Pattie, R. W. and Pérez Galván, A. and Phillips, D. G. and Picker, R. and Pitt, M. L. and Plaster, B. and Ramsey, J. C. and Rios, R. and Salvat, D. J. and Saunders, A. and Sondheim, W. and Sjue, S. and Slutsky, S. and Swank, C. and Swift, G. and Tatar, E. and Vogelaar, R. B. and VornDick, B. and Wang, Z. and Wei, W. and Wexler, J. and Womack, T. and Wrede, C. and Young, A. R. and Zeck, B. A., “Search for dark matter decay of the free neutron from the UCNA experiment: $n \to \chi + e^+e^-$”, Phys. Rev. C **97**, 052501 (2018).

[25]A. García, “Searching for chirality–flipping interactions in nuclear β decays”, International Journal of Modern Physics E **27**, 1840002 (2018), DOE Supported.

9.2 Papers submitted or to be published

[26]E. G. a. A. Terrano W. A. andAdelberger and B. R. Heckel, *Constraints on axionlike dark matter with masses down to* 10^{-23} eV/c^2, NSF supported.

[27]S. I. Alvis, I. J. Arnquist, F. T. Avignone III, A. S. Barabash, C. J. Barton, F. E. Bertrand, B. Bos, M. Buuck, T. S. Caldwell, Y. Chan, C. D. Christofferson, P.-H. Chu, C. Cuesta, J. A. Detwiler, H. Ejiri, S. R. Elliott, T. Gilliss, G. K. Giovanetti, M. P. Green, J. Gruszko, I. S. Guinn, V. E. Guiseppe, C. R. Haufe, R. J. Hegedus, L. Hehn, R. Henning, D. Hervas Aguilar, E. W. Hoppe, M. A. Howe, K. J. Keeter, M. F. Kidd, S. I. Konovalov, R. T. Kouzes, A. M. Lopez, R. D. Martin, R. Massarczyk, S. J. Meijer, S. Mertens, J. Myslik, G. Othman, W. Pettus, A. Piliounis, A. W. P. Poon, D. C. Radford, J. Rager, A. L. Reine, K. Rielage, N. W. Ruof, B. Shanks, M. Shirchenko, D. Tedeschi, R. L. Varner, S. Vasilyev, Vasundhara, B. R. White, J. F. Wilkerson, C. Wiseman, W. Xu, E. Yakushev, C.-H. Yu, V. Yumatov, I. Zhitnikov, and B. X. Zhu,

"Multi-site event discrimination for the MAJORANA DEMONSTRATOR", arXiv e-prints (2019), DOE Supported.

[28]S. I. Alvis, I. J. Arnquist, F. T. Avignone III, A. S. Barabash, C. J. Barton, V. Basu, F. E. Bertrand, B. Bos, M. Busch, M. Buuck, T. S. Caldwell, Y. Chan, C. D. Christofferson, P.-H. Chu, C. Cuesta, J. A. Detwiler, Y. Efremenko, H. Ejiri, S. R. Elliott, T. Gilliss, G. K. Giovanetti, M. P. Green, J. Gruszko, I. S. Guinn, V. E. Guiseppe, C. R. Haufe, R. J. Hegedus, L. Hehn, R. Henning, D. Hervas Aguilar, E. W. Hoppe, M. A. Howe, M. F. Kidd, S. I. Konovalov, R. T. Kouzes, A. M. Lopez, R. D. Martin, R. Massarczyk, S. J. Meijer, S. Mertens, J. Myslik, G. Othman, W. Pettus, A. Piliounis, A. W. P. Poon, D. C. Radford, J. Rager, A. L. Reine, K. Rielage, N. W. Ruof, B. Shanks, M. Shirchenko, D. Tedeschi, R. L. Varner, S. Vasilyev, B. R. White, J. F. Wilkerson, C. Wiseman, W. Xu, E. Yakushev, C.-H. Yu, V. Yumatov, I. Zhitnikov, and B. X. Zhu, "A Search for Neutrinoless Double-Beta Decay in ^{76}Ge with 26 kg-yr of Exposure from the MAJORANA DEMONSTRATOR", arXiv e-prints (2019), DOE Supported.

[29]K. Altenmueller et al., "Gamma-induced background in the KATRIN main spectrometer", (2019), DOE Supported.

[30]S. Mertens et al., "A novel detector system for KATRIN to search for keV-scale sterile neutrinos", (2018), DOE Supported.

[31]B. Aharmim et al., "Measurement of neutron production in atmospheric neutrino interactions at the Sudbury Neutrino Observatory", (2019), DOE Supported.

[32]H. E. Swanson, C. D. Bass, T. D. Bass, B. E. Crawford, D. J. M., K. Gan, B. R. Heckel, J. C. Horton, C. Huffer, D. Luo, D. M. Markoff, A. M. Micherdzinska, H. P. Mumm, J. S. Nico, M. Sarsour, E. I. Sharapov, W. M. Snow, S. B. Walbridge, and V. Zhumabekova, "Experimental Upper Bound and Theoretical Expectations for Parity-Violating Neutron Spin Rotation in 4He", 2019, DOE Supported.

9.3 Invited talks at conferences

[33]E. Adelberger, *Recent Eöt-Wash Results*, invited, Testing Gravity 2019, workshop at Simon Frazer University, Vancouver BC (January 23-26, 2019), 2019, NSF Supported.

[34]E. Adelberger, *Probing quantum speculations with classical techniques: taking advantage of avrogadro's number*, invited, First Arizona Workshop on Precision Searches for Fundamental Physics, Arizona State University, Tempe AZ (February 4-6), 2019, NSF Supported.

[35]M. Buuck, *First limit on neutrinoless double-beta decay from the* MAJORANA DEMONSTRATOR, invited, Heavy Quarks and Leptons 2018, Yamagata, Japan, May 2018, DOE Supported.

[36]M. Fertl, *Project 8: A frequency based approach to measure the neutrino mass scale*, TRIUMF colloquium, TRIUMF, Vancouver, BC, Canada, 2018.

[37]M. Fertl, *Review of absolute neutrino mass measurements*, Aachen, Germany: 7$^{\text{th}}$ International Symposium on Symmetries in Subatomic Physics (SSP2018), DOE supported.

[38]P. Kammel, *Precision muon physics*, invited, Lake Louise Winter Institute 2018, Chateau Lake Louise, Canada, February, 2018, DOE Supported.

[39]P. Kammel, *Muon capture, tpcs and nucleon axial structure*, invited, Program INT-18-2a, Fundamental Physics with Electroweak Probes of Light Nuclei, Seattle, July, 2018, DOE Supported.

[40]P. Kammel, *Muon capture as a probe of the weak axial current*, invited, 3th Conference on the Intersections of Particle and Nuclear Physics CIPANP 2018, Palm Springs, CA, May, 2018, DOE Supported.

[41]W. C. Pettus, *The liquid argon veto for LEGEND*, invited, Low-Radioactivity Underground Argon Workshop, PNNL, Richland, WA, March 2018, 2018, DOE Supported.

[42]W. C. Pettus, *Perspective for LEGEND:* MAJORANA*, GERDA, and the* ^{76}*Ge program*, invited, Gas-Phase, Ton-Scale $0\nu\beta\beta$ Decay Searches Workshop, June 2018, 2018, DOE Supported.

[43]R. G. H. Robertson, *SNO: The neutrino's day in the sun*, Invited talk, 5th International Conference on Solar Neutrinos, Dresden, Germany, 2018, DOE Supported.

[44]C. Wiseman, *The* MAJORANA DEMONSTRATOR*: current status and outlook to legend*, invited, 3rd Conference on Science at the Sanford Underground Research Facility, South Dakota School of Mines, Rapid City, SD, May 2019, 2019, DOE Supported.

[45]A. Garcia, *Searching for Tensor Currents by Detection of Cyclotron Radiation*, Workshop on "Bridging the Standard Model", Mainz Institute for Theoretical Physics, Mainz, Germany, April 26, 2018, 2018.

[46]A. Garcia, *Overview of Nuclear Beta Decay Tests of Fundamental Symmetries*, Conference on the Intersections between Particle and Nuclear Physics. Indian Wells, CA, May 29–June 3rd, 2018, 2018.

[47]A. Garcia, *Searches for beyond the Standard Model physics with single beta decays*, Workshop Fundamental Physics with Electroweak Probes of Light Nuclei, Seattle, WA, June 25th, 2018, 2018.

[48]A. Garcia, *Beta decay as a probe of new physics*, Workshop "Beta decay as a probe of new physics" at Amherst Center for Fundamental Interactions, Nov. 1st, 2018, 2018.

[49]A. Garcia, *Cyclotron radiation detection to search for new physics*, Colloquioum, University of Notre Dame, Dec. 6th, 2018, 2018.

[50]L. Kippenbrock, *Status of the KATRIN experiment*, PASCOS 2018, Case Western Reserve University, Cleveland, USA, 2018, DOE Supported.

[51]D. W. Hertzog, *Report from NSAC: Status since the 2015 Long Range Plan, IUPAP meeting*, Bologna, Italy, 2018, DOE Supported.

[52]D. W. Hertzog, *Overview and status of the muon g-2 experiment at Fermilab, Invited Plenary Talk*, SPIN2018: 23rd International Spin Symposium, Ferrara, Italy, 2018, DOE Supported.

[53]D. W. Hertzog, *Overview and status of the muon g-2 experiment at Fermilab, Invited Talk*, Swedish nuclear physics meeting XXXVIII, 2018.

[54]D. W. Hertzog, *Fundamental Physics in a Storage Ring: Muon g-2, Invited Talk*, New Forms of Matter: A symposium honoring Tord Johansson, Uppsala, Sweden, 2018.

[55]D. W. Hertzog, *Overview and status of the muon g-2 experiment at Fermilab, Colloquium*, University of Illinois at Urbana-Champaign, 2018.

[56]D. W. Hertzog, *Overview and status of the muon g-2 experiment at Fermilab*, Kirby Kemper Colloquium: Florida State University, 2019.

[57]D. W. Hertzog, *2019 Report of the Status of the 2015 U.S. Long Range Plan for Nuclear Science, Invited (remote) presentation*, NuPECC meeting, 2019.

[58]D. W. Hertzog, *Next-Generation Muon g-2: An indirect, but highly sensitive search for New Physics*, Colloquium: Carnegie Mellon University, 2019.

9.4 Abstracts and contributed talks

[59]M. Buuck, *LEGEND: the large enriched germanium experiment for neutrinoless double-beta decay*, contributed, International Workshop on Next Generation Nucleon Decay and Neutrino Detectors 2018, Vancouver, BC, Canada, Nov. 2018, DOE Supported.

[60]M. Fertl, *Project 8: A frequency-based approach to measure the absolute neutrino mass scale*, Contributed talk, Joint Meeting of the APS-DNP and JPS, Waikoloa, HI, Oct. 2018, DOE supported.

[61]P. Kammel, *High pressure, ultra-high purity hydrogen tpcs for muon capture experiments*, 5th Joint Meeting of the APS Division of Nuclear Physics and the Physical Society of Japan, Waikoloa, Hawaii, October, 2018, DOE Supported.

[62]P. Kammel, *Muon capture in hydrogen and deuterium as a probe of the weak axial current*, 5th Joint Meeting of the APS Division of Nuclear Physics and the Physical Society of Japan, Waikoloa, Hawaii, October, 2018, DOE Supported.

[63]W. C. Pettus, *Project 8 Phase II: Measuring the Tritium Beta-Decay Spectrum using Cyclotron Radiation Emission Spectroscopy*, Contributed talk, Joint Meeting of the APS-DNP and JPS, Waikoloa, HI, Oct. 2018, DOE Supported.

[64]R. Cervantes, *Extending the ADMX QCD Dark-Matter Axion Search to Higher Masses*, Tacoma, WA: APS Northwest, DOE Supported.

[65]R. Cervantes, *Orpheus: Extending the ADMX QCD Dark-Matter Axion Search to Higher Masses*, Livermore, CA: Lawrence Livermore National Laboratory, DOE Supported.

9.5 Reports, white papers and proceedings

[66]M. Fertl, *Review of absolute neutrino mass measurements*, 2018, DOE supported.

[67]T. Alexander, H. O. Back, W. Bonivento, M. Boulay, P. Collon, Z. Feng, M. Foxe, P. García Abia, P. Giampa, C. Jackson, C. Johnson, E. Mace, P. Mueller, L. Palcsu, W. Pettus, R. Purtschert, A. Renshaw, R. Saldanha, K. Scholberg, M. Simeone, O. Šrámek, R. Tayloe, W. TeGrotenhuis, S. White, and R. Williams, "The Low-Radioactivity Underground Argon Workshop: A workshop synopsis", arXiv e-prints (2019), DOE Supported.

9.6 Seminars

[68]W. C. Pettus, *First Search for* $0\nu\beta\beta$ *in* ^{76}*Ge with the* MAJORANA DEMONSTRATOR, University of Washington CENPA Seminar, Apr. 2018.

[69]W. C. Pettus, *Project 8: Towards the Atomic Tritium Future of Neutrino Mass Measurement*, Oak Ridge National Laboratory Physics Division Seminar, July 2018.

[70]W. C. Pettus, *Weighing a Ghost: The Quest to Measure the Neutrino Mass*, University of North Carolina - Chapel Hill, Physics and Astronomy Colloquium, Jan. 2019.

[71]W. C. Pettus, *Backwards is Better: Next-Generation Detectors for Nuclear Physics*, University of North Carolina - Chapel Hill, Physics and Astronomy Chalk Talk, Jan. 2019.

9.7 Ph.D. degrees granted

[72]N. Froemming, "Optimization of muon injection and storage in the fermilab $g-2$ experiment: from simulation to reality", http://hdl.handle.net/1773/43445, PhD thesis (University of Washington, Department of Physics, Aug. 2018).

[73]R. Ryan, "MuSun: A Precision Measurement of Nuclear Muon Capture in Deuterium with a Cryogenic Time Projection Chamber", http://hdl.handle.net/1773/43734, PhD thesis (University of Washington, Department of Physics, Mar. 2019).

[74]L. Kippenbrock, "Investigation of background from the inter-spectrometer penning trap and secondary electron emission in the katrin experiment", http://hdl.handle.net/1773/43737, PhD thesis (University of Washington, Department of Physics, Mar. 2019).

[75]A. Fienberg, "Measuring the precession frequency in the e989 muon $g-2$ experiment", http://hdl.handle.net/1773/43736, PhD thesis (University of Washington, Department of Physics, Jan. 2019).

Back row: Gray Rybka, Thomas Braine, Felix Kell, Grant Leum, Seth Kimes, Ethan Muldoon, Aaron Fienberg, Kim Siang Khaw, Menglei Sun, Nicholas Orndorff, William (Drew) Byron, Brynn MacCoy, Matthew Stortini, Brent Graner, Tim Van Wechel, Ian Guinn, Ting Lin, Duncan Prindle, Walter Pettus, Kavic Kumar

Second-to-back row: Jason Detwiler, Michael Ross, Peter Kammel, Madison Durand, Joshua LaBounty, Libby (Jue) Wang, Ida Boeckstiegel, Rachel Osofsky, Micah Buuck, Hannah Binney, Alexandru Hostiuc, Gulden Othman, Keira Hansen, Zachary Wuthrich, Nick Du, Matthew Kallander, Erik Shaw, Alejandro Garcia

Second row: Megan Ivory, Erik Swanson, Martin Fertl, Derek Storm, Eric Adelberger, Charlie Hagedorn, Douglas Will, John Cramer, Hamish Robertson, David Hertzog, Alvaro Chavarria, Eric Smith, David Peterson, Pitam Mitra

Front row: Elise Novitski, Anni Xiong, Rachel Ryan, Krishna Venkateswara, Chelsea Bartram, Ali Ashtari Esfahani, Eric Machado, Bradley Dodson, Johan Pedersen, Clint Wiseman, Yifei Bai, Gary Holman